# High resolution geodetic GNSS surveys of the present day deformation along the South-Caribbean margin. Implications for earthquake hazard assessment in western and north-eastern Venezuela

Carlos Eduardo Reinoza Gomez

UNIVERSITÉ DE GRENOBLE

# THÈSE

Pour obtenir le grade de

## DOCTEUR DE L'UNIVERSITÉ DE GRENOBLE

Spécialité : **Sciences de la Terre et de l'Univers et de l'Environnement**

Arrêté ministériel : 7 août 2006

Présentée par


## Carlos Eduardo REINOZA GÓMEZ


Thèse dirigée par **François JOUANNE** et
codirigée par **Franck AUDEMARD**

préparée au sein du **L'Institut des Sciences de la Terre**
dans **l'École Doctorale Terre, Univers, Environnement**

# Application de la géodésie satellitaire GNSS à haute résolution à la déformation de la marge Sud-Caraïbe. Implication pour l'aléa sismique dans l'Ouest et le Nord-Est du Venezuela

Thèse soutenue publiquement le **15 Décembre 2014**,
devant le jury composé de :

**M. Pierre BRIOLE**
Directeur de recherche CNRS, Ecole Normale Supérieure, Rapporteur
**M. Jean CHÉRY**
Directeur de recherche CNRS, Université Montpellier 2, Rapporteur
**M. Christian BECK**
Professeur émérite, ISTerre, Université de Savoie, Président du jury
**Mme. Aurélia HUBERT**
Professeur, Université de Liège, Examinatrice
**Mme. Cécile LASSERRE**
Chargée de recherche CNRS, ISTerre, Université Joseph Fourier, Examinatrice
**M. François JOUANNE**
Professeur, ISTerre, Université de Savoie, Directeur de thèse
**M. Franck AUDEMARD**
Professeur, FUNVISIS, Universidad Central de Venezuela, Co-directeur de thèse


*Université Joseph Fourier / Université Pierre Mendès France /*
*Université Stendhal / Université de Savoie / Grenoble INP*

*A la memoria de:*

*Mi recordada "belle-mère" Digna Useche de Colón y*

*A mi primer amigo Ingeniero y Hermano Cooperador*

*Wilmer Salazar (Bicho)*

# Acknowledgements

Among the first recommendations made along these years was the importance to talk in first person. This with the purpose to stand out my personal contribution to the work. However, this is a difficult task when you know that this dissertation is a contribution of many people. My special gratitude for all the people.

This path began some years ago, before my participation, by three researchers: François Jouanne, Franck Audemard, and Christian Beck (Bill). This dissertation is in a large part result of their efforts. My special gratitude for these great geologists. François Jouanne, an extraordinary advisor, thank for their guidance and support. Franck Audemard, it is not easy to find a co-worker, an advisor and overall a friend in a one person.

Good data allow getting good results. The acquisition of data used in this thesis has been a work of more than 10 years and an enormous group of people. I do not wish downplay the team responsible of 2003 and 2005 acquisition campaigns. However, I would like to express my gratitude to a large list of colleagues and their respective institutions who helped me in this hard task during the recent years: (in the field work) Javier Oropeza, Victor Rocabado, Jélime Aray, Walter Reategui, Alí Gómez, Luis Yegres, Maxlimer Vallée, Alexi Suarez, Pedro Medina, Osmar Zambrano, Antonio Dasco, Franck Audemard, Michael Schmitz, (in the administration) Ana Maldonado, Milagros Naveda, Arianna Bravo, Victor Cano, Aura Fernandez, Guy Vernaez, Francisco Garcés from FUNVISIS, Lenin Ortega, Carlos Martínez, Pedro Oropeza, Ramón Gómez, Luis Martinez, Yeraldine Rivera, Manuel Rondón, and Gustavo Rodríguez from PDVSA-INTEVEP, Carlos Mijares, Tomás Solarte, Abdenago Nahmens, Reny Espinosa, Emiliano Morón, Mario Forgione, and Annio Moreno from PDVSA Servicios, Eliezer Concha, and Johana Bautista from IGVSB. The field work was possible thanks to the financial and logistic support offered by FUNVISIS and ISterre [FONACIT-ECOS Nord grants PI 200300009 (French code V10U01) and PI-2009000818, FONACIT-2002000478 (GEODINOS), and FONACIT-2012002202 (GIAME)].

I thank the “Coordinación Técnica de Geodesia” - IGVSB (Napoleón Hernandez, Tirza Ramirez ) for the continuous GNSS data. I thank Sylvain Barbot (Nanyang Technological University), Miguel Palma, Rafael Abreu, Leonardo Alvarado, and Donata Liuzzi (former co-worker) from FUNVISIS, and Carlos Mendoza (Centro de Geociencias, UNAM) for their collaborations. I thank Hector Mora from “Servicio Geológico Colombiano”and Victor Cioce from “Universidad del Zulia” for their appropriate comments and delivery GNSS data.

I would like to thank the members of the jury: Pierre Briole, Jean Chéry, Cecile Lassere, and Aurelia Hubert-Ferrari for reviewing this work and their contribution in order to improve the manuscript.

I express my gratitude to Fundación Gran Mariscal de Ayacucho and the French Embassy in Venezuela for Grant N° 756514C during my stay in ISTerre.

Je voudrais aussi remercier à tout l’ensemble du laboratoire ISTerre – Chambéry ainsi comment l’équipe Mécanique de Failles, spécialement François Renard. Ici, j’ai connu des gens sur le domaine académique auxquelles j’espère garder son amitié. Merci à Agus (Budy), Anaïs, Camille, Cécile, Fabien, Hervé, Joaquin, Elodie (Lalo), Laure, Léa, Olivier, Pascale, et Tomas, (et bien sûr Elodie, Adrien, Marion, François et Marguerite). Merci à Philippe Lesage et sa famille.

Esta experiencia francesa no dejó de tener su toque patrio. Mis gracias infinitas a Oswaldo y Corina por aquel primer recibimiento y por su permanente ayuda durante el tiempo que compartimos. Gracias a mis otros paisanos por todo su apoyo: Iliana, Enzo, Patrick, Javier O., José Ángel y José Alfredo. Ha sido un gran alivio poder encontrarlos para poder transmitir exactamente lo que sentía sin utilizar el traductor. Gracias a mis otros hermanos “latinoamericanos”, Eva la más venezolana de las mexicanas que conozco, Alexis, Lisa y David, entre muchos otros.

Como no agradecer a Sarín e Ignacio, con quienes compartimos la experiencia de vivir por un rato de este lado del mundo. Gracias por todo el apoyo y cariño, ha sido una bendición con ustedes poder tener la familia tan cerquita. De igual forma, quiero agradecer a todos los familiares y amigos que

hicieron ese gran esfuerzo de venir a visitarnos. Esos momentos de recuentro, te dan la fuerza para continuar. Quisiera dedicar unas palabras especiales a la Sra. Digna, quien desde siempre fue un gran apoyo, y a pesar de no estar físicamente entre nosotros, su espíritu y su recuerdo son una motivación constante para seguir luchando.

I thank to Crelia Padron family's, and Victor Rocabado family's for being the best hosts during my stays in Venezuela. Also, my colleagues and friends for many years from Geophysics Department of FUNVISIS.

As my father said: the woman does the man and the man does the woman. I am deeply grateful with my lovely wife Sirel. She could be mentioned in almost all paragraphs. She has been a colleague in the acquisition campaign, an officemate, co-PhD student and roommate. Thank you for your support, patience, total surrender, and greatest love.

# Abstract

The Caribbean-South American plate boundary is described as a wide active transpressional zone. This dissertation presents GNSS observations in Western and Northeastern Venezuela, and Trinidad, used to constrain the regional geodynamics and study the kinematics of the principal faults along this plate boundary.

Here, a whole work of conception, installation of network and measurements with two campaigns of GNSS observations in Western Venezuela is presented. In the case of Northeastern Venezuela, a GNSS data acquisition campaign was carried out measuring pre-existing sites installed since 2003and occupied by FUNVISIS and University of Savoie team. The data processing for these sites includes data from previous acquisition campaigns and permanent GNSS stations.

In Western Venezuela, observed velocities correspond roughly with the motion of Caribbean and South American plates. Nonetheless, the slow rate of fault-slip of main faults and the short span between the data acquisition campaigns in Western Venezuela do not allow assessing the velocity field with sufficient accuracy.

In northeastern Venezuela, I focused on the effects of variable elastic properties of the El Pilar Fault (EPF) and surrounding medium on inferred slip rates and locking depths. The asymmetric velocity field on both sides of EPF have been evaluated with five approaches. In a first step, a simple elastic half-space model was applied showing a 1.8 km locking depth. Next, a model considering contrast of material properties across the EPF depicts out 3 km locking depth and a 0.37 asymmetric coefficient indicating that the igneous-metamorphic northern side has a rigidity ~1.7 times higher than the sedimentary southern side. From a three-dimensional elastostatic model, the presence of a near-fault low-rigidity compliant zone has been evaluated suggesting a zone in the upper 3 km in depth and going from 1 to 5 km width with a 30 per cent of rigidity reduction. The creep associated to the shallow locking depth was clearly shown with the slip distribution model and the displacement simulation method. The results show a widespread partially-creep pattern in

the eastern upper segment, while the upper western segment exhibits a partially locked area which coincides with the rupture surface of 1797 and 1929 earthquakes.

From the compilation of GNSS observations and triangulation-to-GPS comparison of previous studies, the kinematic of main faults in Trinidad has been studied. The velocity field across the Central Range Fault (CRF) points out an asymmetry of velocity gradient on both sides. The heterogeneous asymmetric model point out a 2.5 km locking depth with a 0.20 asymmetric coefficient indicating that the northern side has a rigidity ~3.3 times higher to the southern side. Similar approaches have been applied to the Arima Fault (AF). The creep in the upper part of CRF as response to the shallow locking depth was quantified using a slip distribution model. A creep of 12 mm/yr was calculated in the southwestern onshore portion of the CRF and the Warm Springs Fault, nevertheless, this behavior changes northeastward where the CRF show a significant decrease of slip in the upper part. The slip along the AF appears locked along its upper and lower part in the onshore portion demonstrating that this segment section is not needed to simulate observed velocities and is inactive. Furthermore, the Los Bajos Fault is shown with a slip of 7 mm/yr in the segment upon which the EPF in Venezuela transfers its slip eastward and that act as a synthetic Riedel shears.

The localized aseismic displacement pattern associated with creeping or partially creeping fault segments could explain the low level of historical seismicity in the Northeastern Venezuela and Trinidad. The EPF in Venezuela and the CRF accommodate between 50 and 60% of the plate boundary zone motion that points out a reduction of the seismic hazard almost by half.

# Résumé

La frontière de plaque sud-Caraïbe est une zone large et active de transpression. Cette thèse présente des observations GNSS dans l'Ouest et le Nord-Est Vénézuélien, et Trinidad utilisées pour contraindre la géodynamique de la zone d'étude et la cinématique des principales failles dans cette frontière des plaques.

Dans ce manuscrit, je présente un travail intégral de conception, installations d'un réseau géodésique dans l'ouest du Venezuela et deux campagnes d'acquisition des données GNSS. Dans le Nord-Est Vénézuélien, une campagne d'acquisition des données a été réalisée avec la réoccupation des repères installés et mesurés depuis 2003 par un groupe des chercheurs de FUNVISIS et l'Université de Savoie. Lors du traitement des données, j'ai inclus l'ensemble des campagnes antérieures disponibles et les données des stations GNSS permanentes de la région. Les vitesses observées dans l'Ouest Vénézuélien correspondent bien avec le mouvement des plaques Caraïbes et Sud Amérique. Cependant, le lent taux de déplacement des failles principales et le court intervalle de temps entre les observations n'a pas permis d'obtenir un champ des vitesses avec suffisamment de précision. Au contraire, les observations épisodiques réalisées sur dix ans dans le Nord-Est du Venezuela ont permis contraindre la cinématique de la faille d'El Pilar (EPF).

Dans cette région, pour comprendre le champ de vélocité mesuré, nous avons étudié les effets de la variation des propriétés élastiques sur la faille et de part et d'autre de celle-ci. Le champ de vitesses asymétrique obtenu sur les deux côtés de la faille a été simulé avec cinq approches. Un premier modèle simple dans un demi-espace homogène montre une profondeur de blocage de 1,8 km. À l'aide d'un modèle hétérogène en considérant des contrastes entre les propriétés du matériel de part et d'autre de l'EPF, nous avons montré une profondeur de blocage de 3 km et un coefficient de rigidité de 0,37. Cette dernière valeur indique que le côté nord à l'EPF composé de roches ignées et métamorphiques présente une rigidité ~1,7 fois supérieure au côté sud composé de formations sédimentaires. À partir d'un modèle tridimensionnel élastostatique, la présence d'une zone de

compliance a été suggérée. Cette zone proche de la faille caractérisée par une faible rigidité serait présente de la surface à 3 km de profondeur et présenterait une largeur de 1 à 5 km et une réduction de rigidité de 30%.

La simulation des vélocités avec un modèle de distribution du glissement le long du plan de faille montre la présence de glissements asismiques dans toute la partie supérieure du segment Ouest tandis que la partie supérieure du segment Est se montre partialement bloquée, ce secteur partiellement bloqué correspondrait à la rupture en surface des séismes de 1797 et 1929.

En se basant sur la combinaison des vélocités obtenues par comparaison GPS/GPS et triangulation/GPS nous avons étudié la cinématique des failles principales de Trinidad. Le champ de vitesses de part et d'autre de la faille de la cordillère centrale de Trinidad (CRF) indique une asymétrie du gradient de vitesse de part et d'autre de la faille. Le modèle simple de déformation interseismique montre une profondeur de blocage de 10 km et le modèle hétérogène asymétrique suggère une profondeur de blocage de 2,5 km avec un coefficient de rigidité de 0,20 %, qui suggère une rigidité trois fois supérieure du côté nord par rapport au côté sud.

La simulation du glissement le long des failles de Trinidad montre un glissement asismique atteignant 12 mm/an le long de la partie supérieure de la CRF et de sa prolongation en mer la Warm Spring Fault. Ce comportement change vers le nord-est avec une diminution importante du creep le long de la partie supérieure de la faille. La faille d'Arima se montre inactive à Trinidad. L'existence d'un creep important le long des failles d'El Pilar et de la faille de la cordillère centrale de Trinidad pourrait expliquer le bas niveau de sismicité instrumentale, historique et préhistorique de ces accidents qui localisent pourtant un coulissement de 20mm/an. L'existence de ce creep induirait une réduction de l'aléa sismique de moitié.

## Table of Contents

## CHAPTER 1:

# INTRODUCTION

Accurate geodetic measurements with Global Navigation Satellite System (GNSS) have allowed determining tectonic plate rate movements, behavior of plate boundaries, crustal and inter-crustal deformation and fault kinematic among different aspects in a short-time span (e.g. Beutler et al., 1987, DeMets et al., 1990, Lisowski et al., 1991). Likewise, numerical models based on geodetic observations (e.g. surveyed trilateration, Global Navigation Satellite System (GNSS) observations and Interferometric synthetic aperture radar - InSAR) have been used to study the main strike-slip faults around the world (e.g. San Andreas Fault, North Anatolian Fault, Altyin Tagh Fault) with the purpose of determining rate of deformation, to constraint properties of fault and surrounding medium, etc.

The aim of this dissertation is to apply many aspects of GNSS methodology to the kinematic characterization of important faults in the Caribbean-South America plate boundary. Venezuela and Trinidad show an exceptional target for such a study, as the southern limit of the Caribbean plate is well represented by the right-lateral strike-slip Boconó–San Sebastián–El Pilar–Los Bajos/El Soldado–Warm Springs-Central Range fault system (Audemard 1999b; Audemard et al., 2000; Weber et al., 2001; Trenkamp et al., 2002; Soto et al., 2007) . These faults associated with this boundary can generate important events as the Mw=6.9 1997 Cariaco and the Mw=6.2, 2009 Golfo Triste earthquakes (http://www.funvisis.gob.ve). The knowledge of their activity is essential to estimate the earthquake hazard assessment along Venezuela and Trinidad. Although the Venezuelan active tectonics has been developed by several authors along decades (e.g. Bucher, 1952, Molnar & Skyes, 1969, Pérez & Aggarwal, 1981, Stéphan et al., 1990, Beltrán, 1993, Audemard et al., 2000) yet there are still many issues of strong debate.

In this study I focus upon three main zones: two first ones in Western and northeastern Venezuela, and Trinidad and Tobago zone (Figure 1.1).

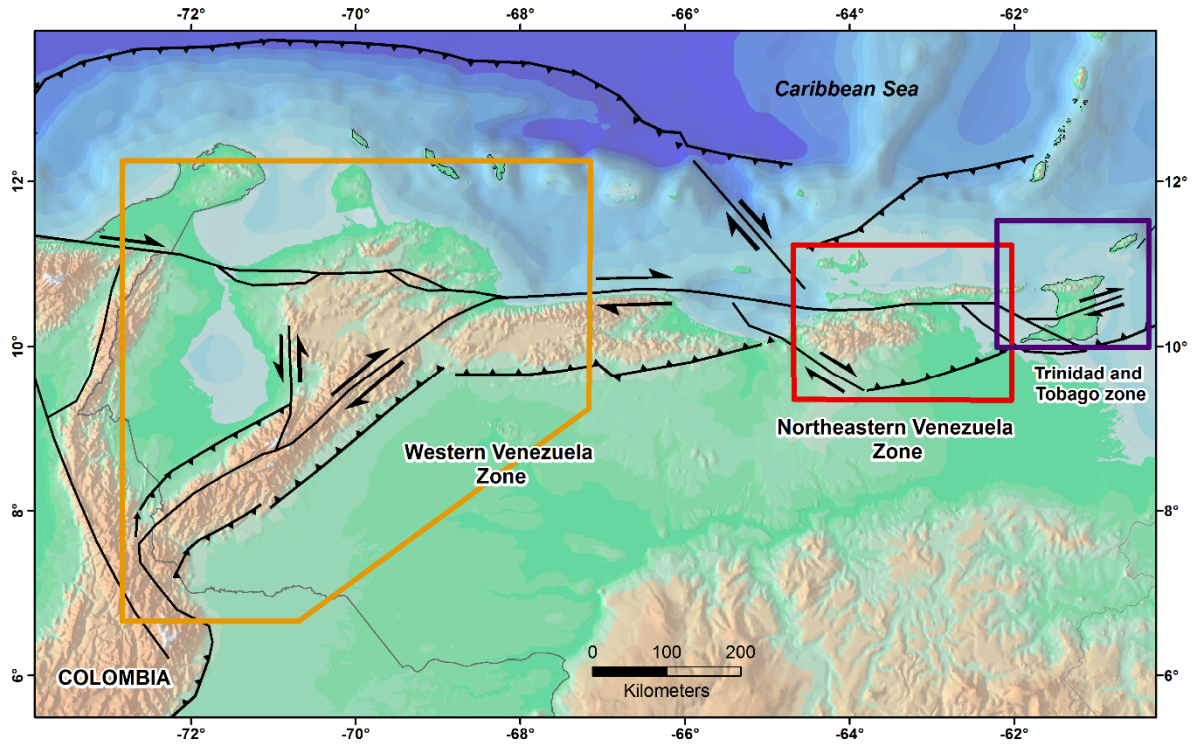


***Figure 1.1.*** *The principal study zones in this dissertation: Western and Northeastern Venezuela, and Trinidad and Tobago. (Schematic geodetic map based in Audemard 1999b; Audemard et al., 2000; Weber et al., 2001; Trenkamp et al., 2002; Soto et al., 2007).*

Since 1988, fault kinematic studies based on geodetic observations have been applied in Venezuela with the CASA UNO Project (Kellogg & Dixon et al., 1990) and certainly, there have been important efforts in this sense (Pérez et al., 2001a; 2001b, 2011; Baumbach et al., 2004; Jouanne et al., 2011); however, this dissertation supposes a work more complete than the previous one, because it covers almost all Venezuelan territory including the Trinidad and Tobago as study zone. Furthermore, a whole work of conception, installation; and two acquisition campaigns has been carried out in western Venezuela (Fig. 1.2). Adding sites measured in the northeast Venezuela, the network of sites observed is even greater in terms of

number and density of benchmarks. Otherwise, the processing includes acquisition campaign data from 1994 to 2013, permanent GNSS data of neighboring and local networks for a span of more than ten years.

The study of geodetic velocity field through the numerical models allows constraining the geometry of the faults and properties of the surrounding medium. From the simplest screw model (Chinnery, 1961; Weertman and Weertman, 1964; Savage and Burford, 1973) to determine locking depth and far-field velocity in an elastic half-space, a geodetic modelling exploration is carried out including several aspects step by step as: inhomogeneity of medium, contrast of rigidity across the fault, asymmetry of velocity gradient, the presence of a near fault low rigidity zone, possibility of dipping segments and variations in the fault-slip distribution.

***Figure 1.2.*** *The brass spit installed on an existing concrete benchmark in MCH0 (Chacopata cape, Sucre state) site- Northeastern network.*

## 1.1 Organization of the manuscript

This dissertation comprises two introductory chapters, two chapters containing the collection and analysis strategy of data (with an introductory manuscript about “the state of art” of geodetic measurements applied in Venezuela), two chapters that include manuscripts containing the main results, and a conclusion chapter.

The second chapter (after general introduction) presents an overview of the geological and geodynamic setting of the plate-boundary zone between Caribbean and South American plates. Because this study covers an important extension of territory, I propose two main study zones: Northeastern Venezuela and Trinidad, and Western Venezuela. In the third chapter I introduce a general idea of numerical models applied to strike slip faults in order to study the instantaneous deformation. Elastic models, evaluation of low rigidity zones, and distribution of displacements are presented here. The four and fifth chapters show a complete work of conception, installation and two measuring of a GNNS network in the western Venezuelan. For the northeastern Venezuela, I show details about the re-occupation in early 2013 of sites installed since 2003 by FUNVISIS and University of Savoie team. Additionally, for the processing and with the purpose of establishing an overview on the GNSS geodetic measurements in Venezuela and its surroundings, an exhaustive compilation of existent data was carried out. Previous acquisition campaigns: CARIVEN 1994, Trinidad 1994, Venezuela 1998, and Caribbean 1999, as well as, a large set of cGNSS stations of several networks including: the Red de Estaciones de Monitoreo Satelital GPS - REMOS - (GPS Satellite Monitoring Station Network of Venezuela), GEORED - Colombian Geological Survey (former INGEOMINAS), the International GNSS Service (IGS), networks associated to the University Navstar Consortium (UNAVCO) with the Continuously Operating Caribbean GPS Observational Network (COCONet), and GNNS Trinidad and Tobago Active Geodetic Network.

The sixth chapter, which comprises a submitted manuscript, shows a detailed evaluation by applying several methods aiming at studying the velocity field along the El Pilar Fault (EPF) in Northeastern Venezuela. From geodetic velocities obtained and referenced to the South American frame, and in order to constraining the kinematic of the EPF, the effects of variable elastic properties of surrounding medium and fault geometry on inferred slip rates, far-field velocity and locking depths are presented. The seventh chapter also presented a manuscript focused on the current deformation of Trinidad, where the eastward prolongation of Caribbean and South-American plate boundary is studied. Existent geodetic data was compiled with the purpose of characterizing the main faults across this two island nation.

Eventually, an eighth chapter with general discussions, conclusions and perspectives is provided. I argue about the methodology, results and contributions to the knowledge of geodynamic in Trinidad, Western and Northeastern Venezuela. The broad perspectives that follow depict out an interesting future for the kinematic studies in Venezuela. Many aspects are envisioned as the consolidation of existing networks, installation of permanent GNSS stations and the inclusion of new methodologies (Interferograms, creep-meter) among others.

# CHAPTER 2:

# GEOLOGICAL AND GEODYNAMIC SETTING

## 2.1. Introduction

Northern Venezuela is essentially a plate-boundary zone between Caribbean and South America plates (Figure 2.1), where a complex set of blocks or microplates are involved. This 1,600 km-long active plate margin is considered as a broad zone of tectonic transpression or strain partitioning with the association of strike-slip and convergence (Stéphan, 1985; Babb and Mann, 1999; Audemard, 2001; Audemard et al., 2005). This wide active transpresional zone (Soulas, 1986; Audemard, 1993, 1998; Beltrán, 1994; Singer and Audemard, 1997) comprises the right-lateral strike-slip Boconó–San Sebastián–El Pilar–Los Bajos/El Soldado–Central Range (Warm Springs) fault system (Molnar and Sykes, 1969; Minster and Jordan, 1978; Pérez and Aggarwal, 1981; Stéphan, 1982; Aggarwal, 1983; Schubert, 1984; Soulas, 1986; Beltrán and Giraldo, 1989; Speed et al., 1991; Singer and Audemard, 1997; Pérez et al., 2001a, b; Weber et al., 2001, 2011; Pindell and Kennan, 2007; Audemard, 2009). The Caribbean/South American plate oblique convergence extends on Trinidad where the regional structure of this zone is also affected by subduction of the oceanic lithosphere of the Atlantic plate beneath the Caribbean plate at the Lesser Antilles Arc (Weber et al., 2001).

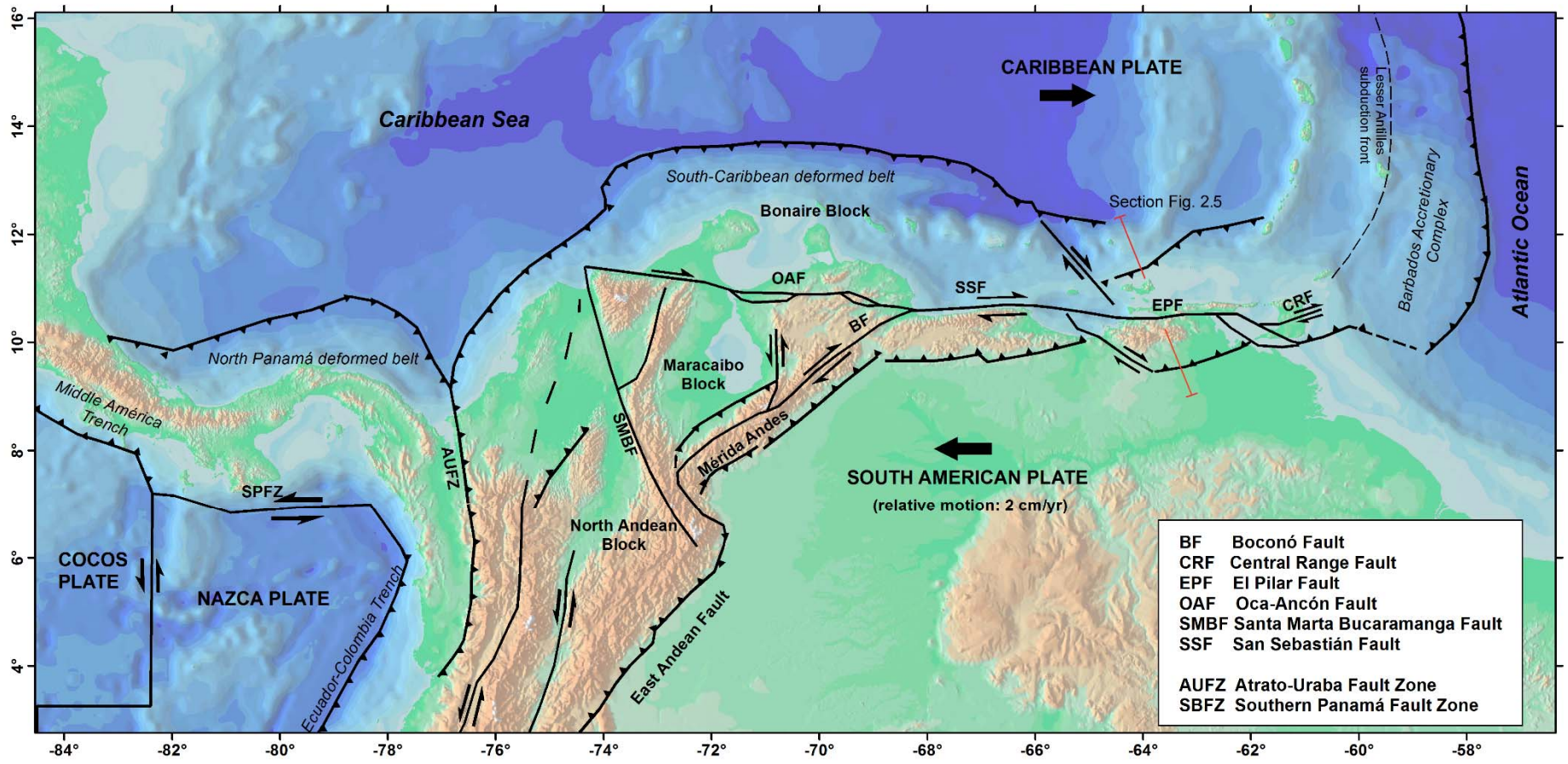


***Figure 2.1.*** *Schematic geodynamic map of the southeastern Caribbean (Audemard, 1999b; Audemard et al., 2000; Weber et al., 2001; Trenkamp et al., 2002; Soto et al. 2007). We show the principal blocks: Bonaire, Maracaibo, and North Andean interacting with the Caribbean, Nazca, and South American plates.*

## 2.2. Northeast Venezuela and Trinidad

### 2.2.1. The El Pilar Fault zone

The EPF is an almost pure strike-slip fault that extends eastward for some 350 km (e.g. Soulas, 1986; Beltrán, 1993, 1994; Audemard et al., 2000), from the Cariaco Trough to the Gulf of Paria (Figure 2.2). Conversely, the depth extent of the EPF is not well-constrained. From steep gravity gradient across the fault, Vierbuchen (1984) inferred that the fault is nearly vertical down to a depth of at least 5 to 10 km; Schubert (1984) proposed a depth of approximately 8 km from seismic-reflection profiles when an average P-wave velocity of 5.2 km/s is assumed. A depth extent of 15 to 20 km was obtained by Rossi et al. (1987) based on a joint-interpretation of seismic, magnetic, and gravimetric data. More recently, works related to the 1997 Mw=6.9 Cariaco earthquake have permitted to define the brittle-ductile transition for the EPF at 12 km according to the depth distribution of aftershocks (Figure 2.3; Baumbach et al., 2004) and at 14 ± 2 km based on geodetic observations (Pérez et al., 2011). Clark et al. (2008) based on wide-angle onshore-offshore reflection/refraction modelling determined a depth of Moho reaching 48 km beneath the EPF. This corresponds to a depth increase of 16 km coinciding with the dextral strike-slip system between the Coche fault and the EPF. However, the region is mainly characterized by an intra-continental shallow seismicity in the first 20 km associated to the EPF. The seismicity deeper than 40 km is related to the southern tip of the Lesser Antilles subduction under Trinidad and Tobago, the Paria Peninsula and the active island arc of the Lesser Antilles (Figure 2.4).

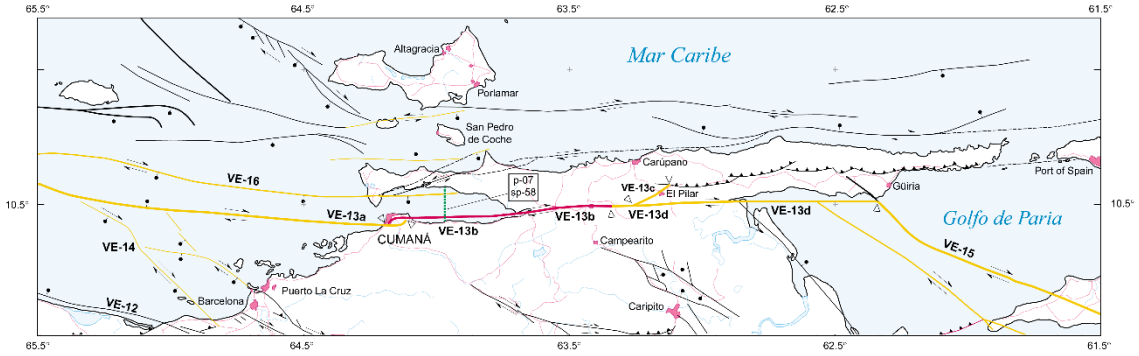


***Figure 2.2.*** *EPF separated in four fault segments are shown in a portion of the Map of Quaternary Faults of Venezuela (Audemard et al., 2000).The original nomenclature VE-13a, VE-13b, VE-13c, and VE-13d represent western to eastern segments of the EPF. Los Bajos Fault is indicated by the code VE-15. Green pointed line represents the pinger line 07 and sparker line 58 shown in the figure 2.8.*

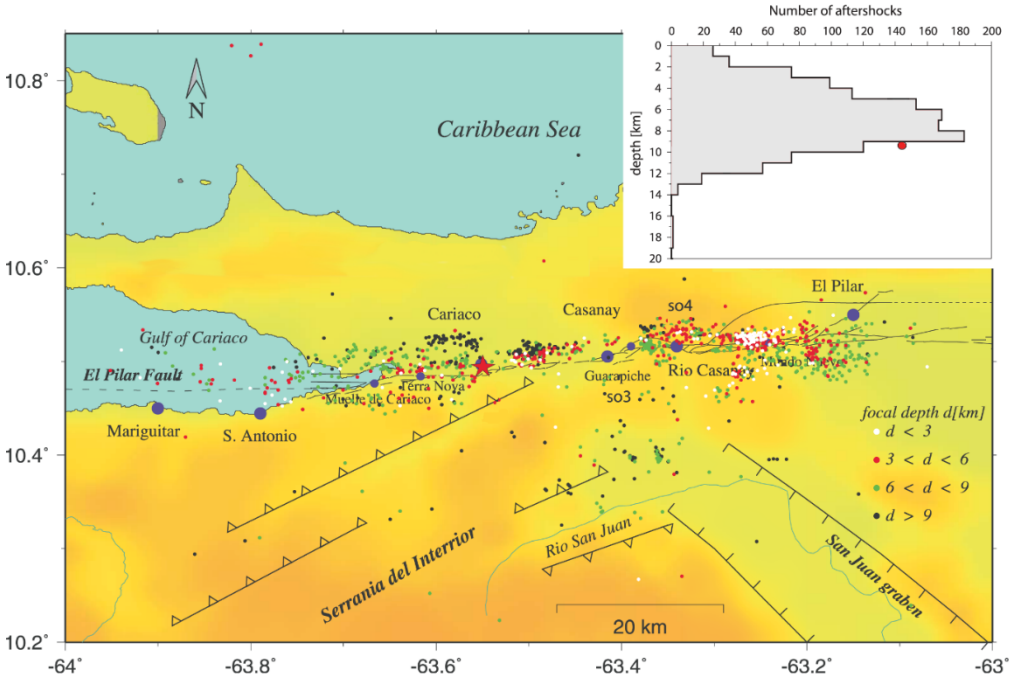


***Figure 2.3.*** *Distribution of Cariaco earthquake aftershocks along the EPF zone indicating the focal depth. Above and right, depth-frequency distribution of 1306 Cariaco earthquake aftershocks. The red star and circle in the large and small figures respectively show the epicenter and focal depth of the main shock. (Both figures are taken and modified from Baumbach et al., 2004).*

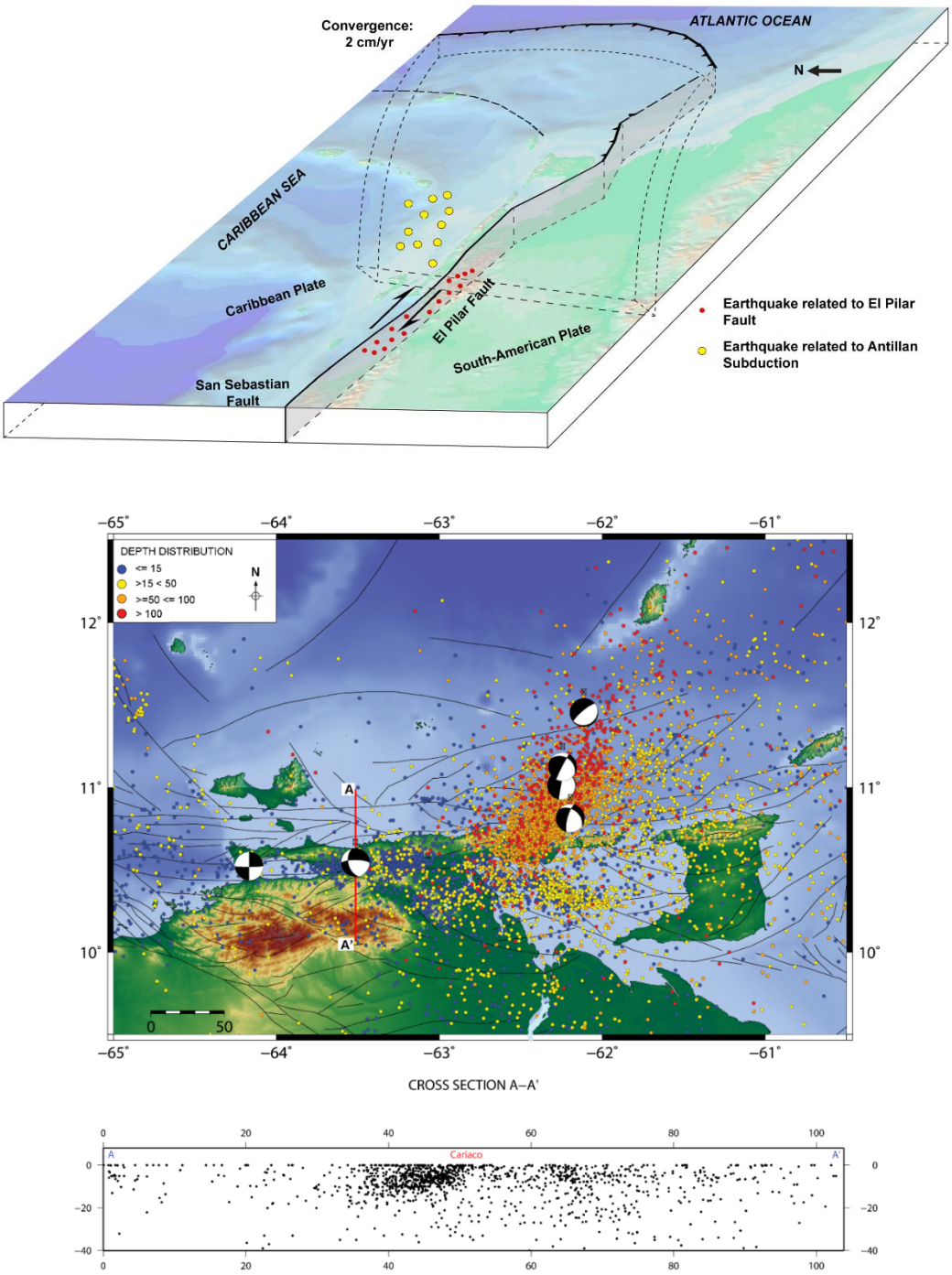


***Figure 2.4.*** *(Above) Tridimensional scheme and distribution of seismicity in northeastern Venezuela indicating the existence of two different types of seismicity: a first associated to the crustal activity of the EPF and other crustal faults and a second seismicity with deepest earthquakes mainly related to the Antillean subduction (Modified from Jouanne et al. 2011). (Below) Distribution of seismicity in northeastern Venezuela from the 1910-2010 FUNVISIS*

*catalog. The active faults are from Beltrán (1993) and focal mechanism from Audemard (1999); Audemard et al. (2005), and Palma et al. (2010).*

The EPF roughly separates two very different geological provinces (Figures 2.5). On the north side, it is the Eastern Cordillera de la Costa, composed of Lower Cretaceous metasediments and igneous rocks accumulated in a tectonically and volcanically active environment. These rocks were metamorphosed into greenschist facies, and deformed by imbricated folds and thrust faults; metavolcanic rocks and ophiolitic remnants, metamorphosed in blueschist facies, are also included (Campos, 1981). On the south side of the EPF the Serranía del Interior exposes a fold-and-thrust belt, made of non-metamorphosed Cretaceous and Paleogene sediments (Metz, 1965; Vierbuchen, 1984; Jacome et al., 1999). Moreover, Grosser et al. (2001) showed that the shear strength of the material north of the EPF is higher than that for the material south of the fault from a 3-D velocity tomography study. Besides, Baumbach et al. (2004) pointed out that the aftershock distribution of the 1997 Mw=6.9 Cariaco earthquake had a very sharp boundary on the north of the EPF, as opposed to the south of the fault the boundary is more diffused. From wide-angle seismic reflection/refraction Clark et al. (2008) also shown velocities decreasing southward to the EPF from 3.5 km/s to 2.2 km/s and a shallow region of relatively high velocities (>6.5 km/s) probably related to exhumated metamorphics of Margarita Island and the Araya-Paria peninsula. With a similar methodology, Christeson et al. (2008) presented results of a regional wide-angle seismic profile indicating the transition from allochthonous terrane of forearc affinity to the passive margin of northern South America (Figure.2.6).

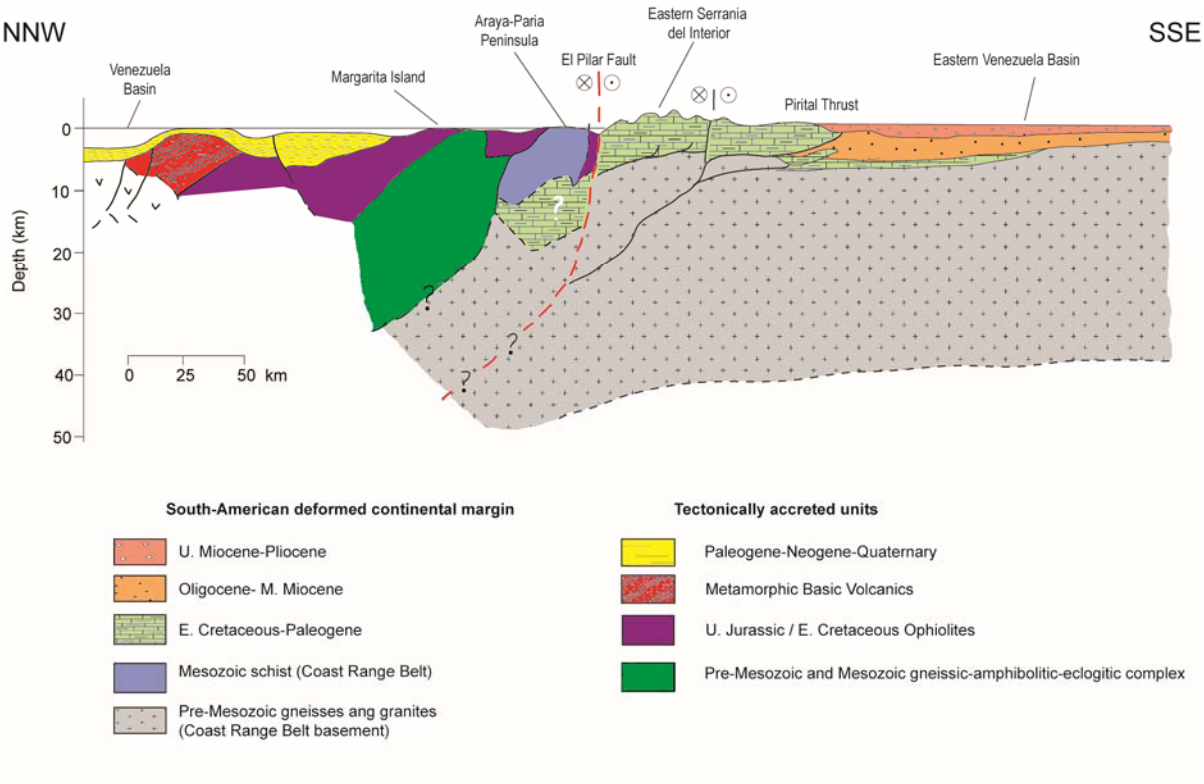


***Figure 2.5.*** *Simplified cross section of the southeastern Caribbean margin (Based on maps and sections compiled from Bellizzia et al., (1976); Stéphan et al., (1980); Campos (1981); Beck (1986); Chevalier (1987); location in figure 2.1).*

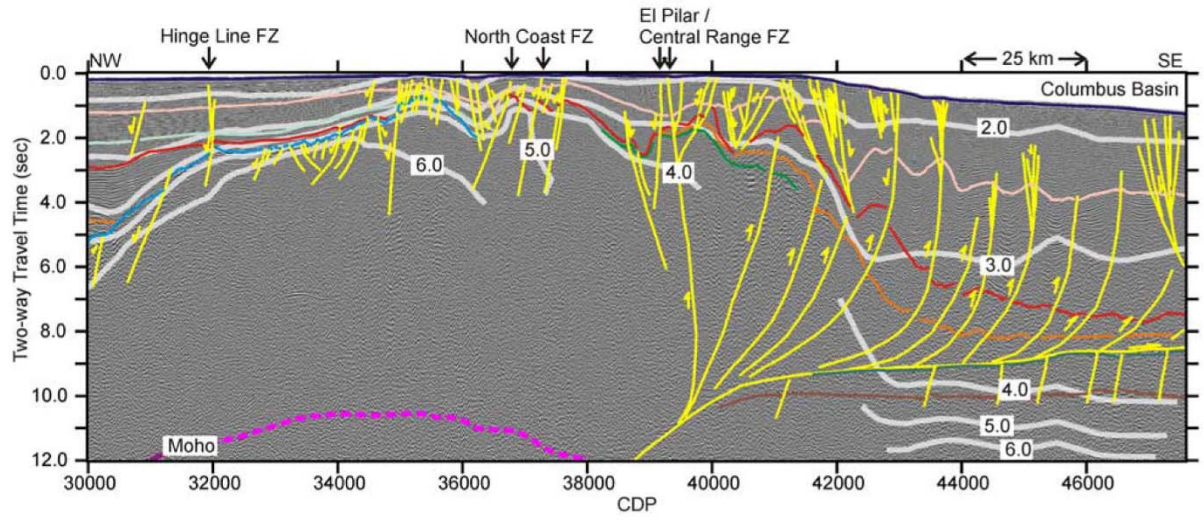


***Figure 2.6.*** *Seismic reflection image in the southeastern Caribbean crossing the EPF (from Christeson et al. 2008).*

The dextral sense of slip of this fault has been suggested on geological data since Metz (1965) and few available focal mechanisms depicted by Pérez and Aggarwal (1981). Even though the existence of faulting or “rents” has been reported since 1799 by Alexander von Humboldt and the fault zone has been studied previously (Maxwell & Dengo, 1951; Rod, 1956; Alberding, 1957; Christensen, 1961) even named as El Pilar, after a small village in the depression, by Liddle (1946). Geomorphic evidence of tectonic activity as right-laterally offset drainages, fault trenches, pop-ups, pressure ridges, fault saddles, sag or fault ponds, and fault scarps have contributed to establish the dextral sense (FUNVISIS, 1994; Beltrán et al., 1996). Recently, the slip direction of this fault has been unequivocally confirmed by the dextral character of the surface break associated with the 1997 Mw=6.9 Cariaco earthquake (Audemard, 1997, 1999a, 2006), and by focal mechanism solutions for this event and its aftershocks (Pérez, 1998; Baumbach et al., 1999, 2004; Romero et al., 2002; Audemard et al., 2005). Furthermore, the recent GPS studies carried out along the EPF depict a clear evidence of dextral slip (Pérez et al. 2001; Weber et al., 2001; Jouanne et al., 2011). Weber et al. (2001) derived a rate of 20 ±2 mm/year for the eastward Caribbean plate motion in a N89°E direction in the vicinity of the 1997 Mw=6.9 Cariaco main shock. For their part, Pérez et al. (2001) calculated a rate of 20.5 ± 2 mm/year along N 84° ± 2° E azimuth at 65° W longitude for the Caribbean plate relative to the South American plate. Indeed, they explained that east of 68°W longitude, the velocity field across the Caribbean-South American plate boundary is confined to a narrow shear zone and 80 per cent of the surface deformation is contained within an 80-km-wide zone centered a few kilometers northward of the EPF; whilst, Jouanne et al. (2011) pointed out the lack of significant displacement (specially shortening) in the Serranía del Interior and eastward motion of up to 22 mm/y (relative to fixed South American plate) of benchmarks located on the north side of the EPF (Figure 2.7). From uniform elastic half-space models for simulating current velocities (Okada, 1985) using a set of dislocations, these authors

showed that the whole Caribbean-South American relative displacement takes place along the EPF, as well as an important component of aseismic displacement along the upper part of EPF.

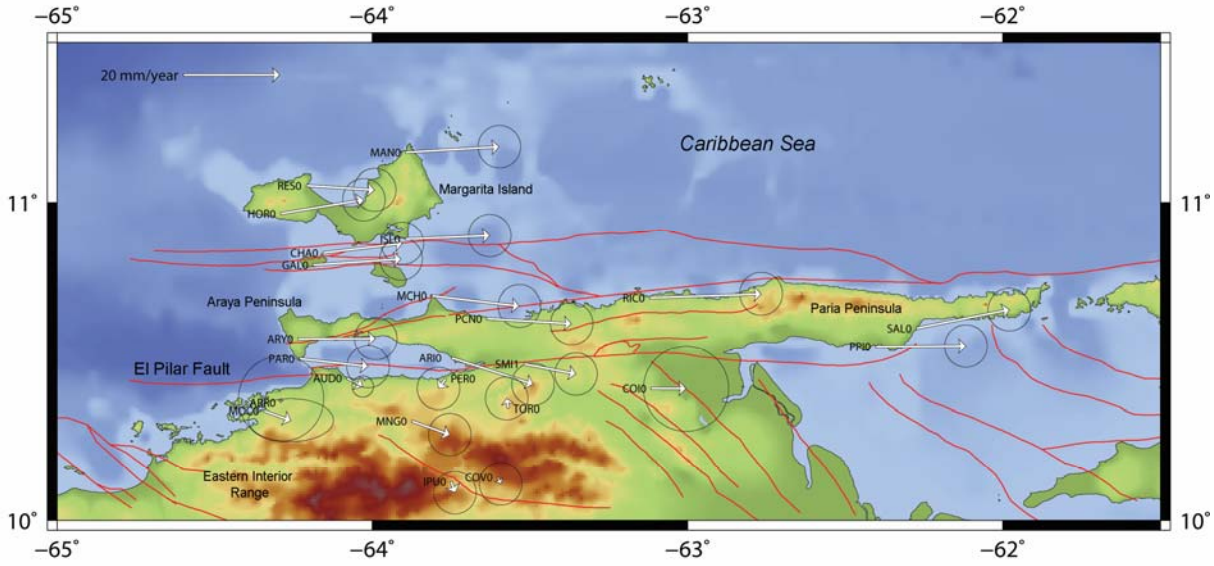


***Figure 2.7.*** *Observed velocities (white) with error ellipses drawn for 66% confidence level derived from comparison of 2003 and 2005 GNSS campaign measurements (Data from Jouanne et al. 2011). Velocities are expressed in the South America plate reference frame, using the rotation pole proposed by Altamimi et al. (2007). The active faults in northeastern Venezuela are from Audemard et al. (2000). Topography and bathymetry data are from Lindquist et al. (2004).*

The current activity of the fault is underlined by an important historical seismicity; since the beginning of the Spanish conquest in the early 16$^{th}$ century, the northeast of Venezuela underwent several events in 1530, 1684, 1766, 1797, 1853, 1929, (Audemard, 1999b, 2007) and recently by the July 9, 1997 Mw=6.9 Cariaco earthquake along the strike-slip EPF. The field reconnaissance of the ground breaks after the 1997 earthquake confirms that this event took place on the ENE–WSW trending onshore portion (~80 km) of the dextral EPF between the Gulfs of Cariaco and Paria (Audemard, 2006). The deformation associated to the active

traces of the EPF has been also identified using high-resolution reflection seismic surveys (Audemard et al., 2007; Van Daele et al., 2011) and the excavations of trenches (Beltrán et al., 1996; Audemard, 2011). The EPF active fault trace has been subdivided in four different segments (Figure 2.2) according to the Quaternary faults map presented by Audemard et al. (2000): 1) Offshore section characterized by a submarine trace west of Cumaná that bounds the Cariaco Trough on the south and dies out at the Caigüire Hills, at Cumaná in a restraining stepover (VE-13a); 2) Cumaná to Casanay section that includes the 1929 and 1997 rupture surfaces and it extends from the north side of Cumana restraining stepover to the village of Río Casanay (VE-13b). The submarine trace divided in two parts has been observed in the high resolution reflection seismic survey (Audemard et al., 2007; Van Daele et al., 2011) indicating a dextral transtensive overlap of the EPF in the Guaracayal depression (Figure 2.8); 3) Casanay to El Pilar 30 km long section that slightly diverges to the ENE (VE-13c); and 4) Guaraúnos section described as an east-west trending segment from the Sabanas de Venturini to south of the Paria Peninsula in an offshore part (VE-13d). The EPF connects in a transtensional stepover with the Warm Springs fault, an active dextral strike-slip fault in Trinidad's western offshore, member of homonymous system that is named the Central Range fault zone when it enters western-central Trinidad (Weber et al., 2001; 2011).

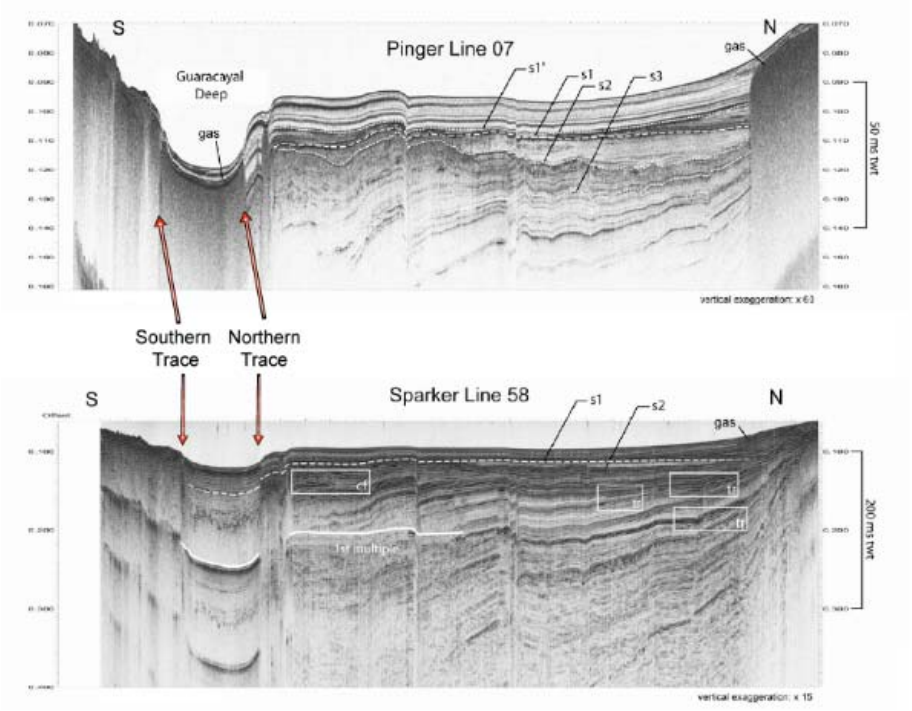


***Figure 2.8.*** *The southern and northern EPF traces are shown in 3.5 kHz-pinger (Top) and sparker (Bottom) seismic reflection profiles (Base profiles after Van Welden, 2007; location in figure 2.2).*

### 2.2.2. The Central Range Fault zone

The Central Range fault is the principal active structure that accommodates at least 60% of the total rate of strike-slip motion (~20 mm/yr) at the Caribbean-South American plate boundary in Trinidad. This fault is characterized by a topographically prominent lineament in the central part of this island (Figures 2.9 a, b). The dextral sense assumption is based in geodetic investigations (Saleh et al., 2004; Rodríguez, 2008; Weber et al., 2011) and neotectonics studies (Soto 2007, Soto et al., 2007, 2011, Prentice et al., 2010). The recent GPS-based geodetic studies show a 12±3 mm/year dextral strike-slip and depict that most part of the present-day shearing is taken up along the CRF predicting a highly transpressional style of deformation (Figures 2.10 a, b). It must be noticed that the alleged eastward prolongation of the EPF in northern Trinidad (The Arima Fault) accommodates no significant right-lateral motion.

In fact, the reverse Arima fault of northern Trinidad that bounds the southern foothills of the Northern range of Trinidad has been not suggested as the eastward prolongation of the EPF but of the reverse Tunapuy fault in the Paria peninsula (Beltrán, 1998; Audemard, 2000; Audemard et al., 2005).

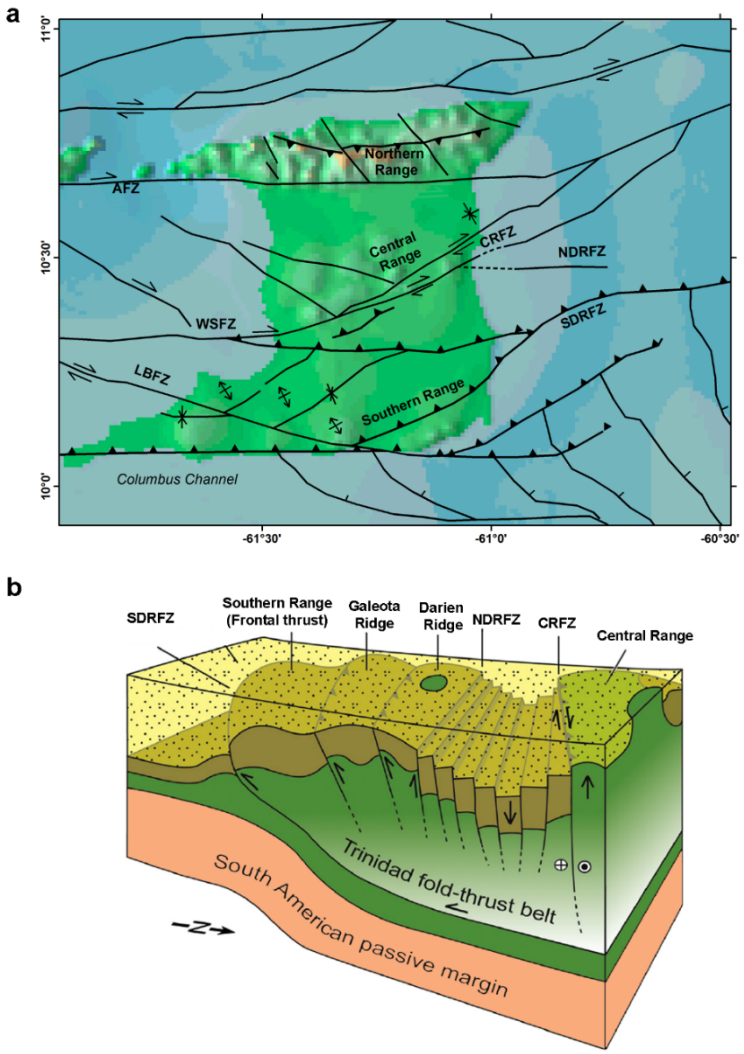


***Figure 2.9.*** *(a) Distribution of onshore and offshore fault systems of Trinidad. We show the location of three main ranges of Trinidad, Northern, Central and Southern range, as well as the principal structures including: The Arima Fault zone (AFZ), the Central Range Fault zone (CRFZ), Los Bajos Fault zone (LBFZ), the North Darien Ridge Fault zone (NDRFZ), the South Darien Ridge Fault zone (SDRFZ) and Warm Springs Fault zone (WSFZ). The location and*

*character of faults were compiled from Soto et al. (2007; 2011). (b) Block diagram of major structures in Central and Southern Trinidad (Modified from Soto et al. 2011).*

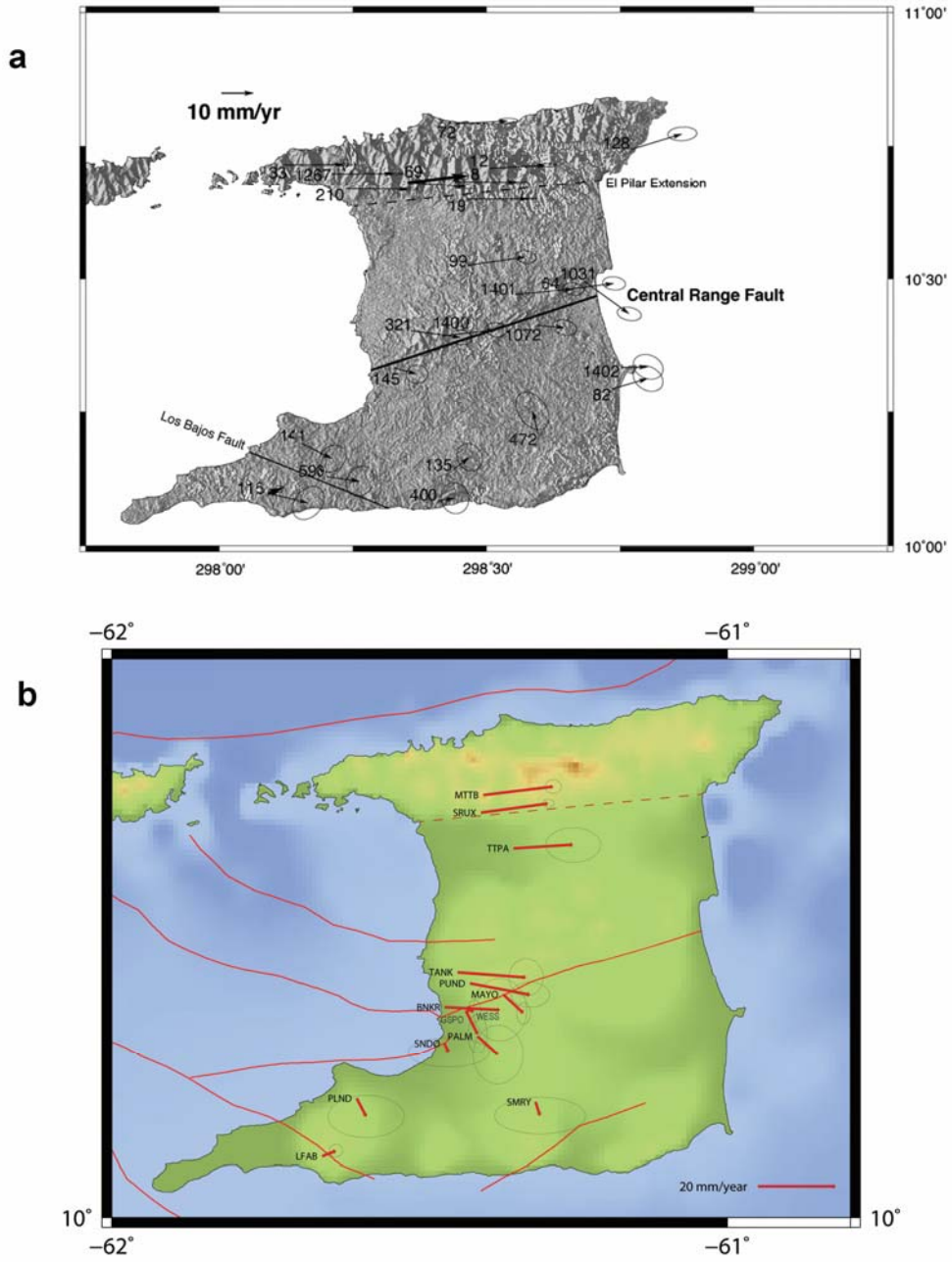


***Figure 2.10.*** *a) Thin black arrows indicate 1901-1903 to 1994-1995 triangulation-to-GPS velocities with 20 ± 3 mm/yr eastward added to transform velocities to put them into South American reference frame of Weber et al. (2001). b) Observed velocities (red arrows) from repeat GPS data collected between 1994 and 2005 (Rodríguez et al., 2008; Weber et al., 2011).*

*MTTB and LFAB correspond with the 69 and 115 stations (heavy arrows in figure a) respectively.*

Paleoseismic studies presented by Prentice et al. (2010) suggest that the CRF is a Holocene fault with at least a large earthquake able to rupture the ground surface between 2,710 yr and 550 yr BP which is consistent with the lack of historical seismicity on the CRF since the arrival of the first Europeans (Robson, 1964). Furthermore, these authors underlined the possibility of a large earthquake (M>7) considering at least 4.9 m of potential slip accumulated in the last 550 yr based on the assumption of a geodetic slip of 9-15 mm/yr (Weber et al., 2011) for the Holocene.

### 2.3. Western Venezuela

In western Venezuela (Figures 2.1), the plate boundary between the Caribbean and South American plates covers around 600 km wide zone from the South-Caribbean deformed belt to the Mérida Andes (Silver et al., 1975; Ladd et al., 1984; Audemard, 1993, 1998; Audemard & Audemard, 2002), a prominent mountain range that extends in a SW-NE direction for some 350 km from the Colombian-Venezuelan border in the southwest to the city of Barquisimeto in the northeast with a maximal elevation of 4,978 m a.s.l known as Pico Bolívar. The western area comprises a set of discrete tectonics or microplates as Maracaibo, Bonaire, and North Andean blocks, which move independently among the surrounding larger plates (Caribbean, South America and Nazca; Figures 2.11, 2.12 and 2.13). This area shows an intense deformation and active faults, among them one can mention the Oca-Ancon fault zone, a right-lateral strike-slip fault system that cuts across the northwestern margin of South America and forms the westernmost strand of a subparallel zone of right-lateral strike-slip faults that includes the San Sebastian and EPF zones (Audemard, 2001). Another major structure is the Boconó fault, a NE-SW trending fault that extends for about 500 km from the border between Colombia

and Venezuela to the Caribbean coast. On Colombian side the left-lateral-strike slip Santa Marta-Bucaramanga fault bounds the Maracaibo Block to the southwest and definitively this fault has impact over the geodynamic of this region.

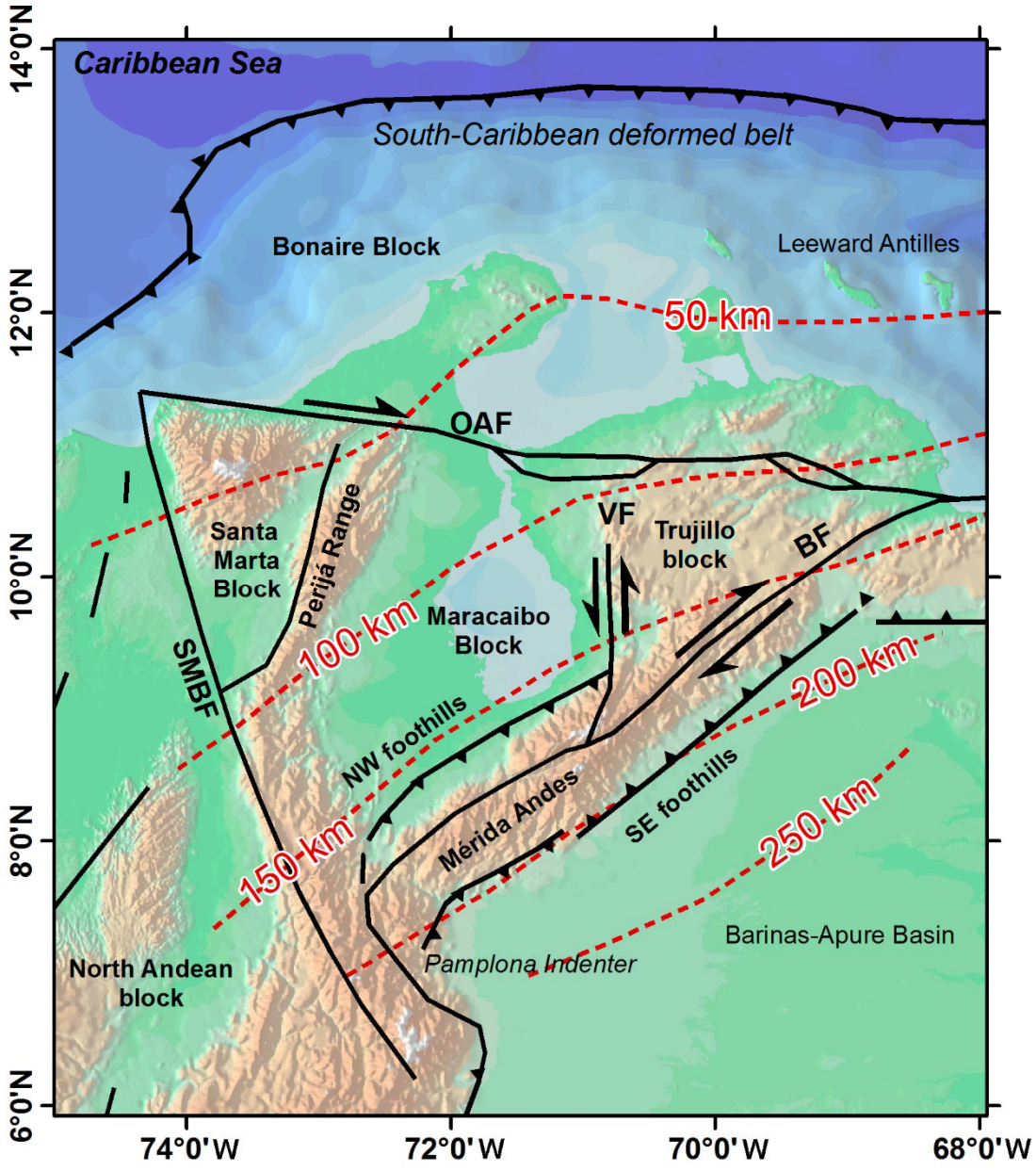


***Figure 2.11.*** *Schematic geodynamic map of western Venezuela. The main faults are shown: The Boconó Fault (BF), the Oca Ancón Fault (OAF), the Santa Marta-Bucaramanga Fault, and the Valera Fault (VF). Red dashed lines represent depth contours to the top of the*

*subducting Caribbean slap beneath northwestern South America (based on tomographic studies by Van der Hilst and Mann, 1994).*

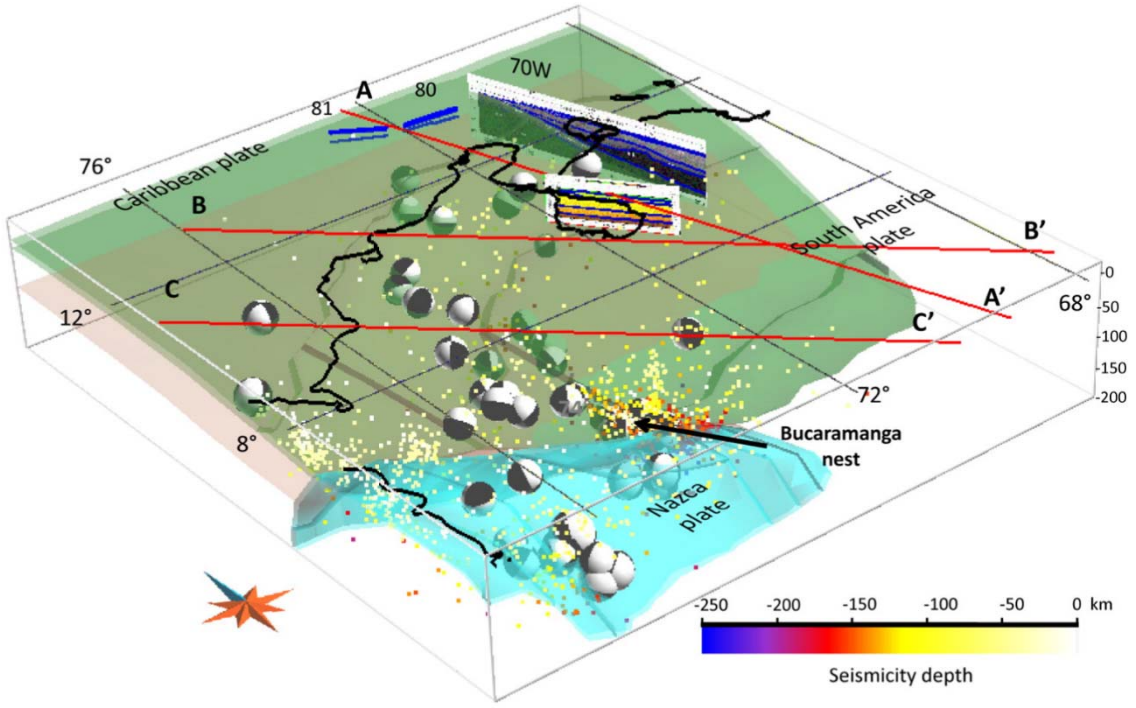


***Figure 2.12.*** *Three-dimensional view of interaction between Caribbean, Nazca, and South American plates (from Sanchez-Rojas and Palma, 2014). The seismic hypocenters and focal mechanism solutions in northwestern South America are also shown.*

North of the Leeward Antilles, the Caribbean plate underthrusts the South American plate ((Figure 2.13) characterized by an oblique convergence according to the geodetic observations (Pérez et al., 2001b, 2011; Weber et al., 2001; Trenkamp et al., 2002). This north-south convergence took place along a thrust with a very low angle and dips steeply to the ESE under the Mérida Andes and deformation occurred within the broad plate boundary zone between the Caribbean and South American plates (Kellogg, 1984; Van der Hilst and Mann, 1994; Malavé & Suarez, 1995; Taboada et al., 2000; Colmenares & Zoback, 2003; Dhont et al., 2005; Backé et al., 2006; Bezada et al., 2010). This North-south shortening has been attributed

to north-south Cenozoic convergence between the North and South American plates (Pindell & Dewey, 1982; Colmenares & Zoback, 2003) suggesting a period of particularly fast convergence (~10 mm/yr) that likely began in the early Miocene and continues to the present-day (Kellogg, 1984). Pindell & Barrett (1990) suggest a total of 250–300 km of north-northwest–directed convergence between North and South America since the middle Eocene. Conversely, Müller et al. (1999) described several stages of north-northwest–directed interpolate convergence at varying rates beginning in the early Eocene but in a broader range of 200–400 km of north-south convergence.

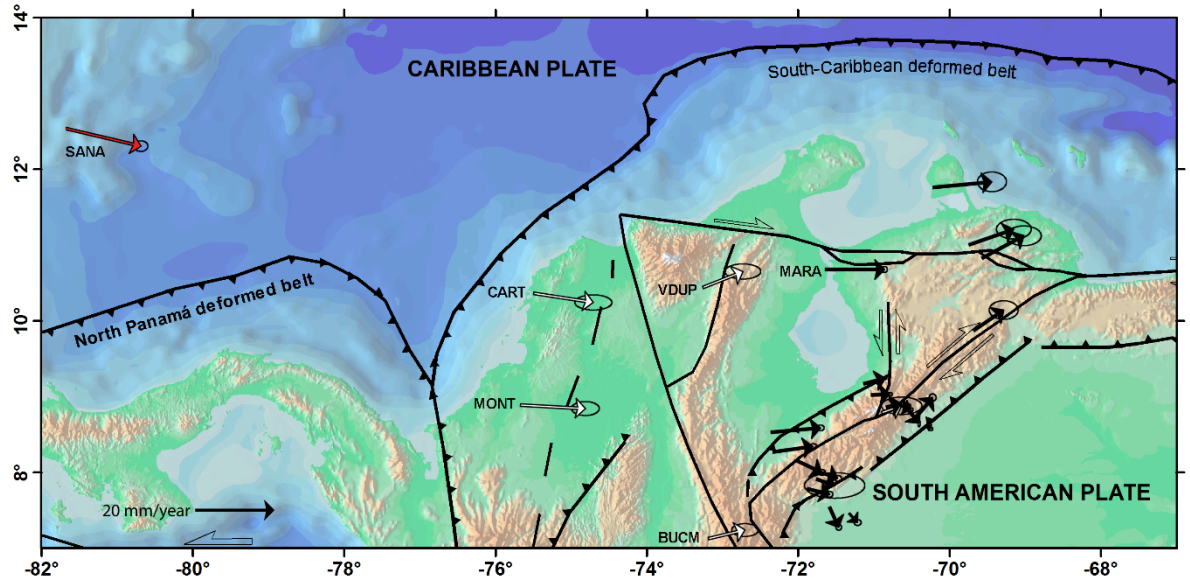


***Figure 2.13.*** *Geodetic observations in the southwestern Caribbean indicate an oblique convergence between the Caribbean and South-American plates. The red vector shows the San Andrés (SANA) Island Station calculated by Weber et al. (2001). The white vectors show the results of Trenkamp et al. (2002) work and the black arrows depict the geodetic measurements of Pérez et al. (2001b, 2011).*

Audemard & Audemard (2002) propose a Pliocene-Quaternary transpression due to oblique convergence between the South American plate and Maracaibo block to explain the

Mérida Andes buildup, also known as Venezuelan Andes (Figures 2.14 and 2.15). The strain partitioning along the chain with the foothills and the mountain belt have been shortened transversely in a NW-SE direction, whilst the Boconó Fault accommodates dextral slip (Audemard & Audemard). The uplift of Eastern Cordillera is likely related to flat slab subduction of the southern edge of Caribbean plate under northern South American plate (Kellogg and Bonini, 1982; Bezada et al., 2010). The Eastern Cordillera is composed of the Mérida Andes and the Perijá Range (Fig. 2.11), extending along the Venezuelan-Colombian border, and the Santa Marta block in Colombia. Nonetheless the timing of the uplift is generally related to the Panamá Arc-South America collision (Molnar and Skyes, 1969). The volcanic gap in Western Venezuela could be related to the shallow dip of subduction as has been reported in Peru and Chile where the effectively no asthenospheric wedge exists to produce source material for volcanism (McGeary et al., 1985; Gutscher et al., 2000).

The Pliocene to Holocene subduction of the Nazca plate in western South America and the collision of the Panamá Arc with western Colombia is responsible of the east-west plate convergence (Kellogg, 1984; Mann and Burke, 1984; Trenkamp et al., 1995). Many authors have related the collision of the Panamá Arc (Figures 2.1 and 2.13) to the northward extrusion or escape of continental fragments (The Maracaibo block, the northern Andes and the Bonaire block) in a north-to-northeasterly direction (Pennington, 1981; Mann and Burke, 1984; Mann et al., 1990; Stéphan et al., 1990; Audemard, 1993, 1998; Van der Hilst and Mann, 1994; Trenkamp et al., 1995, 2002; Egbue and Kellogg, 2010). From stratigraphic and paleontological studies Duque-Caro (1979) and Coates et al. (2004) infer that the collision between Panamá and South America started at 10 Ma, and Audemard (1993, 1998), Audemard and Audemard (2002), and Audemard et al. (2005) propose an effective later suturing date of about 5 Ma.

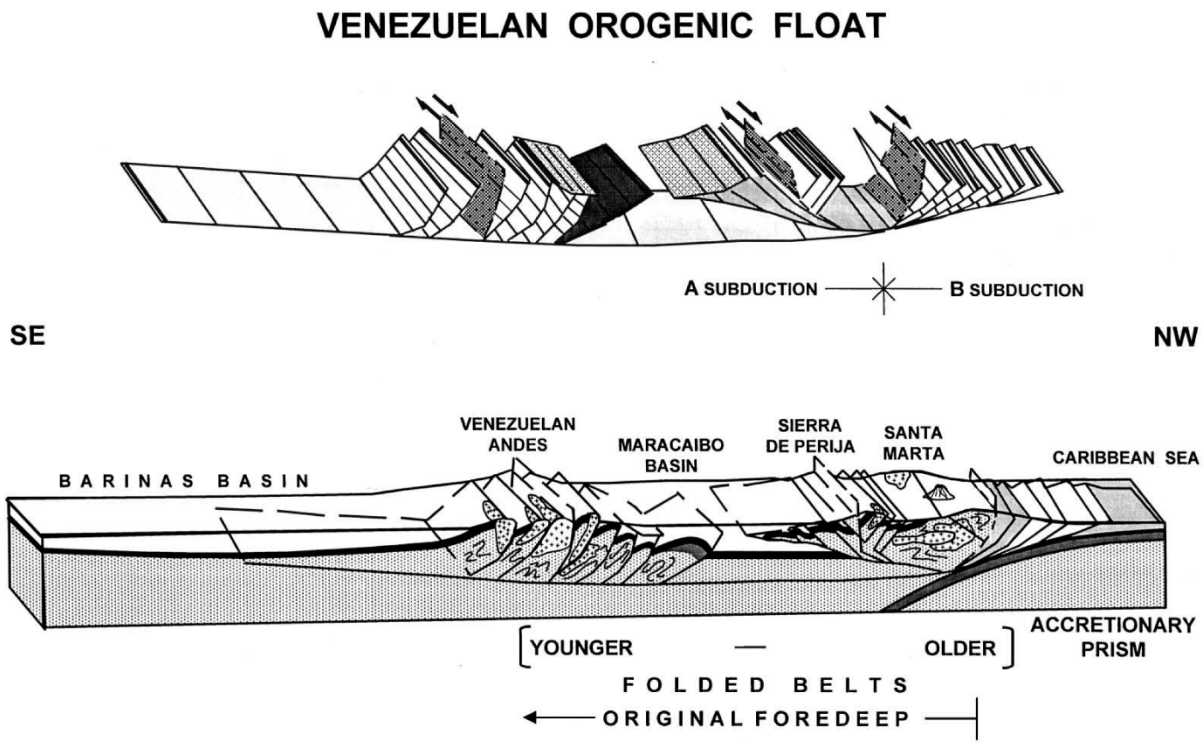


***Figure 2.14.*** *Crustal cross-section presented in Audemard and Audemard (2002) from the northwestern tip of the Santa Marta Block to the Llanos Basin, across the southernmost Mérida Andes, at the Pamplona indenter. Bottom figure displays major geologic units and structures, whereas top figure only exhibits major structures—brittle thrust and strike-slip faults, detachments and triangle zones—to give a more legible view of their interplays.*

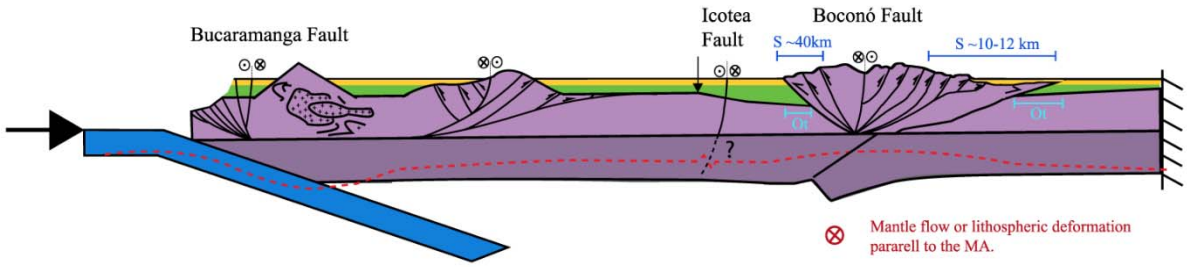


***Figure 2.15.*** *Cross-section of Pliocene stage in the geodynamic evolution of Western Venezuela (From Arnaiz-Rodríguez & Audemard, 2014). The Caribbean subduction and the South American lithosphere subsidence are shown.*

Since 2011, GIAME project (in Spanish “Geociencia Integral de los Andes de Mérida) started with the aim of illuminating the lithospheric structure the Mérida Andes. This research includes a part of advances presented in this dissertation, gravimetric measurements and three deep seismic profiles crossing the chain (Schmitz et al., 2014). Preliminary results of the central profile of the 380km long allow defining critical PmP reflections at distances of about 60 km for the northern part of the profile (Falcón Basin), and distances of 120 to 90 km for the central and southern part of the profile, corresponding to the axis of the orogen and the Barinas Basin, respectively. Derived values for the depth of the Moho discontinuity range from 29 km depth for north-western Venezuela, to 40-45 km close to the core of the chain, and 35 km at the southern end of the profile in Barinas basin (Yegres et al., 2014).

# CHAPTER 3:

# AN OVERVIEW OF NUMERICAL MODELS APPLIED TO INSTANTANEOUS DEFORMATION ALONG MAJOR STRIKE SLIP FAULTS

## 3.1. Introduction

Numerical models based on geodetic observations have been used to study the main strike slip faults around the world (e.g. San Andreas Fault, North Anatolian Fault, Altyn Tagh Fault). Geodetic observations include mainly surveyed trilateration, Global Navigation Satellite System (GNSS) observations and Interferometric synthetic aperture radar (InSAR). In general, concepts as slip and elastic locking depth are repeatedly considered. The slip, also known as actual relative movement or total displacement, is the actual relative displacement along a fault plane of two points which were formerly adjacent on either side of the fault (Parker, 2003). The elastic locking depth is defined as the level below which there is a transition from a locked fault plane inducing elastic deformation of the plate to a ductile slip along the fault. The value of the parameter is related directly to the mechanical strength of the fault. Strong faults and wide zones undergoing elastic deformation correspond to deeper locking depths (Kearey et al. 2009). In next sections, a revision of main approaches to evaluate velocity fields is presented.

## 3.2. Elastic models

Slip distribution at depth of a fault may be inferred from the deformation observed on the surface. The most classical way to interpret a geodetic velocity field across a strike slip fault is to use the screw dislocation model (Chinnery, 1961; Weertman & Weertman, 1964; Savage & Burford, 1973).

$$v(x) = \frac{V_T}{\pi} \tan^{-1}(\frac{x}{D}) \quad \text{(eq. 3.1)}$$

where v(x) is the velocity at a distance x from the fault, VT is the far-field velocity and D is the locking depth of the fault. Nonetheless, for the case of simple half-space earth model the inversion of surface deformation to obtain slip at depth on faults is not completely successful for two reason: the inversion is inherently unstable, and measurements of surface deformation are generally sparse and imprecise (Savage, 1987).

In order to develop the formulations in a more realistic earth model, Lisowski et al. (1991), following McHugh and Johnston (1997) and Rybicki and Kasahara (1977), pointed the effects of lateral inhomogeneity in the Earth model upon asymmetric velocity profiles. The simplest model where two fault blocks are modeled by elastic material of different rigidity $\mu_1$ and $\mu_3$ is shown in figure 3.1. One can see the effect of increased rigidity in the left-hand fault block concentrating deformation in the right-hand fault block. Le Pichon et al. (2005) quantified several cases of significant asymmetry in interseismic and coseismic effects along large continental strike-slip faults using simple two-dimensional edge dislocation model such as the North Anatolian Fault and Sumatra Fault. For the case of a vertical fault that juxtapose two different geologic materials, the solution is linear in the angle $\theta=\tan^{-1}(x/D)$ but the slips are different. Thus, $s_1$ is the total accumulated velocity at the side where $x < 0$, and $s_2$ is the accumulated velocity on the opposite side of the fault. The ratio $s_2/s_1$ indicates the rigidity contrast of both sides of the fault's locked portion.

$$v(x) = s_1 + 2\frac{s_2}{\pi} \tan^{-1}(\frac{x}{D}); x \geq 0 \quad \text{(eq. 3.2)}$$

$$v(x) = s_1 + 2\frac{s_1}{\pi} \tan^{-1}(\frac{x}{D}); x < 0 \quad \text{(eq. 3.3)}$$

where the fault is at x=0 and x is defined positive on the side of the fault where $v(x) \rightarrow s$ when $x \rightarrow \infty$.

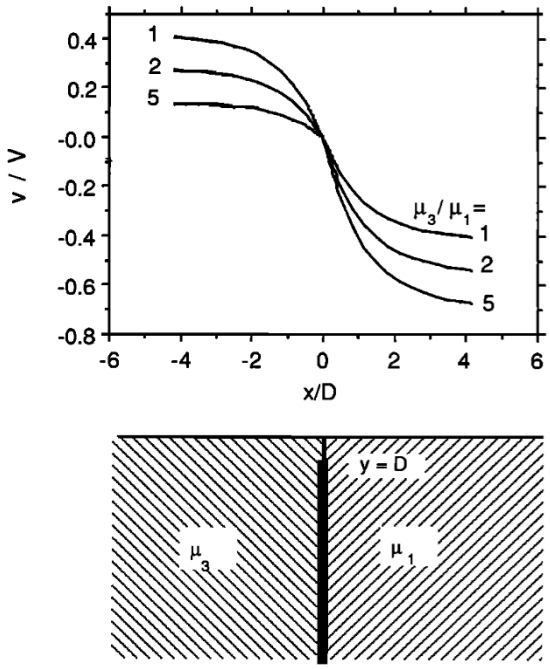


***Figure 3.1.*** *Normalized surface velocity v as a function of distance across a vertical strike slip fault calculated with the half-space model in the case where the two fault blocks have different rigidities (from Lisowski et al., 1991). Profiles of the surface velocity are shown for three different* $\mu_3/\mu_1$ *ratios. The model with* $\mu_3/\mu_{1=1}$ *is equivalent to the simple elastic half-space model (Savage & Burford, 1973).*

Chéry (2008) examined the idea that interseismic strain variations also occur in response to lateral variations in the elastic thickness of the lithosphere. From stress balance principle and some simplifying assumptions he has shown that the elastic thickness is inversely proportional to strain rate for the simple case of pure strike-slip faulting (Figure 3.2) concluding that in the case of classic screw model (Savage and Burford, 1973) faults do not play a direct role during the interseismic phase because they are locked; opposite, interseismic strain is therefore mainly controlled by elastic plate properties.

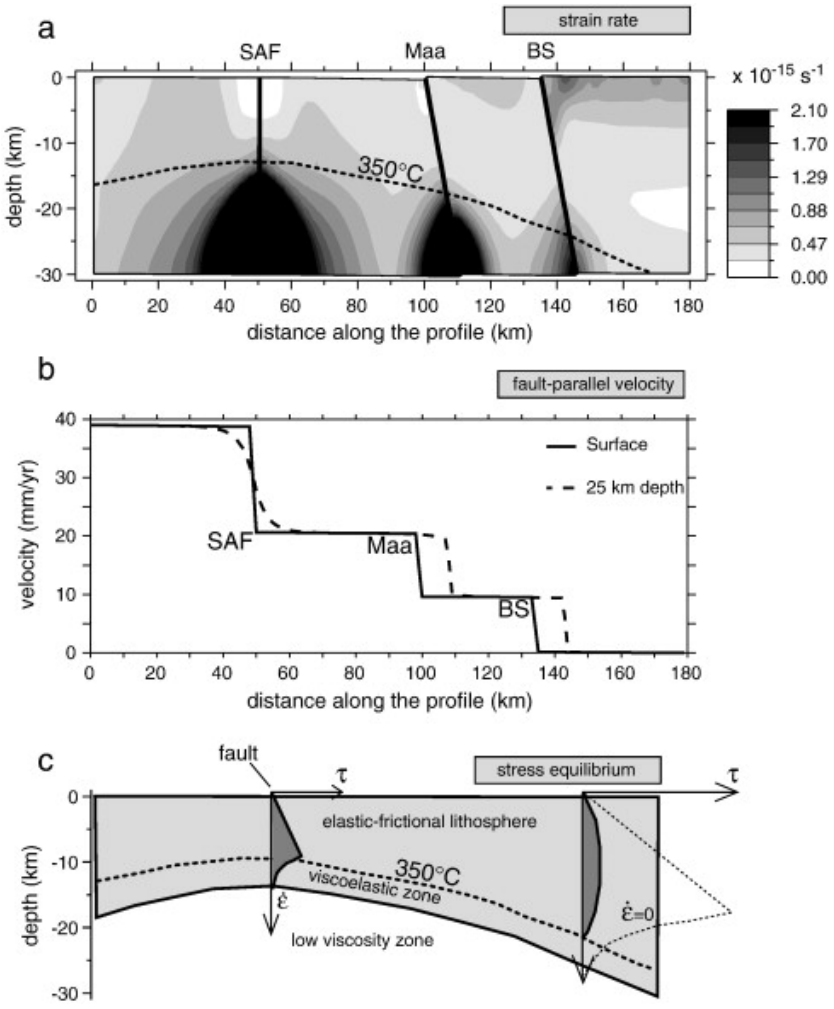


***Figure 3.2.*** *a) Strain rate invariant associated with parallel strike-slip faults of northern California. (Maa = Maacama fault; BS = Bartlett Springs fault); b) interseismic velocity in the fault-parallel direction at the surface (solid line) and at 25 km depth (dashed line); c) fault-parallel stress profiles for the fault zone located on the SAF and for the crust. The profile to the left corresponds to the maximum fault strength for this slip rate. The profile to the right inside the crust remains much below the maximum sustainable stress corresponding to the dashed curve. Stress integrals with depth must be equal on the two profile to ensure stress equilibrium. (From Chéry, 2008).*

For other cases than vertical strike-slip faults, numerous inversion processes to simulate current velocities; including the displacement simulation method applied to EPF in the chapter

5, are based in analytical expressions provided by Okada (1985). In the original work, a complete suite of formulations was presented for the surface displacements, strains, and tilts induced by inclined shear and tensile faults in a half space for both point and finite rectangular sources.

### 3.2.1. Compliant zone approach

Interseismic geodetic velocities can present important gradient in both sides of the fault. One explanation for the high interseismic strain can be associated with the presence of a low rigidity zone. Additionally, if we observe a zone of highly cracked and damaged rocks around the main slip surface; it is possible that we have the presence of a compliant zone (CZ). Such zones introduce significant lateral variations in the crustal rigidity, and likely affects patterns of deformation in the Earth's surface (co-seismic, post-seismic, and inter-seismic phases of the earthquake cycle). Furthermore, these zones might present marked reductions in seismic velocities (Cochran et al., 2009).

CZs have been identified from geodetic studies in important faults around the world as the San Andreas Fault zone and North Anatolian Fault. From GPS observations and Electronic Distance Measuring; Chen and Freymueller et al. (2002) detected a compliant zone along the SAF in northern California. These authors modelled the interseismic velocity field following Rybicki and Kasahara (1977) and suggest a narrow fault zone with rigidity reduction respect to surrounding rocks (Figure 3.3). Likewise, Jolivet et al. (2009) using the same approach but including Interferometric Synthetic Aperture Radar (InSAR) data to study interseimic displacement in the northern San Andreas Fault zone (Figure 3.4). Other authors have combined the INSAR and GNSS observations in order to study coseismic and post-seismic displacements (e.g. Fialko et al., 2002; Fialko, 2004, Hamiel & Fialko, 2007; Figure 3.5).

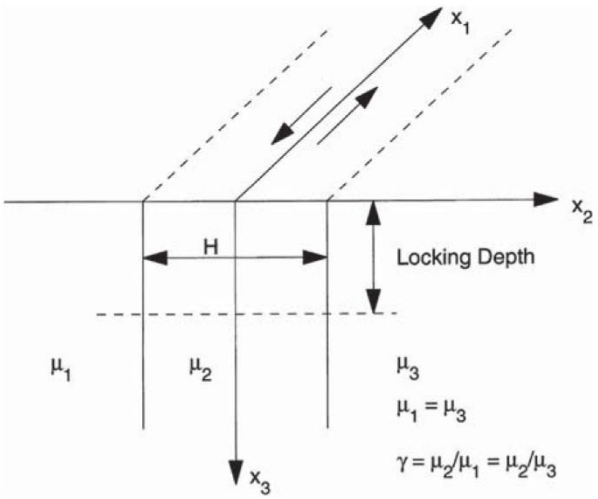


***Figure 3.3.*** *2D Model in a laterally inhomogeneous model proposed by Chen and Freymueller (2002). A near fault zone of rigidity $\mu_2$ is shown with respect to surrounding area with rigidities $\mu_1$ and $\mu_3$.*

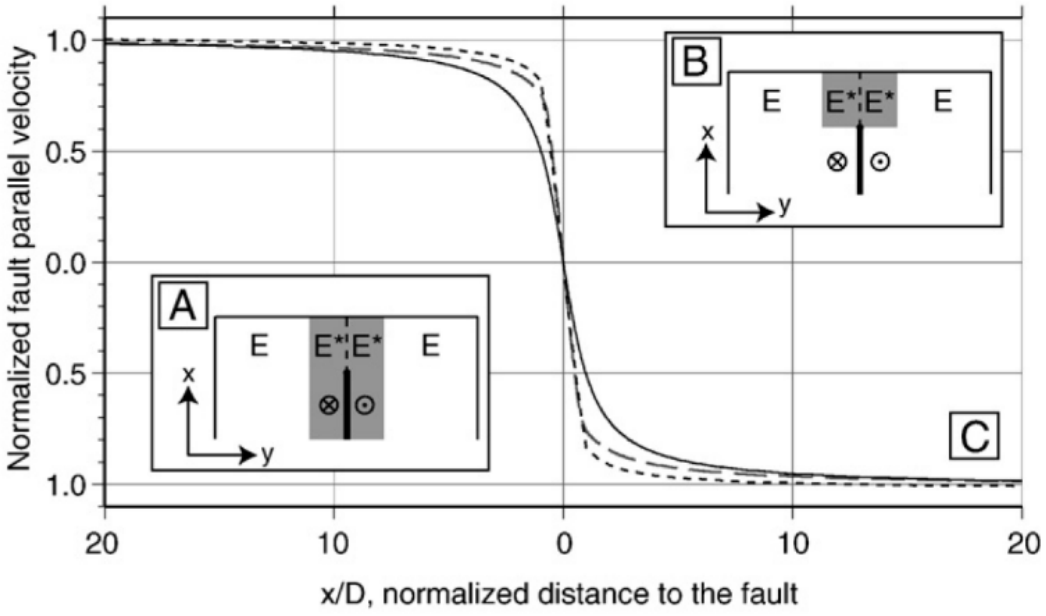


***Figure 3.4.*** *Geometry fault of deep (A) and shallow (B) CZ models proposed by Jolivet et al. (2009). (C) Fault perpendicular profiles showing a 10 km locking depth simple elastic half-space model (continuous lines), a 10 km locking depth deep CZ model (long-dashed line) and a 10 km locking depth shallow CZ model (dashed line).*

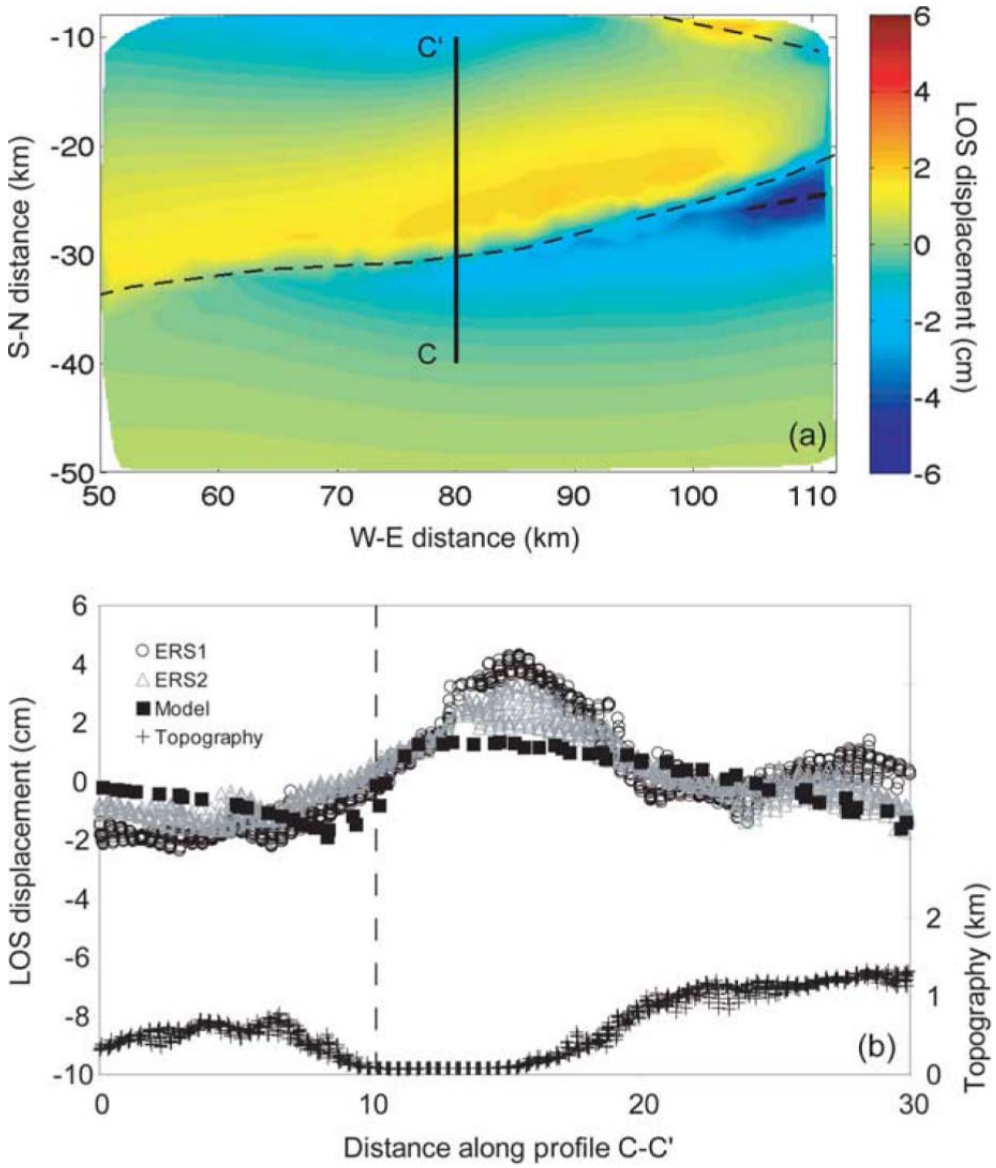


***Figure 3.5.*** *Three-dimensional numerical model to analyse the coseismic deformation due to the 1999 Izmit (Turkey) earthquake (From Hamiel & Fialko, 2007). (Above) Dashed black line indicates the location of the mapped faults and the modeled compliant zones in the area. Location of the faults that are approximately 3 km wide, extend to the depth of 20 km, and have shear moduli ratio of 1/3. (Below) A comparison between the residual LOS displacements from ERS-1 (black circles) and ERS-2 (gray triangles) interferograms and the calculated displacements shown in the figure above along profile C-C'. Dashed black line indicates the location of the mapped fault along the profile.*

The modellings applied to EPF and presented in the chapter 6 as a publication summited to Journal of Geophysical Research, have been applied in detail to compliant fault zones in the Eastern California Shear Zone and San Andreas Fault (Barbot et al., 2009; Lindsey and Fialko, 2013). This method adapted to the case of 3-D deformation develop by Barbot et al. (2009) is based in a numerical approach presented by Barbot et al. (2008). Originally, the goal of this method was to investigate the effect of a soft damage around a fault affected by an earthquake on the co-seismic displacement field, and on the earthquake slip distribution inferred from inversions of geodetic data. For this case, the fault slip is assumed to be constant in the uppermost crust, and gradually tapered to zero toward the bottom of the seismogenic zone according to the following expression,

$$s(x_3) = s_0 \left( \prod_\beta \left[ \frac{2x_3 - L}{2L} \right] + \prod_\beta \left[ \frac{2x_3 + L}{2L} \right] \right) \qquad \text{(eq. 3.4)}$$

where $s_0$ is slip in the upper part of a strike slip fault extending from the surface to a depth L. Π represents a linear taper controlled by a roll-off parameters β. In figure 3.6, the case for an isotropic medium with a contrast in shear modulus across a strike slip fault, is compared with the deformation due to slip on a fault embedded in a compliant zone.

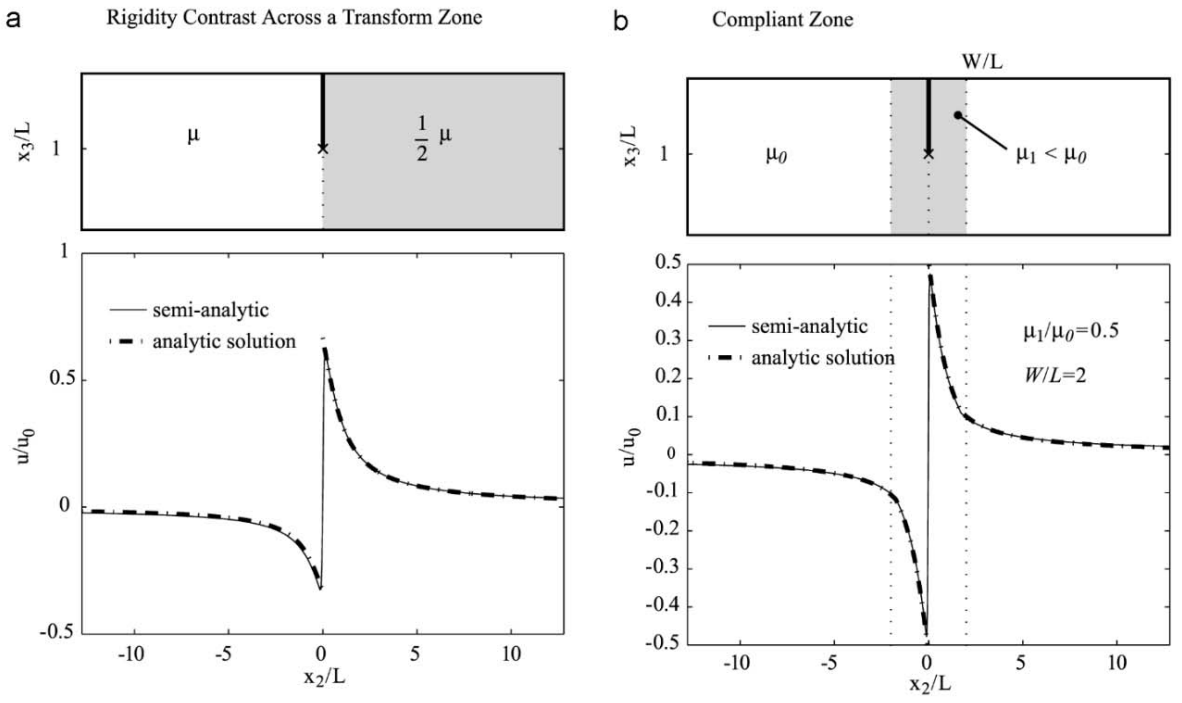

***Figure 3.6.*** *Comparison between the analytic expressions and the numerical solutions for surface displacements (coseismic) due to a fault slip in heterogenous media of Barbot et al. (2008). a) Isotropic medium with a contrast of shear modulus across the transform fault zone. b) Isotropic medium with the compliant fault zone with total width 2W. The wavelength of deformation is larger in the softer anisotropic crust, to the left of the rupture.*

### 3.2.2. Slip distribution approach

Based on the fact that the friction along the fault plane is not uniform in strength, the fault-slip distribution can be evaluated in multiple finite discrete fault patches with the aim to detect the stuck or locked zones, partially locked and creeping zones. The use of a slip inversion procedure based on the constrained least squares method allows infers about these zones (Wang et al., 2013). The slip distribution method is carried out using by example the SDM2011 software, which has been applied recently in other geodetic studies (Motagh et al., 2008, 2010; Wang et al., 2009, 2011, Xu et al., 2010, Diao et al., 2010, 2011). The observed slip data are related to the discrete fault displacement using Green function of the earth model calculated through linear elastic dislocation theory. In order to obtain a slip model with high resolution, the fault plane is presented by a number of small rectangular dislocation patches with uniform slip (Figure 3.7). The patch size must be reasonably small with the purpose of having a reasonable representation of the true continuous slip distribution. Indeed, if the available data do not include enough information for determining the slip distribution with the desired resolution, the inversion system becomes underdetermined. For that reason, a priori or artificial conditions (fixed fault geometry and restricted variation for the rake angle) and physical constraints (smooth spatial distribution of slip or stress drop) are required to avoid unwieldy large variations in the slip distribution. Based on idea that the areas of large stress drop occurs

also have large slip (Bouchon, 1997), the slip models are adjusted according to suitable roughness in the stress drop. The objective function is defined as follows:

$$F(\mathbf{b}) = \|\mathbf{G}\mathbf{b}-\mathbf{y}\|^2 + \alpha^2 \|\mathbf{H}\boldsymbol{\tau}\|^2 \qquad \text{(eq. 3.5)}$$

where G is the Green function, b is the slip of sub-faults, y indicates the ground observation, τ is the shear stress drop related to the slip distribution on the whole fault plane, H represents the finite difference approximation of the Laplacian operator multiplied by a weighting factor proportional to the slip amplitude, and $\alpha^2$ is the positive smoothing factor. In this dissertation, this method was applied to EPF and main faults in Trinidad (Chapters 6 and 7 respectively).

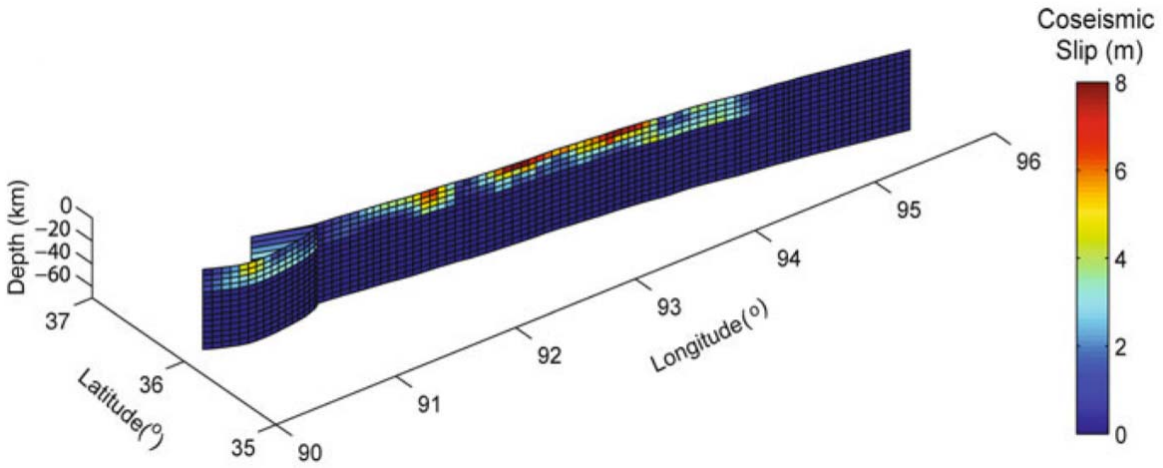


***Figure 3.7.*** *Slip distribution model for the 2011 Kokoxili earthquake (from Diao et al., 2011) constrained from the INSAR Observation by Lasserre et al. (2005).*

# CHAPTER 4:

# GNSS DATA COLLECTION

## 4.1. Introduction

In this chapter, I show the GNSS data collection and analysis considering two separate/independent regions: Northeastern and Western Venezuela. A thorough review of previous geodetic observations in the region was carried out. I compiled values of observed velocities in Venezuela and neighboring countries with the purpose of establishing an overview on the GNSS geodetic measurements in Venezuela and its surroundings. Most recent acquisition campaigns carry out in this thesis, in both Northeastern and Western Venezuela are presented. The more relevant aspects related to the previous studies and GPS data acquisition campaigns in Venezuela are presented in section 4.2.1. as an article in press for the Special Publication of GEODINOS Project in La Revista de la Facultad de Ingeniería (Journal of Faculty of Engineering) of Central University of Venezuela. Likewise, in the next section 4.2.2, I describe some points related to the acquisition campaigns undeveloped in the mentioned publication.

In the next sections, I include details on the compilation of supplementary data for the processing including previous acquisition campaigns: CARIVEN 1994, Trinidad 1994, Venezuela 1998, and Caribbean 1999. Likewise, a large set of cGNSS stations of several networks has been compiled including: the Red de Estaciones de Monitoreo Satelital GPS - REMOS - (GPS Satellite Monitoring Station Network of Venezuela), GEORED - Colombian Geological Survey (SGC; former INGEOMINAS), the International GNSS Service (IGS), networks associated to the University Navstar Consortium (UNAVCO) with the COCONet network, and GNNS Trinidad and Tobago Active Geodetic Network.

## 4.2. Acquisition campaigns

In order to monitor and determine present-day displacement on northeastern Venezuela, a GNNS network was established since 2003 (Table 4.2). A team composed of researchers from FUNVISIS and University of Savoie measured this network later in late 2003 and 2005. These sites were recently reoccupied in early 2013 during this dissertation. Additionally, the western network has been conceived, installed and then measured twice in late 2011 and early 2013; all this in the frame of this thesis.

### 4.2.1. An overview of the GNSS geodetic Measurements applied to Geodynamic studies in Venezuela

# AN OVERVIEW OF THE GNNS GEODETIC MEASUREMENTS APPLIED TO GEODYNAMIC STUDIES IN VENEZUELA

**Carlos Reinoza, Franck A. Audemard, François Jouanne y Christian Beck**

**Abstract.** In 1988, the history of GNSS geodetic measurements with the goal of studying fault kinematics in Venezuela begins with one of the first civil efforts, the Central and South America (CASA) Project. Since then, and for more than two decades now, several authors have been contributing with the ultimate target: To determine slip rates of plate boundary faults in order to understand the active tectonics at the Caribbean South America plate interactions. Recently, the interest on kinematics GNSS has increased with the occurrence of the 1997 Cariaco Earthquake. In this work, we make an overview of the acquisition methodologies, data processing and contributions to the understanding of local and regional geodynamics. We show the significant contributions from the group headed by the Simón Bolívar University, and FUNVISIS team, in scientific collaboration with researchers of Savoie University, France, without to forget the significant contributions of other authors. Finally, we evaluate the future perspectives: modeling of faults (minor faults) from GNSS observations, densification of present-day networks, installation of continuous GNSS networks , exchange of data with researchers from neighboring countries and definitely, the efforts directed to conformation of the national pool of GNSS equipment available to the whole Venezuelan scientific community involved in this subject.

*Keywords:* GNSS networks, Geodynamics, Caribbean, South America, Venezuela.

**Resúmen Extenso.** Aun cuando la tectónica activa en Venezuela ha sido largamente trabajada por diversos autores durante décadas (Bucher, 1952; Molnar & Skyes, 1969; Pérez & Aggarwal, 1981; Stephan *et al.* 1990; Beltran, 1993; Audemard *et al.* 2000), las mediciones GNSS aportan datos precisos que pueden ayudar a esclarecer temas de fuerte debate. En este trabajo damos una mirada a más de dos décadas de mediciones GNSS en Venezuela, particularmente en la instalación de redes, aspectos metodológicos, procesamiento y análisis de datos, y perspectivas de esta disciplina en el futuro próximo.

Las primeras mediciones GPS realizadas en el territorio venezolano, comienzan con el proyecto CASA UNO, iniciado en 1988 por un grupo aproximado de 30 instituciones de 13 países incluyendo Venezuela. El objetivo principal era monitorear deformaciones geodinámicas en la compleja zona tectónica de los límites de las placas Caribe, Cocos, Nazca y Suramérica. Entre enero y febrero de 1988 fueron medidas cinco estaciones situadas a ambos lados de la Falla de Boconó (Figura 1) en sitios seleccionados con el objetivo de unir las redes geodésicas locales (Henneberg, 1983; Henneberg & Schubert, 1986) y conectarse con la red de control gravimétrico instalada a lo largo de la Falla de Boconó (Drewes *et al.* 1991). La red en Venezuela fue remedida en el año 1993, extendiéndose a 21 estaciones que cruzaban las fallas El Pilar y Boconó (Drewes *et al.* 1989, 1995; Kellog & Dixon, 1990). La comparación de la posición de las primeras cinco estaciones medidas en 1988 y 1993, indicó la tendencia de un movimiento transcurrente dextral caracterizado por un movimiento hacia el este de la placa Caribe, y otro hacia el oeste de la placa Suramericana en un orden de 1 cm/año. Los primeros resultados del Proyecto CASA indicaban que la estación Mérida, situada muy cerca de la Falla de Boconó, era el único sitio que parecía seguir el movimiento de la placa Caribe, lo cual simulaba representar una reducción del movimiento de la placa por deformación local en la falla (Drewes *et al.* 1995). Trenkamp *et al.* (2002), a partir de las mediciones de cuarenta y cuatro estaciones pertenecientes al proyecto CASA desde 1991 hasta 1998, entre ellas cinco realizadas en Venezuela (ELBA, URIB, MERI, BARI, JUNQ), se propusieron estudiar la colisión activa entre Panamá y Colombia acompañada de deformación en curso superior a 550 km de la zona de sutura, el permanente acortamiento andino normal al margen y el consistente escape tectónico de los Andes del Norte hacia el noreste a lo largo de aproximadamente 1400 km.

A partir de 1994 se realizaron diversas campañas de medición GPS lideradas por un grupo de trabajo conformado por instituciones nacionales e internacionales, entre ellas la Universidad Simón Bolívar (USB), la Universidad de Colorado (UC), el actual Instituto Geográfico Venezolano “Simón

C. Reinoza, FUNVISIS
creinoza@funvisis.gob.ve

Bolívar" (IGVSB) y la Universidad del Zulia (LUZ). En mayo de 1994 y marzo de 1998, se realizaron dos campañas conocidas comúnmente como CARIVEN94 y Venezuela 1998 respectivamente (Bilham, 1994; www.unavco.org), y seguidamente a estas iniciativas se realizaron mediciones en 1999, 2000, 2004 y 2006 (Tabla 1). Estas observaciones han permitido estimar la tasa y dirección del desplazamiento de la placa del Caribe con respecto a la sudamericana, así como el rol cinemático que juegan el sistema de fallas de Boconó en el acomodo de parte del movimiento relativo entra las placas del Caribe y Suramérica, y además la cuantificación del campo de velocidades en el noroeste del continente y occidente de Venezuela (Figura 2). Adicionalmente, se realizaron observaciones en los sitios Caracas, Maracaibo y Canoa como estaciones de control. Pérez *et al.* (2001b), a partir del análisis de las observaciones GPS realizadas entre 1994 y 2000 en 22 sitios en las Antillas Menores y el norte de Suramérica, determinaron que la placa Caribe, a lo largo de su límite sur, se desplaza a una tasa de 20,5 ± 2 mm/a con un acimut de N 84° ± 2° E en 65° W relativo a la placa Suramérica. Los resultados de este trabajo indicaron que al este de 68°W, el campo de velocidades a través del límite de placas Caribe-Suramérica está confinado a una zona de cizalla angosta (<100 km), y el 80% de la deformación en superficie está contenida dentro de una zona de 80 km de ancho centrada a algunos kilómetros al norte de la Falla El Pilar. Por el contrario, al oeste del 68°W, el límite de placas se amplía a más de 300 km con cizallamiento dextral compartido entre la Falla de Boconó (con 9-11 mm/a y 1 mm/a de convergencia) y un sistema costa-afuera cerca de la costa norte (2-5 mm de cizalla dextral) sobre el sistema de fallas de La Victoria. Adicionalmente, se estimó el deslizamiento co-sísmico asociado con el terremoto de Cariaco de 1997, debido a que las mediciones realizadas entre 1994 y 1999 incluían además de la deformación del límite de placas, una componente importante de deformación co-sísmica. Pérez *et al.* (2011) reportan nuevos resultados a partir de las mediciones realizadas entre 1999 y 2006. Señalan que los vectores de velocidad de los sitios localizados en la parte más noroeste de Sudamérica, a distancias mayores de 200 km del eje central de los Andes venezolanos, muestran un movimiento hacia el este bastante uniforme de esas regiones con respecto al cratón Suramericano, a una tasa de ~15mm/a. La dirección de este movimiento es oblicua a los Andes venezolanos y a la falla de Boconó, de rumbo aproximado N50°E. Esta oblicuidad también se observa en los vectores de velocidad de los sitios localizados a ambos flancos de la Falla de Boconó a lo largo y ancho de los Andes, lo cual de inmediato sugiere que los 20 ±2 mm/año de desplazamiento relativo (Pérez *et al.* 2001b; Weber *et al.* 2001) al este de la placa del Caribe con respecto a la Sudamericana se parten en dos componentes (Pérez *et al.* 1997; Audemard & Audemard, 2002), por un lado en 12 ±2 mm/año de movimiento transcurrente lateral derecho confinados en una zona de deformación de ~100 km de ancho centrada aproximadamente a lo largo de la traza principal de la Falla de Boconó, la cual repta por debajo de una profundidad de bloqueo de 14 ±4 km; y por otro lado una componente de convergencia perpendicular a los Andes, la cual se calcula entre los 12 y 16 mm/año. Aproximadamente un tercio de esta convergencia (4-5 mm/año) se concentra en las cercanías de la Falla de Boconó y se manifiesta a lo largo de fallas inversas subparalelas a ésta, que buzan hacia la cordillera, localizadas a una distancia de ~25km a ambos flancos de la falla. DeMets *et al.* (2000), utilizando la estación AVES más otras tres ubicadas también en la parte interna de la placa (ROJO, SANA, CROI), promediaron 18-20 mm/a (2σ) en varios lugares a lo largo del límite de placa con una estimación máxima de aproximadamente 4-6 mm/a para la deformación interna de la placa Caribe. Weber *et al.* (2001) utilizaron datos de siete sitios más sobre la Placa Caribe (incluyendo la estación AVES) y cinco sobre la placa Suramericana, para indicar un movimiento hacia el este relativo a la placa Suramericana de ~20 mm/a a lo largo del límite de placa, significativamente más rápido que el modelo para la época NUVEL-1A (DeMets *et al.* 1990; 1994); sin embargo mantenía una dirección de acimut similar.

En 1997, el GTFE (German Task Force for Earthquakes), invitado por FUNVISIS, realiza estudios geofísicos e ingenieriles relacionados con el terremoto de Cariaco ocurrido el 9 de Julio de 1997. Entre las diversos estudios que realizó el GTFE, se incluyó la instalación de una pequeña red GPS a lo largo de la Falla El Pilar con el objeto de detectar deformaciones post- sísmicas. Se consiguió determinar un movimiento lateral-derecho de aproximadamente 10cm entre el 19 de Julio y el 22 de Agosto del año 1997 cerca de la terminación este de la zona de ruptura (Baumbach *et al.* 2004). En el año 2003, FUNVISIS instala una densa red GNSS cubriendo ambos lados de la extensión en tierra de la Falla El Pilar, así como estaciones en las

islas de Coche, Cubagua y Margarita (Figura 3). La red consiste de 36 dispositivos de bronce plantados en afloramientos estables, lo que representa una nueva configuración que sustituye la metodología tradicional de usar trípodes para montar la antena geodésica. Con el fin de mejorar la distribución de la red recién instalada, se consideraron 4 sitios pre-existentes (1 de PDVSA y 3 de UNAVCO). Más tarde, en 2003, se midieron 33 estaciones de las 40 posibles, y en 2005 se medirían solo 24 en compañía de investigadores de la Universidad de Savoie (Francia). Estas mediciones se realizaron con el fin de estimar el movimiento relativo de la Falla El Pilar y otras fallas próximas (Figura 4). Los resultados indicaron la ausencia de un desplazamiento significativo (especialmente acortamiento) en la Serranía del Interior, y un desplazamiento superior a 22 mm/a hacia el este (relativo a la placa Suramericana fija) de los vértices localizados al norte de la Falla El Pilar. Se determinó la concentración a lo largo de la Falla El Pilar de todo el desplazamiento relativo Caribe-Suramérica, y la existencia de una importante componente de desplazamiento asísmico a lo largo de la parte superior de la Falla El Pilar. La mejor solución está representada por un modelo de dos segmentos, cada uno con dos dislocaciones: una superior que representa la parte sismogénica de la falla donde el deslizamiento puede estar bloqueado, y una parte inferior afectada por un deslizamiento asísmico con condiciones dúctiles. Se ha determinado que entre 12 km de profundidad y la superficie, solo el 40 % del desplazamiento está bloqueado para el segmento oeste y 50% para el segmento este (Jouanne *et al.* 2011). Recientemente, a comienzos de 2013, se realizó una campaña de recuperación de los sitios en el oriente y una nueva medición de 30 estaciones. En los últimos años FUNVISIS ha dirigido su mirada sobre el occidente venezolano (Figura 5). Entre 2011 y 2013 hemos realizado mediciones en un total de 33 sitios, de los cuales 19 fueron instalados previamente, siguiendo la metodología de marcas de bronce plantados en los afloramientos rocosos, y el resto se complementó con sitios pre-existentes (Redes PDVSA, IGVSB y USB). Es importante mencionar que la distribución geográfica de los sitios instalados por FUNVISIS desde 2003, responde a objetivos específicos como la tasa de desplazamiento de fallas individuales y la rotación de bloques tectónicos discretos.

El futuro de la disciplina GNSS aplicada a la cinemática de fallas debe estar concentrado en primer lugar en la recuperación de los sitios pre-existentes, densificación de las redes actuales considerando criterios geológicos, durabilidad en el tiempo y seguridad del personal y equipos durante las campañas de medición. Otro aspecto importante que se debe desarrollar es la conformación de la red cGNSS. Adicionalmente, desde hace algunos años se ha contemplado la idea de conformar un fondo nacional de equipos GNSS, un conjunto de equipos pertenecientes a instituciones y universidades disponible para realizar campañas de re-ocupación y ocurrencia de eventos extraordinarios. Los resultados GNSS deben seguir resolviendo incertidumbres científicas. Las campañas periódicas y el uso de estaciones cGNSS permiten detectar y medir desplazamientos de tipo co-, inter- y post-símicos, así como la deformación de bloques limitados por fallas, el estudio de fallas “menores” pero con igual o mayor poder sismogénico, la concepción de nuevos modelos considerando algoritmos modernos. Todo esto reportaría resultados significativos en términos de amenaza sísmica.

*Palabras claves:* Redes GNSS, Geodinámica, Caribe, Suramérica, Venezuela.

## INTRODUCTION

Accurate geodetic measurements with Global Navigation Satellite System (GNSS) have allowed determining tectonic plate rate movements, behavior of plate boundaries, crustal and inter-crustal deformation, and fault kinematic among different aspects in a short-time span (Beutler *et al.* 1987; DeMets *et al.* 1990; Lisowski *et al.* 1991). Although the Venezuelan active tectonics has been developed by several authors along decades (Bucher, 1952; Molnar & Skyes, 1969; Pérez & Aggarwal, 1981; Stephan *et al.* 1990; Beltran, 1993; Audemard *et al.* 2000), yet there are still many issues of strong debate. The application of GNSS methodology to the kinematic characterization of most important Venezuelan faults and of the northeast South-American boundary plate is helping to solve certain aspects. Here, we review more than two decades of GNSS measurements in Venezuela, particularly at network installation, methodological approach, processing and data analyses and future perspectives.

## GNSS MEASUREMENTS IN VENEZUELA

### Geodetic network-acquisition

Fault kinematic studies with Global Position System (GPS) geodesy in Venezuela began in 1988 with the CASA UNO Project (UNO in spanish to designate the first epoch of measurements), one of the first civil efforts to establish a GPS network (Kellogg & Dixon, 1990). A working group of 30 organizations from 13 countries initiated this project with the main approach of monitoring geodynamic deformation in the complex interaction zone between Caribbean, Cocos, Nazca and South-American plates. They observed five stations in Venezuela between January and February 1988 (Figure 1A) in four two-day and two three-day discontinuous 6 hours sessions over sites marked by concrete monuments, and embedded stainless steel markers surrounded by several reference markers. These measurements were also helpful in order to link the local geodetic networks (Henneberg, 1983; Henneberg & Schubert, 1986), and to connect the GPS network to the gravimetric observations (Drewes *et al.* 1991). The first repetition for the major part of the CASA network was carried out in 1991. However, the Venezuelan stations were not measured due to logistic problems related with the Persian Gulf War. In fact, the Venezuelan network measured in 1993 increased to 21 stations which covered El Pilar and Boconó faults with six profiles of 3 stations each; the remaining stations were used as stable reference (Figure 1B). The measurements were realized between February 15 and 25, 1993 during at least 3 sessions of 7h per day. In addition, the Maracaibo-Mamón and Merida stations were measured during the whole campaign, as well as the International Terrestrial Reference Frame (ITRF) station at the U.S. Naval Observatory-Ritchmond, Florida (Drewes *et al.* 1989; 1995; Kellogg & Dixon, 1990).

Since 1994, several campaigns of GPS measurements (Table 1) have been headed by a working- group comprising national and international institutions: the University Simón Bolívar (USB), University of Colorado (UC), National Cartography Institute (now Simón Bolívar Geographical Institute of Venezuela -IGVSB) and University of Zulia (LUZ). In order to estimate the direction and rate of the Caribbean plate displacement relative to South-America, as well as the kinematic role of the Boconó fault in the accommodation of relative motion between the Caribbean and South American plates, and furthermore to calculate the velocity field in northeastern and western Venezuela (Figure 2). In May 1994, the working group carried out a campaign known as CARIVEN94 (Bilham, 1994; www.unavco.org) with measurements at 20 sites for three two-day or four-day multiple 8-hour sessions with simultaneous measurements at 8 to 10 sites. In 1998, they re-measured seven sites (ARAY, AVES, CANO, CARU, COCH, JUAN, MARG; See: Venezuela 1998 in www.unavco.org), and in June 1999 they measured 11 sites (CARIVEN99), and 10 sites in March 2000. Again, they repeated observations in December 2004 and April 2006, respectively. Between 1999 and 2006 the measuring time at the stations increased to five-day time spans during 12 hours per day. During all campaigns, dual frequency GPS receivers with 30 s sampling intervals and antennas mounted on tripods with an elevation mask of 15° in sites comprising stainless steel markers embedded in concrete monuments, were used. Caracas, Maracaibo and Canoa sites have been usually used as control stations (Pérez *et al.* 2001ab, 2011).

In 1997, the GTFE (German Task Force for Earthquakes) was invited by FUNVISIS (Venezuelan Foundation for Seismological Research) to carry out geophysical and engineering studies after the Cariaco Earthquake. As to GPS studies, they installed dual-frequency GPS receivers with 30 s sampling intervals between July 19 and August 22, 1997 close to both ends of the visible surface rupture, while another equipment was installed as a reference stations in Cumaná. They calculated a right-lateral displacement of about 10 cm near the western end of the rupture zone, and they pointed out that the north-south and the vertical components were considerably smaller (Baumbach *et al.* 2004).

In early 2003, FUNVISIS personnel installed 36 new brass benchmarks covering eastern Venezuela from islands in the north to the supposed stable Precambrian craton in the south (south of the Orinoco river). All these benchmarks were planted to stable natural rock outcrops. In late 2003

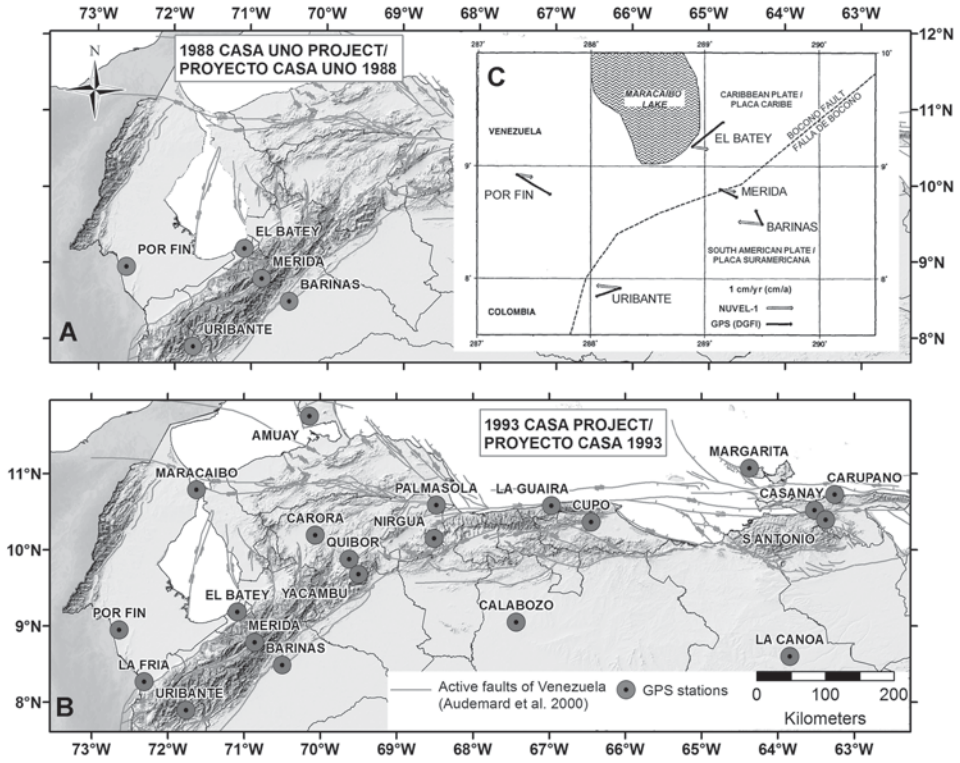


**Figure 1.** Distribution of CASA Project stations. (A) The network installed and measured in 1988. (B) The sites measured in 1993 and (C) the vectors reported by Drewes *et al.* 1995 (Relief map from Garrity *et al.* 2004).

**Figura 1.** Distribución de las estaciones del Proyecto Casa. (A) Red instalada y medida en 1988, (B) sitios medidos en 1993 y (C) vectores reportados por Drewes *et al.* 1995 (Mapa de relieve de Garrity *et al.* 2004).

(November 29 through December 14), 33 stations of the 40 existing (36 sites of FUNVISIS network and 4 existing ones -1 from Petroleos de Venezuela S.A.-PDVSA and 3 from University Navstar Consortium - UNAVCO) were occupied, and 24 sites were re-occupied in late 2005 by a team of FUNVISIS and University of Savoie researchers (Figures 3 and 4). The sites have been measured in several campaigns with dual-frequency GPS and geodetic antennas at least two sessions of 24 hours while the AUD0 station has been measured continuously during whole campaigns. This effort intends to estimate the relative movement of El Pilar Fault and other near faults. In early 2013, we installed a new site (UVA0) in the Coche Island and recovered two pre-existing sites (MAN1-HOR1). In this opportunity, 30 sites were re-occupied.

Recently, FUNVISIS has targeted to western Venezuela (Figure 5), where 19 new brass rocks outcrop-glued sites were installed in late 2011. Late the same year, FUNVISIS, with the support of PDVSA and IGVSB, measured 30 sites, of which some were new sites, and others were existing benchmarks. In early 2013, 26 sites were re-occupied. The dual-frequency GPS receivers remained at each site between 48 and 72 hours continuously with 30 s sampling intervals. It is worth mentioning that the sites installed by FUNVISIS since 2003 show two new aspects: a) the brass spits are glued to stable bedrock outcrops or existing concrete benchmarks from other institutions (IGVSB, UNAVCO, among others), suppressing the use of tripods, since antennas sit on brass screwed rods or extensions. b) The geographic spreading of the spits responds to two scientific aims: 1) slip rate of individual faults, regardless of their seismogenic potentials; not just interested in the relative plate motion between Caribbean and South America and 2) tectonic rotation of discrete tectonic blocks.

## Processing

Since the first measurements of CASA project, several authors (Drewes *et al.* 1995; Pérez *et al.*

2001b, 2011; Jouanne *et al.* 2011) have used the Bernese package software of the University of Berna (Rothacher *et al.* 1993; Hugentobler *et al.* 2005) as well as parameters provided from the International GNSS Service (IGS), in order to process data. Other authors (DeMets *et al.* 2000; Weber *et al.* 2001; Trenkamp *et al.* 2002) have chosen the GYPSY software (GYPSY OASIS, GYPSY OASIS II or simply GYPSY) developed at the Jet Propulsion Laboratory (JPL) from California Technology Institute (CALTECH), with their satellite ephemeris and clock files (Lichten & Border, 1987; Blewitt, 1989, 1990; Zumberge *et al.* 1997). Most of the authors have referred the results to ITRF96, ITRF97 or ITRF2005 (Boucher *et al.* 1999; Altamimi *et al.* 2007), except for the 1988 CASA project data because the ITRF was not in existence at that moment (Drewes *et al.* 1995). Usually, they have followed the standard processing indicated by others authors (Blewitt *et al.* 1992; Dixon *et al.* 1997; 1998; Dragert *et al.* 2001).

**Contribution of the GNSS application to geodynamic studies**

Comparison between 1988 and 1993 CASA project measurements allowed deriving an eastward motion of the Caribbean plate and a westward motion of the South American plate in the order of 1 cm/year; in other words, a relative right lateral strike slip notion between both plates (Drewes *et al.* 1995). In spite of the few stations, the lower accuracy due to the less dense satellite constellation, and the poor orbit quality of the GPS at the time, the results provided provisional data for the detection of crustal movements along the Boconó fault (Drewes *et al.* 1995). Although Pennington (1981), and later other authors (Audemard, 1993; Ego *et al.* 1993, among others), but still contemporary to the CASA Project, had proposed the ongoing escape of the North Andean Block, Drewes *et al.* (1995) did not realize that the Maracaibo block was being extruded to NNE from their vectors. In addition, the Mérida station may be reflecting the NNE escape, combined or accompanied by a local kinematic process, whose vectorial addition points to the east. Trenkamp *et al.* (2002), from 44 stations belonging to CASA Project (measured several times in 1991, 1994, 1996 and 1998), of which five were in Venezuela (ELBA, URIB, MERI, BARI and JUNQ), helped to determine: the active collision of the Panama Arc with Colombia and the associated ongoing deformation up to 550 km from the rupture zone, the Caribbean plate subduction, the escape of the North Andes, the earthquake strain accumulation and the oblique subduction at the Ecuador trench. Nonetheless, the measurements were not dense enough to delineate the several blocks in the Northern Andes and the Maracaibo block (Mann & Burke, 1984), even when the results were consistent with the sinistral strike-slip of the Santa Marta-Bucaramanga fault. DeMets *et al.* (2000) pointed out a motion of 18-20±3 mm/y (2σ) in several places along the Caribbean-South America plate boundary. They suggested an approximate upper bound of 4-6 mm/year for internal deformation in the Caribbean plate, using the AVES station in Venezuela and three more stations located in the inner part of Caribbean plate (ROJO, SANA and CROI). In the same way, Weber *et al.* (2001), using data from 7 sites in the Caribbean plate, including the AVES station, and 5 sites in the South America plate, point out that eastward displacement of the South American plate of ~20 mm/year along most of the plate boundary is significantly faster than NUVEL-1A model (DeMets *et al.* 1990; 1994). However, the motion kept a similar azimuth. Unfortunately, the AVES station, measured in 1994 and 1998, and used to estimate the Caribbean plate motion, was destroyed by the Hurricane Mitch in late 1998 (DeMets *et al.* 2000).

Pérez *et al.* (2001ab), from GPS observations at 22 sites in the Lesser Antilles and Venezuela between 1994 and 2000, calculated a rate of 20.5 ± 2 mm/year along N 84° ± 2° E azimuth at 65° W for the Caribbean plate relative to the South-American plate. Indeed, they explained that east of 68°W, the velocity field across the Caribbean-South America plate boundary is confined to a narrow shear zone, and 80 per cent of the surface deformation is contained within an 80-km-wide zone centered a few kilometers northward of the El Pilar Fault. In contrast, the width of the plate boundary west of 68°W increases to more than 300 km, characterized by right-lateral shear. This slip is shared between the Boconó fault (9-11 mm/year with a minor convergence of 1 mm/year) and 2-5

**Table 1.** List of stations measured by the USB group between 1994 and 2006.
**Tabla 1.** Estaciones medidas por el grupo USB según el año de observación desde 1994 hasta 2006.

| STATIONS/ Estaciones | 1994 | 1998 | 1999 | 2000 | 2004 | 2006 |
|---|---|---|---|---|---|---|
| Source/Fuente : | www.unavco.org/ Pérez *et al.* 2001ab | www.unavco.org/ Pérez *et al.* 2001ab | Pérez *et al.* 2001ab | Pérez *et al.* 2001 ab | Gavotti, 2005 / Pérez *et al.* 2011 | Molina, 2006 / Pérez *et al.* 2011 |
| AMUA | X | | X | | | |
| ARAY | X | X | | | | |
| AVES | X | X | | | | |
| BAUL | X | | | | | |
| BLAN | X | | X | | | |
| CALA | X | | X | | | |
| CANO | X | X | X | X | X | X |
| CARU | X | X | | | | |
| CHUR | X | | X | | | |
| COCH | X | X | | | | |
| GOYA | X | | X | | | |
| GUAI | X | | | | | |
| JUAN | X | X | | | | |
| MARG | X | X | | | | |
| QUIB | X | | X | | | |
| ROQU | X | | X | | | |
| CASI/SCAS | X | | X | | | |
| TORT | X | | X | | | |
| YACA | X | | X | | | |
| MARA | | | X | X | X | X |
| CRCS/USB0 | | | X | X | X | X |
| BARI | | | X | | X | |
| ALTA | | | X | | X | |
| PIED | | | X | | X | |
| FRAI | | | X | | X | |
| TORO | | | X | | X | |
| BATE | | | X | | X | |
| DOMI | | | X | | X | |
| GUAC | | | | X | | X |
| PEDR | | | | X | | X |
| FUND | | | | X | | X |
| PREG | | | | X | | X |
| GRIT | | | | X | | X |
| DALI | | | | X | | X |
| GUAY | | | | X | | X |
| MERI* | | | | | | |
| BART* | | | | | | |

(*)Stations mentioned in Pérez *et al.* (2011) without a precise date of measurement / Sitios mencionados en Pérez *et al.* (2011) sin información de fecha de medición.

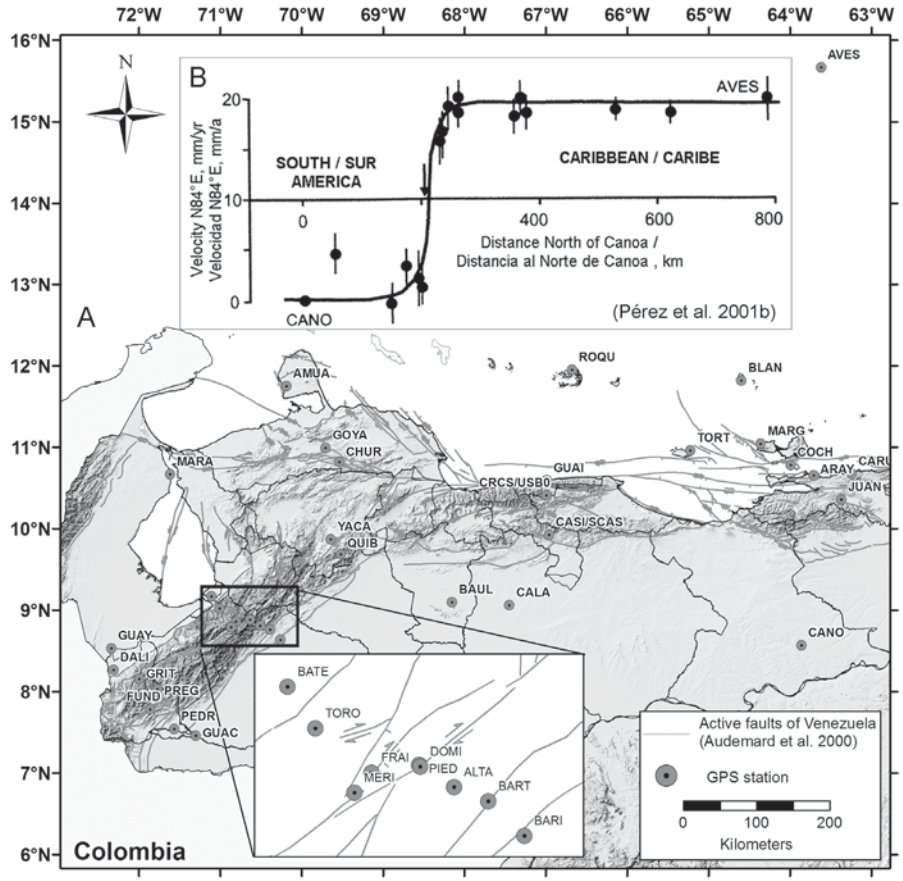


**Figure 2. (A)** Distribution of GPS stations observed for the working-group headed by the University Simón Bolívar. (B) Velocity field in the northeastern Venezuela (after Pérez *et al*. 2001b).

**Figura 2. (A)** Estaciones GPS observadas por el grupo liderado por la Universidad Simón Bolívar. (B) Campo de velocidades en el noreste de Venezuela (tomado de Pérez *et al*. 2001b).

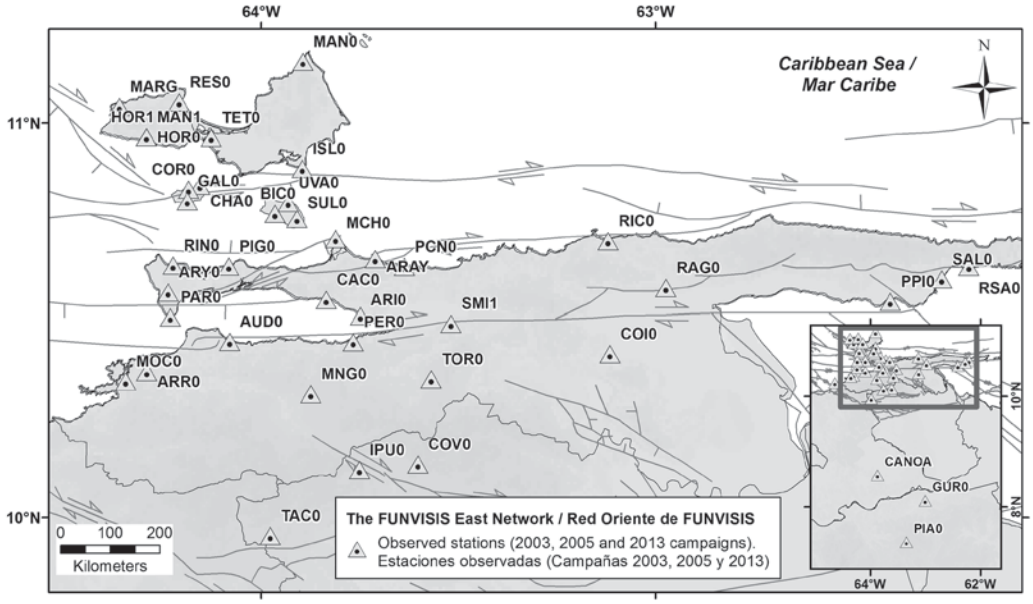


**Figure 3.** Location of FUNVISIS East Network sites measured in 2003, 2005 and 2013.

**Figura 3.** Ubicación de los sitios pertenecientes a la Red Oriente de FUNVISIS, medidos en los años 2003, 2005 y 2013.

mm of dextral shear on the La Victoria fault system. In addition, they estimated the co-seismic slip at depth responsible for the 1997 Cariaco earthquake using boundary element methods (King & Nostro, 1999) to estimate surface fault displacements (Okada, 1985). The best solution corresponds to a fault plane segmented in three patches, and striking N 84° E. Locking depth was set at 14 ± 2 km, and co-seismic slips estimated of 0.94, 1.25 and 1.1 m for each rectangular segment, from west to east.

Pérez *et al.* (2011) reported new results from measures realized from 1999 to 2006. They indicated that velocity vectors from sites in northwestern South America, at a distance of over 200 km from the Venezuelan Andes axis, showed an eastward uniform motion of ~15mm/year relative to the South-American craton. The displacement direction is oblique to the Venezuelan Andes and the Boconó fault, with an approximate N50°E strike. This obliquity is also observed in the slip vectors at the sites located at both flanks of the Boconó fault. This suggest that the 20 ±2 mm/year of eastward Caribbean plate motion (Pérez *et al.* 2001b; Weber *et al.* 2001) relative to South-American plate is partitioned in two components (Pérez *et al.* 1997; Audemard & Audemard, 2002): 12 ±2 mm/year of right lateral strike-slip confined within ~100 km-wide deformation zone, centered on the Boconó fault with a locking depth of 14 ±4 km, and 12-16 mm/year normal-to-chain convergence. Approximately 1/3 of this convergence (4-5 mm/year) is concentrated close to the Boconó fault and results in sub-parallel thrust faults running ~25km apart along both sides of the fault (Pérez *et al.* 2011).

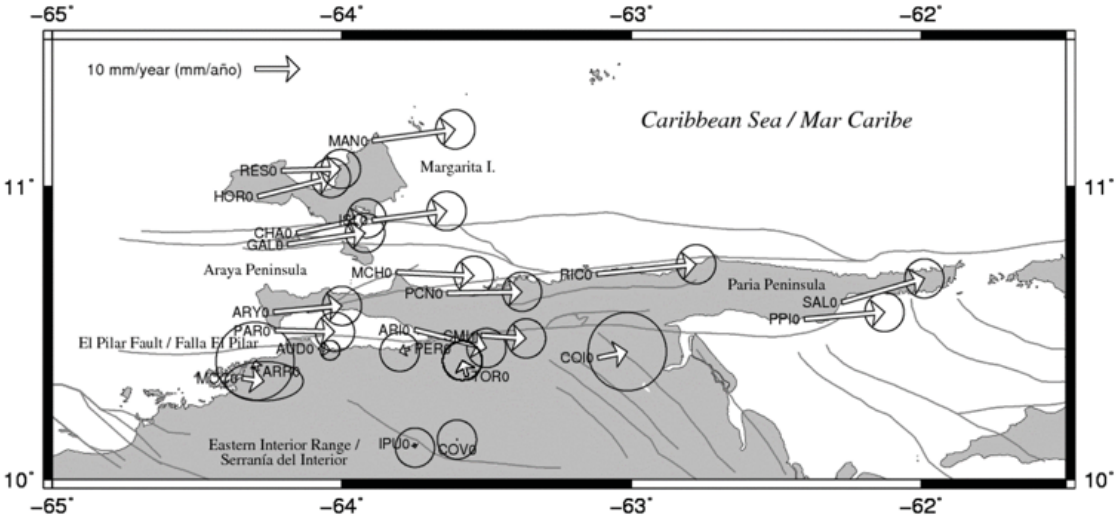


**Figure 4.** Observed velocities (white) from 2002 and 2005 GPS campaign data with error ellipses drawn for 66% confidence level (Jouanne *et al.* 2011) expressed in the South America plate reference frame.

**Figura 4.** Velocidades observadas (en blanco) a partir de las campañas de medición GPS realizadas en 2002 y 2005 con elipses de error de 66% de nivel de confidencia (Jouanne *et al.* 2011) con el cratón Suramericano fijo como referencia.

Jouanne *et al.* (2011) pointed out the lack of significant displacement (specially shortening) in the Serranía del Interior and eastward motion of up to 22 mm/y (relative to fixed South-American plate) of benchmarks located on the northern side of the El Pilar Fault. From uniform elastic half-space models for simulating current velocities (Okada, 1985), using a set of dislocations, they showed that the whole Caribbean-South America relative displacement takes place along the El Pilar Fault. They also indicated an important component of aseismic displacement along the upper part of El Pilar Fault. The preferred model comprises two segments of two dislocations each one, an upper locked or partially locked seismogenic dislocation, and a lower ductile part affected by an aseismic creep. This model suggests that between the surface and 12 km depth, only 40 per cent of displacement is locked for the western segment, and 50 per cent for the eastern segment. The transition between the upper and lower dislocations was fixed at 12 km according to the depth distribution of the 1997

Cariaco Earthquake aftershocks (Baumbach *et al.* 2004).

## PERSPECTIVES

Future works must focus on the recovering of sites already measured in the past (CASA, CARIVEN, UNAVCO, among others), as well as the corresponding data, densification of sites with geological, durability and security (personal and equipment) criteria. Another important aspect is the creation of a continuous GNSS (cGNSS) network linked with the present-day REMOS network (Satellite monitoring network) from IGVSB and neighboring countries networks (GEORED of Colombia, Trinidad & Tobago). In this sense, the NSF-funded COCONET project, running from 2011 through 2015, plans to install 5 cGNSS stations (3 on the Leeward Antilles islands, and 2 on the mainland at existing seismological BB stations run by FUNVISIS), and help with the installation of a sixth one on Aves Island. In parallel, FUNVISIS has received funding from the LOCTI (Ley Orgánica de Ciencia, Tecnología e Innovación) program in 2012 in order to refresh, enlarge and update the seismological BB stations network, as well as the purchase and installation of 9 cGNSS stations spread over the country. In addition, for some time there have been discussions on creating a National GNSS pool for repeated measurement of campaign sites: A set of equipments belonging to public institutions and universities available for campaigns reoccupations and extraordinary events (large earthquakes, among others). The results of GNSS observations must keep aiming at solving scientific epistemic uncertainties. The periodically campaigns or particular scientific objectives (e.g. slow-slip events, among others), and cGNSS

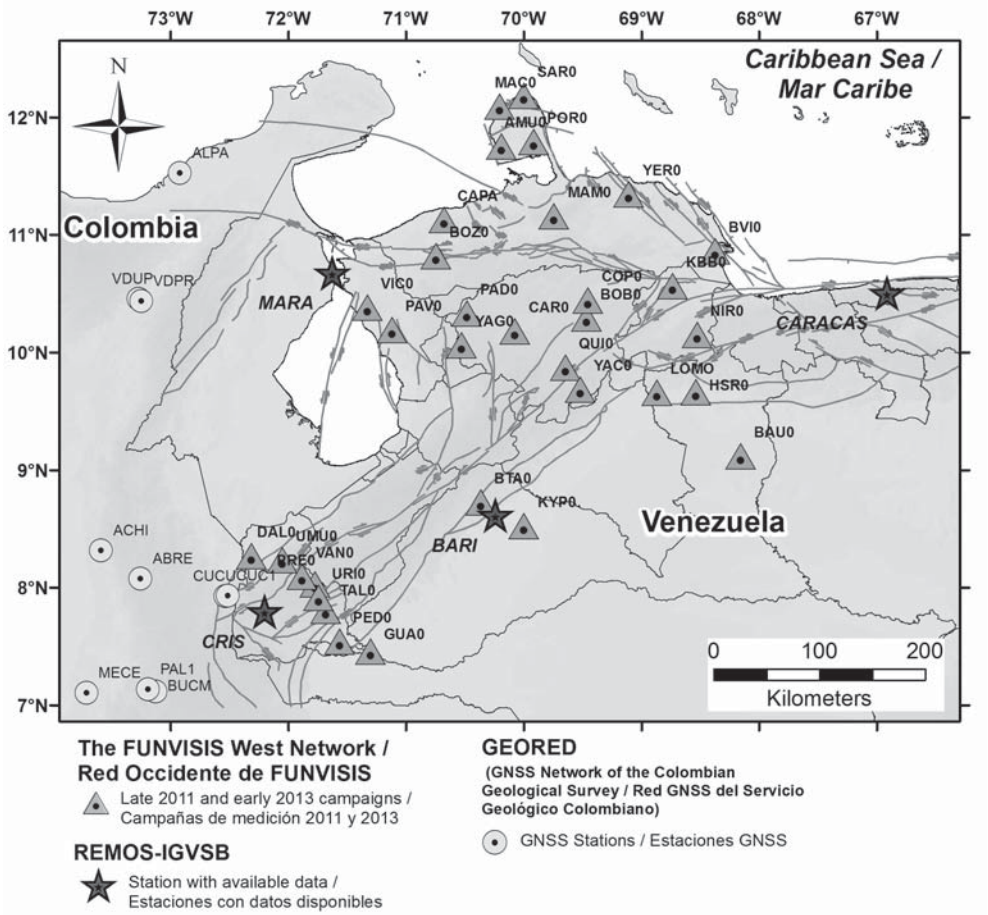


**Figure 5.** Localization of sites of the FUNVISIS western network measured in 2011 and 2013. Present-day situation of REMOS (from IGVSB) and GEORED (from Colombian Geological Survey).

**Figura 5.** Campaña de adquisición de datos GNSS en 2011 y 2013 en el occidente de Venezuela, más estaciones REMOS (del IGVSB) y GEORED (del Servicio Geológico Colombiano).

stations, allow detecting and measuring co-, inter- and post- seismic displacements, as well as the straining in fault-limited blocks allows significant advances in seismic hazard calculation. The efforts should focus also in the minor faults with equal o major seismogenic potential, with the support of the modeling based in modern algorithms, interaction with other disciplines, dense seismological networks, satellite images, and evidences taken directly from fault zones, among others.

## CONCLUSIONS

More than two decades of GNSS measurements in Venezuela with geodynamical objectives have reported significant results; nonetheless, it is necessary to joint efforts to improve the current situation. Looking for new challenges that allow a major developed of this discipline, from conception of campaigns, kind of equipments, processing and analysis of data, storage and guaranty of data. It is imperative to work in the building of better network of GNSS sites, a continuous monitoring network, and conformation of a national GPS pool for repeated measurement of campaign sites, belonging to the Venezuelan scientific community. Since 1988, the CASA project opened the way for this discipline. For two decades, many authors have contributed results, but still there are many options that never have been explored. Since 2003, from FUNVISIS, two new aspects were proposed in Venezuela: the brass spits glued to stable bed-rock outcrops or existing concrete benchmarks, suppressing the tripod-antenna configuration, and working in the geographic spreading of the spits with two scientific aims: 1) slip rate of individual faults, regardless of their seismogenic potentials; not just interested in the relative plate motion between Caribbean and South America, and 2) rotation of discrete tectonic blocks. Today, we know that the national territory presents a complex tectonic activity with important faults, which could produce earthquakes with magnitudes > 7, reasons to focus our efforts on the seismic risk mitigation.

## ACKNOWLEDGEMENTS

Carlos Reinoza PhD thesis and stay in ISTerre Laboratory is funded through Venezuela's FUNDAYACUCHO Grant N° 756514C. This research is a contribution to FONACIT-ECOS Nord grant V10U01.

## REFERENCES

Altamimi, Z., Collilieux, X., Legrand, J., Garayt, B., Boucher, C. (2007). ITRF2005: a new release of the international terrestrial reference frame based on time series of station positions and earth orientation parameters. J. Geophys. Res. 112, B09401, doi:10.1029/2007JB004949/.

Audemard, F. A. (1993). Néotectonique, Sismotectonique et Aléa Sismique du Nord-ouest du Vénézuéla (Système de failles d'Oca-Ancón). PhD Thesis, Université Montpellier II, France, 369 pp + appendix.

Audemard, F. A., Machette, M., Cox, J., Hart, R., Haller, K. (2000). Map of Quaternary Faults of Venezuela. Scale 1:2,000,000. Accompanied by report: Map and Database of Quaternary Faults in Venezuela and Offshore regions (USGS Open-File Report 00-18, 78 p). A project of the International Lithosphere Program Task Group II-2: Major active Faults of the World (Regional Coord.: Carlos Costa, Univ. San Luis-Argentina, ILP II-2 co-chairman Western Hemisphere: Michael Machette, USGS-Colorado). Also in http://greenwood.cr. usgs.gov/pub/open-file-reports/ofr-00-0018 (pdf).

Audemard, F. E. & Audemard, F. A. (2002). Structure of the Mérida Andes, Venezuela: Relations with the South America-Caribbean geodynamic interaction. Tectonophysics, 345, 299-327.

Baumbach, M., Grosser, H., Romero, G., Rojas, J., Sobiesiak, M., Welle, W. (2004). Aftershock pattern of the July 9, 1997 Mw= 6.9 Cariaco earthquake in Northeastern Venezuela. Tectonophysics, 379, 1–23.

Beltran, C. (1993). Neotectonic Map of Venezuela, scale 1:2 000 000, FUNVISIS, Caracas, Venezuela.

Beutler, G., Bauersima, I. Gurtner, W., Rothacher, M., Schildknecht, T., Mader, G. L., Abell. M. D. (1987). Evaluation of the 1984 Alaska Global Positioning System campaign with the Bernese GPS Software. J. Geophys. Res., 92(B2), 1295–1303, doi:10.1029/JB092iB02p01295.

Bilham, R. (1994). Project CARIVEN: Caribbean / Venezuela relative motion from GPS geodesy. NFS Proposal and Project.

Blewitt, G. (1989). Carrier phase ambiguity resolution for the Global Positioning System applied to geodetic baselines up to 2000 km. J. Geophys. Res. 94 (B8), 10187-10283.

Blewitt, G. (1990). An automatic editing algorithm for GPS data. Geophys. Res. Lett. 17 (3), 199-202.

Blewitt, G., Heflin M. B., Webb F. H, Lindqwister U. J., Malla R. P. (1992). Global coordinates with

centimeter accuracy in the International Terrestrial Reference Frame using the Global Positioning System. Geophys. Res. Lett, 19, 853-856.

Boucher, C., Altamimi, Z., Sillard, P. (1999). The 1997 International Terrestrial Reference Frame (ITRF 1997). IERS Technical Note 27, Observatoire de Paris, Paris.

Bucher, W. H. (1952). Geologic structure and orogenic history of Venezuela. Geol. Soc. Am. Mem. 49, 113 pp.

Demets, C., Gordon, R. G., Argus, D.F., Stein, S. (1990). Current plate motions. Geophys. J. Int. 101 (2), 425-478, doi: 10.1111/j.1365-246X.1990. tb06579.x.

Demets, C., Gordon, R. G., Argus, D. F., Stein, S. (1994). Effect of recent revisions to the geomagnetic reversal time scale on estimates of current plate motions. Geophys. Res. Lett. 21 (20), 2191-2194, doi: 10.1029/94GL02118.

Demets, C., Jansma, P. E., Mattioli, G. S., Dixon, T. H., Farina, F., Bilham, R., Calais E., Mann, P. (2000). GPS geodetic constraints on Caribbean North America Plate Motion. Geophys. Res. Lett. 27 (3), 437–440, doi:10.1029/1999GL005436.

Dixon, T. H., Farina, F., Demets, C., Jansma, P., Mann, O., Calais, E. (1998). Relative motion between the Caribbean and North American plates and related boundary zone of deformation from a decade of GPS observations. J. Geophys. Res. 103, 15157-15182.

Dixon, T. H., Mao, A., Bursik, M. I., Heflin, M. B., Langbein, J., Stein, R. S., Webb, F. H. (1997). Continuous monitoring of surface deformation at Long Valley Caldera, California, with GPS. J. Geophys. Res. 102 (B6), 12,017-12,034.

Dragert, H., Wang, K., James, T. S. (2001). A silent event on the deeper Cascadia subduction interface. Science, 292, 1525-1528.

Drewes, H., Torge, W., Roder, R. H., Badell, C., Bravo, D., Chourio, O. (1991). Absolute and relative gravimetric surveys of national and geodynamic networks in Venezuela. J. South Am. Earth Sci. 4 (4), 273-286.

Drewes, H., Kaniuth, K., Stuber, K., Tremel, H., Kahle, H.G., Straub, C., Hernandez, N., Hoyer, M., Wildermann, E. (1995). The CASA'93 GPS Campaign for Crustal Deformation Research along the South Caribbean Plate Boundary. J. Geodyn. 20 (2), 129-144.

Drewes, H., Reigber, C., Stuber, K., Suarez, M., Tremel, H., Henneberg, H., Hoyer M., Chourio, O., Rekkedal, S. (1989). The Venezuelan part of the CASA/UNO GPS Project. Manuscripta Geodaetica, 14, 339-344.

Ego, F., Sebried, M., Lavenu, A., Yepez, H., Eguez, A. (1993). A new geodynamical model for the northern Ecuador Andes. EUG VII, 4-8 April 1933, Terra abstract 5 (1), 203.

Garrity, C., Hackley, D., Urbani, F. (2004). Digital shaded – relief map of Venezuela. http://pubs.usgs.gov/of/2004/1322.

Gavotti, P. (2005). Cuantificación del desplazamiento actual de la Falla de Boconó a partir de observaciones GPS. Unpublished Geophysical Engineer disertation, Universidad Simón Bolívar; Caracas, Venezuela, 139 p.

Henneberg, H. G. & Schubert, C. (1986). Geodetic networks along the Caribbean-South-American plate boundary. Tectonophysics, 130 (1-4), 77-94.

Henneberg, H. G. (1983). Geodetic control of neotectonics in Venezuela. Tectonophysics, 97 (1-4), 1-15.

Hugentobler, U., Dach, R., Fridez, P. (2005). Bernese GPS Software. Version 5.0. Astronomical Institute. University of Bern, Switzerland, 388 pp.

Jouanne, F., Audemard, F., Beck, C., Van Velden, A., Ollarves, R., Reinoza, C. (2011). Present-day deformation along the El Pilar Fault in Eastern Venezuela: Evidence of creep along a major strike-slip fault. J. Geodyn. 51, 398–410.

Kellogg, J. N. & Dixon, T. H. (1990). Central and South America GPS geodesy - CASA Uno. Geophys. Res. Lett. 17(3), 195–198, doi:10.1029/GL017i003 p00195.

King, G. & Nostro, C. (1999). Almond Lite v.2.02: A program to calculate Coulomb stresses around rectangular faults or dykes. Manual d' Utilisation, Institute de Physique du globe, Paris.

Lichten, S. M. & Border, J. S. (1987). Strategies for High-Precision Global Positioning System Orbit Determination. J. Geophys. Res. 92(B12), 12,751–12,762, doi:10.1029/JB092iB12p12751.

Lisowski, M., Savage, J. C., Prescott, W. H. (1991). The velocity field along the San Andreas Fault in central and southern California, J. Geophys. Res. 96, 8369-8389.

Mann, P. & Burke, K. (1984). Neotectonics of the Caribbean. Rev. Geophys. Space Phys. 22, 309-362.

Molina, L. (2006). Campo de velocidades de la Falla de Boconó a partir de observaciones GPS. Unpublished Geophysical Engineer disertation, Universidad Simón Bolívar; Caracas, Venezuela, 84 p.

Molnar, P. & Sykes, L. R. (1969). Tectonics of the Caribbean and Middle America regions from focal mechanisms and seismicity. Geol. Soc. Am. Bull. 60, 1639-1684.

Okada, Y. (1985). Surface deformation due to shear and tensile faults in a half-space. Bull. Seismol. Soc. Am.

75 (4), 1135–1154.

Pennington, W. (1981). Subduction of the eastern Panama basin and seismotectonics of northwestern South America. J. Geophys. Res. 86 (B11), 10753–10770.

Perez, O. J. & Aggarwal, Y. P. (1981). Present-day tectonics of the southeastern Caribbean and northeastern Venezuela. J. Geophys. Res. 86(B11), 10791-10804.

Perez, O. J., Jaimes, M., Garciacaro, E. (1997). Microseismicity evidence for subduction of the Caribbean plate beneath the South-American plate in northwestern Venezuela. J. Geophys. Res. 102, 17875-17881.

Pérez, O. J., Bilham, R., Bendick, R., Hernández, N., Hoyer, M., Velandia, J., Moncayo, C., Kozuch, M. (2001a). Velocidad relativa entre las placas del Caribe y Sudamérica a partir de observaciones dentro del sistema de posicionamiento global (GPS) en el norte de Venezuela. Interciencia, 26 (2), 69–74.

Pérez, O. J., Bilham, R., Bendick, R., Velandia, J. R., Hernandez, N., Moncayo, C., Hoyer, M., Kozuch, M. (2001b). Velocity field across the southern Caribbean plate boundary and estimates of Caribbean/South-American plate motion using GPS geodesy 1994–2000. Geophys. Res. Lett. 28, 2987–2990.

Perez, O., Bilham, R., Sequera, M., Molina, L., Gavotti, P., Codallo, H., Moncayo, C., Rodríguez, C., Velandia, R., Guzman, M., Molnar, P. (2011). Campo de Velocidades GPS en el Occidente de Venezuela: Componente Lateral Derecha asociada a la Falla de Boconó y Componente Convergente perpendicular a Los Andes. Interciencia, 36 (1), 39-44.

Rothacher, M., Beutler, G. Gurtner, W. Brockmann, E., Mervart, L. (1993). Bernese GPS Software version 4.0 Documentation, Astronomical Institute, University of Berne.

Stephan, J. F., Mercier De Lepinay, B., Calais, E., Tardy, M., Beck, C., Carfantan, J. C., Olivet, J. L., Vila, J. M., Bouysse, P., Mauffret, A., Bourgois, J., Thery, J. M., Tournon, J., Blanchet, R., Dercourt, J. (1990). Paleo-geodynamic maps of the Caribbean: 14 steps from Lias to Present. Bull. Société Géologique de France 8 (VI), 915–919, 14 appendices.

Trenkamp, R., Kellogg J. N., Freymueller J. T., Mora, H. P. (2002). Wide plate margin deformation, southern Central America and northwestern South America, CASA GPS observations. J. South Am. Earth Sci. 15 (2), 157-171.

Weber, J., Dixon, T., Demets, C., Ambeh, W., Jansma, P., Mattioli, G., Saleh, J., Sella, G., Bilham, R., Pérez, O. (2001). GPS estimate of relative motion between the Caribbean and South American plates and geologic implications for Trinidad and Venezuela. Geology, 29 (1), 75–78.

Zumberge, J. F., Heflin, M. B., Jefferson D. C., Watkins M. M., Webb, F. H. (1997). Precise point positioning for the efficient and robust analysis of GPS data from large networks. J. Geophys. Res. 102(B3), 5005–5017, doi:10.1029/96JB03860.

***Table 4.2.*** *Sites belonging to the Eastern Venezuela network collected in 2003, 2005 and 2013 by FUNVISIS-University of Savoie team.*

| Station | Long (deg) | Lat (deg) | 2003 | 2005 | 2013 |
|---|---|---|---|---|---|
| ARAY | -63.711 | 10.655 | X | - | - |
| ARI0 | -63.749 | 10.511 | X | X | X |
| ARR0 | -64.291 | 10.370 | X | X | X |
| ARY0 | -64.236 | 10.571 | X | X | X |
| AUD0 | -64.081 | 10.447 | X | X | X |
| BIC0 | -63.965 | 10.770 | X | X | X |
| CAC0 | -63.837 | 10.553 | X | X | X |
| CANOA | -63.861 | 8.568 | X | - | - |
| CHA0 | -64.156 | 10.841 | X | X | X |
| COI0 | -63.116 | 10.415 | X | X | X |
| COR0 | -64.184 | 10.831 | - | X | X |
| COV0 | -63.603 | 10.136 | X | X | X |
| GAL0 | -64.188 | 10.802 | X | X | X |
| GUR0 | -62.995 | 8.112 | - | X | - |
| HOR0* | -64.291 | 10.965 | X | X | X |
| IPU0 | -63.751 | 10.122 | X | X | - |
| ISL0 | -63.896 | 10.884 | X | X | X |
| MAN0* | -63.895 | 11.156 | X | X | X |
| MARG | -64.360 | 11.042 | - | X | X |
| MCH0 | -63.811 | 10.707 | X | X | X |
| MNG0 | -63.875 | 10.314 | X | X | - |
| MOC0 | -64.344 | 10.346 | X | X | X |
| PAR0 | -64.231 | 10.508 | X | X | X |
| PCN0 | -63.637 | 10.636 | X | X | X |
| PDV0 | -64.633 | 10.238 | - | X | - |

| | | | | | |
|---|---|---|---|---|---|
| PER0 | -63.767 | 10.446 | - | X | X |
| PIA0 | -63.337 | 7.358 | X | X | - |
| PIG0 | -64.083 | 10.637 | X | - | X |
| PPI0 | -62.404 | 10.547 | X | X | - |
| RAG0 | -62.974 | 10.582 | X | - | X |
| RES0 | -64.209 | 11.053 | X | X | X |
| RIC0 | -63.120 | 10.701 | X | X | X |
| RSA0 | -62.205 | 10.636 | X | X | - |
| SAL0 | -62.274 | 10.604 | X | X | - |
| SMI1 | -63.519 | 10.492 | X | X | X |
| SUL0 | -63.910 | 10.757 | - | X | X |
| TAC0 | -63.977 | 9.954 | - | X | X |
| TET0 | -64.127 | 10.963 | - | X | X |
| TOR0 | -63.569 | 10.352 | X | X | X |
| UVA0 | -63.932 | 10.798 | - | - | X |

(*) Sites recovered in 2013. Former HOR0 and MAN0 are present-day renamed HOR1 and MAN1 respectively.

### 4.2.2. Installation of network in Western Venezuela

As I mentioned above in sections 4.1 and 4.2., 19 new brass rocks outcrop-glued sites were installed in late 2011 (Figure 4.6, Table 4.3). The selection of these sites was according a detailed review of possible sites. First, I compiled data of almost 500 benchmarks belonging to REGVEN (Figure 4.7 -http://www.igvsb.gob.ve/regven.html) with the purpose of reuse some benchmarks. This list of sites was added to the existing benchmarks list of previous campaigns: CASA, Cariven 1994, Venezuela 1998 and, other sites reported in Pérez et al. (2001a; b, 2011).

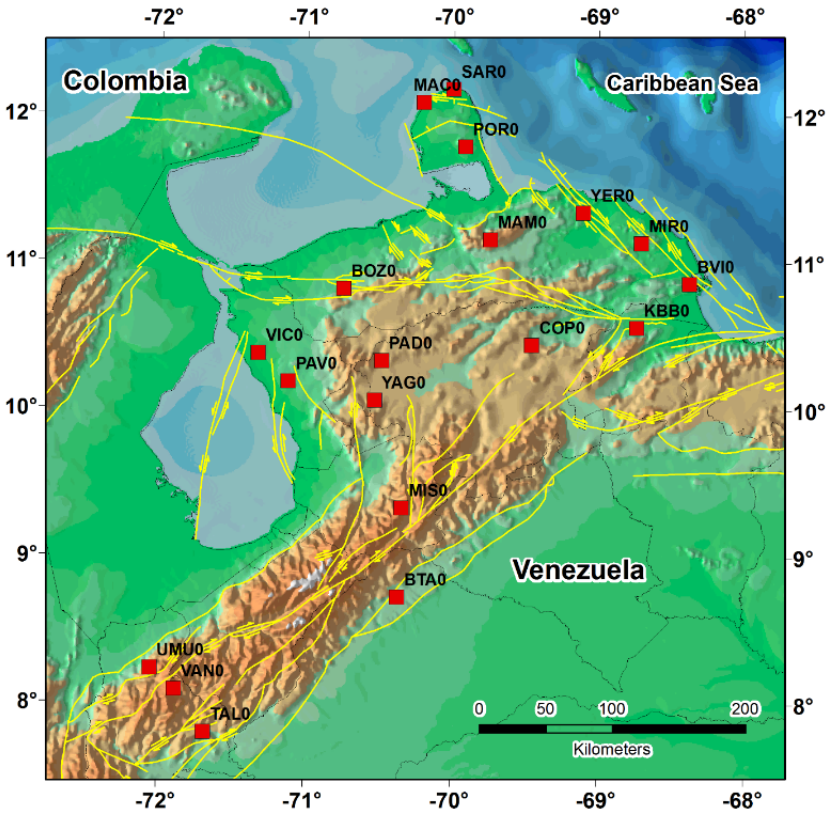


***Figure 4.6**. Distribution of 19 new brass rocks outcrop-glues sites installed in late 2011.*

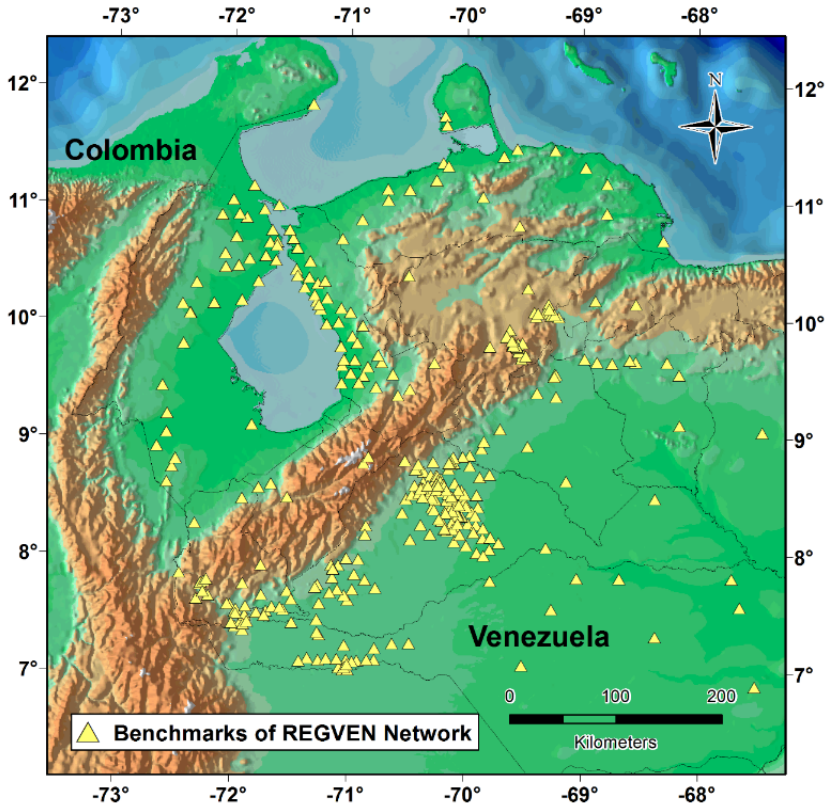


***Figure 4.7.** Distribution of benchmarks belonging to REGVEN Network.*

The preliminary selection included: integration of sites within a SIG, revision of the emplacement for each site: presence or not of stable bedrock outcrop, stability, hazards, etc. according to the existing geological maps and revision of available satellite images and/or aerial photographs. After the first sorting, a field reconnaissance of probable new sites and existing benchmarks was carried out (Between August-September 2011). For a second pre-selection, I included sites considering, apart from stable bedrock outcrop, existing concrete benchmarks or structures in guarded safe places. Moreover, in order to estimate the slip rate of individual faults and tectonic rotation of blocks, and not just the relative plate motion between plates, the geographic spreading of sites was established according to the distance to the faults and distribution on tectonic blocks. In October 2011, the brass spits were installed in 19 sites. As mentioned in the publication (Section 4.2.1), 30 sites was measured in late 2011 including new sites and already existing benchmarks. In early 2013, 26 sites were re-occupied (Figure 5, Table 4.3).

***Table 4.3.*** *Sites of the Western Venezuela network*

| Station | Long (deg) | Lat (deg) | Late 2011 | Early 2013 |
|---|---|---|---|---|
| **Western Venezuela Campaigns** | | | | |
| AMU0 | -70.188 | 11.753 | X | X |
| BAU0 | -68.158 | 9.118 | X | X |
| BOB0 | -69.465 | 10.287 | - | X |
| BOZ0* | -70.746 | 10.819 | X | X |
| BTA0* | -70.367 | 8.726 | X | X |
| BVI0* | -68.374 | 10.861 | X | - |
| CAPA | -70.677 | 11.128 | X | - |
| CAR0 | -70.074 | 11.128 | X | X |
| COP0* | -69.454 | 10.442 | X | X |
| DAL0 | -72.314 | 8.267 | X | X |

| | | | | |
|---|---|---|---|---|
| GUA0 | -71.303 | 7.455 | X | - |
| HSR0 | -68.538 | 9.661 | X | X |
| KBB0* | -68.737 | 10.562 | X | - |
| KYP0 | -69.999 | 8.524 | X | X |
| LOM0 | -68.870 | 9.658 | - | X |
| MAC0* | -70.204 | 12.089 | X | X |
| MAM0* | -70.204 | 12.088 | X | - |
| MIR0* | -68.707 | 11.137 | - | - |
| MIS0* | -70.340 | 9.332 | - | - |
| NIR0 | -68.536 | 10.152 | X | X |
| PAD0* | -70.483 | 10.331 | - | X |
| PAV0* | -71.120 | 10.189 | X | X |
| PED0 | -71.566 | 7.540 | X | X |
| POR0* | -69.917 | 11.789 | X | X |
| PRE0 | -71.775 | 8.029 | X | X |
| QUI0 | -69.646 | 9.871 | X | X |
| SAR0* | -70.001 | 12.180 | X | X |
| TAL0* | -71.681 | 7.801 | X | X |
| UMU0* | -72.050 | 8.235 | X | X |
| URI0 | -71.743 | 7.913 | X | X |
| VAN0* | -71.882 | 8.092 | X | X |
| VIC0* | -71.327 | 10.379 | X | X |
| YAC0 | -69.519 | 9.685 | X | - |
| YAG0* | -70.530 | 10.062 | X | X |
| YER0* | -69.108 | 11.343 | X | - |

(*) New brass rocks outcrop-glues sites installed in late 2011.

### 4.3. Permanent GNSS Networks

#### 4.3.1. REMOS Network

The Red de Estaciones de Monitoreo Satelital GPS - REMOS - (GPS Satellite Monitoring Station Network of Venezuela), belonging to the Instituto Geográfico Venezolano Simón Bolívar - IGVSB - (Geographic Institute of Venezuela) is a set of cGNSS stations distributed in Venezuela. Data is available at http://www.igvsb.gob.ve/remos.html. For the processing, I included the available data from four cGNSS stations between 2007 and 2013: Barinas, Caracas, Cumaná, and Maracaibo (This last one is under the responsibility of Universidad of Zulia; Table 4.4, Figure 4.8). Time series of theses stations are shown in Appendix A1.

***Table 4.4.*** *The REMOS stations indicating approximate coordinates, location, time span of occupation (Difference between first and last observation in years) and data available for years.*

| Station | Long (deg) | Lat (deg) | Location | Time Span (yr) | Years | | | | | | |
|---|---|---|---|---|---|---|---|---|---|---|---|
| | | | | | 2007 | 2008 | 2009 | 2010 | 2011 | 2012 | 2013 |
| BARI | -70.239 | 8.613 | Barinas | 0.5 | X | X | | | | | |
| CARA | -66.914 | 10.503 | Caracas | 2.4 | | | | X | X | X | |
| CUMA | -64.195 | 10.429 | Cumaná | 5.0 | | X | | X | | X | X |
| MARA | -71.624 | 10.674 | Maracaibo | 6.0 | X | X | X | X | X | X | X |

#### 4.3.2. GEORED – Colombian Geological Survey

GEORED, the short name adopted for the project "Implementation of the National GPS Network for geodynamics" and the acronym for "Geodesia: Red de Estudios de Deformación", is a research and development project based on GNSS instrumentation and the specific field

application for the study and analysis of crustal deformation in Colombia. This project is proposed and initiated by the Servicio Geológico Colombiano (Colombian Geological Survey – former INGEOMINAS) in 2007. I included in the processing data from five cGNSS stations and two stations measured two times between 2006 and 2007 (Table 4.5; Figure 4.8). Time series for all GEORED stations considered in this study are shown in Appendix A.

***Table 4.5.*** *The GEORED stations indicating approximate coordinates, location, time span of occupation (Difference between first and last observation in years), and data available for years.*

| Station | Long (deg) | Lat (deg) | Time Span (yr) | Years | | | | |
|---|---|---|---|---|---|---|---|---|
| | | | | 2009 | 2010 | 2011 | 2012 | 2013 |
| ALPA | -72,918 | 11,528 | 3.0 | X | X | X | X | |
| CUC1 | -72,513 | 7,932 | 1.3 | - | - | X | X | |
| PAL1 | -73,189 | 7,136 | 3.3 | X | X | X | X | |
| UWAS | -72,391 | 6,451 | 2.8 | X | X | X | X | |
| VMAG | -74,847 | 9,287 | 3,2 | | X | X | X | X |
| ABRE* | -73,226 | 8,087 | | | | | | |
| ACHI* | -73,577 | 8,246 | | | | | | |

(*) Stations measured in two field acquisition campaigns between 2006 and 2007

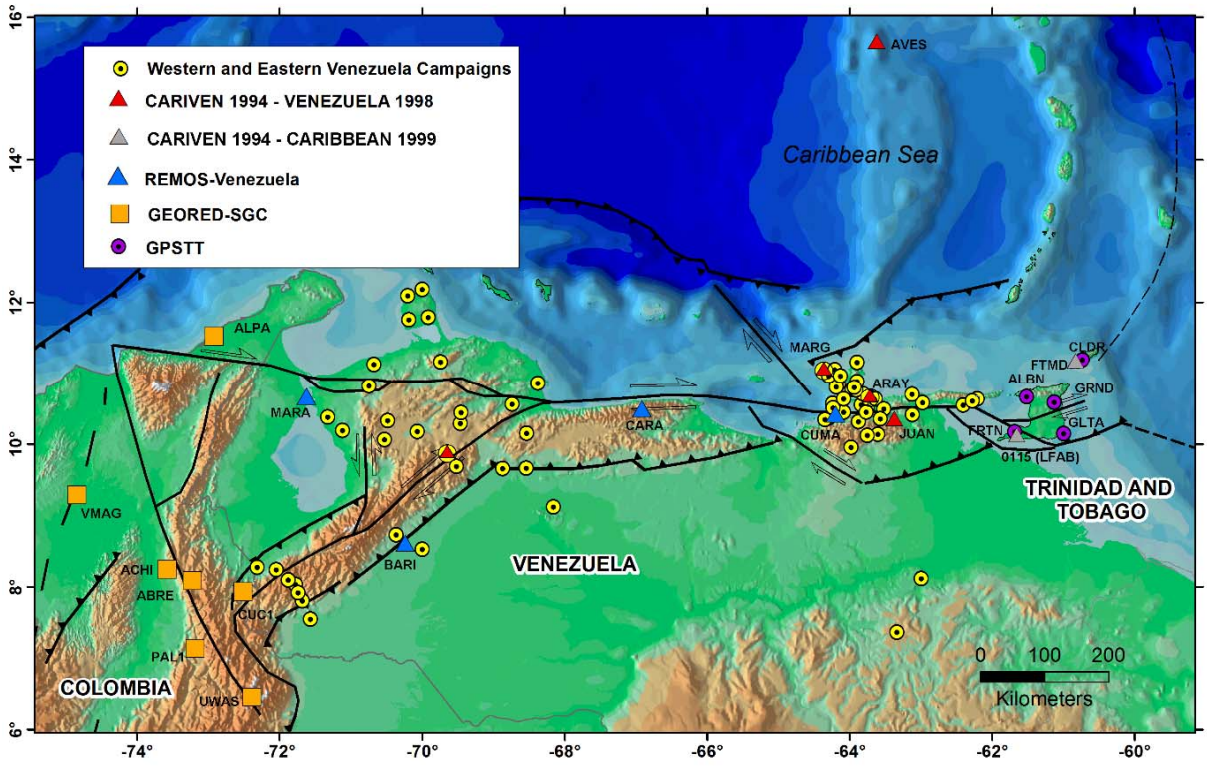


***Figure 4.8.*** *Set of stations belonging to REMOS Network, GEORED-SGC, GPSTT and acquisition campaigns: CARIVEN 1994, VENEZUELA 1998, CARIBBEAN 1999, 2003-2013 Western and Eastern Venezuela (names of sites are not represented), that were included in the processing.*

### 4.3.3. International GNSS Service

The International GNSS Service (IGS), formerly the International GPS Service, is presented as the highest-precision international civilian GPS community. It is a voluntary federation of more than 200 worldwide agencies that pool resources and permanent GPS and GLONASS station data to generate precise GPS and GLONASS products. The IGS stations included in the data processing are listed in the table 4.6 and represented in figure 4.9.

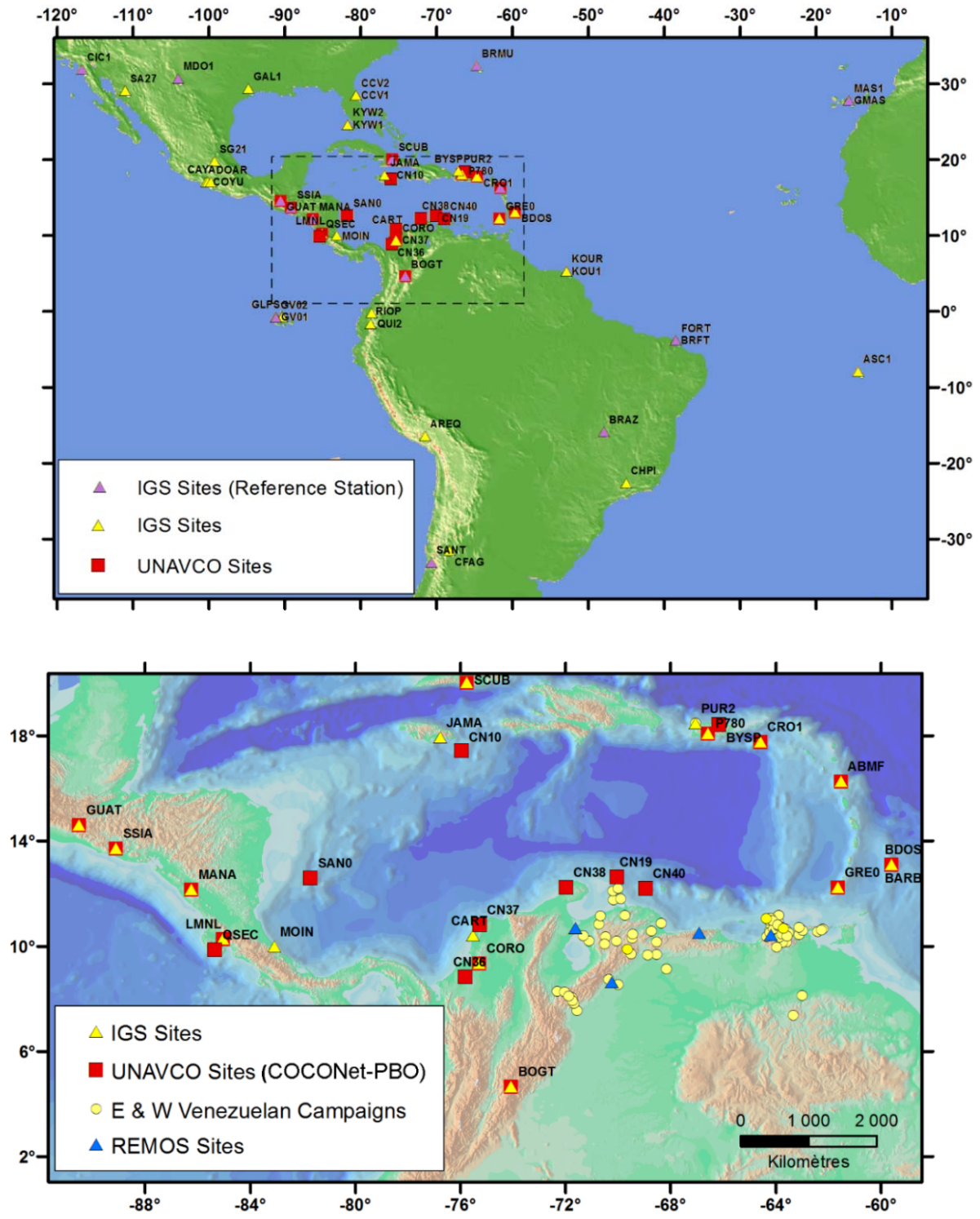


***Figure 4.9.*** *Site locations of IGS and UNAVCO (COCONet and PBO Networks) sites used in the data processing. (Below) All COCONet Project stations processed are shown in the zoomed view. Also, the Eastern and Western Venezuela Campaigns and REMOS Sites are incorporated in this figure.*

### 4.3.4. University Navstar Consortium

UNAVCO is a non-profit university-governed consortium created in 1984 in response to the challenge of applying GPS to geosciences. Nowadays, UNAVCO facilitates geoscience research and education using geodesy. It also provides the data archive interface v2 (http://facility.unavco.org/data/dai2/app/dai2.html#). This platform gives access to secure long-term storage for data and data products from deformation measurements. Data and data products are available to the scientific community and to the public. The interface propose two categories according to the collection style: permanent station and campaign.

Additionally, UNAVCO carries out several large projects; among them the Continuously Operating Caribbean GPS Observational Network (COCONet) and EarthScope - Plate Boundary Observatory (PBO). Furthermore, UNAVCO is responsible for monitoring a large set of stations that comprise the NASA Global GPS Network (GGN) and the International GNSS Service (IGS) Network. In the next paragraph, I describe the COCONet project because of its relevance for the region.

#### 4.3.4.1. COCONet

The Continuously Operating Caribbean GPS Observational Network shows a dense array of continuous Global Positioning System (cGPS) and meteorology stations (Figure 4.10). This project was conceived with the aim of developing a large-scale geodetic and atmospheric infrastructure in the Caribbean for a broad range of geoscience and atmospheric investigations. COCONet provide raw GPS data, GPS-PWV, surface meteorology measurements, time series of daily positions, as well as a station velocity field to support a broad range of geoscience investigations. Geodetic data product is available from the UNAVCO public data archive and potential regional data partners in the Caribbean.

This project has intended the installation of five stations in Venezuelan territory. For the moment that this manuscript is being written the equipment and material are being unloaded at FUNVISIS headquarters in Caracas. The installation will be carry out in the coming months. The COCONet project has established new stations but also integrated existing station operating in the Caribbean, as well as refurbished other stations; which explains why a COCONet station can be associated to other networks and agencies (Table 4.6). For the processing, I used 21 cGNSS stations belonging to the COCONet project (Figure 4.9).

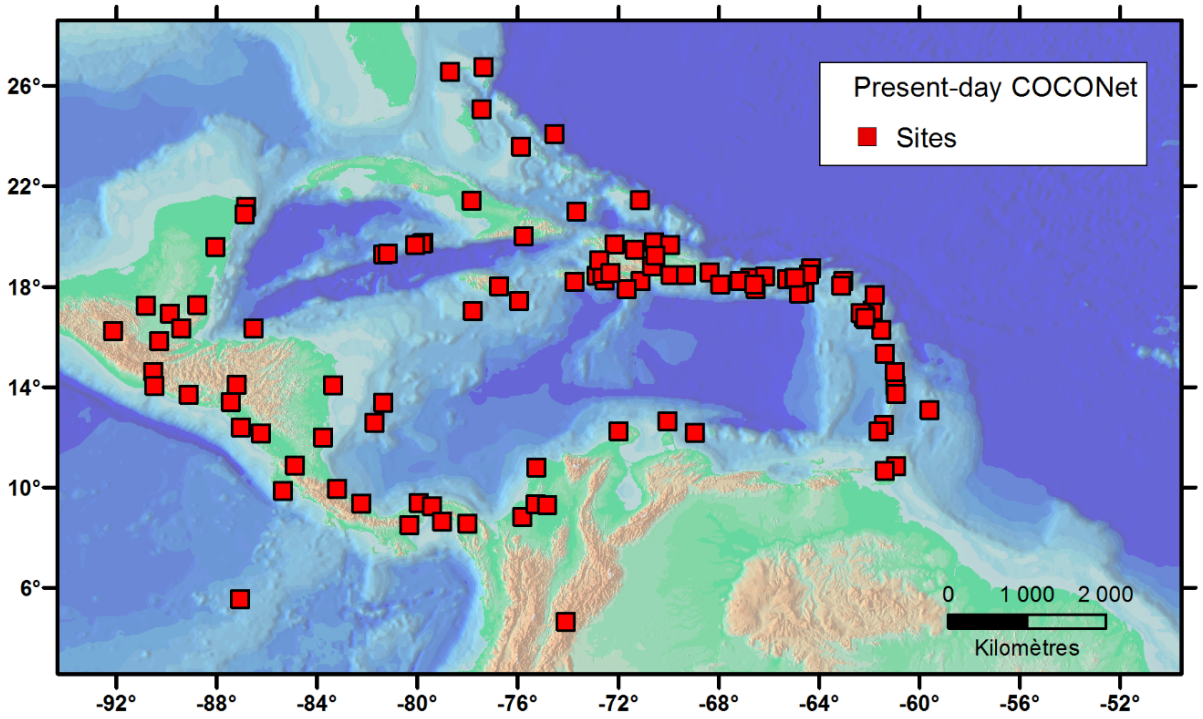


***Figure 4.10.*** *Site locations of COCONet stations available in the UNAVCO Data archive.*

***Table 4.6.*** *Complementary cGNSS stations used in the processing indicating approximate coordinates, location, network(s) and agency(ies) associated.*

| Station | Long (deg) | Lat (deg) | Location | Network | Agency |
|---|---|---|---|---|---|
| ABMF | -61.528 | 16.262 | Les Abymes, Guadeloupe | COCONet, IGS, PBO | IGN-SGN, UNAVCO |
| AREQ[1] | -71.493 | -16.466 | Arequipa, Peru | IGS, GGN | JPL, UNAVCO |
| ASC1[1] | -14.4121 | -7.9512 | Ascension Island | IGS, GGN | |
| BARB | -59.609076 | 13.088 | Barbados | IGS | |
| BDOS | -59.609 | 13.088 | Barbados | COCONet, CORS IGS, PBO | UNAVCO, NOAA-NGS:, CZMU |
| BOGT* | -74.081 | 4.640 | Bogotá, Colombia | COCONet, IGS, PBO | JPL, UNAVCO, SGC |
| BRAZ* | -47.878 | -15.947 | Brazilia, Brasil | IGS | IBGE |
| BRFT* | -38.426 | -3.877 | Fortaleza, Brasil | IGS | IBGE, NOAA-NGS |
| BRMU* | -64.696 | 32.370 | Bermuda, UK | IGS | NOAA-NGS |
| BYSP[1] | -66.161 | 18.408 | Bayamon, Puerto Rico | COCONet, IGS, PBO | UNAVCO, |
| CART[1] | -75.534 | 10.391 | Cartagena, Colombia | IGS, MAGNA-ECO, TOS | IGAC, DIMAR, CIOH, DGFI |
| CAYA[1] | -100.267 | 17.048 | Cayaco, Mexico | IGS | UNAM |
| CCV1[1] | -80.543 | 28.460 | Cape Canaveral, USA | CORS, IGS | USCG-NOAA |
| CCV2[1] | -80.543 | 28.460 | Cape Canaveral, USA | CORS, IGS | USCG-NOAAA |
| CFAG | -68.233 | -31.602 | Caucete, Argentina | IGS | CERI |
| CHPI | -44.985 | -22.687 | Cachoeira Paulista, Brazil | IGS | JPL |
| CIC1* | -116.666 | 31.871 | Ensenada, Mexico | IGS08, RGNA-INEGI | SCIGN, JPL, UNAVCO, CICESE |
| CN10 | -75.971 | 17.415 | Jamaica | COCONet, PBO | UNAVCO |
| CN19 | -70.049 | 12.612 | Aruba | COCONet, PBO | UNAVCO |
| CN36 | -75.821 | 8.82 | Montería, Colombia | COCONet, PBO | UNAVCO |
| CN37 | -75.263 | 10.793 | Galerazamba, Colombia | COCONet, PBO | UNAVCO |
| CN38 | -71.988 | 12.222 | Cerrejon, Colombia | COCONet, PBO | UNAVCO |
| CN40 | -68.958 | 12.180 | Curacao | COCONet, PBO | UNAVCO |
| CORD | -64.470 | -31.528 | Cordoba, Argentina | GGN, IGS | JPL |
| CORO | -75.288 | 9.328 | Corozal, Colombia | COCONet, PBO | UNAVCO |
| COYU | -100.081 | 17.008 | Coyuca, Mexico | IGS | UNAM |
| CRO1* | -64.584 | 17.757 | St. Croix, VI, USA | COCONet, GGN, IGS, PBO | UNAVCO, JPL |
| DOAR[1] | -99.651 | 17.021 | Dos Arroyos, Mexico | IGS | UNAM |
| FORT[1]* | -38.426 | -3.877 | Fortaleza, Brasil | IGS | - |
| GAL1 | -94.737 | 29.330 | Galveston, USA | CORS, IGS | |
| GALA[1] | -90.304 | -0.743 | Galapagos Island, Ecuador | IGS | |
| GLPS* | -90.304 | -0.743 | Galapagos | IGS | JPL |
| GMAS* | -15.634 | 27.765 | Maspalomas, Spain | IGS | JAXA |
| GRE0 | -61.640 | 12.222 | Grenada | CHPGN, COCONet, PBO, | UNAVCO |
| GUAT* | -90.520 | 14.590 | Guatemala city, Guatemala | COCONet, CORS, IGS, PBO | IGN-GT, UNAVCO |
| GV01 | -91.113 | -0.782 | Isabella Island, Ecuador | IGS | - |

| | | | | | |
|---|---|---|---|---|---|
| GV02 | -91.133 | -0.815 | Isabella Island, Ecuador | IGS | - |
| JAMA[1] | -76.781 | 17.939 | Jamaica | CORS, IGS | USCG - NOAA |
| KOU1[1] | -52.806 | 5.252 | Kourou, French Guyana | IGS | - |
| KOUR | -52.806 | 5.252 | Kourou, French Guyana | IGS | ESOC |
| KYW1 | -81.653 | 24.582 | Key West, Florida, USA | CORS, IGS | USCG , NOAA |
| KYW2 | -81.653 | 24.582 | Key West, Florida, USA | CORS, IGS | USCG , NOAA |
| LMMF | -60.996 | 14.595 | Le Lamentin, Martinique | COCONet, IGS | IGN-SGN, UNAVCO |
| LMNL | -85.053 | 10.268 | Limonal, Costa Rica | IGS, PBO | UNAVCO |
| MANA* | -86.249 | 12.149 | Managua, Nicaragua | COCONet, IGS, PBO | INETER, UNAVCO |
| MAS1* | -15.633 | 27.764 | Maspalomas, Spain | IGS | ESOC |
| MDO1* | -104.015 | 30.681 | Texas, USA | IGS | JPL |
| MOIN[1] | -83.094 | 9.987 | Moin, Costa Rica | GGN, IGS | JPL, UNAVCO |
| P780 | -66.579 | 18.075 | Cerrillos, Puerto Rico | COCONet, PBO | UNAVCO |
| PUR2 | -67.067 | 18.463 | Puerto Rico | CORS, IGS | USCG, NOAA |
| PUR3 | -67.067 | 18.463 | Puerto Rico | CORS, IGS | USCG, NOAA |
| QSEC | -85.357 | 9.840 | Quebrada Seca, Costa Rica | COCONet, PBO | UNAVCO |
| QUI2 | -78.494 | -0.215 | Quito, Ecuador | IGS | NGA |
| RIOP | -78.651 | -1.651 | Riobamba, Ecuador | IGS | IG |
| SA27 | -110.961 | 29.082 | Sonora, Mexico | IGS, SuomiNet | - |
| SAN0 | -81.716 | 12.580 | San Andreas, Colombia | CHPGN, COCONet, PBO | UNAVCO |
| SANT* | -70.669 | -33.150 | Santiago, Chile | IGS | JPL |
| SCUB* | -75.762 | 20.012 | Santiago, Cuba | IGS, COCONet, PBO | CENAIS, UNAVCO |
| SG21 | -99.189 | 19.741 | Teoloyucan, Mexico | IGS, SuomiNet | SNG-UCAR |
| SSIA* | -89.117 | 13.697 | San Salvador, El Salvador | COCONet, IGS, PBO | CNR, UNAVCO |

[1] These stations are not listed in the last update IGS stations of 24 August 2014, * IGS sites used as reference stations.

This table is based on IGS site: http://igscb.jpl.nasa.gov/network/list.html, UNAVCO data manager: http://facility.unavco.org/data/dai2/app/dai2.html#, SIRGAS project site: http://www.sirgas.org/index.php?id=148 and, Script Orbit and Permanent Array Center (SOPAC) site: http://sopac.ucsd.edu/.

**Networks abrév.: CHPGN:** Caribbean Hurricane Prediction and Geodetic Network, **COCONet:** Continuously Operating Caribbean GPS Observational Network, **CORS :** Continuously Operating Reference Station, **GGN :** GPS Global Network, **IGS:** International GNSS Service, **MAGNA-ECO:** Marco Geocéntrico Nacional de Referencia - Estaciones Continuas (Colombia), **PBO:** Plate Boundary Observatory, **RGNA-INEGI:** Red Geodésica Nacional Activa-Instituto Nacional de Geografía y Estadística (Mexico), **TOS:** Tide Gauge Observating Station.

**Agencies abrév.: CENAIS:** Centro Nacional de Investigaciones Sismológicas (Cuba), **CERI:** Center for Earthquake Research and Information at the University of Memphis (USA), **CNR:** Centro Nacional de Registros (El Salvador), **CICESE:** Center for Scientific Research and Higher Education at Ensenada, Baja California, **CZMU:** Coastal Zone Management Unit (Barbados), **ESOC:** European Space Operation Center, **GA**: Geoscience Australia, **IBGE:** Brazilian Institute of Geography and Statistics, **IGAC-DIMAR-CIOH-DGFI:** Instituto Geográfico Agustin Codazzi - Direccion General Maritima - Centro de Investigaciones Oceanograficas e Hidrograficas (Colombia) - German Geodetic Research Institute**, IG:** Instituto Geofísico de Ecuador, **IGN-GT:** Instituto Geográfico Nacional (Guatemala) **IGN-SGN:** l'Institut national de l'information géographique et forestière français- le Service de Géodésie et de Nivellement, **INETER:** Instituto Nicaragüense de Estudios Territoriales, **JAXA:** Japan Aerospace Exploration Agency, **JPL:** NASA Jet Propulsion Laboratory, **NGA:** National Geospatial-Intelligence Agency, **NOAA-NGS :** National Oceanic and Atmospheric Administration - National Geodetic Survey, **SCIGN:** Southern California Integrated GPS Network, **SGC:** Servicio Geológico Colombiano, **SNG-UCAR :** SuomiNet Geodetic- University Corporation for Atmospheric Research **UNAM:** Universidad Autónoma de México, **UNAVCO:** University NAVSTAR Consortium, **USCG-NOAA**: United States Coast Guard-NOAA.

# CHAPTER 5:

# DATA ANALYSIS STRATEGY

## 5.1. Introduction

Data of a set of 142 stations have been processed, of which approximately 70 stations belong to Eastern and Western Venezuela. Those data were collected from 2003 to this study framework. Additionally, in order to improve the processing and understanding of the region, data from neighboring networks (cGNSS and campaign sites) have completed the whole data set. Data have been analyzed with Bernese GNSS software Version 5.2 (Dach & Walser, 2013), using absolute antenna phase center offsets models, as well as, IGS final precise orbits (Beutler et al., 1999) and IGS Earth rotation parameters.

The Bernese GNSS Software, developed by the Astronomical Institute of the University of Berne (AIUB), is a sophisticated tool meeting highest quality standards for geodetic and further applications using Global Navigation Satellite Systems (GNSS). For the data processing this software displays three important areas located in the ${HOME}/GPSDATA directory: (1) the DATAPOOL area, which is intended as an interface where all external files can be deposited after their download, (2) the CAMPAING52 directory that contains all processing campaigns and, (3) the SAVEDISK area that allows to collect and archive the results files (Dach et al., 2007; Dach & Welser, 2013). The strategy of processing shown in figure 5.1 is detailed in the next sections.

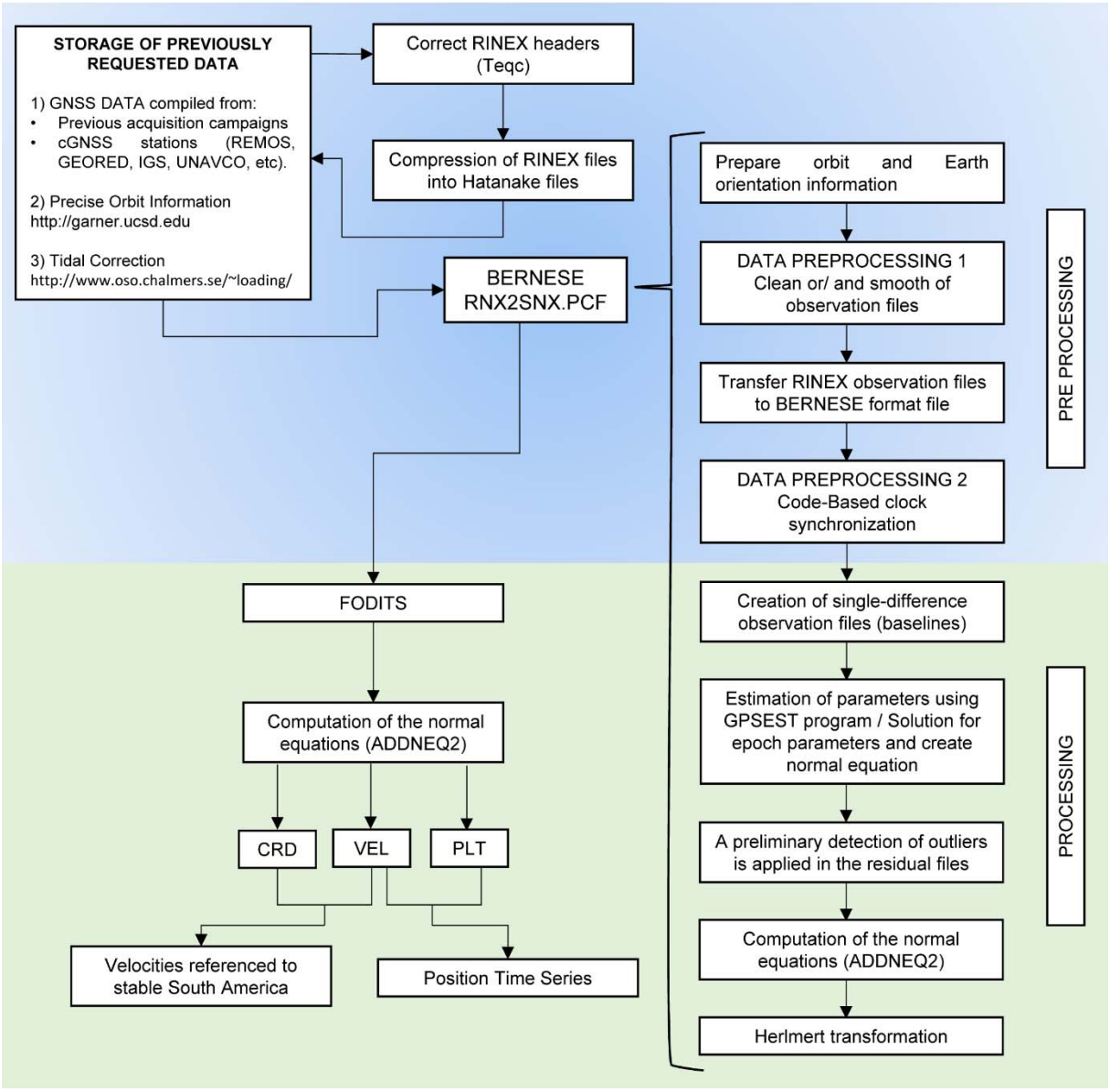


***Figure 5.1.*** *Flowchart of processing strategy including data collection, pre-processing and processing with Bernese GNSS software. The Process File Control is based in processing steps for a zero-difference solutions (Dach et al., 2007).*

## 5.2. Data processing

For the processing is required that all daily RINEX files of each station show at least a marker name, receiver and antenna type, and the antenna height (Figure 5.2). The naming conventions for receivers and antennas are specified in the IGS site

(http://igscb.jpl.nasa.gov/igscb/station/general/rcvr_ant.tab). Additionally, all used observations in the analysis process are, in our study, 30 second RINEX format. In order to adjust all data with the standards, the Teqc (translate, edit and quality check) tool was used. This executable is a simple yet powerful and unified approach to solving many processing problems with practically all positioning systems (e.g.: GPS, GLONAASS, Galileo, etc.) especially in RINEX or BINEX format. At this moment, each file is compressed in a hatanaka file (a smaller ASCII format used by the GIS) using RNXCMP software (Hatanaka, 2008). After, all data is transferred to ${HOME}/GPSDATA/DATAPOOL/ directory.

```
1.0                 COMPACT RINEX FORMAT                    CRINEX VERS   / TYPE
RNX2CRX ver.4.0.5                       18-Jun-13 12:45     CRINEX PROG / DATE
     2.11           OBSERVATION DATA    G (GPS)             RINEX VERSION / TYPE
teqc  2013Mar15                         20130612 14:35:07UTCPGM / RUN BY / DATE
MSXP|IAx86-PII|bcc32 5.0|MSWin95->XP|486/DX+                COMMENT
teqc  2013Mar15                         20130605 09:42:23UTCCOMMENT
cnvtToRINEX 2.11.0  convertToRINEX OPR  05-Dec-11 13:05 UTC COMMENT
------------------------------------------------------------ COMMENT
DAL0                                                         MARKER NAME
                                                             MARKER NUMBER
Reinoza-Concha      FUNVISIS IGVSB                           OBSERVER / AGENCY
0220264305          TRIMBLE 5700        1.04                 REC # / TYPE / VERS
S/N                 TRM41249.00                              ANT # / TYPE
  1917692.7765 -6014024.1038   911042.2679                   APPROX POSITION XYZ
        1.3314        0.0000        0.0000                   ANTENNA: DELTA H/E/N
     1     1                                                 WAVELENGTH FACT L1/2
     4    C1    L1    L2    P2                               # / TYPES OF OBSERV
     0                                                       RCV CLOCK OFFS APPL
    15                                                       LEAP SECONDS
CARRIER PHASE MEASUREMENTS: PHASE SHIFTS REMOVED             COMMENT
  2011    10    26    16    32   30.0000000     GPS         TIME OF FIRST OBS
                                                             END OF HEADER
```

***Figure 5.2.*** *Header of RINEX file underlining the marker name and receiver-antenna types for the DAL0 stations.*

According to the flowchart presented in the figure 5.1, the Process Control File (RNX2SNX.PCF) of Bernese GNSS Software shows a first phase of data pre-processing and processing detailed as follows:

**Precise orbits determination**

Precise GNSS orbits are a prerequisite for all applications of the GNSS where high accuracy is required. In our analysis we took IGS final orbits expressed in the IGb08 reference frame, and for the older observation recomputed orbits in the IGb08 reference provided by the Center for Orbit Determination for Europe (CODE). Precise orbit files given in Standard Product 3 Orbit (SP3) format are transformed into the tabular orbit format. This conversion includes the transformation of the orbit information from the Earth-fixed frame to the inertial frame. The standard orbit is the result of a numerical integration of the equations of motions. The STD file is a binary file containing the satellite orbit information as a polynomial representation of inertial Cartesian positions. This standard orbit is estimated by the ORBGEN software that supports several force models: Earth's potential, the gravitational attractions of Sun, Moon and major planets (Jupiter, Venus, and Mars) described by their ephemerides, the elastic Earth tidal corrections, pole tide, ocean tides, and general relativistic corrections, the force induced by the earth rotation with the use of the Earth Rotation Parameter file provided with IGS or CODE precise files, and the influence of radiation pressure in the orbit.

**Data preprocessing**

After the conversion of the RINEX observation files into the Bernese observation file, the synchronization of receiver clocks with GPS time and the determination of approximate station coordinates using code zero-difference measurements if necessary is done. At this step, observations associated with CODE with high residuals are detected and marked in the observation files.

**Data processing**

The data are processed using phase center correction taking in consideration the GPS antenna type, the elevation and the azimuth of satellites. In Bernese, external phase center

offsets and patterns (format NGS or ANTEX up to version 1.4; http://www.ngs.noaa.gov/ANTAL/) are converted into the internal Bernese format for phase center corrections. The influence of the ocean tide on the position is estimated using the ocean tidal model FES2004 (Hans–Georg Scherneck's web tool (http://www.oso.chalmers.se/~loading/), whereas the atmospheric tidal loading is estimated by Bernese.

**Formation of singles differences files**

Single-difference observation (baselines) files are created from zero-difference phase or code observation files. Because Bernese 5.2 software use only selected baselines, this must be selected with care. The strategy proposed is to select the baselines with the maximum of simultaneous observations and as second criteria, to select according to the length of the baseline, shorter baselines are preferred. In order to clean or/and smooth phase observation files, unpaired observations and outliers are detected and repaired.

**Daily solution estimation**

Based on a least-squares adjustment using un-differenced (zero-difference) or double-differenced phase or/and code measurements the Bernese software can estimate several parameters: station coordinates, receiver clock parameters (including GPS/GLONASS clock biases), orbital elements, ambiguities, receiver antenna offsets, troposphere parameters for individual stations, Differential Code Biases (DCBs), Earth Rotation Parameters (ERPs), stochastic orbit parameters, satellite antenna offsets, geo-center coordinates, stochastic ionosphere parameters, receiver antenna phase center variations, global (and station-specific) ionosphere model parameters, epoch-specific station coordinates, scaling factors for Vienna grid file, epoch-specific station clocks, epoch-specific satellite clocks, satellite antenna phase center variations, range bias parameters, scaling factors for higher-order ionosphere corrections, and GNSS-specific station translations, and troposphere biases.

To determine ambiguities, coordinates and troposphere biases, basically in our study, the resolution strategy is resumed as followed: (a) initial ionosphere-free analysis with computation of residuals, (b) residuals analysis, (c) Code-Based Widelane (WL) Ambiguity Resolution for all the baselines (Melbourne, 1985; Wübbena, 1985); using DCB files when available, and computation of ionosphere free solution with introduction of the resolved Melbourne-Wübbena linear combination ambiguities, (d) Phase-Based Widelane, (L5) Ambiguity Resolution for baselines <200 km and computation of ionosphere free solution with the introduction of resolved ambiguities, (e) resolution of the previously not resolved ambiguities for baselines < 2000 km using the Quasi Ionosphere free strategy of resolution, and (6) direct L1/L2 ambiguity resolution for baselines < 20 km and (f) computation of normal equations.

As final step, the daily GNSS solutions are transformed in the IGb08 reference frame (an IGS-specific realization of the ITRF2008) with a six parameters Helmert solution (three translation parameters and three rotation parameters). A first step, is performed with the detection of IGb08 stations (in our study BOGT, BRAZ, BRFT, BRMU, CIC1, CRO1, FORT, GLPS, GMAS, GUAT, MANA, MAS1, MDO1, SANT, SCUB and SSIA) in good accordance with the IGb08 solution. To perform this selection, Bernese compares two coordinate files determining Helmert parameters (translations, rotations) for the transformation between both coordinates sets, the program automatically removes IGb08 stations with residuals exceeding a user-specified threshold from the estimation of the Helmert parameters.

**Velocity estimations**

The daily normal equations are analyzed together to determine coordinates and velocities. During this estimation, coordinates and velocities of points defined in the IGb08 are constrained at theirs IGb08 values. As a last cleaning, outliers and discontinuities are detected with FODITS (Find Outliers and Discontinuities in Time Series), a tool integrated within

Bernese software that reduce, step-by-step, the discrepancy between the functional model and the time series from statistical adjustment (Ostini et al., 2008). Well known discontinuities as earthquakes and equipment changes can be introduced in the analysis. As well as, change of velocities can be allowed or not after a discontinuity, while semiannual and annual seasonal changes of time series can be estimated (Figure 5.3). The collection of the FODITS analysis results allows it finally to update a priori information for a subsequent ADDNEQ2 solution which takes into account found peculiar events in the time series. The final solutions of processing are done in two main files: .CRD and .VEL files containing the coordinates and velocities respectively.

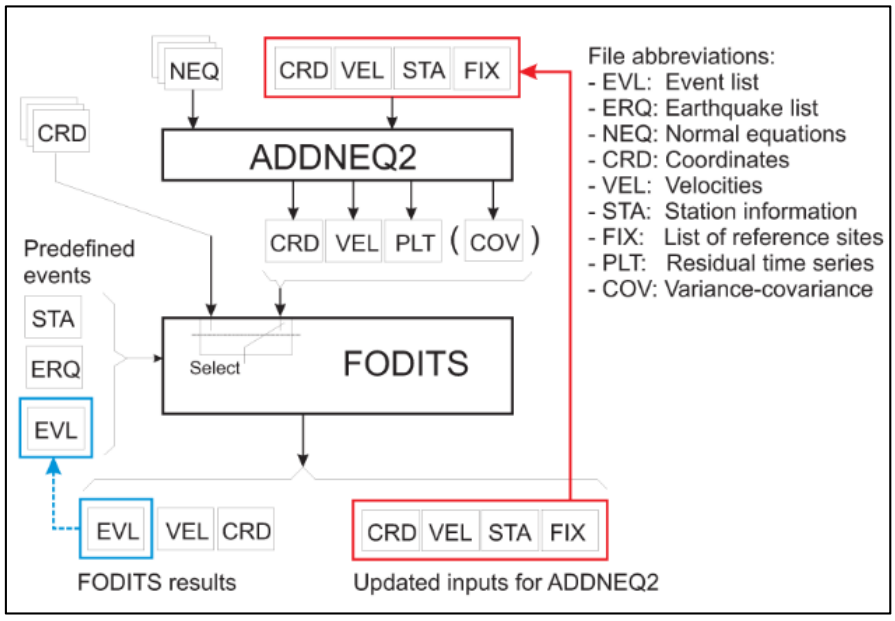


***Figure 5.3.*** *FODITS as a complementary tool in the Bernese GNSS software (from Ostini et al. 2008).*

The final solutions of processing are done in two main files: .CRD and .VEL files containing the coordinates and velocities respectively. A complementary output file associated with this solution is presented as an ASCII file containing the data to be plotted (.PLT). From this file, position time series plots have been elaborated. These diagrams show the progression

of location in mm/yr versus the time in years allowing to estimate jumps, trends, and seasonal variations of permanent stations. In the Figure 5.4 a, b the time series of MARA stations are shown before and after the outlier detection with FODITS. Time series of local and neighboring country cGNNS stations, and Venezuelan campaign stations are shown in the APPENDIX A.2.

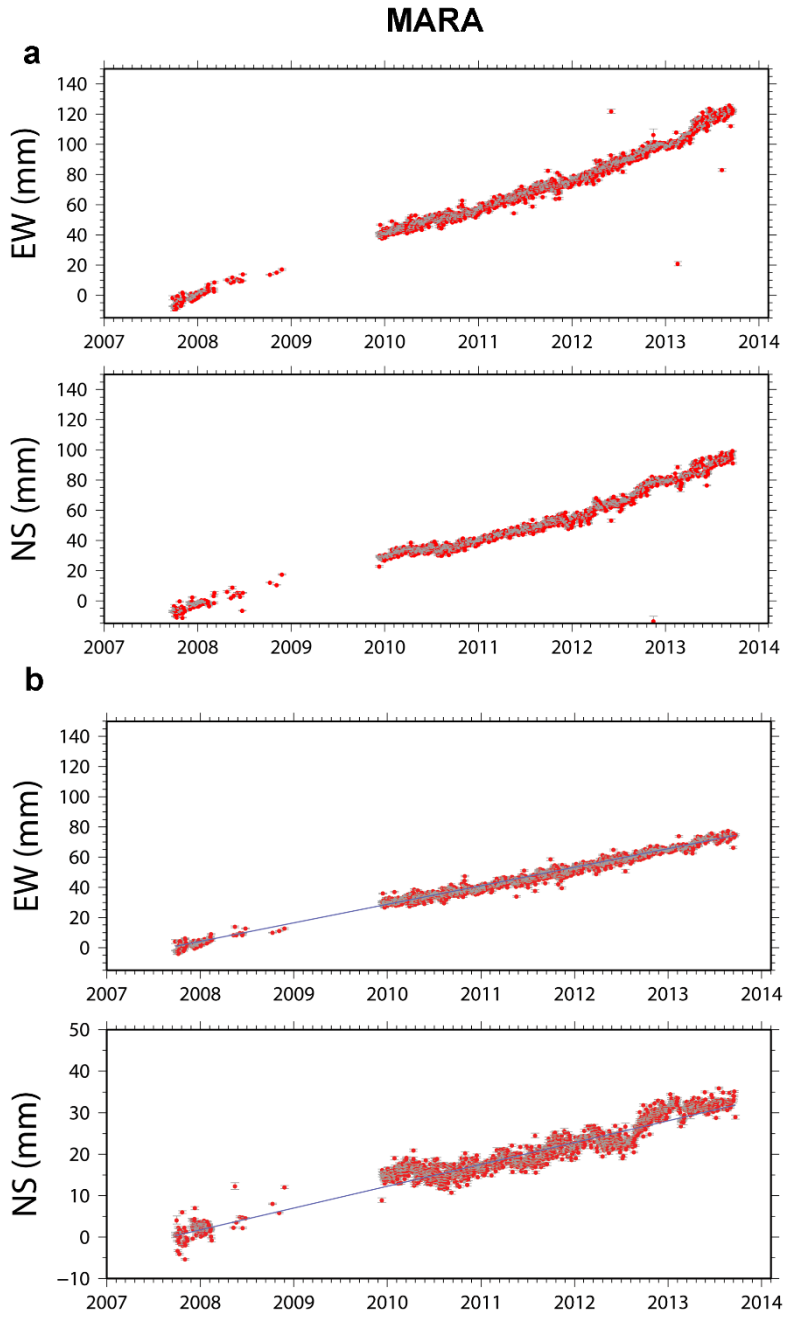


***Figure 5.4.*** *Time series of Maracaibo station (MARA) (a) before and (b) after the outlier detection with FODITS. Blue line indicates the best fit line for the velocity adjusted with FODITS.*

It is recognized that the Bernese software underestimates the daily coordinate errors because systematic errors or mis-modelled parameters are not included in the formal error (Hugentobler et al., 2001). In order to obtain a realistic estimated error the formal errors have been multiplied by a factor of 10 as currently done and recommended. Velocities have been estimated in the IGb08 reference frame (APPENDIX B.1, Figure 5.5) and after expressed in the South America reference frame.

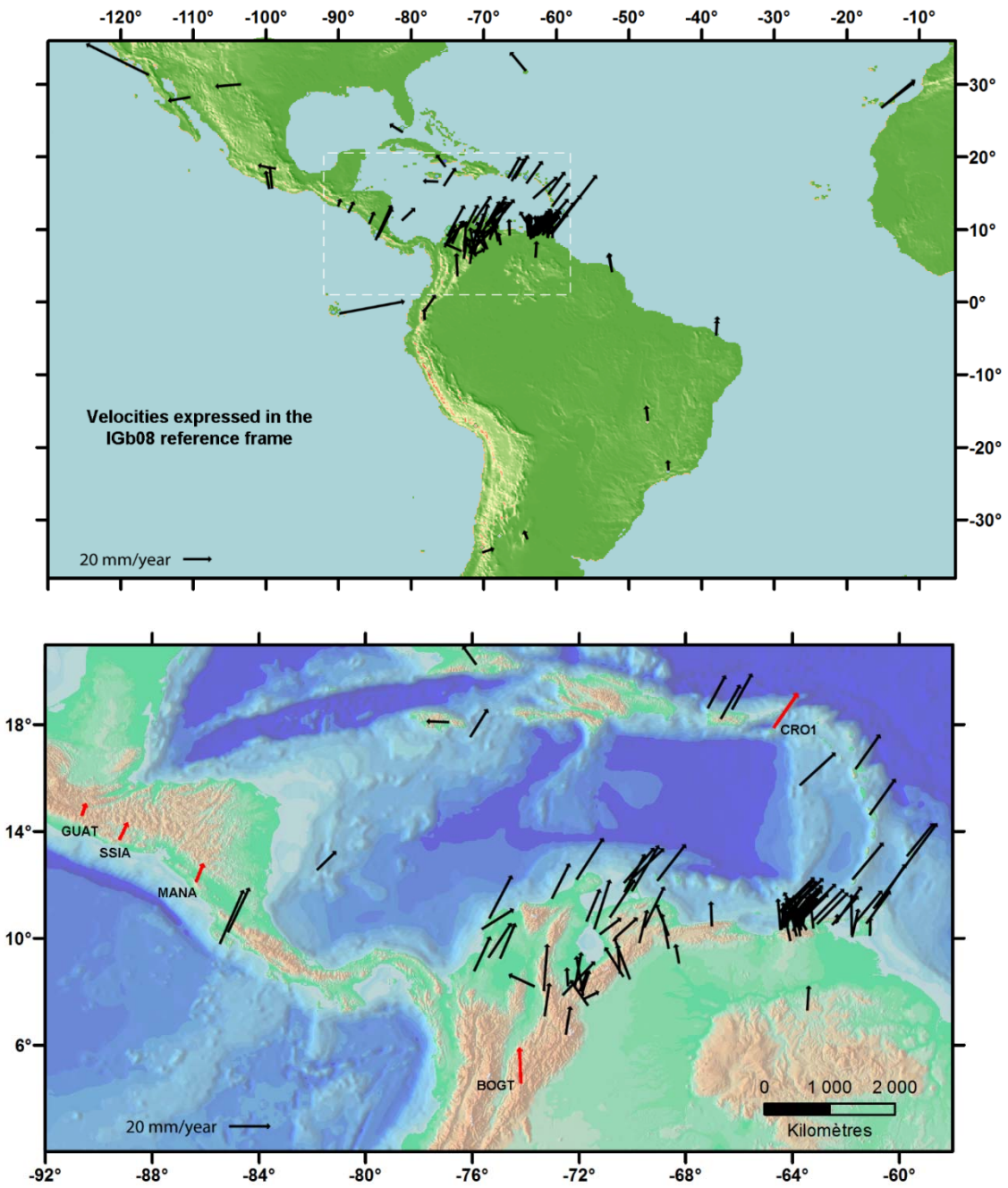

***Figure 5.5.*** *Velocity field obtained from processing expressed in the IGb08 reference frame. (Below) Zoomed view of velocity field showing IGS reference sites as red arrows.*

### 5.3. South American reference frame

The velocities estimated in the IGb08 reference frame have been expressed in the stable South American reference frame using the ITRF2008 absolute plate rotation pole (Table 5.1) proposed by Altamimi et al. (2012).

***Table 5.1.*** *ITRF2008 Absolute Plate Rotation for South America (Altamimi et al., 2012) including unit transformation to °/Myr.*

| | | | | | WRMS | |
|---|---|---|---|---|---|---|
| NS[a] | $\omega_x$ (mas/a) | $\omega_y$ (mas/a) | $\omega_z$ (mas/a) | ω (°/Ma) | E | W |
| 10 | -0.243 ± 0.009 | -0.311 ± 0.010 | -0.154 ± 0.009 | 0.118 ± 0.002 | 0.44 | 0.34 |
| Transformation to Cartesian components (°/Myr) | | | | | | |
| | x-component | y-component | z-component | | | |
| | -0,067500 | -0,086389 | -0,042778 | | | |

This procedure was carried out using the Plate Motion Calculator. This geodetic utility of UNAVCO allows to calculate tectonic plate motion at any location on Earth using one or more plate motion models. In order to reference the solutions, the absolute plate rotation for South America (Altamimi et al., 2012) was used to define the angular velocity of attributed motion and the reference angular velocity was fixed at 0 for the x, y, and z components. Velocities expressed in the stable South America reference frame for the station in Venezuela are shown in the APPENDIX B.2, as well as, velocity fields in the eastern and western Venezuela are presented in the figures 5.6 and 5.7 respectively.

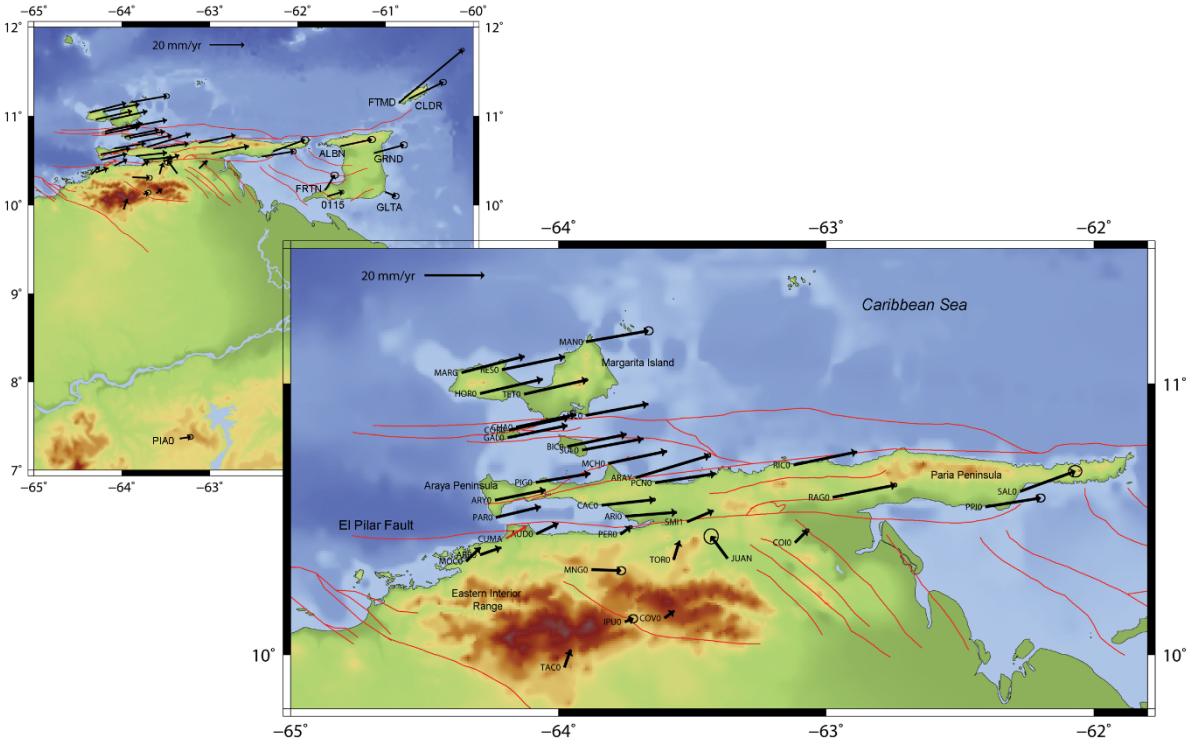


***Figure 5.6.*** *GNNS velocity field obtained for eastern Venezuela and Trinidad and Tobago. Observed velocities with error ellipses plotted for a 66% confidence level. Red arrows represent cGNSS sites. All velocities are expressed in the South American reference frame.*

## 5.4. Velocity field along western Venezuela

The short span between two acquisition campaigns in western Venezuela (late 2011 and early 2013) does not allow obtaining robust velocity estimation. However, a preliminary analysis of observed velocities of this study zone, dominated by important geological features such as Boconó, Oca-Ancón, Valera strike slip faults, and Maracaibo and Trujillo tectonic blocks (Figures 5.7 and 5.8 ), is presented.

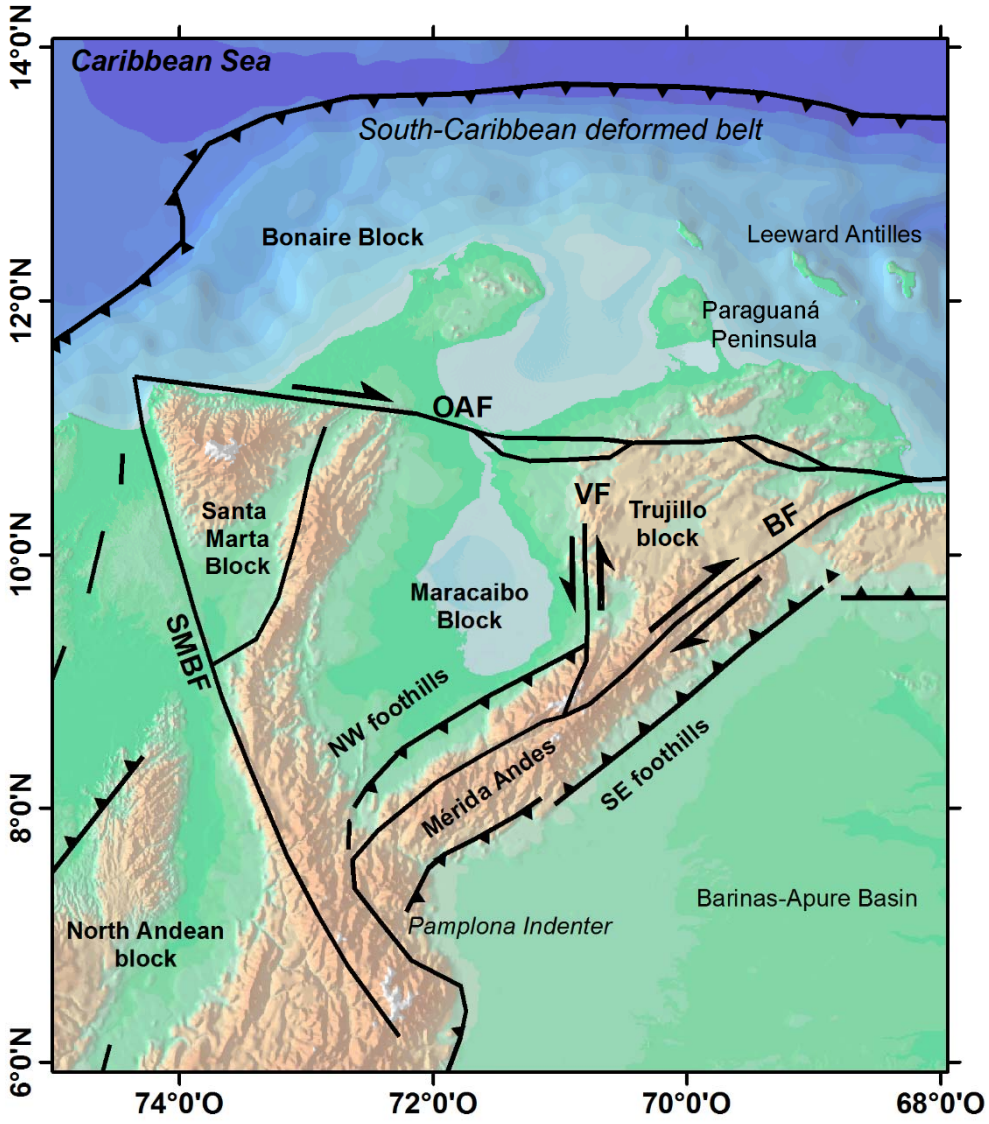


***Figure 5.7.*** *Schematic geodynamic map showing the main features in western Venezuela and Colombia-Venezuela border. BF: Boconó Fault, OAF: Oca-Ancón Fault, SSF: San Sebastian Fault, VF: Valera Fault (Audemard 1999b; Audemard et al., 2000; Trenkamp et al., 2002).*

From a comparison between the sites in the Leeward Antilles and the GNSS station CARA in central Venezuela, the right lateral strike slip motion of San Sebastian Fault is confirmed. AMU0, MAC0, POR0, and SAR0 velocities located on the Paraguaná Peninsula (12° N and 70°W) appear to be similar to CN40, CN38, and ALPA cGNSS velocities. All these sites appear to follow the Caribbean plate motion; however, small relative displacement among

Paraguaná Peninsula sites might be related to minor fault displacements within this block. The MARA site shows certain similarity with VIC0 and BOZ0 (next to Oca-Ancón Fault) benchmarks. Nonetheless, it must be underlined that the velocities of these two episodic points are less reliable than the permanent GNSS MARA site.

Furthermore, if one compares MARA and COP0 sites, the left-lateral strike slip of Valera Fault is shown. Moreover, from a comparison of N-S component velocities of PAV0 and YAG0 sites (Fault-parallel velocities to Valera Fault), the west side of Valera Fault shows -2.45 mm/yr and the east side shows -0.70 mm/yr. This gradient appears point out the left-lateral pattern across the Valera Fault. On Cabudare to Morón section of Boconó Fault (Northeastern section), HSR0 and NIR0 relative velocities are suggesting compression.

If one rules out the BTA0 site in the Andean foothill, KYP0 and BARI are also depicting compression on Anzoátegui-Barquisimeto section of Boconó Fault (Central section). UWAS, PAL1, CUC1, and ABRE sites in the Colombian territory next to the set of sites in the southern Boconó Fault might help to understand the geodynamic at the Colombia-Venezuela border. In this region the Boconó Fault is taken into the Pamplona indenter (Boinet, 1985). The sites in the southwestern Andes (DAL0, UMU0, VANO, PRE0, URI0 and TAL0) show no a homogeneous pattern that it is difficult to interpret at this moment. PED0 site show a similar motion to velocities observed in the BARI site at the southern foothill on central Boconó Fault. Eventually, COPO and QUI0 sites appear to follow the Northeast expulsion of Trujillo block.

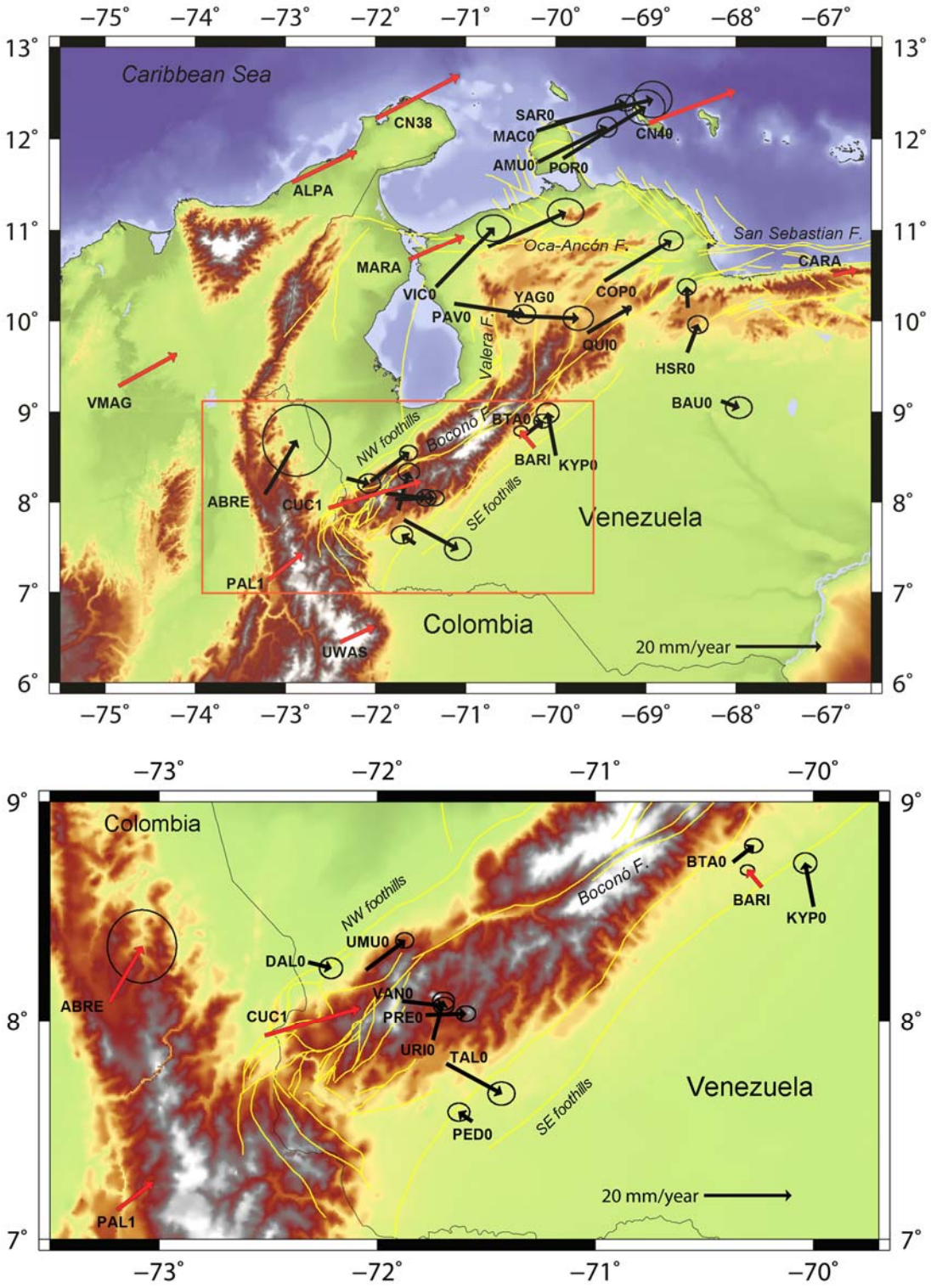


***Figure 5.8.*** *GNNS velocity field of west Venezuela. Observed velocities with error ellipses plotted for a 66% confidence level. Red arrows represent cGNSS sites. All velocities are expressed in the South American reference frame. (Bottom) Details on Venezuela-Colombia border.*

The future occupations and densification of the western network in the years to come will allow obtaining more robust results. A geodetic velocity field based on these observations will permits constraining a mechanical modelling with the aim of estimating the rotation pole of discrete tectonic blocks, calculate locking depth and slip at depth along the major active fault and even, secondary faults. The seismic profiles of the GIAME project realized in order to study the lithospheric structure of the Mérida Andes will probably constrain the geometry of Boconó Fault and of the external thrusts. It will be a valuable information for the input files for numerical models.

## CHAPTER 6:

# GEODETIC EXPLORATION OF STRAIN ALONG THE EL PILAR FAULT IN NORTHEASTERN VENEZUELA

The results obtained in the EPF are presented in this chapter as an article summited to Journal of Geophysical Research.

**Geodetic exploration of strain along the El Pilar Fault in northeastern Venezuela**

C. Reinoza[1, 2], F. Jouanne[1], F.A. Audemard[2], M.Schmitz[2], C. Beck[1]

[1] Université de Savoie Mont Blanc, ISTerre, F-73376 Le Bourget du Lac, France

[2] Venezuelan Foundation for Seismological Research, FUNVISIS, El Llanito, Caracas 1070, Venezuela

Carlos Reinoza, Franck A. Audemard, Michael Schmitz Venezuelan Foundation for Seismological Research, FUNVISIS, El Llanito, Caracas 1070, Venezuela

Carlos Reinoza, François Jouanne, Christian Beck, Université de Savoie Mont Blanc, ISTerre, F-73376 Le Bourget du Lac, France

Corresponding author: C. Reinoza[1, 2] (creinoza@funvisis.gob.ve)

**Abstract**

We use GNSS observations in northeastern Venezuela to constrain the El Pilar Fault (EPF) kinematics and explore the effects of the variable elastic properties of the surrounding medium and of fault geometry on inferred slip rates and locking depth. The velocity field exhibits an asymmetric velocity gradient on either side of the EPF that has been evaluated using five approaches. We apply elastic half-space models using the simple homogeneous approach, which indicates a 1.8 km locking depth, and the heterogeneous asymmetric model associated

with contrasting material properties on either side of a vertical fault elastic half-space model. This second method, suggesting a 3 km locking depth, presents a 0.37 asymmetric coefficient, indicating that the igneous-metamorphic northern side is ~1.7 times more rigid than the sedimentary southern side. From a three-dimensional elasto-static model, we evaluate the presence of a near-fault low-rigidity compliant zone (CZ), suggesting a zone in the upper 3 km in depth and from 1 to 5 km wide, with a 30 percent rigidity reduction. A fourth model, evaluating a fault-slip distribution from interseismic displacement, reveals a widespread partial-creep pattern in the eastern upper segment, while the upper western segment exhibits a partially locked area, which coincides with the rupture surface of the 1797 and 1929 earthquakes. To supplement these models, we upgrade the previously published displacement simulation method using non-vertical dislocations with 2013 data. The localized aseismic displacement pattern associated with creeping or partially creeping fault segments could explain the low level of historical seismicity.

## 1. Introduction

Interpretations of Global Navigation Satellite System (GNSS) velocity fields across active strike-slip faults around the world have made it possible to determine several mechanical properties of crust. Geodetic exploration has contributed to constraining fault geometry through (i) the study of asymmetric velocity gradients related to the juxtaposition of differing physical materials [e.g. *Le Pichon et al*., 2005; *Jolivet et al*., 2008, 2009; *Houlié and Romanowicz*, 2011], (ii) the existence of fault damage zones [e.g. *Chen and Freymueller*, 2002; *Fialko et al*., 2002, *Fialko*, 2004, *Hamiel and Fialko*, 2007; *Barbot et al*., 2009], and (iii) partial or complete aseismic displacement [e.g. *Bürgmann et al., 2000*; *Lyons et al. 2002*; *Wdowinski*, 2009; *Jouanne et al.*, 2011; *Smith-Konter et al*., 2011; *Weber et al*., 2001].

In this work we focus on the El Pilar Fault (EPF), a strike slip fault that extends eastward for some 350 km [e.g. *Soulas*, 1986; *Beltrán*, 1993, 1994; *Audemard et al*., 2000] from the Cariaco

Trough to the Gulf of Paria (Figure 1). The deformation associated with the active traces of the EPF has been identified using high-resolution offshore seismic reflection data [*Audemard et al*., 2007; *Van Daele et al*., 2011] and trenches [*Beltrán et al*., 1996; *Audemard*, 2011]. The historical record shows that the current activity of the EPF is not new; since records began with the Spanish conquest in the early sixteenth century, northeastern Venezuela has experienced seismic events in 1530, 1684, 1766, 1797, 1853, 1929, and the 9 July 1997 Ms 6.8 Cariaco earthquake along the strike-slip EPF [*Audemard*, 1999b, 2007]. Field reconnaissance of the ground breaks after the 1997 earthquake confirms that this event took place on the ENE–WSW trending onshore portion (~ 80 km) of the dextral EPF between the Gulfs of Cariaco and Paria, which is part of the major wrenching system within the Caribbean–South America plate boundary zone [*Audemard*, 2006]. The slip direction of this fault has been unequivocally confirmed by the dextral character of the surface break associated with the 1997 Cariaco earthquake [*Audemard*, 1997, 1999a, 2006] and by focal mechanism solutions for this event and its aftershocks [*Pérez*, 1998; *Baumbach et al*., 1999, 2004; *Romero et al.*, 2002; *Audemard et al*., 2005].

In this paper, we present results including GNSS data from late 2003, late 2005, and more recent early 2013 observation campaign, and a cGNSS CUMA station. This recent effort is intended to constrain the velocity field along the EPF. We focus on the structure of the crust to better constrain seismic hazard assessment through the evaluation of locking depth, far-field velocity, and aseismic slip.

This manuscript is structured as follows: In section 2, we describe GNSS data collection and processing. In section 3 and its subsections, we introduce several modeling approaches and develop the corresponding methodologies: the simple elastic half-space model, the asymmetric model, the CZ model, the slip distribution model, and the displacement simulation method using non-vertical dislocations. In section 4, we compare the models using the Fisher-Snedecor test

and in section 5 we discuss several methods used in this paper and their significance for the EPF.

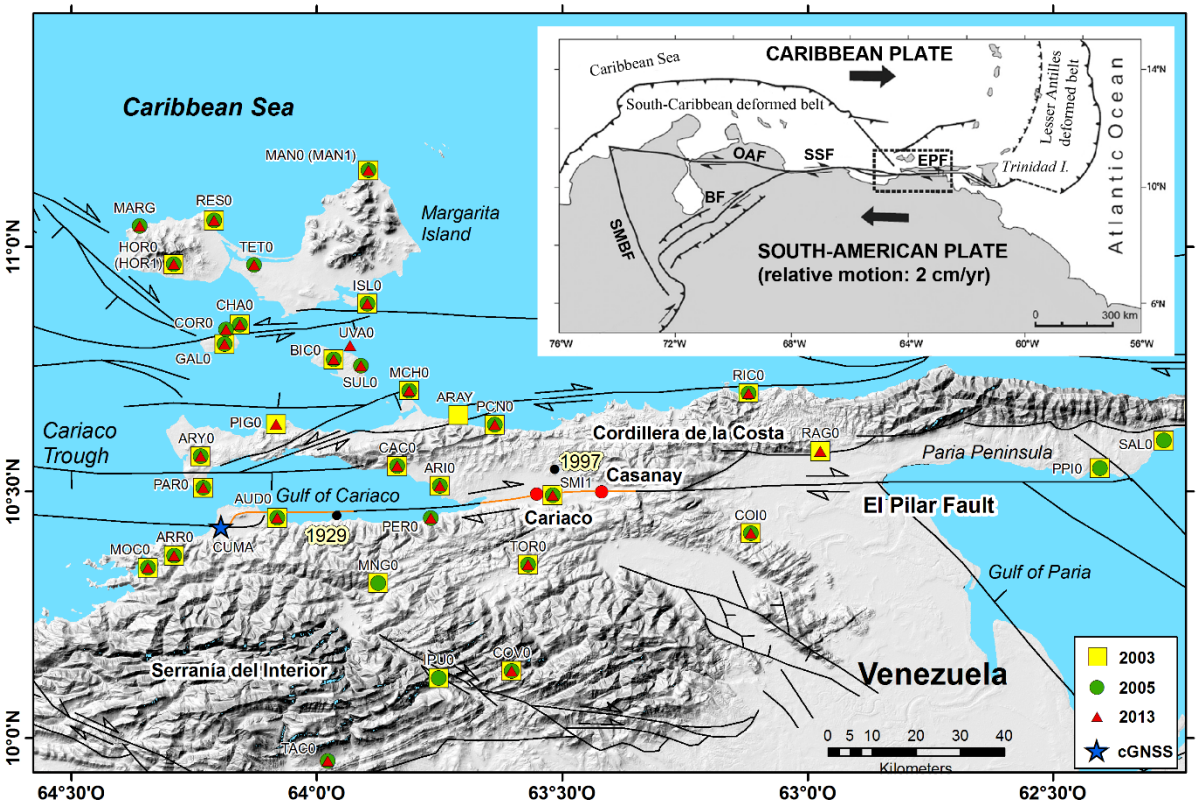


**Figure 1.** Location map of the active faults in northeastern Venezuela [*Audemard et al.*, 2000] showing distribution of the GNSS stations: yellow squares, green circles and red triangles are GNSS sites on which the acquisition campaigns were carried out in 2003, 2005, and 2013 respectively; the blue star corresponds to the cGNSS CUMA station of REMOS-IGVSB Network. We show the epicenter location of 1929 and 1997 events with their respective proposed ruptures [orange lines; *Audemard*, 2007]. (Top right) The inset box shows a schematic geodynamic map of the southeastern Caribbean [*Audemard*, 1999b; *Audemard et al.*, 2000; *Weber et al.*, 2001]. Legend: BF-Boconó Fault. EPF- El Pilar Fault. OAF-Oca Ancón Fault. SMBF- Santa Marta Bucaramanga Fault. SSF- San Sebastian Fault.

### 1.1. Previous studies

Deformation in northeastern Venezuela based on geodetic measurements has been studied recently by at least two main research teams. *Pérez et al.* [2001a, b] estimated the co-seismic slip at depth responsible for the 1997 Cariaco earthquake using boundary element methods

[*King and Nostro*, 1999] to calculate surface fault displacements [*Okada*, 1985]. The best solution corresponds to a fault plane segmented into three patches and striking N 84° E with co-seismic slips estimated at 0.94, 1.25, and 1.1 m for each rectangular segment from west to east. A locking depth of 14 ± 2 km for the EPF was required for satisfactory solutions. Current derived velocities of the EPF by GNSS studies have been simulated in *Jouanne et al*. [2011] using the Okada formulations [*Okada*, 1985] for an isotropic homogeneous half-space. Interseismic velocities simulated by *Jouanne et al*. [2011] indicate asymmetric velocity gradients on each side of the EPF as a result of dipping fault segments and a lack of significant displacement (particularly shortening) in the Serranía del Interior on the southern side and eastward motion of up to 22 mm/yr (relative to the fixed South-American plate) of benchmarks on the northern side of the EPF. That work demonstrated also the existence of substantial creep along the upper part of the EPF. Localized aseismic displacement along the fault has been revealed by the slip of markers (roads, gutters, sidewalks, constructions, etc.) observed in the field in the years 1997–2003 following the 1997 earthquake [*Audemard*, 2006].

## 2. Geological setting

Northeastern Venezuela is part of the complex plate-boundary zone of the Caribbean, South American, and Atlantic plates. The Caribbean–South American plate boundary is described as a very wide active transpressional zone [*Soulas*, 1986; *Audemard*, 1993, 1998; *Beltrán*, 1994; *Singer and Audemard*, 1997] where plate motion is accommodated predominantly by the right-lateral strike-slip Boconó–San Sebastián–El Pilar–Los Bajos/El Soldado–Warm Springs fault system [*Molnar and Sykes*, 1969; *Minster and Jordan*, 1978; *Pérez and Aggarwal*, 1981; *Stephan*, 1982; *Aggarwal*, 1983; *Schubert*, 1984; *Soulas*, 1986; *Beltrán and Giraldo*, 1989; *Speed et al.*, 1991; *Singer and Audemard*, 1997; *Pérez et al*., 2001a, b; *Weber et al*., 2001; *Pindell and Kennan*, 2007*; Audemard*, 2009].

The strike-slip EPF extends for some 350 km; however, its depth is not well-constrained. *Vierbuchen* [1984] inferred from the steep gravity gradient across the EPF that the fault is nearly vertical down to a depth of at least 5 to 10 km; *Schubert* [1984] suggested a depth of approximately 8 km from seismic-reflection profiles assuming an average P-wave velocity of 5.2 km/s. *Rossi et al.* [1987] suggested a depth of 15 to 20 km based on a joint interpretation of seismic, magnetic, and gravimetric data. More recently, studies related to the 1997 Cariaco earthquake have placed the seismogenic part of the EPF at 12 km based on the depth distribution of aftershocks [*Baumbach et al.,* 2004] and at 14 ± 2 km of locking depth based on geodetic observations [*Pérez et al., 2011*]. *Clark et al.* [2008] based on wide-angle onshore–offshore reflection/refraction modeling determined a Moho depth of 48 km beneath the EPF. This corresponds to a depth increase of 16 km coinciding with the dextral strike-slip system between the Coche fault and the EPF. However, the region is mainly characterized by shallow intra-continental seismicity (in the first 20 km) associated with the EPF. Seismicity deeper than 40 km is related to the southern tip of the Lesser Antilles subduction zone under Trinidad and Tobago, the Paria Peninsula, and the active island arc of the Lesser Antilles (Figure 2).

The EPF roughly separates two very different geological provinces. On the northern side lies the Eastern Cordillera de la Costa, made up of Lower Cretaceous metasediments, metavolcanics, igneous rocks, and ophiolite remnants. These rocks have been metamorphosed into greenschist and blueschist facies and deformed by imbricated folds and thrust faults. On the southern side of the EPF, the Serranía del Interior exposes a fold-and-thrust belt, made up of non-metamorphosed Cretaceous and Paleogene sediments [*Metz*, 1965; *Vierbuchen*, 1984; *Jacome et al*. 1999]. A 3-D velocity tomography study by *Grosser et al*. [2001] reveals that the material north of the EPF has a higher shear strength than the material south of the fault. *Baumbach et al*. [2004] point out that the aftershock distribution of the 1997 Cariaco earthquake had a very sharp boundary on the northern side of the EPF contrasting with the more diffuse

boundary on the southern side. From wide-angle seismic reflection/refraction, *Clark et al.* [2008] also report velocities decreasing southward to the EPF from 3.5 km/s to 2.2 km/s and a shallow region of relatively high velocities (> 6.5 km/s) probably related to the exhumed metamorphic rocks of Margarita Island and the Araya-Paria peninsula. Using a similar methodology *Christeson et al.* [2008] present the results of a regional wide-angle seismic profile indicating the transition from allochthonous terrane of forearc affinity to the passive margin of northern South America. The suture farther east between the Caribbean and South American plates could be marked by The North Coast fault zone transferring the present-day strike-slip motion between both plates some 30 km to the south.

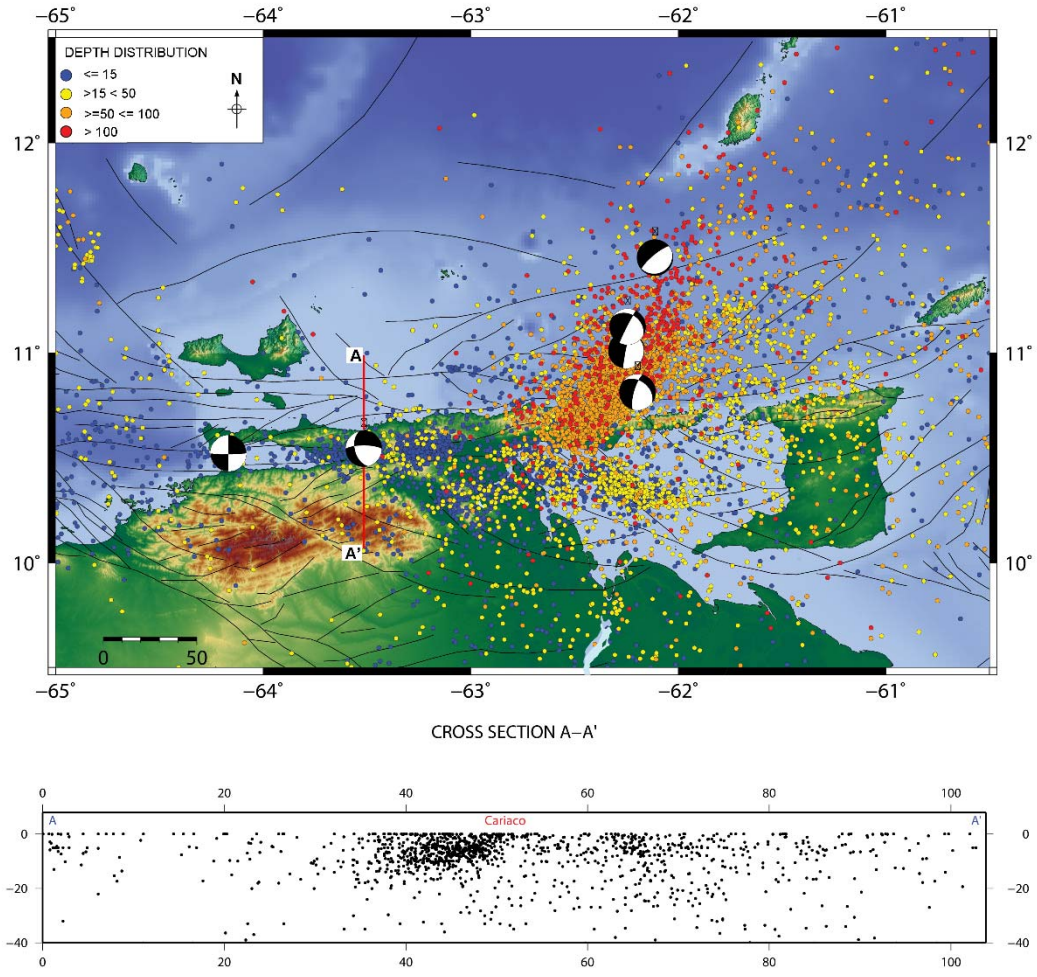


**Figure 2.** Distribution of seismicity in northeastern Venezuela from the 1910-2010 FUNVISIS catalog. The active faults are from *Beltrán* [1993] and focal mechanism from Audemard [1999], Audemard et al. [2005], and *Palma et al.* [2010].

## 3. GNSS data collection and analysis

In order to monitor and determine present-day displacements in northeastern Venezuela, a GNNS network was established in 2003 (Figure 1). Early in 2003, FUNVISIS personnel installed 36 new brass benchmarks covering eastern Venezuela from the islands in the north to the supposedly stable Precambrian craton in the south (south of the Orinoco River). Four existing sites (one from Petroleos de Venezuela S.A.-PDVSA- and three from University Navstar Consortium - UNAVCO) were included to complete a set of 40 campaign stations. The Cumaná station (CUMA) belonging to the Red de Estaciones de Monitoreo Satelital GPS - REMOS - (GPS Satellite Monitoring Station Network of Venezuela) from Instituto Geográfico Venezolano Simón Bolívar - IGVSB - (Geographic Institute of Venezuela) was also included in this study. The GNSS network was measured in late 2003, late 2005, and early 2013 (Figure 3) providing data for 32 sites on at least two occasions. We used direct centering benchmarks with dual-frequency GNSS and geodetic antennas, measuring at least two 24-hour sessions for each site, while the AUD0 station was measured continuously throughout the campaigns. The available data from cGNSS CUMA (2008.5-2008.7, 2012.5-2013.5) was included.

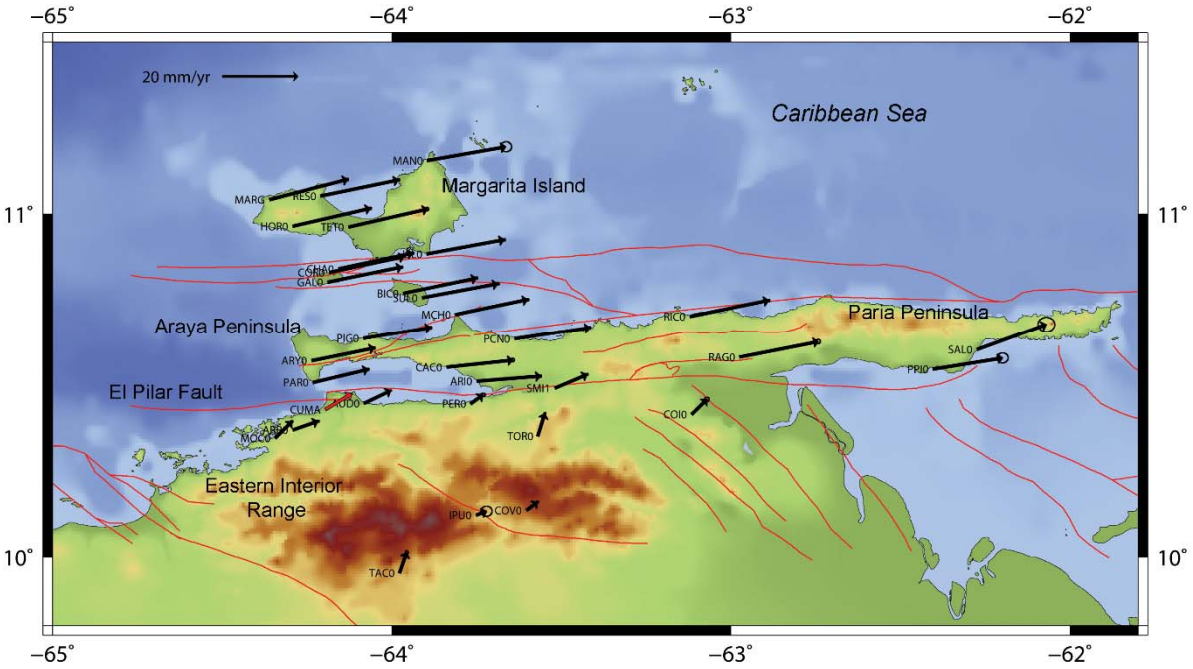

**Figure 3.** Observed velocities (black arrows) derived from comparison of 2003, 2005, and 2013 GNSS campaign measurements with error ellipses drawn for 66% confidence level [*Jouanne et al.*, 2011] and expressed within the South America plate reference frame using the rotation pole proposed by *Altamimi et al.* [2012]. The red vector is the CUMA station (REMOS-IGVSB). The active faults in northeastern Venezuela are from *Audemard et al*. [2000]. Topography and bathymetry data are from *Lindquist et al.* [2004].

Data from 33 stations (including the CUMA station) were analyzed with Bernese 5.2 software [*Dach and Walser*, 2013], using absolute antenna phase center offset models together with IGS final precise orbits [*Beutler et al.*, 1999], IGS Earth rotation parameters, and data from nearby permanent GNSS stations. We used the FES2004 ocean tidal model to calculate corrections for all GNSS stations using Hans–Georg Scherneck's web tool (http://www.oso.chalmers.se/~loading/). Velocities (Table 1) were estimated in the IGb08 frame of reference (an IGS-specific realization of ITRF2008) and expressed in the South America reference frame using the ITRF2008 absolute plate rotation pole proposed by *Altamimi et al.* [2012]. We followed the resolution strategy with: (1) initial ionosphere-free analysis with computation of residuals, (2) residuals analysis, (3) Code-Based Widelane (WL) Ambiguity Resolution for all the baselines [*Melbourne*, 1985; *Wübbena*, 1985]; using DCB files when available and computation of the ionosphere-free solution with the introduction of the resolved Melbourne-Wübbena linear combination ambiguities, (4) Phase-Based Widelane (L5) Ambiguity Resolution for baselines < 200 km and computation of the ionosphere-free solution with the introduction of resolved ambiguities, (5) resolution of the previously unresolved ambiguities for baselines < 2000 km using the Quasi Ionosphere-free strategy of resolution, (6) direct L1/L2 ambiguity resolution for baselines < 20 km, and (7) computation of the normal equations. The daily GNSS solutions were transformed in the IGb08 reference frame [*Altamimi* et al., 2012] with a six-parameter Helmert solution (three translation parameters and three rotation parameters) using the IGS stations: BOGT, BRAZ, BRFT, BRMU, CIC1, CRO1, FORT, GLPS, GMAS, GUAT, MANA, MAS1, MDO1, SANT, SCUB and SSIA. We detected

outliers with the FODITS (Find Outliers and Discontinuities in Time Series) tool in the Bernese software that reduces, step-by-step, the discrepancy between the functional model and the time series from statistical adjustment [*Ostini* et al., 2008]. It is recognized that the Bernese software underestimates the daily coordinate errors because systematic errors or mis-modeled parameters are not included in the formal error [*Hugentobler et al.*, 2001]. In order to obtain a realistic estimated error, we rescaled the formal errors multiplying by a factor of 10.

**4. Modeling approaches**

The velocity field across the EPF zone exhibits two separate patterns. Sites south of the EPF show smaller displacements than those north of the fault (Figures 3 and 4). The IPU0 site velocity with respect to South America does not exceed 3 mm/yr. Similarly, velocities at other sites range from ~ 4 mm/yr (COV0) to ~ 8 mm/yr near to the fault segment. The SMI1 site close to the rupture zone of the 1997 Cariaco earthquake presents a velocity of ~ 9 mm/yr. By contrast, immediately upon crossing the EPF, the ARI0 and PAR0 sites exhibit velocities close to ~ 15 mm/yr. This pattern continues to Margarita Island where a velocity of ~ 21 mm/yr is observed at the MAN0 site. A few kilometers on either side of the EPF, a high displacement gradient crossing the fault suggests a shallow locking depth or an aseismic component along the upper part of the EPF. As mentioned above, the asymmetric displacement gradients on each side of the EPF have been associated with dipping fault segments [*Jouanne et al.*, 2011].

A first-order model of interseismic deformation [*Chinnery,* 1961; *Weertman and Weertman,* 1964; *Savage and Burford et al.*, 1973; eq. 1] is given by

$$v(x) = \frac{V_T}{\pi} \tan^{-1}\left(\frac{x}{D}\right) \quad \textbf{(}\text{eq. 1)}$$

where v(x) is the velocity at a distance x from the fault, $V_T$ is the far-field velocity, and D is the locking depth of the fault. Our results show a 1.6 km locking depth for a far-field velocity

**Table 1**. Velocities expressed in the IGb08 Reference Frame

| Station | Long (deg) | Lat (deg) | Ve (mm/yr) | Vn (mm/yr) | σVe (mm/yr) | σVn (mm/yr) |
|---|---|---|---|---|---|---|
| ARI0 | -63.749 | 10.511 | 11.07 | 12.32 | 0.2 | 0.2 |
| ARR0 | -64.291 | 10.370 | 0.80 | 13.18 | 0.3 | 0.2 |
| ARY0 | -64.236 | 10.571 | 10.75 | 14.28 | 0.2 | 0.2 |
| AUD0 | -64.081 | 10.447 | 1.32 | 14.29 | 0.1 | 0.1 |
| BIC0 | -63.965 | 10.770 | 13.52 | 14.95 | 0.2 | 0.2 |
| CAC0 | -63.837 | 10.553 | 11.63 | 12.80 | 0.3 | 0.3 |
| CHA0 | -64.156 | 10.841 | 13.69 | 15.08 | 0.3 | 0.2 |
| COI0 | -63.116 | 10.415 | -1.59 | 14.99 | 0.4 | 0.4 |
| COR0 | -64.184 | 10.831 | 13.88 | 15.10 | 0.3 | 0.2 |
| COV0 | -63.603 | 10.136 | -2.74 | 13.16 | 0.2 | 0.2 |
| CUMA | -64.195 | 10.429 | 13.69 | 14.90 | 0.1 | 0.1 |
| GAL0 | -64.188 | 10.802 | 14.61 | 15.62 | 0.2 | 0.2 |
| HOR0 | -64.291 | 10.965 | -3.29 | 16.89 | 0.2 | 0.2 |
| IPU0 | -63.751 | 10.122 | -2.91 | 12.00 | 1 | 0.9 |
| ISL0 | -63.896 | 10.884 | 14.66 | 14.72 | 0.2 | 0.2 |
| MAN0 | -63.895 | 11.156 | 14.99 | 14.61 | 1 | 0.9 |
| MARG | -64.360 | 11.042 | 16.65 | 16.48 | 0.2 | 0.2 |
| MCH0 | -63.811 | 10.707 | 13.24 | 14.95 | 0.2 | 0.2 |
| MOC0 | -64.344 | 10.346 | -1.27 | 15.26 | 0.2 | 0.2 |
| PAR0 | -64.231 | 10.508 | 8.67 | 14.36 | 0.2 | 0.2 |
| PCN0 | -63.637 | 10.636 | 14.03 | 13.94 | 0.2 | 0.2 |
| PER0 | -63.767 | 10.446 | -2.42 | 13.30 | 0.4 | 0.3 |
| PIG0 | -64.083 | 10.637 | 11.86 | 13.81 | 0.3 | 0.2 |
| PPI0 | -62.404 | 10.547 | 12.67 | 14.02 | 1.0 | 0.9 |
| RAG0 | -62.974 | 10.582 | 15.00 | 15.10 | 0.4 | 0.4 |
| RES0 | -64.209 | 11.053 | 14.73 | 15.17 | 0.2 | 0.2 |
| RIC0 | -63.120 | 10.701 | 15.01 | 15.33 | 0.2 | 0.2 |
| SAL0 | -62.274 | 10.604 | 12.60 | 17.78 | 1.5 | 1.3 |
| SMI1 | -63.519 | 10.492 | 2.78 | 14.54 | 0.2 | 0.2 |
| SUL0 | -63.910 | 10.757 | 14.13 | 14.65 | 0.3 | 0.2 |
| TAC0 | -63.977 | 9.954 | -3.75 | 16.30 | 0.3 | 0.3 |
| TET0 | -64.127 | 10.963 | 14.94 | 15.66 | 0.3 | 0.3 |
| TOR0 | -63.569 | 10.352 | -3.82 | 16.88 | 0.2 | 0.2 |

of 20 mm/yr according to the most widely accepted Caribbean–South American plate motion values [*DeMets et al.*, 2000; *Pérez et al.*, 2001a, b; *Weber et al.*, 2001].

Although the fault-perpendicular profile based on the homogeneous elastic half-space model shows a relatively good fit (Figure 4), we propose to model this velocity field using four approaches that include other considerations: (1) the possibility of explaining the asymmetric velocity gradients by contrasting material properties on each side of a vertical fault, (2) the presence of a compliance zone (a near-fault low-rigidity tabular zone) on either side of the fault caused by cumulative damage from repeated earthquakes, (3) a slip distribution estimation through using multiple finite discrete fault patches in order to simulate a gradual transition of slip rates rather than a sudden jump, and (4) an upgrade using 2013 data of the displacement simulation method described in *Jouanne et al*. [2011] using non-vertical dislocations to simulate the deeper parts of the EPF.

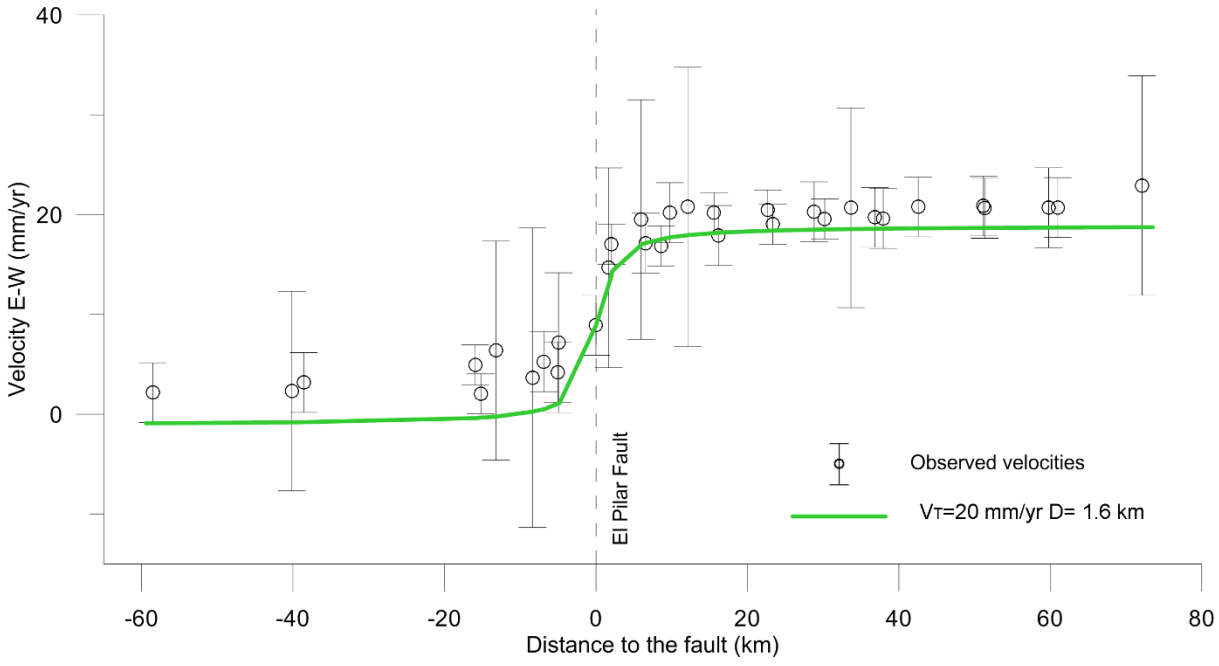


**Figure 4.** Velocity field across the EPF. Fault-perpendicular profile showing the best fit model for the simple half-dislocation (homogeneous) model.

### 4.1. Change in elastic properties on each side of the EPF

Here, we test an asymmetric modeling of velocities on each side of the EPF assuming a single vertical fault separating two geologic terrains with contrasting properties. We use the half-space model modification [*Jolivet et al.*, 2009] to the asymmetric dislocation model proposed by *Le Pichon et al.* [2005] to calculate an asymmetric surface velocity field on each side of the vertical fault located at x = 0 (eqs. 2 and 3). This simplification aims at reducing three parameters: the rigidity contrast between the two sides of the fault, the horizontal offset between the basal shear zone and the surface fault, and the fault slip rate.

$$v(x) = \frac{2KV_T}{\pi}\tan^{-1}(\frac{x}{D}); x < 0 \quad \text{(eq. 2)}$$

$$v(x) = 2(1-K)\frac{V_T}{\pi}\tan^{-1}(\frac{x}{D}); x \geq 0 \quad \text{(eq. 3)}$$

where again v(x) is the velocity at a distance x from the fault, $V_T$ is the far-field velocity, and D is the locking depth of the fault. The asymmetry coefficient K = V1/(V1+ V2); K = V1/ $V_T$ ranges from 0 to 1 and can also be expressed as $E_2/(E_1 + E_2)$. Equations 2 and 3 are equivalent for K = 0.5, meaning there is no rigidity contrast. To evaluate the quality of our models, we calculate an RMS or the quadratic mean value of the misfit (eq. 4), as follows:

$$RMS = \sqrt{\frac{1}{N}\sum(\frac{(Ve_{obs} - Ve_{model})^2}{\sigma^2_{Veobs}})} \quad \text{(eq. 4)}$$

where $\sigma^2_{Veobs}$ is the variance of the observations, $Ve_{obs}$ is the eastern component velocity from interseismic velocities of the northeast Venezuelan GNSS network, $Ve_{model}$ is the simulated velocity, and N is the number of GNSS stations along the EPF.

The best-fit for an unconstrained model suggests a far-field velocity of 17 mm/yr with a 1.5 km locking depth and an asymmetry ratio of 0.33. In order to enhance the robustness of our results we evaluate trade-offs between the rigidity ratio and locking depth, rigidity ratio and slip rate,

and locking depth versus slip rate (Figure 5 a, b, c) for this model. We determine that the rigidity contrast is almost constant despite decreasing or increasing locking depth and slip rate. Nonetheless, there is a significant trade-off between locking depth and slip rate with deeper locking depth leading to higher far-field velocities.

Likewise, we evaluate two possibilities starting from the following two sets of conditions: (1) a far-field velocity constrained to 20 mm/yr similar to the classic half-space dislocation model and (2) a second test fixing the locking depth at 12 km according to the distribution versus depth of microseismicity [*Baumbach et al.*, 2004]. The best fit for the first model is for a 3.0 km locking depth with a K ratio of 0.37. The second test performs best with a 24 mm/yr far-field velocity and an asymmetry ratio of 0.36. For both models, trade-off between the rigidity ratio versus locking depth and slip rate respectively reveals no significant variation in rigidity contrast with decreasing or increasing locking depth and slip rate (Figure 5d, e). Fault-perpendicular velocity profiles show a good correlation for all models (Figure 6a). The observed velocities with their eastern component from GNSS campaigns and simulated velocities are shown in figure 6b.

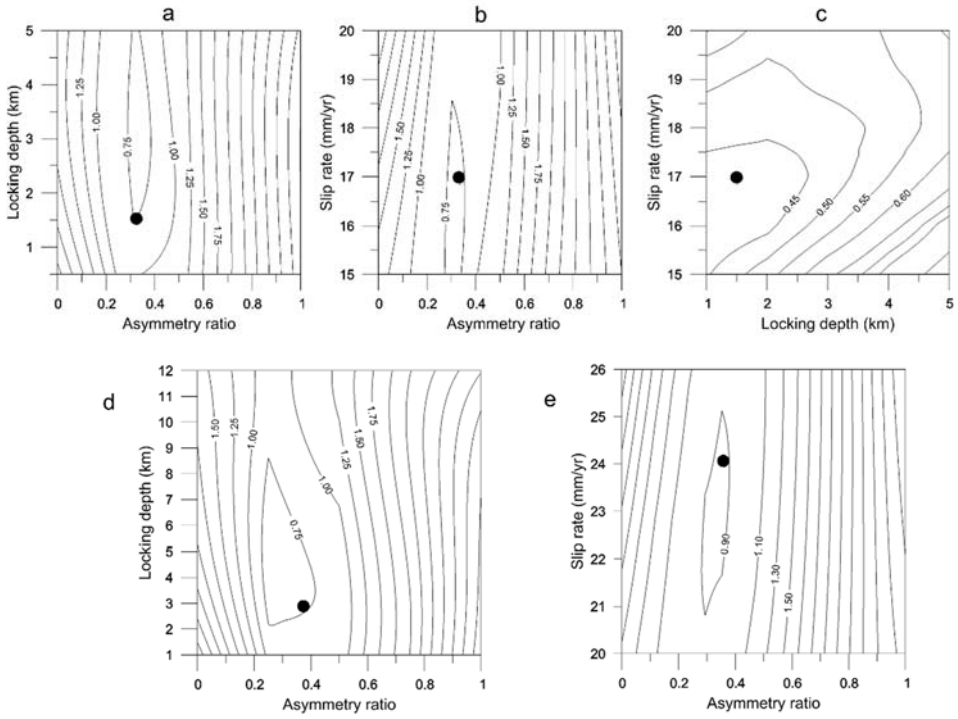

**Figure 5.** Trade-offs between (a) asymmetry ratio and locking depth, (b) asymmetry ratio and slip rate and, (c) locking depth versus slip rate for the unconstrained model (Results. $V_T$= 17 mm/yr. D= 1.5 km and K= 0.33). (d) Trade-off between the asymmetry ratio (K) and the locking depth on the EPF for the model with far-field velocity fixed at 20 mm/yr. (e) Trade-off between the asymmetry ratio (K) and the slip rate on the EPF for the model with locking depth fixed at 12 km. Contoured values are the RMS values and the black dot indicates the best model.

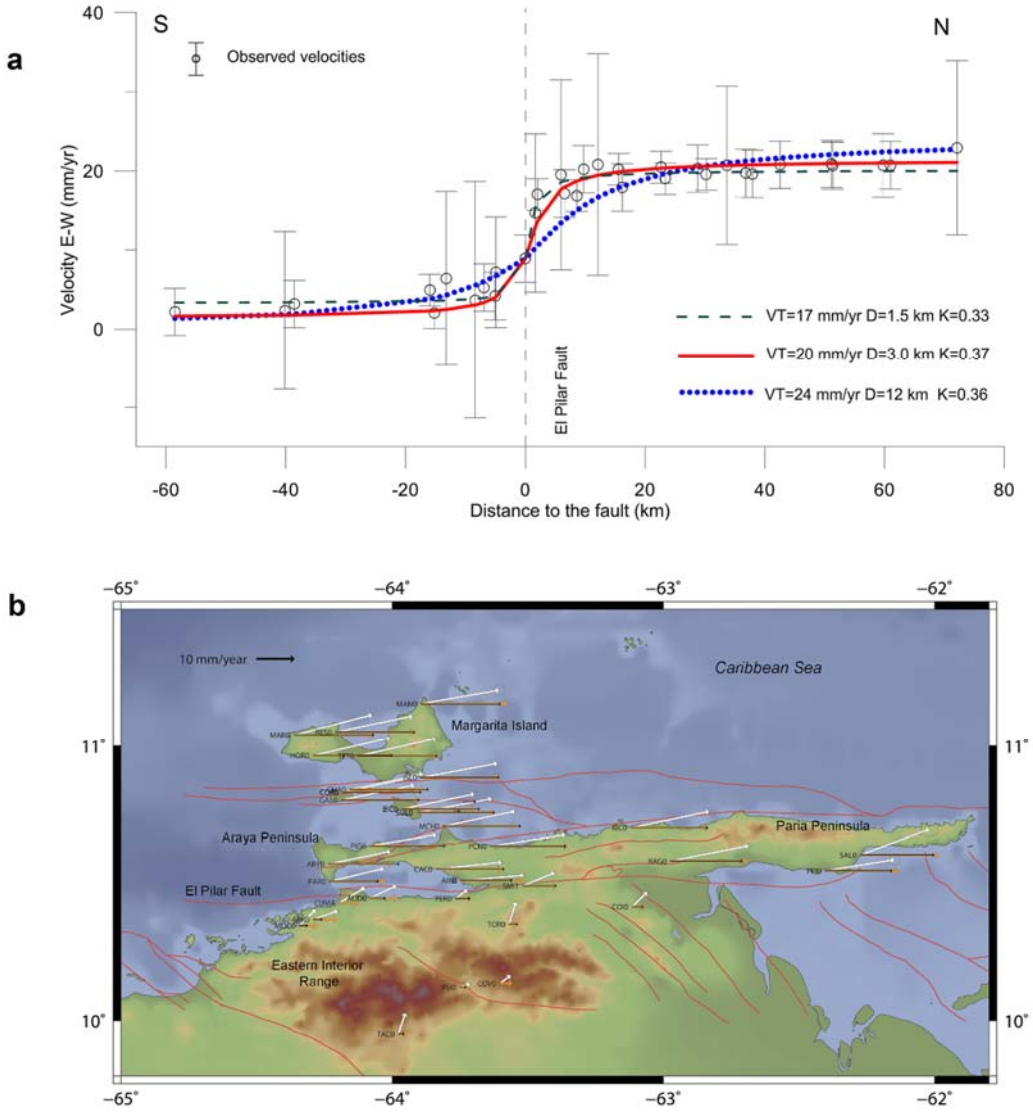


**Figure 6.** (a) Fault-parallel velocity profiles showing the acceptable models from the asymmetric modeling in the EPF zone and the E-W observed velocities from 2003, 2005, and 2013 GNSS campaign measurement data (including cGNSS CUMA station). (b) Observed velocities (white arrows) with their eastern component (yellow arrows) from GNSS campaigns and simulated velocities (black arrows) from the asymmetric modeling for 20 mm/yr far-field velocity. All displacements are based on the South America reference frame.

### 4.2. Compliant fault zone model

Crustal faulting can often be associated with the development of highly fractured and damaged rocks around the main slip surface. The cumulative damage caused by repeated earthquakes might generate a weaker zone than the surrounding medium [*Ambraseys*, 1970; *Wilson et al*., 2004; *Chester et al*., 2005, *Peng and Ben-Zion*, 2006]. We investigate the influence of a compliant zone (CZ) around the EPF using a semi-analytic iterative procedure based on a 3-D model of elastostatic deformation in a semi-infinite solid with a free-surface boundary condition and 3-D variation in elastic properties [*Barbot et al.*, 2009]. This method adapted to the case of 3-D deformation is based on a numerical approach presented by *Barbot et al.* [2008]. This procedure simulates the deformation due to faulting in the presence of arbitrary variations in material properties that are modeled with equivalent body forces and equivalent surface traction in a "homogenized" elastic medium. The surface displacement is obtained in the Fourier domain using a semi-analytic Green function. In this work, we evaluate a CZ that is shallower than the locking depth [*Jolivet et al*., 2009] extending downward from the surface and following the strike of the EPF. *González et al*. [2004] report that damage from the 1997 Cariaco earthquake is most pronounced along the EPF because of a strong anisotropy or directivity effect due to fault orientation and rupture propagation as well as the general W–E alignment of the regional structure.

The input model parameters include the gradient of Lamé parameters $\Delta\lambda$ and $\Delta G$, the CZ width (fault-normal dimension) and depth (down-dip dimension), together with EPF geometry. We constrain several parameters such as strike, dipping, and rake directions for the EPF on the basis of earlier work [e.g. *Audemard et al*., 2000; *Mendoza*, 2000; *Pérez et al*., 2001a, b; *Baumbach et al*., 2004; *Jouanne et al*., 2011]. The transition between the upper seismogenic and lower ductile dislocations was fixed at 12 km on the strength of the aftershock depth distribution of the 1997 Cariaco earthquake [*Baumbach et al*., 2004].

First, to identify the best-fitting model we explore a range of different widths and depths for the CZ, ranging from 0 to 3 km and 0 to 12 km respectively, according to the *W=L/6* ratio presented by *Barbot et al.* [2008] who assumed that the CZ width is six times smaller than the depth extent of the co-seismic slip, where L is the nominal locking depth. Nonetheless, we extend the range of CZ width (to 12 km) in line with *Cochran et al*. [2009] who report that width differences of damaged zones may be related to intrinsic variations along sections of the same fault. In addition, we evaluate the rigidity reduction ranging from -30 to -60 percent (we assume the same values for the ΔG and Δλ parameters for each calculation) relative to the surrounding lithosphere.

We evaluate the quality of our models with an RMS of the misfit based on comparison between simulated and observed interseismic velocities of the northeast Venezuelan GNSS network (eq. 5), as follows:

$$RMS = \sqrt{\frac{1}{N}\left(\sum \frac{(Ve_{obs} - Ve_{model})^2}{\sigma^2_{Ve_{obs}}} + \sum \frac{(Vn_{obs} - Vn_{model})^2}{\sigma^2_{Vn_{obs}}}\right)} \quad \text{(eq. 5)}$$

In order to improve our evaluation we test several possibilities considering EPF as a one-to-four segment fault (2, 4, 6, and even 8 dislocations respectively). However, the best models according to the number of segments (from 1 to 4 segments) show a good adjustment between observed and simulated velocities with similar responses to the CZ parameter variations. Our preferred models, independently of the number of EPF segments, indicate a CZ within the upper 3 km in depth and from 1 to 5 km wide with a slight improvement using a rigidity reduction of ΔG= -30 per cent (Figures 7a, 8).

Nevertheless, in order to evaluate the improvement in the models according to the number of fault segments, we compare the best solutions for each number of segments using the Fisher-Snedecor variance test. This evaluation based on different degrees of freedom and RMS values

is used to estimate the probability of differences between two comparable models (Table 2). To perform this test, we consider the strike-slip displacement component only for the interseismic slip, ruling out the dip-slip contribution for the EPF (the vertical displacement has not been evaluated in this work) in accordance with *Audemard* [2006] who, using a set of geological and structural observations gathered along the surface rupture of the Cariaco 1997 earthquake, indicates that the overall direction of motion on the El Pilar fault is right-lateral with no visible vertical component. Results show that the "CZM4 dislocations – 2 segments" model with its range of 58–87 percent is probably better than the others. The trade-off between CZ depth and width reveals a reduction in adjustment with an increase in these parameters. The differences for several rigidity reduction values are almost imperceptible, for this reason we do not show the respective contour plots.

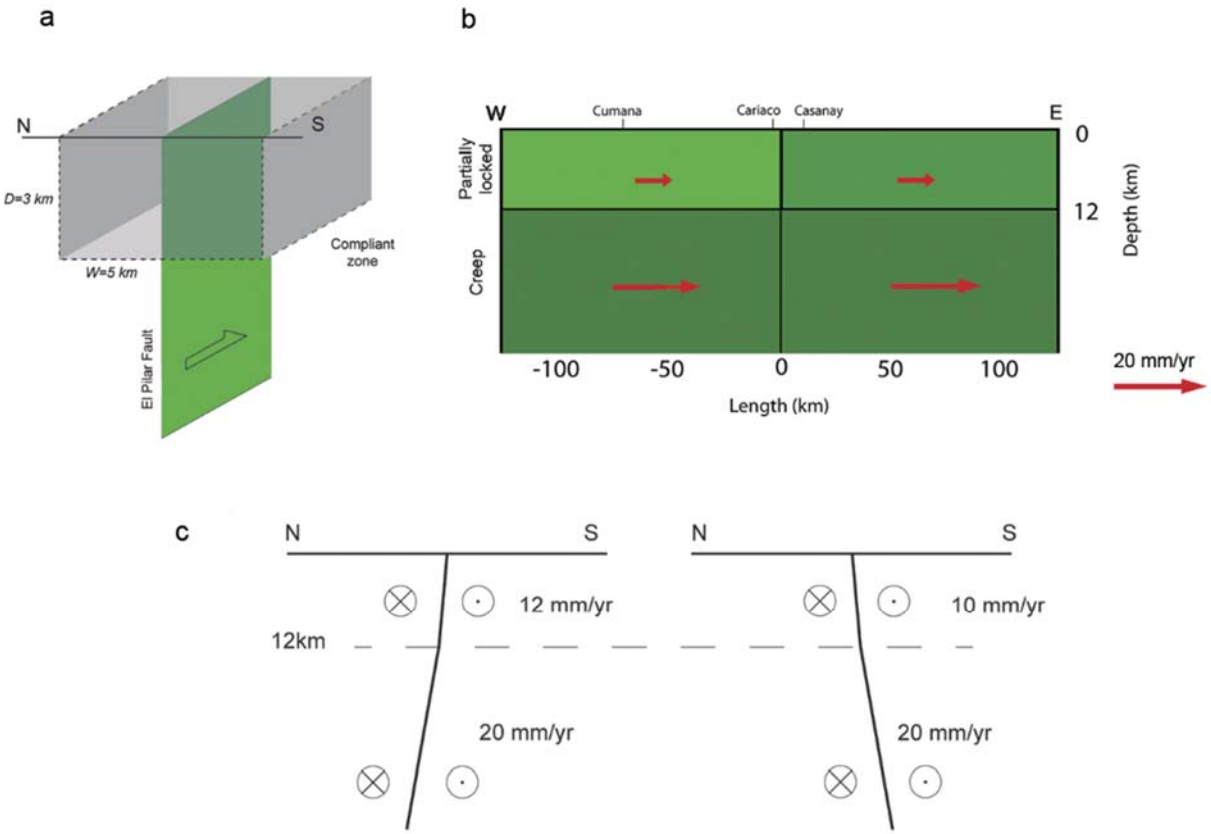

**Figure 7.** (a) Diagram of a CZ within the upper 3 km in depth and a 5 km width surrounding and following the strike of the EPF. (b) Distribution of right lateral slip on the northern side of the EPF and (c) cross sections of western and eastern segments of the EPF according to two-segment CZ dislocation model. The western and eastern segments are shown with a northward and southward dipping fault respectively and substantial aseismic slip along the upper part of the fault.

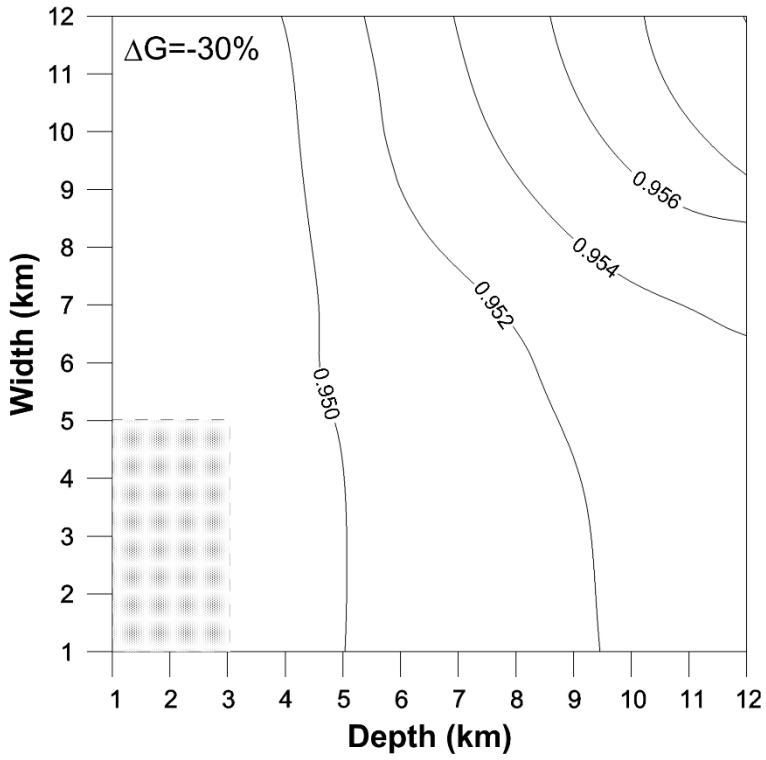


**Figure 8.** Trade-off between depth and width CZ for a rigidity reduction ΔG of 30 per cent. Contoured values are the RMS values and the rectangular zone indicates the preferred models.

The EPF geometry for this preferred model shows in the upper segments an 85° northward dip for the western segment and an 85° southward dip for the eastern segment with 12 mm/yr and 10 mm/yr of displacement respectively. The dextral strike-slip component along the deeper dislocations was constrained at 20 mm/yr to represent the ductile creep at depth. Dip was fixed with an 80° northward dip for the western segment and an 80° southward dip for the eastern segment (Table 3; Figures 7b, c). From the comparison of upper displacement values with the 20 mm/yr of relative velocity motion between the Caribbean and South American plates, we find 40% of locked displacement (20 - 12 = 8 mm/yr, 40% locked) in the western segment and

50% of locked displacement in the eastern segment (20 - 10 = 10 mm/yr, 50% locked), which is consistent with the observation of creep at the surface along the fault [*Audemard*, 2006] and the model proposed by *Jouanne et al.* [2011]. In figure 9, we show the comparison between observed and simulated velocities for a two-segment CZ model.

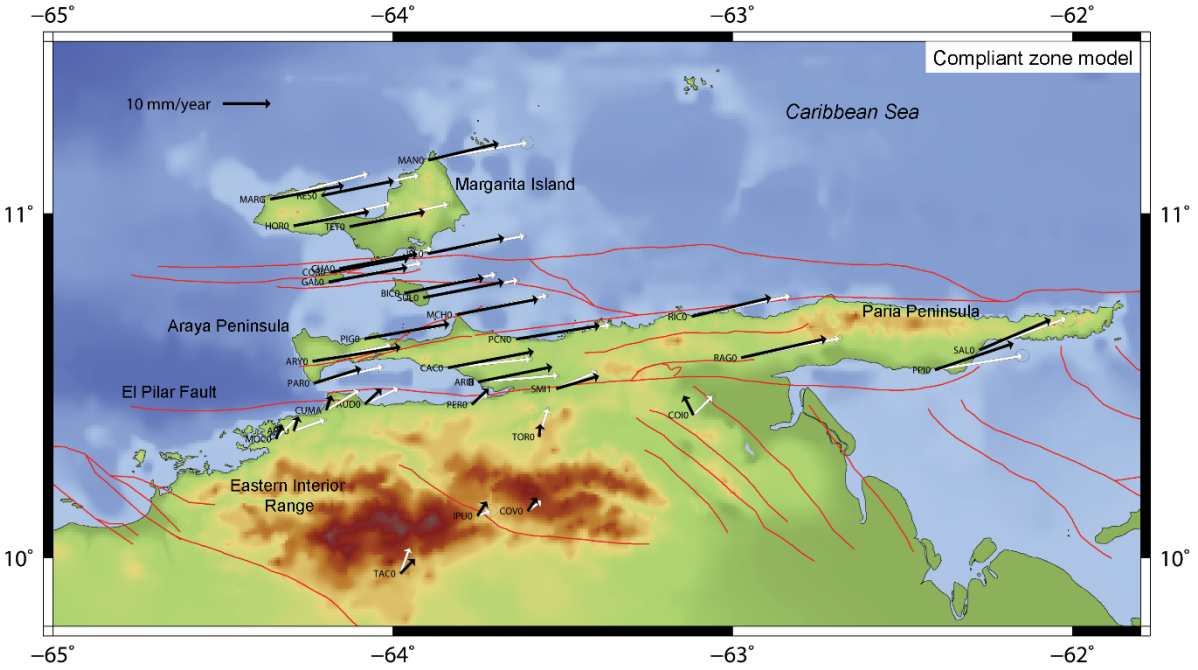


**Figure 9.** Observed velocities (white arrows) with error ellipses for 66% confidence level and simulated velocities (black arrows) according to the two-segment CZ modeling. All displacements are based on the South America reference frame.

**Table 2**. Selection of best CZ model according to Fisher-Snedecor variance test.

| Model | N DATA | N parameters | Degree of freedom | RMS |
|---|---|---|---|---|
| CZM 2 dislocations (1 segment) | 66 | 11 | 55 | 1.291 |
| CZM 4 dislocations (2 segments) | 66 | 15 | 51 | 1.144 |
| CZM 6 dislocations (3 segments) | 66 | 23 | 43 | 1.228 |
| CZM 8 dislocations (4 segments) | 66 | 27 | 39 | 1.211 |

| Comparison of models | Test | Probability | Results |
|---|---|---|---|
| Is the CZM 4 model better than the CZM 8 model? | 1.384 | 0.86 | Yes |
| Is the CZM 4 model better than the CZM 6 model? | 1.273 | 0.80 | Yes |
| Is the CZM 4 model better than model the CZM 2 model? | 1.046 | 0.56 | Maybes |

**Table 3.** Summary of fault geometry input parameters for better models.

| | | Upper segments | | | Lower segments | | |
|---|---|---|---|---|---|---|---|
| | | **Azimuth** | **Dip** | **Slip** | **Azimuth** | **Dip** | **Slip** |
| **Compliant zone model and** | **Western** | 90° | 85° northward | 12 mm/yr | 90° | 80° northward | 20 mm/yr |
| **Slip distribution (model a)** | **Eastern** | 90° | 85° southward | 10 mm/yr | 90° | 80° southward | 20 mm/yr |
| **Displacement sim.** | **Western** | 88° | 87° northward | 12 mm/yr | 88° | 53° northward | 20 mm/yr |
| **[Jouanne et al., 2011]** | **Eastern** | 89° | 77° southward | 10 mm/yr | 89° | 80° southward | 20 mm/yr |

### 4.3. Slip distribution model from GNSS observations

Based on the fact that friction along the fault plane is not uniform in intensity, the fault-slip distribution can be evaluated in multiple finite discrete fault patches in order to detect variations in slip along the fault. The presence of stuck or locked zones, partially locked zones, and creeping zones is evaluated from interseismic displacements using a procedure based on the constrained least squares method [*Wang et al.*, 2013]. This method of slip inversion is performed using SDM2011 software, which has recently been applied in other geodetic studies [*Motagh et al*., 2008, 2010; *Wang et al*., 2009, 2011, *Xu et al*., 2010, *Diao et al*., 2010, 2011]. The observed slip data are related to the discrete fault displacement using a Green function of the earth model calculated through the linear elastic dislocation theory. In order to obtain a slip model with high resolution, the fault plane is presented by a number of small rectangular dislocation patches with uniform slip. The patch size must be small enough to give a reasonable representation of the true continuous slip distribution. If the available data do not include enough information for determining the slip distribution with the desired resolution, the inversion system becomes underdetermined. For that reason, a priori or artificial conditions (fixed fault geometry and restricted variation for the rake angle) and physical constraints (smooth spatial distribution of slip or stress drop) are required to avoid excessive variations in

slip distribution. Based on the idea that the areas where large stress drops occur are also subject to substantial slip [*Bouchon*, 1997], the slip models are adjusted according to suitable roughness in the stress drop. The objective function is defined as follows:

$$F(\mathrm{b}) = \| \mathrm{Gb-y} \|^2 + \alpha^2 \| \mathrm{H\tau} \|^2 \qquad \text{(eq. 6)}$$

where G is the Green function, b is the slip of sub-faults, y indicates the ground observation, $\tau$ is the shear stress drop related to the slip distribution on the whole fault plane, H represents the finite difference approximation of the Laplacian operator multiplied by a weighting factor proportional to the slip amplitude, and $\alpha^2$ is the positive smoothing factor.

To invert the velocity field, we use the observed displacement data related to the discrete fault slips using a homogeneous earth model with a Poisson ratio of 0.25. We constrain the input geometry of the EPF to a western segment of ~ 96 km and an eastern segment of ~ 144 km but we test several values of dip as follows: (a) a geometry similar to preferred CZ model (discussed above) with a northward dip for the western segment and southward dip for the eastern segment, respectively 85° and 80°, for the upper and lower segments; (b) a geometry with the previous dips for the shallower segments but with a vertical segments below 12 km; and (c) a geometry for which all segments are considered to be vertical faults (Figures 10 a, b, and c). In all cases, the upper segments are discretized into an array of ~ 2 km by 2 km patches and the lower parts are discretized into ~ 20 km by 20 km patches, with 90° strike and -180° rake values. Patch size is selected according to the length of sub-faults used in previous studies and the maximum number of point sources permitted by the code. The larger patches were used for the lower parts in order to constraint the far-field velocity to a few iterations. We extend the area limits considerably to avoid any artificial boundary effect.

The correlation for all models is quite good with ~ 95–97 percent using a standard linear least-squares minimization when comparing the interseismic velocities with the simulated velocities.

All segments are characterized by significant creep, nevertheless the upper western segment exhibits a significant decline in slip close to Cumaná city and in a minor area south of the CAC0 site, while the remainder of the segment exhibits a widespread partial-creep pattern with creep larger than 12 mm/yr. In the upper eastern segment, we observe a zone (10–12 km in depth) with decreasing slip values possibly related to the discontinuity effect at 12 km dislocation. We avoid this effect considering all segments with a similar dip (Figure 10 c). The contact between western and eastern upper segments displays a similar pattern near the city of Cariaco. If we dismiss these effects, the eastern upper segments exhibit widespread partial creep of ~ 8–12 mm/yr. Figure 11 shows the comparison between observed and simulated velocities for the vertical fault model.

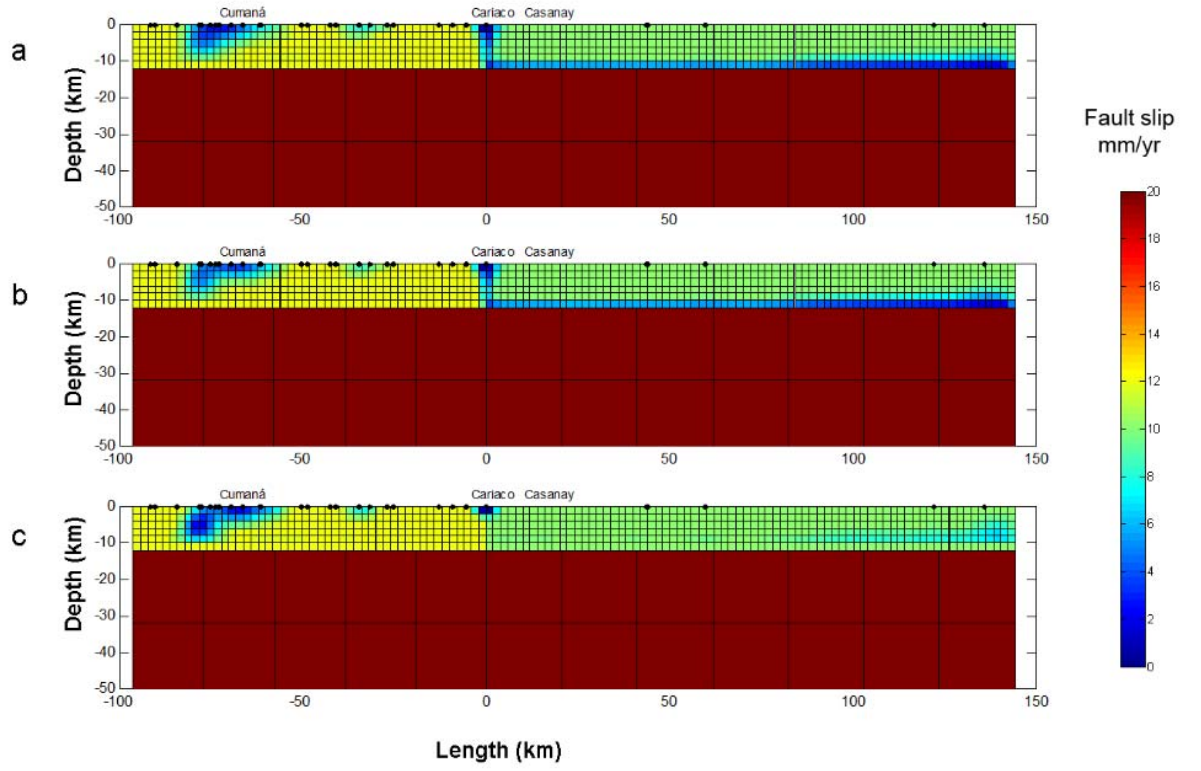


**Figure 10.** Distribution of right-lateral slip (mm/yr) on the EPF from slip distribution modeling for (a) an input geometry similar to the preferred CZ model (Figure 3c). (b) Similar geometry in upper segments and lower segments dip (>12 km depth) fixed to 90° and (c) upper and lower vertical segments.

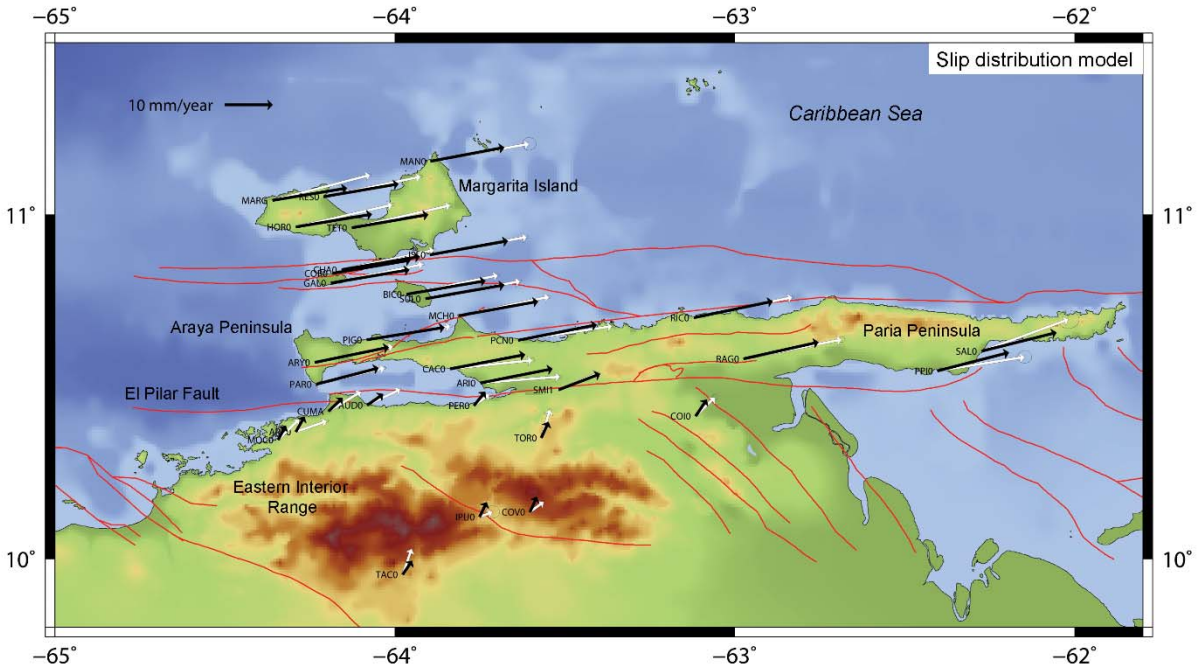


**Figure 11.** Observed velocities (white arrows) with error ellipses for 66% confidence level and simulated velocities (black arrows) according to the slip distribution modeling for the vertical fault geometry. All displacements are based on the South America reference frame.

### 4.4. Displacement simulation method using non-vertical dislocations

Here, we propose an upgrade of the model presented by *Jouanne et al*. [2011] including the 2013 data to supplement data from the 2003 and 2005 campaigns. In order to simulate the velocity field we present a set of dislocations in a uniform elastic half-space for rectangular sources [*Okada*, 1985]. The inversion procedure is based on iterative least squares adjustments of free parameters such as dip, azimuth, dip-slip, strike-slip, and rake.

For this study, we increase the number of GNNS stations from the 23 stations simulated by *Jouanne et al*. [2011] to 33 stations (Figure 12). Nonetheless, we keep two segments (western and eastern) representing the EPF with upper and lower dislocation separations at 12 km in line with the depth distribution of 1997 event. We consider as free parameters the dip of the deeper dislocation dip and the slip rates along both parts (upper and lower) of the EPF whereas the location, orientations, and upper dislocation dip are considered to be fixed parameters. Similarly

to the results of *Jouanne et al.* [2011] our preferred model shows the western segment to have an almost vertical upper segment and a 53° northward dipping deep segment. The eastern segment is characterized by a 77° southward dipping upper segment and an 80° southward dipping lower segment [Table 3, See *Jouanne et al*., 2011]. Likewise, the 12 mm/yr and 10 mm/yr of interseismic displacement are calculated for the western and eastern upper segments respectively and the dextral strike slip component along the lower dislocations is fixed at 20 mm/yr.

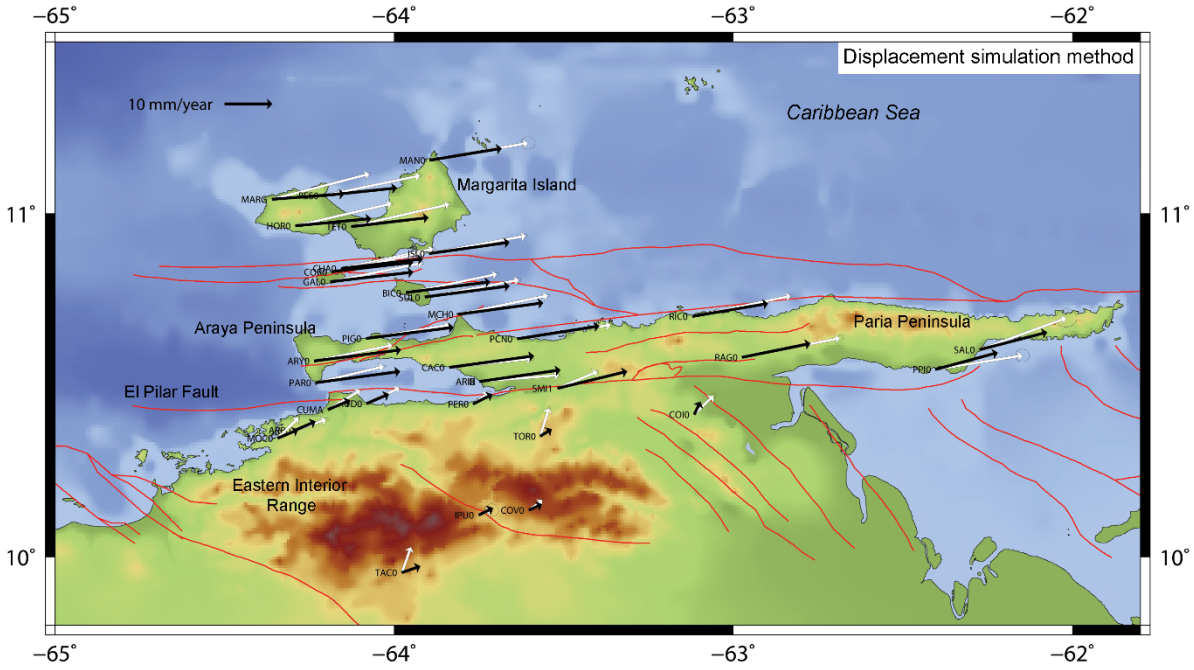


**Figure 12.** Observed velocities (white arrows) with error ellipses for 66% confidence level and simulated velocities (black arrows) according to the upgrade of displacement simulation method. All displacements are based on the South America reference frame.

## 5. Comparison of the various models

In order to discuss the best solution from models analyzed in this paper, we plot the E–W velocities versus the distance to the fault and residuals for different models (Figure 13a, b). A better fit of the asymmetry model can be observed mainly on the north side of the EPF with respect to other inversions. Nevertheless, for the south side of the EPF, it is difficult to identify a best model at first sight. The simplest half-space elastic model provides a relatively good fit

on the north side; however, it results in a misfit south of the EPF. For this reason we apply a Fisher-Snedecor variance test to compare our best results from the homogeneous model, asymmetric model, near-fault reduced rigidity zone model, and displacement simulation method using non-vertical dislocations. We omit the slip distribution model from this comparison because the discretization of segments into patches generates a much lower degree of freedom, making it incomparable with the other models.

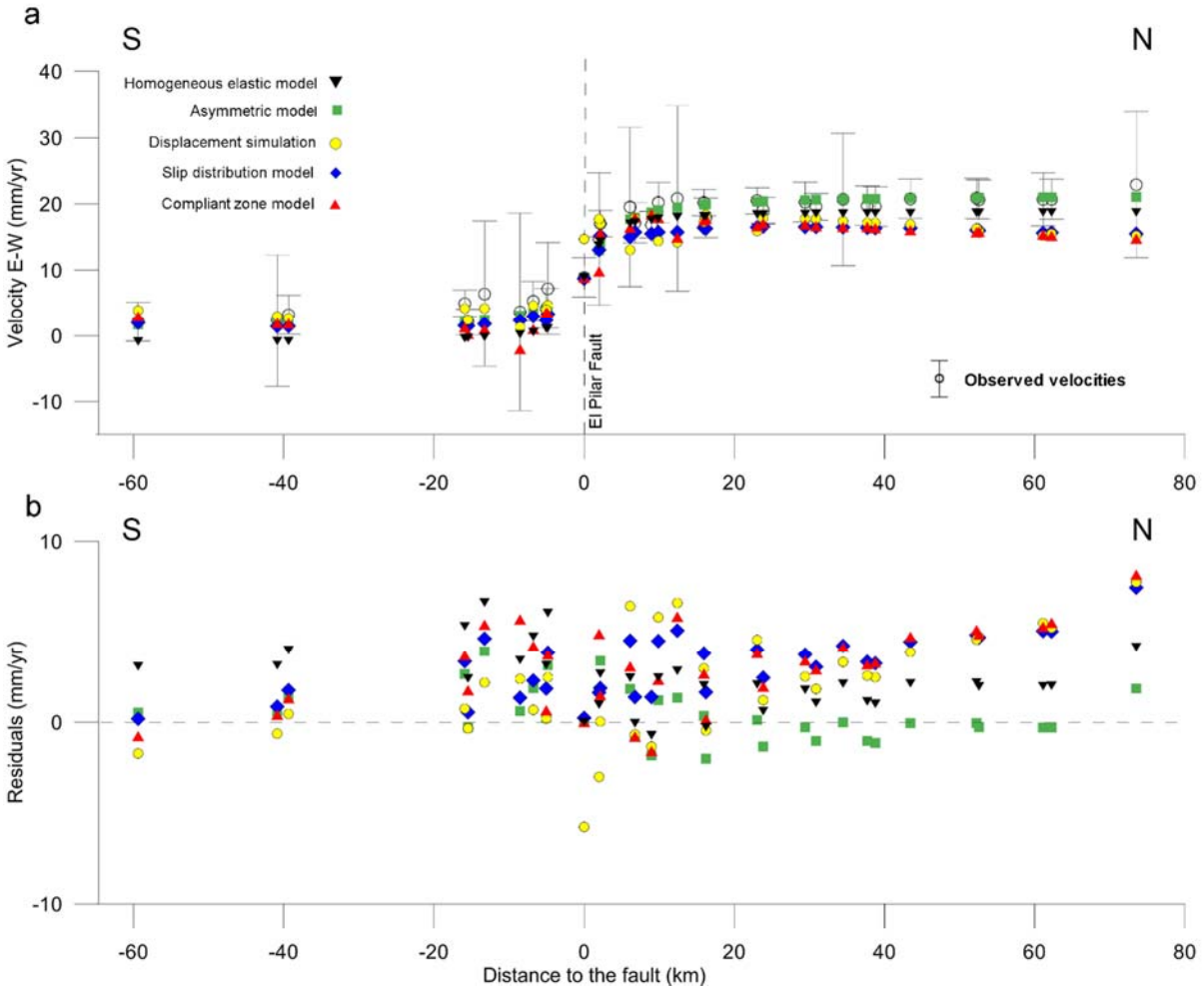


**Figure 13.** (a) Velocity field across EPF for several models applied in this work. We show E-W observed velocities and simulated velocities from the single-fault homogeneous elastic half-space model (Homogeneous elastic model), the asymmetric model with 20 mm/y far-field velocity, the displacement simulation method, the two segment slip distribution model, and the two segment compliant zone model. (b) Residuals for the different models.

We select our preferred result for each category of model (Table 4). Using the Fisher-Snedecor test of variances, we determine the probability of one model being better than another. The asymmetric model for 20 mm/yr far-field velocity is probably the best model with 80% probability of being better than the CZ model with four dislocations from the statistical point of view. But it must be noticed that the existence of progressively displaced markers suggests the occurrence of substantial creep, and this aspect is not included in the asymmetric model. Nonetheless, the CZ model is probably a better model than the others with more than 70% probability with respect to the homogeneous and displacement simulation models. Likewise, the displacement simulation could be a better model than the simple half-space model.

**Table 4.** Comparison between the displacement simulations. Asymmetric and CZ models using Fisher-Snedecor variances test.

| Model | N DATA | N parameters | Degree of freedom | RMS |
|---|---|---|---|---|
| Homogeneous model | 33 | 2 | 31 | 0.858 |
| Asymmetric model V=20 mm/yr | 33 | 3 | 30 | 0.501 |
| CZM 4 dislocations (2 segments) | 66 | 15 | 51 | 1.144 |
| Displacement simulations | 66 | 20 | 46 | 1.242 |
| Comparison of models | | Test | Probability | Results |
| Is the CZM4 Model better than the homogeneous model? | | 1.234 | 0.75 | Yes |
| Is the CZM4 model better than the asymmetric model? | | 0.745 | 0.20 | No |
| Is the CZM4 model better than the displacement simulations model? | | 1.204 | 0.74 | Yes |
| Is the displacement simulation model better than the homogeneous model? | | 1.025 | 0.54 | Maybe |

## 6. Discussion

In this paper we have applied five different methods of analyzing the velocity field across the EPF. From observation of parallel-fault velocities and the Fisher-Snedecor variance test we

have identified the asymmetric model for a 20 mm/yr far-field velocity as the best model. Nonetheless, each inversion test shows an interesting approach that we discuss in the following subsections.

### 6.1. Change in elastic properties on each side of the fault

Asymmetric interseismic strain, recognized for major faults around the world [e.g. North Anatolian fault, San Andreas fault, Great Sumatra fault), has been explained by lateral variations in the depth of the brittle-ductile layer [*Schmalzle et al*., 2006; *Chéry*, 2008; *Fulton et al*., 2010], lateral variations in viscosity [*Malservisi et al*., 2001], and the juxtaposition of materials with different physical properties [*Le Pichon et al*., 2005; *Jolivet et al*., 2008, 2009; *Houlié and Romanowicz*, 2011]. We have tested the hypothesis that asymmetric elastic properties may explain the observed velocity field on both sides of the EPF. From the results of this work, we show that the heterogeneous model assuming a single vertical fault separating two blocks with different elastic properties can provide a possible answer to the asymmetry of displacement gradients and it can be an alternative to the assumption of dipping fault segments presented by *Jouanne et al.* [2011]. In this study, we evaluate this explanation for the asymmetric velocity field, taking into account the fact that the discontinuously changing elastic effect across the fault produces an asymmetry that can be quantified. We evaluate this model based on the idea that the EPF roughly separates two very different geological provinces. The different tests applied to the EPF point out a contrast of rigidity between the northern and southern sides of the EPF. The K ratio values of 0.33, 0.37, and 0.36 (Figure 6a) show that the igneous-metamorphic northern side has a rigidity respectively 2.0, 1.7, and 1.8 times higher than the sedimentary southern side. Therefore, the idea of geological property differences on each side of the EPF helps explain the asymmetric velocity field.

The marked displacement gradient across a few kilometers on either side of the fault suggests the possibility of a shallow locking depth or an aseismic component along the upper part of the

fault plane [*Jouanne et al.*, 2011]. As results from the asymmetric model, we find a 3.0 km locking depth for the most widely accepted far-field velocity of 20 mm/yr between the Caribbean and the South America plates. The locking depth value is significantly shallower than the seismogenic depth of 12 km. Previous results for the EPF [*Pérez et al*., 2001b] indicate a locking depth of 14 ± 2 km; equal to the depth of the deepest aftershocks of the 1997 Cariaco earthquake. However, geodetic locking depths that are shallower than the seismogenic depths have been also observed along the creeping segment of the San Andreas Fault [*Smith-Konter et al*., 2011] and the San Jacinto fault zone [*Wdowinski*, 2009]. Moreover, closer to the EPF, *Weber et al*. [2011] discuss a similar behavior on the Caribbean–South America plate boundary, specifically in the Central Range Fault of Trinidad and Tobago, obtaining a best-fit single-fault elastic dislocation model with a 1–2 km locking depth and 12 ± 3 mm/yr of dextral strike-slip; suggesting essentially fault creep across that fault. The shallow locking depth indicates that steady motion along the fault also occurs within the seismogenic crust of the EPF (0–12 km depth) in accordance with the idea that a significant slip associated with creeping or partially creeping fault segments can also occur within the seismogenic crust and it is related to seismic or micro-seismic activity. Although eastern Venezuela is the most seismically active area on the southern Caribbean plate boundary, as documented by the FUNVISIS 1910-to-date instrumental seismicity catalog, most of the earthquakes are of magnitude 2–3. The main part of the Cariaco earthquake aftershocks (~ 80 percent) with magnitudes between -0.5 and 4.1 occurred in the depth range from 4.5 to 12 km [*Baumbach et al*., 2004], below the shallow locking depth obtained in this present study. The discrepancies between the maximum seismicity depths and the geodetic locking depth could be related to the possibility of shallow creep or temporary variations in strain release throughout the earthquake cycle [*Smith-Konter et al.*, 2011].

### 6.2. Compliant zone modeling

As a consequence of crustal faulting, CZs have been observed around major faults [e.g. San Andreas Fault, North Anatolian Fault). The fault damage zones have been observed geologically in the field [e.g., *Chester and Chester*, 1998; *Ben-Zion and Sammis*, 2003; *Faulkner et al*., 2003; *Oskin and Iriondo*, 2004; *Dor et al*., 2006]. In addition, theoretical models [e.g., *Kachanov*, 1986; *Lyakhovsky et al*., 2001; *Turcotte et al*., 2003] and geodetic [e.g., *Chen and Freymueller*, 2002; *Fialko et al*., 2002, *Fialko*, 2004, *Hamiel and Fialko*, 2007; *Barbot et al*., 2009] and seismic observations [e.g., *Li et al*., 1994; *Ben-Zion et al*., 2003; *Thurber et al*., 2003; *Cochran et al*., 2009] have predicted and evidenced the reduction in the effective elastic shear modulus of the fault zone material related to intense damage. In specific relation to the EPF, the surface breaks at different sites associated with the 1997 Cariaco earthquake [*Audemard*, 2006] reveal possible damage related to previous events. Besides, earlier studies have shown the reduction in effective elastic moduli associated with reduction in seismic velocities *[Cochran et al*., 2009]. The EPF has been imaged as a low velocity zone from the surface down to 14 km depth using seismic tomography [*Grosser et al.*, 2001] and a reduced velocity layer has been identified with a maximum depth of 5 km below the unconsolidated sediments of the village of Cariaco using deep seismic refraction [*Liuzzi et al*., 2006].

Our model suggests a much wider CZ than the *W=L/6* ratio [*Barbot et al*., 2008]. Nonetheless, *Cochran et al.* [2009] reported that the differences may be related to intrinsic variations in the width of damaged zones along the sections of the same fault. The width and depth extent of compliant fault zones are still under debate in the community [*Duan*, 2011]. Moreover, there are other factors not developed in this work such as the highly porous and permeable fault gouge zone [*Lees and Malin*, 1990*; Byerlee*, 1993; *Unsworth et al*., 1997] and the brittle–plastic transition [*Scholz*, 1988] that may be associated with development of CZs [*Chen and Freymueller*, 2002]. The CZ model also underlines the existence of substantial creep along the

upper part of the EPF (0–12 km) with 12 mm/yr in the western segment and 10 mm/yr in the eastern segment. According to these results, the displacement is locked between 40 and 50 percent.

### 6.3. Slip distribution model

In order to assert the idea of a partially locked fault in the upper segments, we determined a slip inversion along the EPF using a procedure based on fault patches. Our results point to a partial creep in the upper segments (0–12 km) but the discretization of segments in several patches suggests that the velocity is not uniform. We identify two main zones with reduced slip values; a first zone roughly 12 km wide and 8 km deep close to Cumaná city and a smaller second area south of the CAC0 site and 32 km west of Cariaco. The first and larger zone with reduced creep was not affected by the 1997 event judging from the distribution of Cariaco aftershocks [*Baumbach et al*., 2004]. It corresponds rather to the surface rupture of the 17 January 1929 Cumaná earthquake as documented by *Paige* [1930], *Rodriguez and Chacín* [1996], and *Mocquet et al*. [1996] and probably to the rupture of the 1797 earthquake [*Audemard*, 2007]. This area may then correspond to an asperity which previously ruptured during the 1929 earthquake but probably also during the 1797 event.

Despite, the 1929 and 1997 ruptures may have completed the total length of a rather continuous and linear section [*Audemard et al*., 2006*; Audemard*, 2007], and the EPF segment from the Caigüire Hills (Cumaná) to the Casanay-Guarapiche restraining bend has been considered as one subdivision of four segments that form the whole EPF [*Audemard et al*., 2000], our results indicate that this segment must be analyzed in at least two separate portions. Unfortunately, the major part of the western subdivision is underwater precluding the observation of surface creep.

### 6.4. Displacement simulation method using non-vertical dislocations

In this paper we reevaluate the set of dislocations in a uniform elastic half-space applied to the EPF and proposed by *Jouanne et al.* [2011]. In the upgrade, we do not observe significant changes of relationship with the displacement pattern. In fact, our preferred model shows two segments with four non-vertical dislocation planes, much as in the earlier work. We take into account the dislocations along the EPF that imply that the relative displacements for the Caribbean–South America plate boundary in the study zone are concentrated on the EPF. We reaffirm the idea of sizeable aseismic displacement along the upper part of the EPF with 40 and 50 percent respectively for the upper western and eastern segments.

## 7. Conclusions

Modeling from GNSS observations since 2003 has made it possible to identify creep in the upper part of the EPF. This conclusion is reinforced by the observation of progressively displaced markers [*Audemard*, 2006]. Additionally, the simple and asymmetric elastic half-space approaches indicate a shallow locking depth that suggests fault creep, and the near-fault low-rigidity model and displacement simulation method using non-vertical dislocations indicate between 40 and 50 percent of locked displacement between 12 km depth and the surface. As suggested by *Jouanne et al.* [2011] this behavior is probably related to either the existence of serpentinite lenses [*Moore et al*., 1997] or deep-seated fluid-escape. The weathered serpentinites have been reported forming a narrow ridge separating two faults near Casanay [*Metz*, 1965]. The western portion of the western segment of the EPF corresponds to the segment affected by the 1929 event [*Audemard*, 2007] and the eastern segment is related more to the 1997 Cariaco earthquake [*Audemard*, 2006*; Jouanne et al*., 2011]. Moreover, from discretization of segments into several patches, we conclude that the interseismic slip is not uniform. Nevertheless, creep or partial creep is present in both segments of the EPF. The post-seismic afterslip following the 1997 event could help explain the creep in the eastern segment;

for the western segment, the creep might be explained in several ways; a post-seismic effect following the 1929 earthquake, after which the creep must have continued to decrease with time or as a consequence of a post-seismic effect following the 1997 earthquake that affected another segment of the EPF. We highlight a low slip-rate zone eastward of Cumaná city roughly 12 km wide and 8 km deep and probably related to the rupture zone of the 1929 earthquake that may then correspond to an asperity along the fault.

In a recent study *Audemard* [2011] revealed at least 13 events around Ms 7.0 (moderate earthquakes) in the last 5.6 kyr, representing an average return period of 430 yr which is significantly different from the 195 yr return period estimated in the case of full locking of the upper 12 km of the El Pilar Fault [*Jouanne et al.,* 2011]. This observation supports the hypothesis of significant creep during interseismic periods and not only after major earthquakes. As a consequence the observed creep cannot be interpreted as "classical" after-slip following a major earthquake. The seismicity distribution with depth could suggest the occurrence of shallow creep in the upper part with a gradual transition to a partially locked seismogenic zone confined between 3.0 and 12 km, and the existence of ductile shear below 12 km (Figure 14).

From comparisons of fault-perpendicular velocity profiles and using the Fisher-Snedecor test of variances we select the asymmetric model for 20 mm/yr far-field velocity as the best model. This model is likely the best model with 80% of probability of being better than the CZ model with four dislocations. Nevertheless, field observations and the results of several models present the creep in the EPF as a significant issue to take into account. This leads to the conclusion that the CZ model is a better model from the geological and geodetic point of view than the statistically superior asymmetric model. Likewise, the CZ model is a better model, with more than a 70% confidence level, than the displacement simulation using the non-vertical dislocation model and the simple elastic half-space model. The slip distribution model was

omitted from the comparison because the discretization of segments into patches generates a far lower degree of freedom, precluding comparison with the other models. Nonetheless, this model with a quite good correlation is based on the same EPF geometry as the CZ model.

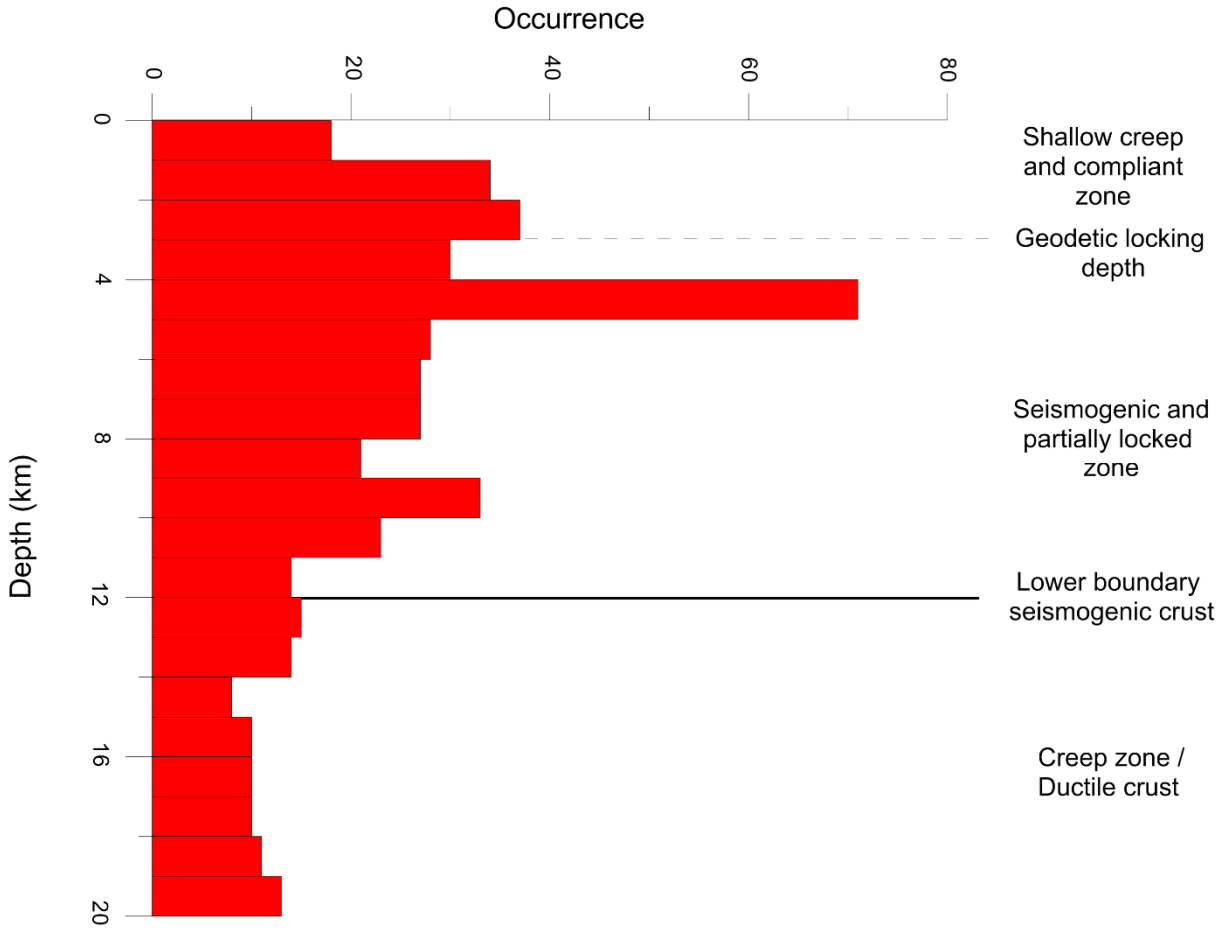


**Figure 14.** Distribution of seismicity (Occurrence) post-1997 Cariaco earthquake to 2009 (ISC Catalogue) versus depth showing peak activity in the seismogenic and partially locked zone. We show the hypothetic zones versus depth for the EPF according to the results of this work.

## Acknowledgments

The authors thank the associate editor Robert Nowack and two anonymous reviewers for their helpful comments and suggestions. We thank Sylvain Barbot for his support with the STATICI code and for comments and recommendations. We are also grateful to Miguel Palma, Rafael Abreu, Leonardo Alvarado, and Donata Liuzzi (former co-worker) from FUNVISIS, and Carlos

Mendoza (Centro de Geociencias, UNAM). The recent update of data in 2013 was made possible by the collaboration of Javier Oropeza, Walter Reategui, Alí Gómez and Maxlimer Vallée from FUNVISIS, Lenin Ortega, Carlos Martínez, Pedro Oropeza, and Gustavo Rodríguez from PDVSA-INTEVEP, Annio Moreno from PDVSA Servicios, and Johana Bautista from IGVSB. We thank the “Coordinación Técnica de Geodesia” - IGVSB for the Cumaná station data. We are grateful to the Audemard family for allowing us to install the base camp and GNSS base station (AUD0). C. Reinoza’s PhD thesis and stay at ISTerre Laboratory are funded through Venezuela’s FUNDAYACUCHO Grant N° 756514C. We would like to thank the financial and logistic support offered by FUNVISIS and ISterre. This research is a contribution to FONACIT-ECOS Nord grants PI 2003000090 (French code V10U01) and PI-2009000818, FONACIT-2002000478 (GEODINOS), and FONACIT-2012002202 (GIAME).

## REFERENCES

Aggarwal, Y. (1983), Neotectonics of the southern Caribbean: Recent data, new ideas, *Acta Cientifica Venezolana*, 34, 1, 17.

Altamimi, Z., L. Métivier, and X. Collilieux (2012), ITRF2008 plate motion model, *Journal of Geophysical Research: Solid Earth*, *117*(B7), B07402, doi:10.1029/2011JB008930.

Ambraseys, N. N. (1970), Some characteristic features of the Anatolian fault zone, *Tectonophysics*, 9(2–3), 143-165, doi:http://dx.doi.org/10.1016/0040-1951(70)90014-4.

Audemard, F. A. (1993), Néotectonique, sismotectonique et aléa sismique du nord-ouest du Vénézuela (système de failles d’Oca-Ancón), PhD thesis, 369 pp, University of Montpellier II.

Audemard, F. A. (1997), Preliminary Geological Report on the Cariaco Earthquake July 09, 1997, Venezuela, *International Center for Disaster-Mitigation Engineering Newsletter*, 6, 2, 7.

Audemard, F. A. (1998), Evolution géodynamique de la facade nord Sud-américaine: nouveaux apports de l'histoire géologique du Bassin de Falcón, Vénézuéla, paper presented at XIV Caribbean Geological Conference, Trinidad.

Audemard, F. A. (1999a), El sismo de Cariaco del 09 de julio de 1997, edo. Sucre, Venezuela: Nucleación y progresión de la ruptura a partir de observaciones geológicas, *Proceedings, VI Congreso Venezolano de Sismología e Ingeniería Sísmica, Mérida, Venezuela (CD-ROM).*

Audemard, F. A. (1999b), Nueva percepción de la sismicidad histórica del segmento en tierra de la falla de El Pilar. Venezuela nororiental. A partir de primeros resultados paleosísmicos, *Proceedings VI Congreso Venezolano de Sismología e Ingeniería Sísmica, Mérida*, 10.

Audemard, F. A. (2006), Surface rupture of the Cariaco July 09, 1997 earthquake on the El Pilar fault, northeastern Venezuela, *Tectonophysics*, *424*(1–2), 19-39, doi:http://dx.doi.org/10.1016/j.tecto.2006.04.018.

Audemard, F. A. (2007), Revised seismic history of the El Pilar fault. Northeastern Venezuela. From the Cariaco 1997 earthquake and recent preliminary paleoseismic results. *Journal of Seismology*, 11 (3), 311–326.

Audemard, F. A. (2009), Key issues on the post-Mesozoic southern Caribbean plate boundary, *in* Gloaguen, R., and Ratschbacher, L., eds., Growth and Collapse of the Tibetan Plateau: *Geological Society of London Special Publication*, 328, 569–586, doi:10.1144/SP328.23.

Audemard, F. A., et al. (2007), La depresión submarina de Guaracayal, estado Sucre, Venezuela: Una barrera para la propagación de la ruptura cosísmica a lo largo de la falla de El pilar, *Interciencia*, *32*, 735-741.

Audemard, F. A., G. Romero, H. Rendon, and V. Cano (2005), Quaternary fault kinematics and stress tensors along the southern Caribbean from fault-slip data and focal mechanism solutions, *Earth-Science Reviews*, *69*(3-4), 181-233, doi:10.1016/j.earscirev.2004.08.001.

Audemard, F. A., M. N. Machette, J. W. Cox, R. L. Dart, and K. M. Haller (2000), Map of Quaternary Faults of Venezuela, *USGS Open-File report 00-0018*.

Audemard,, F. A. (2011), Multiple-trench investigations across the newly ruptured segment of the El Pilar fault in northeastern Venezuela after the 1997 Cariaco earthquake, *Geological Society of America Special Papers*, *479*, 133-157, doi:10.1130/2011.2479(06).

Barbot, S., Y. Fialko and D. Sandwell (2008), Effect of a compliant fault zone on the inferred earthquake slip distribution, *J. Geophys. Res.*, 113, B06404, doi:10.1029/2007JB005256.

Barbot, S., Y. Fialko and D. Sandwell (2009), Three-dimensional models of elasto-static deformation in heterogeneous media, with applications to the Eastern California Shear Zone, *Geophys. J. Int.*, 179, 500-520.

Baumbach, M., H. Grosser, G. Romero Torres, J. L. Rojas Gonzales, M. Sobiesiak, and W. Welle (2004), Aftershock pattern of the July 9, 1997 Mw=6.9 Cariaco earthquake in Northeastern Venezuela, *Tectonophysics*, *379*(1-4), 1-23.

Baumbach, M., H. Grosser, G. Romero, J. Rojas and M. Sobiesiak (1999), Aftershock studies of the July 9, 1997, Cariaco earthquake: *American Geophysical Union 1999 Spring Meeting*, Boston: Eos (Transactions, American Geophysical Union), 80, 17, supplement S226, abstract S42A-01.

Beltrán, C., (1994), Trazas activas y síntesis neotectónica de Venezuela a escala 1:2.000.000, *in Proceedings, 7th Congreso Venezolano de Geofísica*: Caracas, p. 541–547.

Beltrán, C., A. Singer, and J. A. Rodríguez (1996), The El Pilar fault active trace (northeastern Venezuela): Neotectonic evidences and paleoseismic data, *in Proceedings, 3rd International Symposium on Andean Geodynamics*, Saint-Malo, France, 153–156.

Beltrán, C., and C. Giraldo (1989), Aspectos neotectónicos de la región nororiental de Venezuela, *in VII Congreso Geológico Venezolano*, Caracas, Venezuela, Barquisimeto, 3, 999–1021.

Beltrán, C., compiler (1993), Mapa Neotectónico de Venezuela: Caracas, Venezuela, Fundación Venezolana de Investigaciones Sismológicas, scale 1:2,000,000.

Ben-Zion, Y. and C. G. Sammis, (2003), Characterization of fault zones. *Pure Appl. Geophys.*, 160, 677–715, doi:10.1007/PL00012554.

Ben-Zion, Y., Z. Peng, D. Okaya, L. Seeber, J. G. Armbruster, N. Ozer, A. J. Michael, S. Baris, and M. Aktar (2003), A shallow fault-zone structure illuminated by trapped waves in the Karadere–Duzce branch of the North Anatolian Fault, western Turkey, *Geophysical Journal International*, *152*(3), 699-717, doi:10.1046/j.1365-246X.2003.01870.x.

Beutler, G., M. Rothacher, S. Schaer, T. A. Springer, J. Kouba, and R.E. Neilan (1999), The International GNSS Service (IGS): An interdisciplinary service in support of Earth sciences, *Advances in Space Research*, 23, 631-653.

Bouchon, M. (1997), The state of stress on some faults of the San Andreas System as inferred from near-field strong motion data, Journal of Geophysical Research: Solid Earth, 102(B6), 11731-11744, doi:10.1029/97JB00623.

Bürgmann, R., D. Schmidt, R. M. Nadeau, M. d'Alessio, E. Fielding, D. Manaker, T. V. McEvilly, and M. H. Murray (2000), Earthquake Potential Along the Northern Hayward Fault, California, Science, 289(5482), 1178-1182, doi:10.1126/science.289.5482.1178.

Byerlee, J. (1993), Model for episodic flow of high-pressure water in fault zones before earthquakes, *Geology,* 21, 303–306.

Chen, Q. and J. T. Freymueller (2002), Geodetic evidence for a near-fault compliant zone along the San Andreas Fault in the San Francisco Bay Area, *Bull. Seismol. Soc. Am.*, 92 (2), 656–671.

Chéry, J., 2008. Geodetic strain across the San Andreas Fault reflects elastic plate thickness variations (rather than fault slip rate). *Earth Planet. Sci. Lett.* 269, 352–365.

Chester, F. M. and J. S. Chester (1998), Ultracataclasite structure and friction processes of the Punchbowl fault, San Andreas system, California, *Tectonophysics,* 295, 199–221, doi:10.1016/S0040-1951(98)00121-8.

Christeson, G. L., P. Mann, A. Escalona, and T. J. Aitken (2008), Crustal structure of the Caribbean–northeastern South America arc-continent collision zone, J. Geophys. Res., 113(B8), B08104, doi:10.1029/2007jb005373.

Clark, S. A., C. A. Zelt, M. B. Magnani, and A. Levander (2008), Characterizing the Caribbean-South American plate boundary at 64°W using wide-angle seismic data, J. Geophys. Res., 113(B7), B07401, doi:10.1029/2007jb005329.

Cochran, E., Y.-G. Li, P. Shearer, S. Barbot, Y. Fialko and J. Vidale (2009), Seismic and geodetic evidence for extensive, long-lived fault damage zones, *Geology,* 37(4), 315–318.

Dach, R. and P. Walser (2013), Bernese GPS Software, Version. 5.2, Astronomical Institute, University of Bern.

DeMets, C., P. E. Jansma, G. S. Mattioli, T. H. Dixon, F. Farina, R. Bilham, E. Calais, and P. Mann (2000), GPS geodetic constraints on Caribbean-North America Plate Motion, *Geophys Res Lett*, *27*(3), 437-440, doi:10.1029/1999GL005436.

Diao, F., X. Xiong, and R. Wang (2011), Mechanisms of Transient Postseismic Deformation Following the 2001 Mw 7.8 Kunlun (China) Earthquake, *Pure and Applied Geophysics*, *168*(5), 767-779, doi:10.1007/s00024-010-0154-5.

Diao, F., X. Xiong, R. Wang, Y. Zheng, and H. Hsu (2010), Slip model of the 2008 Mw 7.9 Wenchuan (China) earthquake derived from the coseismic GPS data, *Earth Planets Space* 62, 869–874.

Dor, O., Y. Ben-Zion, T. Rockwell and J. Brune (2006), Pulverized rocks in the Mojave section of the San Andreas Fault Zone, *Earth Planet. Sci. Lett.*, 245, 642–654.

Duan, B. (2011), Reply to comment by Y. Fialko on "Deformation of compliant fault zones induced by nearby earthquakes: Theorical investigations in two dimensions", *J. geophys. Res.*,116, B12302, doi:10.1029/2011JB008567.

Faulkner, D., A. Lewis and E. Rutter (2003), On the internal structure and mechanics of large strike-slip faults: Field observations from the Carboneras fault, southeastern Spain, *Tectonophysics*, 367, 235–251.

Fialko, Y. (2004), Probing the mechanical properties of seismically active crust with space geodesy: study of the co-seismic deformation due to the 1992 *Mw*7.3 Landers (Southern California) earthquake, *J. geophys. Res.*,109, B03307, doi:10.1029/2003JB002756.

Fialko, Y., D. Sandwell, D. Agnew, M. Simons, P. Shearer, and B. Minster (2002), Deformation on Nearby Faults Induced by the 1999 Hector Mine Earthquake, *Science*, *297*(5588), 1858-1862.

Fulton, P. M., G. Schmalzle, R. N. Harris, and T. Dixon (2010), Reconciling patterns of interseismic strain accumulation with thermal observations across the Carrizo segment of the San Andreas Fault, *Earth and Planetary Science Letters*, *300*(3–4), 402-406, doi:http://dx.doi.org/10.1016/j.epsl.2010.10.024.

González, J., M. Schmitz, F. A. Audemard, R. Contreras, A. Mocquet, J. Delgado and F. De Santis (2004), Site effects of the 1997 Cariaco, Venezuela earthquake, *Engin. Geol.*, 72, 143-177.

Grosser, H., A. Rietbrock, M. Baumbach, G. Romero Torres, and J. Rojas (2001), Seismic tomography in the aftershock region of the Cariaco earthquake 1997, *Eos Trans. AGU 82* (47) (Fall Meet. Suppl., Abstract S32E-03).

Hamiel, Y. and Y. Fialko (2007), Structure and mechanical properties of faults in the North Anatolian Fault system from InSAR observations of coseismic deformation due to the 1999 Izmit (Turkey) earthquake, *J. geophys. Res.*, 112, B07412, doi:10.1029/2006JB004777.

Houlié, N. and B. Romanowicz (2011), Asymmetric deformation across the San Francisco Bay Area faults from GPS observations in northern California, *Phys. Earth Planet. Inter.*, 184, 143-153.

Hugentobler, U., S. Schaer, P. Fridez, G. Beutler, H. Bock, E. Brockmann, R. Dach, W. Gurtner, D. Ineichen, J. Johnson, M. Meindl, L. Mervart, M. Rothacher, T. Springer, and R. Weber (2001), Bernese GPS Software, Version 4.2, University of Bern.

Jacome, M. I., N. Kusznir and S. Flint (1999), Structural and isostatic modelling of Serranía del Interior thrust belt and Monagas foreland basin: Eastern Venezuela. *Fourth International Symposium on Andean Geodynamics Göttingen (Germany)*, Oct. 4 –6, pp. 367–371. Extended abstract.

Jolivet, R., R. Bürgmann and N. Houlié (2009), Geodetic exploration of the elastic properties across and within the northern San Andreas Fault zone, *Earth and Planetary Science Letters* 288, 126–131.

Jolivet, R., R. Cattin, N. Chamot-Rooke, C. Lasserre and G. Peltzer (2008), Thin-plate modelling of interseismic deformation and asymmetry across the Altyn Tagh fault zone, *Geophys. Res. Lett.*, 35 (L02309).

Jouanne, F., F. A. Audemard, C. Beck, A. Van Welden, R. Ollarves, and C. Reinoza (2011), Present-day deformation along the El Pilar Fault in eastern Venezuela: Evidence of creep along a major transform boundary, *Journal of Geodynamics*, *51*(5), 398-410, doi:http://dx.doi.org/10.1016/j.jog.2010.11.003.

Kachanov, L. (1986), Introduction to Continuum Damage Mechanics, *Martinus Nijhoff Publishers*, Dordrecht.

King G. and C. Nostro (1999), Almond Lite v. 2.02: A program to calculate Coulomb stresses around rectangular faults or dykes, Manual d'Utilisation, Institute de Phisique du Globe, Paris.

Le Pichon, X., C. Kreemer and N. Chamot-Rooke (2005), Asymmetry in elastic properties and the evolution of large continental strike-slip faults, *J. Geophys. Res.* 110 (B03405).

Lees, J. M. and P. E. Malin (1990), Tomographic images of P-wave velocity variation, California, *J. Geophys. Res.*, 95, 21,793–21,804.

Li, Y., J. Vidale, K. Aki, C. Marone and W. Lee (1994), Fine-structure of the Landers fault zone—segmentation and the rupture process, *Science*, 265, 367–370.

Lindquist, K., K. Engle, D. Stahlke and E. Price (2004), Global Topography and Bathymetry Grid Improves Research Efforts, *Eos Trans. AGU*, 85(19), 186. Also in: http://www.agu.org/pubs/crossref/2004/2004EO190003.shtml

Liuzzi, D., M. Schmitz, M. Jácome and J. Sánchez (2006), Adelgazamiento de sedimentos Cretácicos-Oligocenos bajo la Serranía del Interior, Noreste de Venezuela: Evidencia a partir de observaciones de sísmica profunda, *IX Simposio Bolivariano de Exploración Petrolera en las Cuencas Subandinas, Cartagena, Colombia*. CD. 1-8.

Lyakhovsky, V., Y. Ben-Zion and A. Agnon (2001), Earthquake cycle, fault zones, and seismicity patterns in a rheologically layered lithosphere, *J. Geophys. Res.*, 106, 4103–4120.

Lyons, S. N., Y. Bock, and D. T. Sandwell (2002), Creep along the Imperial Fault, southern California, from GPS measurements, Journal of Geophysical Research: Solid Earth, 107(B10), 2249, doi:10.1029/2001JB000763.

Malservisi, R., K. P. Furlong, and T. H. Dixon (2001), Influence of the earthquake cycle and lithospheric rheology on the dynamics of the Eastern California shear zone, *Geophys. Res. Lett.*, *28*(14), 2731-2734.

Melbourne, W. G. (1985), The Case in GPS-Based Geodetic Systems, in Goad C.C. (ed), Proc. of First Int. sym. on Precise Position with GPS Rockville, Maryland, 373-386.

Mendoza, C. (2000), Rupture history of the 1997 Cariaco, Venezuela, earthquake from teleseismic P waves, *Geophys. Res. Lett.*, 27 (10) 1555-1158.

Metz, H. (1965), Geology of the El Pilar Fault Zone. State of Sucre, Venezuela, *IV Caribbean Geological Conference*, Trinidad, 293–298.

Minster, J. and T. Jordan (1978), Present-day plate motions, *J. Geophys. Res*, 83, 5, 331–335, 354.

Mocquet, A., C. Beltrán, M. Lugo, J. A. Rodriguez and A. Singer (1996), Seismological interpretation of the historical data related to the 1929 Cumaná earthquake, Venezuela, *Third International Symposium on Andean Geodynamics*, Saint-Malo (France), Sept. 17–19, 203– 206. Extended abstract.

Molnar, P. and L. Sykes (1969), Tectonics of the Caribbean and Middle America regions from focal mechanisms and seismicity, *Geological Society of America Bulletin*, 80, 1639–1684, doi:10.1130/0016-7606 (1969)80[1639:TOTCAM]2.0.CO;2.

Moore, D., D. A. Lockner, M. Shengli, R. Summers and J. Byerlee (1997), Strengths of serpentinite gouges at elevated temperatures, *J. geophys. Res.*,102, 14787–14801.

Motagh, M., B. Schurr, J. Anderssohn, B. Cailleau, T. R. Walter, R. Wang, and J.-P. Villotte (2010), Subduction earthquake deformation associated with 14 November 2007, Mw 7.8 Tocopilla earthquake in Chile: Results from InSAR and aftershocks, *Tectonophysics*, *490*(1–2), 60-68, doi:http://dx.doi.org/10.1016/j.tecto.2010.04.033.

Motagh, M., R. Wang, T. R. Walter, R. Bürgmann, E. Fielding, J. Anderssohn, and J. Zschau (2008), Coseismic slip model of the 2007 August Pisco earthquake (Peru) as constrained by Wide Swath radar observations, *Geophysical Journal International*, *174*(3), 842-848, doi:10.1111/j.1365-246X.2008.03852.x.

Okada, Y. (1985), Surface deformation due to shear and tensile faults in a half-space. *Bull. seism. Soc. Am.* **75** (4), 1135–1154.

Oskin, M. and A. Iriondo (2004), Large-magnitude transient strain accumulation on the Blackwater fault, Eastern California shear zone, *Geology*, 32, 313–316.

Ostini, L., R. Dach, M. Meindl, S. Schaer, and U. Hugentobler (2008), *FODITS:* A new tool of the Bernese GPS software, in *Proceedings of EUREF 2008 Symposium*, edited by Torres, J. A., and H. Hornik, Brussels, Belgium.

Paige, S. (1930), The earthquake at Cumaná, Venezuela, January 17, 1929, *Bulletin of the Seismological Society of America*, 20**,** 1-10.

Palma, M., F. Audemard and G. Romero, 2010, New focal mechanism solutions for Venezuela and neighbouring areas 2005–2008: importance of the National Seismological Network's density and distribution. Rev. Téc. Ing. Univ. Zulia 33, 1–14.

Peng, Z. and Y. Ben-Zion (2006), Temporal changes of shallow seismic velocity around the Karadere-Duzce branch of the north Anatolian fault and strong ground motion, *Pure Appl. Geophys.* 163, 567–600.

Pérez, O. J. (1998), Seismological report on the Mw = 6.8 strong shock of 9 July 1997 in Cariaco, northeastern Venezuela, *Bulletin of the Seismological Society of America, Short Notes*, 23, 2, 101–106.

Pérez, O. J., and Y. P. Aggarwal (1981), Present-day tectonics of the southeastern Caribbean and northeastern Venezuela, *J Geophys Res*, *86*(B11), 10791-10804, doi:10.1029/JB086iB11p10791.

Pérez, O. J., R. Bilham, R. Bendick, J. R. Velandía, N. Hernández, C. Moncayo, M. Hoyer, and M. Kozuch (2001b), Velocity Field Across the Southern Caribbean Plate Boundary and Estimates of Caribbean/South-American Plate Motion Using GPS Geodesy 1994-2000, *Geophys Res Lett*, *28*, doi:10.1029/2001gl013183.

Pérez, O. J., R. Bilham, R. Bendick, N. Hernández, M. Hoyer, J. R. Velandia, C. Moncayo and M. Kozuch (2001a), Velocidad relativa entre las placas del Caribe y Sudamérica a partir de observaciones dentro del sistema de posicionamiento global (GPS) en el norte de Venezuela, *Interciencia* 26 (2), 69–74.

Pindell, J. and L. Kennan (2007), Cenozoic kinematics and dynamics of oblique collision between two convergent plate margins: The Caribbean– South America collision in eastern Venezuela, Trinidad and Barbados, *in* Kennan, L., Pindell, J., and Rosen, N., eds., The Paleogene of the Gulf of Mexico and Caribbean Basins; Processes, Events, and Petroleum Systems: Proceedings, 27th Bob F. Perkins Research Conference, Gulf Coast Section of the Society of Economic Paleontologists and Mineralogists: Houston, Texas, Society of Economic Paleontologists and Mineralogists, 458–553.

Rodríguez, J. A. and C. A. Chacín (1996), Contribución al estudio del sismo de Cumaná año 1929, Compilación y notas. *Bol. Hist. Geocienc. Venez.* 2, 1 –77.

Romero, G., F. A. Audemard, H. Rendón and N. Orihuela (2002), Mapa de Soluciones Focales de Sismos Sentidos en Venezuela y Regiones Vecinas entre 1957 y 2002, *Edición Conmemorativa XXX Aniversario de FUNVISIS*, Caracas, FUNVISIS, scale ~1:2,450,000.

Savage, J. C., and R. O. Burford (1973), Geodetic determination of relative plate motion in central California, J. Geophys. Res., 78, 832–845, doi:10.1029/JB078i005p00832.

Schmalzle, G., T. Dixon, R. Malservisi, and R. Govers (2006), Strain accumulation across the Carrizo segment of the San Andreas Fault, California: Impact of laterally varying crustal properties, *Journal of Geophysical Research: Solid Earth*, *111*(B5), B05403, doi:10.1029/2005JB003843.

Scholz, C. H. (1988), The brittle-plastic transition and the depth of seismic faulting. *Geol. Runds.* **77,** 319–328.

Schubert, C. (1984), Basin formation along the Bocono-Moron-El Pilar Fault System, Venezuela, *J. Geophys. Res.*, *89*(B7), 5711-5718, doi:10.1029/JB089iB07p05711.

Singer, A., and F. A. Audemard (1997), Aportes de Funvisis al desarrollo de la geología de fallas activas y de la paleosismología para los estudios de amenaza y riesgo sísmico, *in* Grases, J., ed., *Diseño Sismorresistente: Especificaciones y Criterios Empleados en Venezuela*, Academia de las Ciencias Naturales, Matemáticas y Físicas Publicación Especial 33, 25–38.

Smith-Konter, B., D. Sandwell and P. Shearer (2011), Locking depths estimated from geodesy and seismology along the San Andreas Fault System: Implications for seismic moment release, *J. Geophys. Res.*, 116, B06401.

Soulas, J.-P., (1986), Neotectónica y tectónica activa en Venezuela y regiones vecinas, *Proceedings of 6th Congreso Geológico Venezolano* (1985): Caracas, Venezuela, 10, 6639–6656.

Speed, R., R. Russo, J. Weber and K. C. Rowley (1991), Evolution of Southern Caribbean plate boundary, vicinity of Trinidad and Tobago, *The American Association of Petroleum Geologists Bulletin*, 75, 11, 1789–1794.

Stephan, J.-F. (1982), Evolution Géodinamique du Domaine Caraïbe, Andes et Chaîne Caraïbe sur la Transversale de Barquisimeto (Vénézuéla) [Ph.D. thesis]: Brest, France, Université de Bretagne Occidentale, 512 pp.

Thurber, C., S. Roecker, K. Roberts, M. Gold, L. Powell, and K. Rittger (2003), Earthquake locations and three-dimensional fault zone structure along the creeping section of the San Andreas fault near Parkfield, CA: Preparing for SAFOD, *Geophys Res Lett*, *30*(3), 1112, doi:10.1029/2002GL016004.

Turcotte, D., W. Newman and R. Shcherbakov (2003), Micro and macroscopic models of rock fracture, *Geophys. J. Int.*, 152, 718–728.

Unsworth, M. J., P. E. Malin, G. D. Egbert and J. R. Booker (1997), Internal structure of the San Andreas fault at Parkfield, California, *Geology* 25, 359–362.

Van Daele, M., et al. (2011), Reconstruction of Late-Quaternary sea- and lake-level changes in a tectonically active marginal basin using seismic stratigraphy: The Gulf of Cariaco, NE Venezuela, *Marine Geology*, *279*(1–4), 37-51, doi:10.1016/j.margeo.2010.10.011.

Vierbuchen, R.C. (1984), The geology of the El Pilar fault zone and adjacent areas in northeastern Venezuela. In: Bonini, W.E., Hargraves, R.B., Shagam, R. (Eds.), The Caribbean –South America boundary and regional tectonics. *Geol. Soc. Am.*, Memoir 162. Boulder, CO, 189– 212.

Wang, L., R. Wang, F. Roth, B. Enescu, S. Hainzl, and S. Ergintav (2009), Afterslip and viscoelastic relaxation following the 1999 M 7.4 İzmit earthquake from GPS measurements, *Geophysical Journal International*, *178*(3), 1220-1237, doi:10.1111/j.1365-246X.2009.04228.x.

Wang, R., B. Schurr, C. Milkereit, Z. Shao, and M. Jin (2011), An Improved Automatic Scheme for Empirical Baseline Correction of Digital Strong-Motion Records, *Bulletin of the Seismological Society of America*, *101*(5), 2029-2044, doi:10.1785/0120110039.

Wang, R., S. Parolai, M. Ge, M. Jin, T. R. Walter, and J. Zschau (2013), The 2011 Mw 9.0 Tohoku Earthquake: Comparison of GPS and Strong-Motion Data, *Bulletin of the Seismological Society of America*, *103*(2B), 1336-1347, doi:10.1785/0120110264.

Wdowinski, S. (2009), Deep creep as a cause for the excess seismicity along the San Jacinto fault, *Nature Geoscience*, 2, 882 – 885.

Weber, J. C., J. Saleh, S. Balkaransingh, T. Dixon, W. Ambeh, T. Leong, A. Rodriguez, and K. Miller (2011), Triangulation-to-GPS and GPS-to-GPS geodesy in Trinidad, West Indies: Neotectonics, seismic risk, and geologic implications, *Marine and Petroleum Geology*, *28*(1), 200-211, doi:http://dx.doi.org/10.1016/j.marpetgeo.2009.07.010.

Weber, J. C., T. H. Dixon, C. DeMets, W. B. Ambeh, P. Jansma, G. Mattioli, J. Saleh, G. Sella, R. Bilham, and O. Pérez (2001), GPS estimate of relative motion between the Caribbean and South American plates, and geologic implications for Trinidad and Venezuela, *Geology*, *29*(1), 75-a-78, doi:10.1130/0091-7613.

Weertman, J. and J. Wertman (1964), Elementary Dislocation Theory, The Macmillan Company, New York. 213 pp.

Wilson, B., T. Dewers, Z. Reches, and J. Brune (2005), Particle size and energetics of gouge from earthquake rupture zones, *Nature*, *434*(7034), 749-752.

Wübbena, G. (1985), Software Development for Geodetic Positioning with GPS Using TI 4100 Code and Carrier Measurements, in Goad C.C. (ed), Proc. of First Int. sym. on Precise Position with GPS Rockville, Maryland, pp.403-412.

Xu, C., Y. Liu, Y. Wen, and R. Wang (2010), Coseismic Slip Distribution of the 2008 Mw 7.9 Wenchuan Earthquake from Joint Inversion of GPS and InSAR Data, *Bulletin of the Seismological Society of America, 100*(5B), 2736-2749, doi:10.1785/0120090253.

## CHAPTER 7:

# ASYMMETRY IN ELASTIC PROPERTIES AND CREEP ALONG MAIN FAULTS IN TRINIDAD

This chapter is presented as a first version of a paper to be submitted in a few months.

C. Reinoza[1, 2], F. Jouanne[1], F.A. Audemard[2]

[1] Université de Savoie Mont Blanc, ISTerre, F-73376 Le Bourget du Lac, France

[2] Venezuelan Foundation for Seismological Research, FUNVISIS, El Llanito, Caracas 1070, Venezuela

**Abstract**

From the compilation of GNSS observations and triangulation-to-GPS comparison of previous studies, we constrain the kinematic of the Central Range Fault (CRF) in Trinidad, as well as the kinematic of the Arima Fault (AF), Los Bajos Fault (LBF), the South Darien Ridge Fault (SDRF) and Warm Springs Fault (WSF). Geodetic velocity field across the CRF points out an asymmetry of velocity gradient on both sides of the fault. To simulate velocities, we test a heterogeneous asymmetric model that point out a 1.5 km locking depth with a 0.20 asymmetric coefficient indicating that the northern side has a rigidity ~3.3 times higher to the southern side. The shallow locking depth is associated to creep in the upper part of the fault. Based on a slip distribution model, used for modelling the main faults in Trinidad, a creep of 12 mm/yr was observed in the southeastward onshore portion of the CRF and the WSF, whereas along the northeastward of CRF onshore and offshore portion a significant decrease of slip is observed in the upper part of the fault. The upper and lower part of the AF appears locked in the onshore portion demonstrating that this alleged prolongation of the El Pilar Fault (EPF) is currently inactive. Furthermore, Los Bajos Fault is affected by a 7 mm/yr slip in the segment upon which

the EPF transfers its slip eastward to the Warm Springs- Central Range Fault system and that act as a synthetic Riedel shears.

## 1. Introduction

Trinidad and Tobago represents the most southeastern part of the complex plate-boundary zone of the Caribbean, South America and Atlantic plates. The purpose of this work is focus on the main faults across of this two-island nation: The Central Range Fault (CRF) that is the principal active structure that accommodates at least 60 % of the total rate of strike-slip motion (~20 mm/yr) at the Caribbean-South American plate boundary in Trinidad (Weber et al., 2011), the Arima Fault (AF), the Los Bajos Fault (LBF), the South Darien Ridge Fault (SDRF) and the Warm Springs Fault (WSF). Geodetic studies developed in recent years have allowed indicating that the AF in northern Trinidad is currently accommodating no right-lateral motion within the error of the measurements *(Saleh et al., 2004; Rodríguez et al., 2008; Weber et al., 2011)*. In fact, the reverse Arima fault of northern Trinidad that bounds the southern foothills of the Northern range of Trinidad could be not considered as the eastward prolongation of the El Pilar Fault (EPF) but of the reverse Tunapuy fault in the Paria peninsula *(Beltrán, 1998; Audemard, 2000; Audemard et al., 2005).*

Despite the lack of historical seismicity on the CRF since the arrival of the first Europeans (*Robson, 1964*); results from paleoseismic investigation in Central Trinidad demonstrate that the CRF ruptured the ground surface most recently between 2710 and 550 yr B.P. (*Prentice et al. 2010*). The tectonic activity associated to the active traces of the main faults in Trinidad has been also supported by tectonic geomorphology research (*Weber and Ritter, 2007; Ritter and Weber, 2007*) and analysis of offshore reflection seismics (*Soto et al., 2007, 2011, Garciacaro et al., 2011 a, b*).

In this study, an integration of data was carried out including the repeat GPS data collected between 1994 and 2005 *(Rodríguez et al., 2008; Weber et al., 2011*) and 1901–1903

to 1994–1995 triangulation-to-GPS comparison (*Saleh et al., 2004; Weber et al., 2011*). Several modellings with different approaches are evaluated to understand the current deformation of Trinidad and Tobago.

## 2. Data collection

Data from previous geodetic investigations was compiled for this study (*Saleh et al., 2004; Rodríguez, 2008; Weber et al., 2011*). Observed velocities of 16 sites from repeat GPS data collected between 1994 and 2005 were included (*Rodríguez et al., 2008; Weber et al., 2011*). In the original work, the velocities were done in IGSb00, which is approximately equivalent to the global ITRF2000 reference frame (*Boucher et al., 2004*). The velocities were transformed into stable South American reference frame of *Weber et al.* (2001; $_{igsb00}\omega_{SA}$=-21.49; -123.08; 0.1089 ± 0.0022). A second set of 1901–1903 to 1994–1995 triangulation-to-GPS site coordinates and velocities was taken in consideration (*Saleh et al., 2004; Weber et al. 2011*). This set of data is shown originally with 20±3 mm/yr Ve added to transform velocities from fixed Northern Range reference frame of Saleh et al. (2004) into stable South American reference frame of *Weber et al*. (2001). After integration of two set of data, three stations were identified as common: MTTB, LFAB and, GSPO with 0069, 0115 and, 0145 respectively. Assuming a lack of temporal velocities variations between 1901 and 2005 and that the scale of the 1901-1903 triangulation is well defined, we have fitted the triangulation reference frame velocities to South American reference frame site velocities at the three common sites (0069, 0115, 0145), with a relative rotation pole defined by lat 61.11°, lon 190.70° and -8.0438°/My. Next, this relative pole rotation was applied to the rest of triangulation-to-GPS velocities to homogenize all values to stable South American reference frame (Table 1).

**Table 1.** Velocities of sites in Trinidad and Tobago expressed in South American reference frame (*Weber et al. 2011*).

| Station | Long (deg) | Lat (deg) | Ve (mm/yr) | Vn (mm/yr) | σVe (mm/yr) | σVn (mm/yr) |
|---|---|---|---|---|---|---|
| **1901-1903 to 1994-1995 triangulation-to-GPs sites** | | | | | | |
| 8 | 10.68205 | -61.30932 | 16.95 | 0.00 | 3.0 | 0.2 |
| 12 | 10.70822 | -61.24515 | 16.55 | 0.91 | 3.1 | 0.5 |
| 19 | 10.6493 | -61.28665 | 17.21 | 0.45 | 3.0 | 0.2 |
| 33 | 10.71458 | -61.63158 | 11.82 | -0.04 | 3.1 | 0.3 |
| 64 | 10.47837 | -61.11556 | 17.98 | 3.94 | 3.7 | 2.2 |
| 72 | 10.79187 | -61.30765 | 13.98 | 0.18 | 3.1 | 0.9 |
| 82 | 10.29387 | -61.01533 | 13.25 | 6.43 | 4.8 | 4.2 |
| 99 | 10.5258 | -61.2842 | 16.05 | 3.98 | 3.3 | 2.1 |
| 128 | 10.74432 | -60.97848 | 18.52 | 4.63 | 4.8 | 2.2 |
| 135 | 10.14272 | -61.31169 | 2.13 | 8.07 | 4.2 | 4.5 |
| 141 | 10.19054 | -61.59507 | 2.31 | -1.09 | 4.5 | 4.4 |
| 210 | 10.66887 | -61.5126 | 13.98 | 0.10 | 3.1 | 0.4 |
| 321 | 10.4029 | -61.39142 | 12.08 | 0.01 | 3.4 | 2.4 |
| 400 | 10.0834 | -61.34146 | 2.07 | 5.52 | 4.5 | 5.0 |
| 472 | 10.20821 | -61.15336 | -2.50 | 11.28 | 5.4 | 6.2 |
| 590 | 10.12893 | -61.5492 | 4.13 | 2.78 | 4.5 | 4.9 |
| 1031 | 10.49572 | -61.06795 | 15.42 | -9.49 | 3.9 | 2.2 |
| 1072 | 10.4128 | -61.15573 | 8.45 | 1.43 | 3.7 | 2.6 |
| 1267 | 10.69746 | -61.53909 | 13.37 | 0.09 | 3.1 | 0.3 |
| 1400 | 10.39308 | -61.33273 | 14.09 | 4.28 | 3.4 | 2.4 |
| 1401 | 10.47065 | -61.19718 | 17.61 | 3.50 | 3.4 | 2.0 |
| 1402 | 10.3341 | -60.99753 | 10.43 | 2.93 | 4.8 | 4.0 |
| **GPS sites observed between 1994 and 2005** | | | | | | |
| BNKR | 10.339 | -61.459 | 14.23 | -0.72 | 4.7 | 5.5 |
| CAMB | 11.32 | -60.556 | 23.87 | 10.59 | 1.5 | 2.3 |
| FTMD | 11.154 | -60.843 | 26.47 | 18.22 | 1.2 | 3.8 |
| GSPO (0145)* | 10.334 | -61.423 | 1.92 | -0.23 | 1.1 | 2.0 |
| LFAB (0115)* | 10.098 | -61.658 | 3.51 | 1.40 | 1.2 | 1.1 |
| MAYO | 10.359 | -61.364 | 5.22 | -4.83 | 1.2 | 1.9 |
| MTTB (0069)* | 10.681 | -61.396 | 17.95 | 2.17 | 1.4 | 1.2 |
| PALM | 10.292 | -61.406 | 5.32 | -4.83 | 4.4 | 5.2 |
| PLND | 10.191 | -61.602 | 2.42 | -4.71 | 6.7 | 3.7 |
| PUND | 10.377 | -61.418 | 15.53 | -2.93 | 3.4 | 2.2 |
| SMRY | 10.185 | -61.311 | 1.11 | -3.54 | 8.0 | 3.2 |
| SNDO | 10.28 | -61.459 | 1.02 | -2.32 | 7.1 | 2.6 |
| SRUX | 10.653 | -61.4 | 17.35 | 2.37 | 1.0 | 0.7 |
| TANK | 10.395 | -61.438 | 17.63 | -1.33 | 3.0 | 3.3 |
| TTPA | 10.594 | -61.347 | 15.34 | 0.97 | 4.8 | 3.1 |
| WESS | 10.333 | -61.425 | 3.02 | -6.03 | 1.7 | 3.5 |

(*) Common sites used for the fitting of stable South American reference frame.

### 3. Velocity field in Trinidad and simple elastic half-space model

From the velocity field depicted in Trinidad Island (Figure 1) one can observe at least two main patterns. Most stations north of the CRF show faster velocities than the southern stations. On the north side of CRF the velocities are constant around the AF (The alleged EPF eastward projection) and systematically decrease southward. The south side of CRF show a pattern more heterogeneous. The sites of GPS-GPS comparison move constantly to the southeast, except for the LFAB (0115) site that moves with a northeast direction. On the other hand, the triangulation-to-GPS sites show a behavior more varied in the south side without a preferable direction and sense. In any case, the major gradient in the velocity field occurs across the right-lateral strike-slip CRF and the AF apparently shows no strike-slip accommodation.

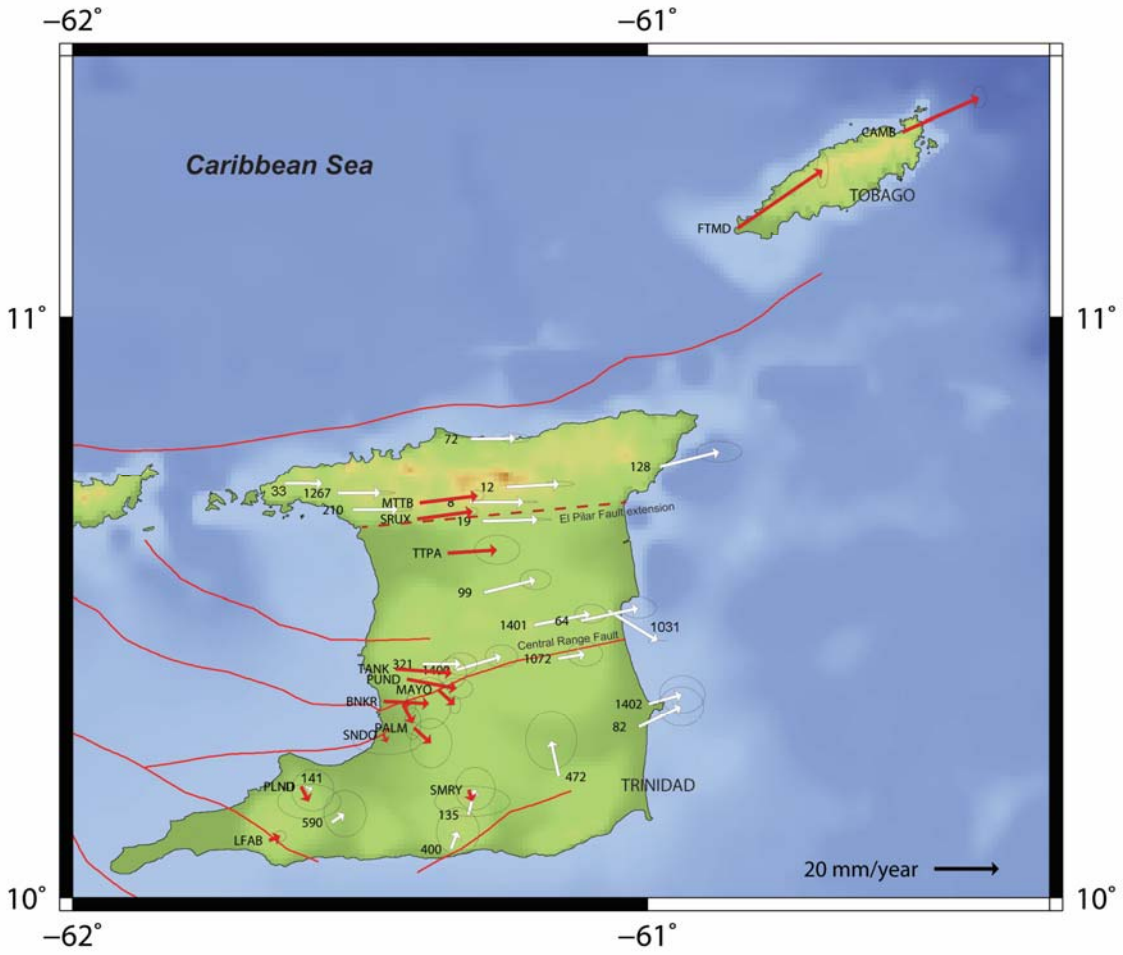

**Figure 1.** Observed velocities from repeat GPS data collected between 1994 and 2005 (red arrows) and 1901–1903 to 1994–1995 triangulation-to-GPS (white arrows) with error ellipses for 66% confidence level expressed in South American reference frame. The active faults in northeastern Venezuela and Trinidad are from *Audemard et al. (2000)* and *Weber et al. (2011*). Topography and bathymetry data are from *Lindquist et al.* (2004).

Interseismic deformation for a vertical infinite strike-slip fault (*Savage and Burford et al., 1973*) is given by the relation (eq. 1)

$$v(x) = \frac{V_T}{\pi} \tan^{-1}\left(\frac{x}{D}\right) \quad \text{(eq. 1)}$$

where v(x) is the velocity at a distance x from the fault, $V_T$ is the far-field velocity and D is the locking depth of the fault. To evaluate the quality of our models, we calculate an RMS or the quadratic mean value of the misfit (eq. 4), as follows:

$$RMS = \sqrt{\frac{1}{N}\sum\left(\frac{(Vpar_{obs} - Vpar_{model})^2}{\sigma^2_{Vpar-obs}}\right)} \qquad \text{(eq. 2)}$$

where $\sigma^2_{Vpar-obs}$ is the variance on the observations, $Vpar_{obs}$ is the fault-parallel component velocity from velocities in Trinidad and Tobago (based in the Table 1) and $Vpar_{model}$ is the simulated velocity and N is the number of stations.

The best simulation of velocities considering the CRF as a single active fault is obtained for a locking depth of 8.2 km considering 18 mm/yr far-field velocity. It must be underlined that the adjustment of observed and simulated velocities is really poor with a RMS of 2.605 (Figure 2a). It was calculated for a set of 36 stations. In the case of the AF this simple model predicts a locking depth of 26 km considering a 33 mm/yr far-field velocity. The adjustment of observed and simulated velocities is also poor (Figure 2b). A RMS value of 1.806 was calculated for a set of 38 stations that include FTMD and CAMB sites in Tobago Island.

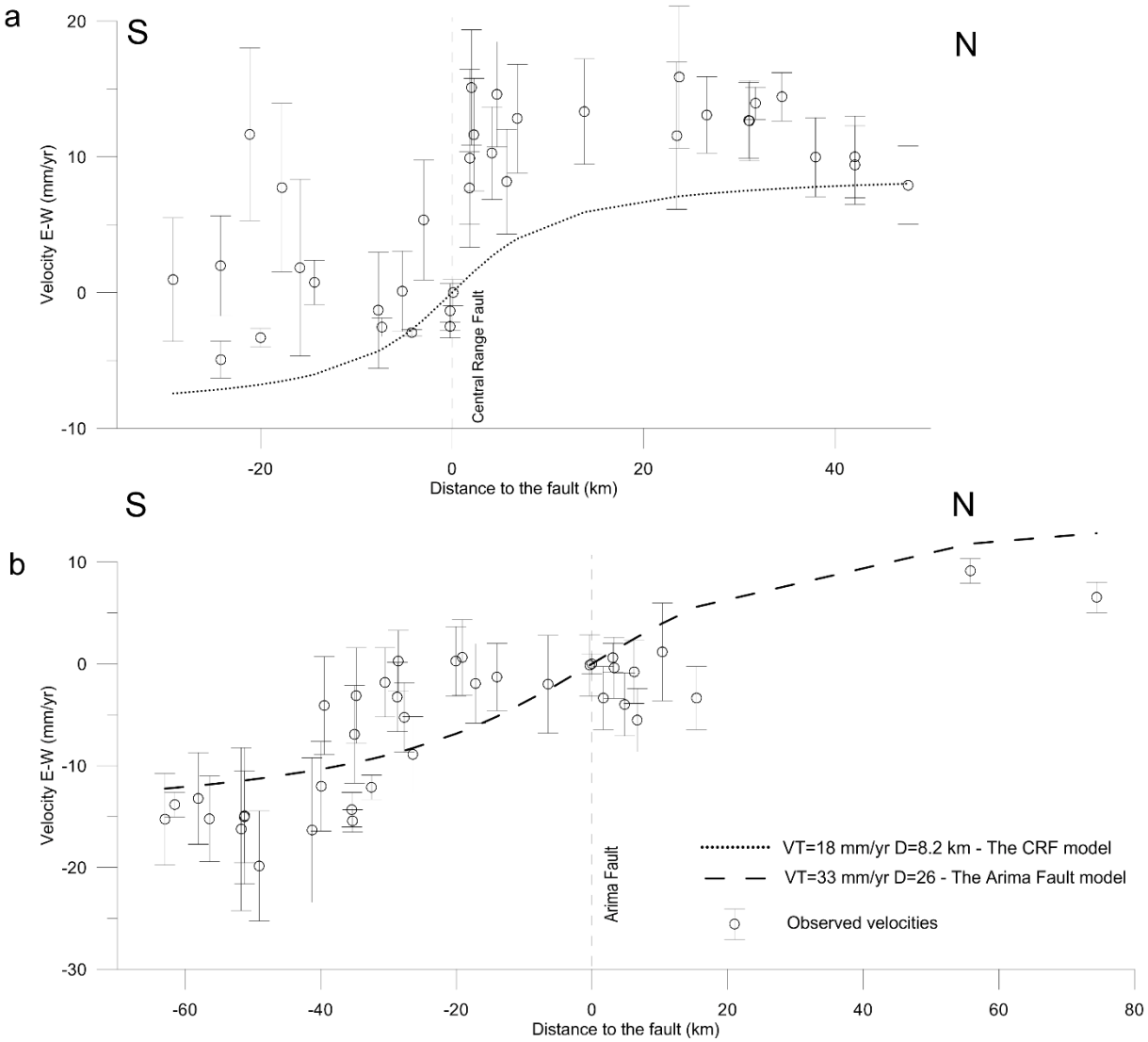


**Figure 2.** E-W observed velocities (relative to the fault) and fault–perpendicular velocity showing the acceptable models from the homogeneous model in (a) the Central Range Fault and (b) the Arima Fault (The alleged EPF eastern prolongation).

## 4. Modelling approaches

In order to better simulate the current velocities measured in Trinidad, we tested several models: change of elastic properties in both sides of the CRF and the Arima Fault, and a heterogeneous slip distribution model along the main faults.

### 4.1. Change of elastic properties

The change of elastic properties model is based on a single vertical strike-slip fault separating two geologic terrains of contrasting properties. A half-space model modification (*Jolivet et al.*, 2009) to the asymmetric dislocation model proposed by *Le Pichon et al*. (2005) is applied to calculate an asymmetric surface velocity field on each side of the vertical fault located at x=0 (eqs. 3 and 4). This simplification aims at reducing three parameters: the rigidity contrast between the two sides of the fault, the far-field velocity, and the horizontal offset between the basal shear zone and the surface fault,

$$v(x) = \frac{2\mathrm{KV}_T}{\pi}\tan^{-1}(\frac{x}{D}); x < 0 \quad \text{(eq. 3)}$$

$$v(x) = 2(1-K)\frac{V_T}{\pi}\tan^{-1}(\frac{x}{D}); x \geq 0 \qquad \text{(eq. 4)}$$

where v(x) is the velocity at a distance x from the fault, $V_T$ is the far-field velocity and D is the locking depth of the fault. The asymmetry coefficient K= V1/(V1+ V2); K = V1/ $V_T$ ranges from 0 to 1 and can also be expressed as $E_2/(E_1 + E_2)$ . The equations 1 and 2 are equivalents for K=0.5, that meaning no rigidity contrast.

#### 4.1.1. Asymmetric model in the Central Range Fault

The best-fit for an unconstrained model suggests a far-field velocity of 15 mm/yr with 0.25 km locking depth and an asymmetry ratio of 0.21 (Figure 3 a, b, c, 4). However, we evaluate two possibilities starting from the two following sets of conditions: 1) a far-field velocity constrained in 20 mm/yr (Figure 3d, 4) that shows a 1.5 km locking depth with a K ratio of 0.20 and 2) a second test fixing the locking depth at 10 km, according to a more standard valued used in previous models for this fault by *Webber et al.* (2011). In this last case, results show 24 mm/yr of far-field velocity and an asymmetry ratio of 0.31 (Figure 3e). According to

the figure 5, fault-perpendicular profiles for all asymmetric models show a good correlation and generally better than the previous homogeneous model.

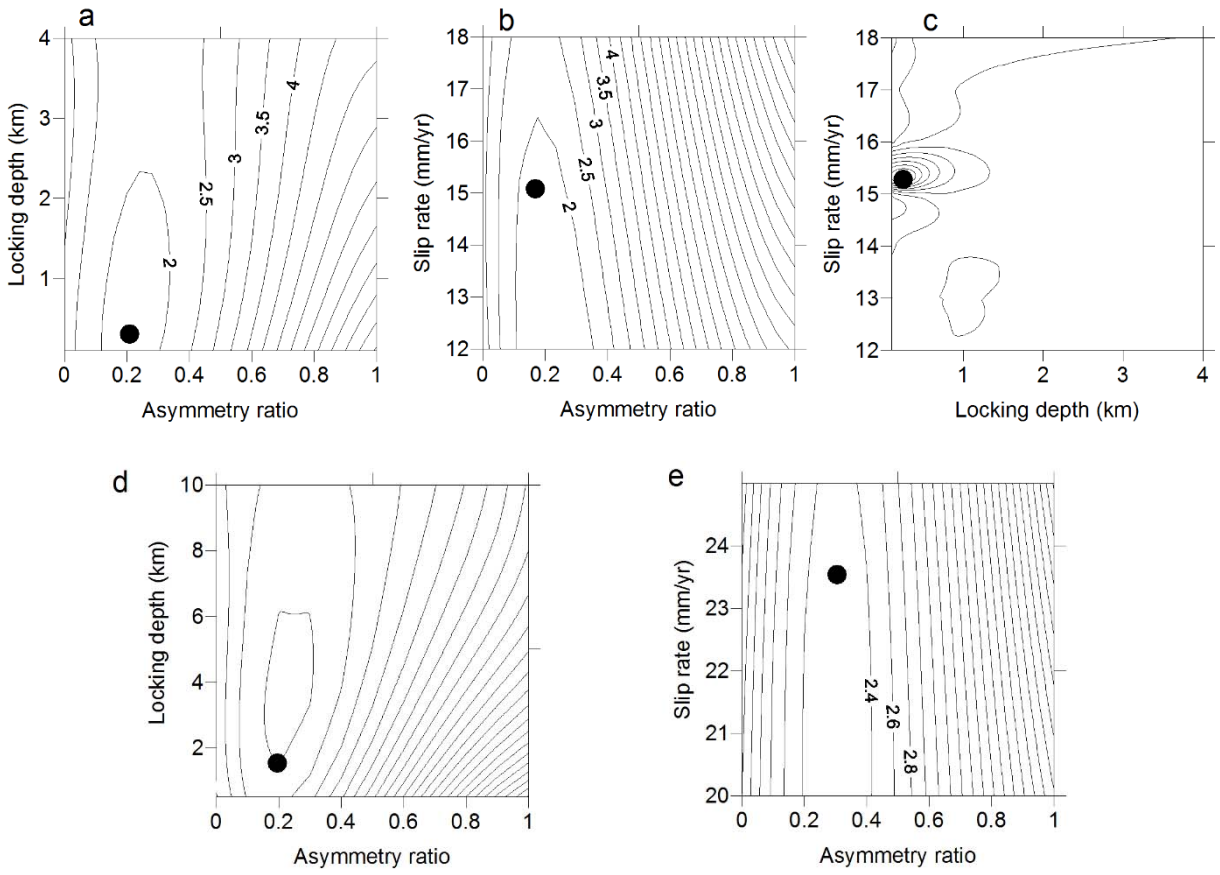


**Figure 3.** Trade-off between (a) the asymmetry ratio and locking depth, (b) asymmetry ratio and slip rate, and (c) locking depth versus slip rate for the unconstrained model on the CRF with a $V_T$=15 mm/yr, D=0.25 km and, K=0.21). (d) Trade-off between the asymmetry ratio and the locking depth on the CRF for the model with far-field velocity fixed at 20 mm/yr. (e) Trade-off between the asymmetry ratio and the slip rate on the CRF for the model with locking depth fixed at 10 km. Contoured values are the RMS values and the black dot indicates the best model.

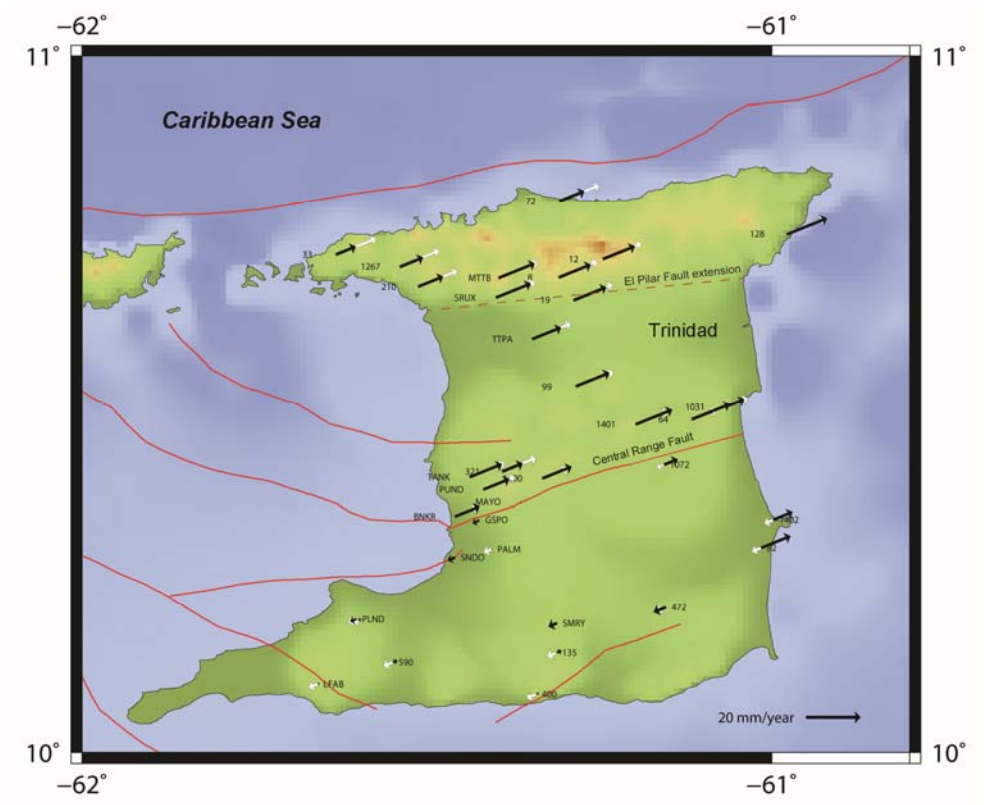


**Figure 4.** Fault-parallel observed velocities (white arrows) and simulated velocities (black arrows) from the asymmetric modeling on CRF for 20 mm/yr far-field velocity. All displacements are based on Trinidad and Tobago observed velocities from Table 1 and relative to MAYO site close to the fault.

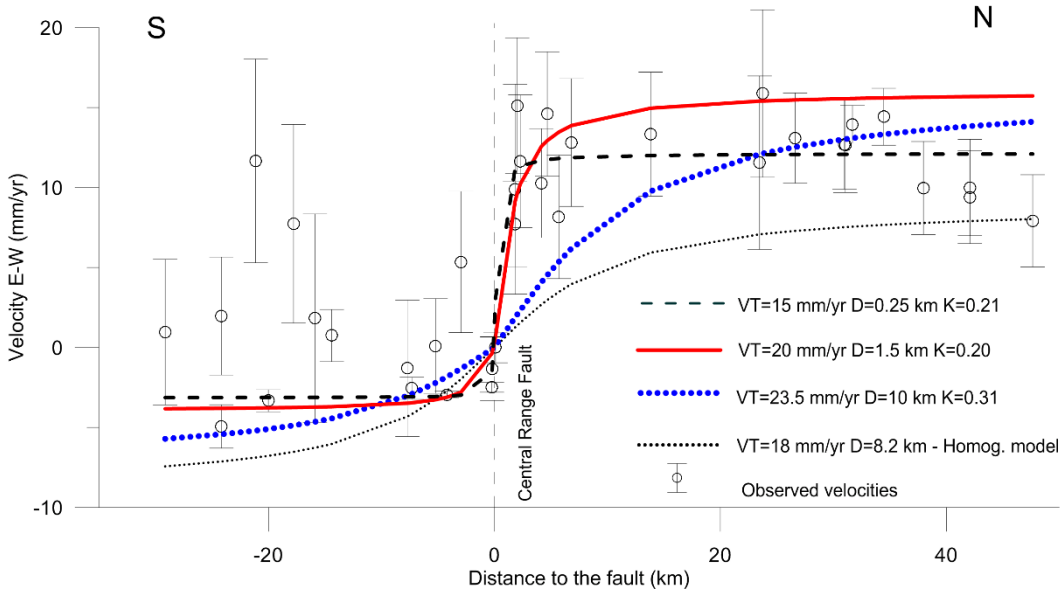


**Figure 5.** Fault-perpendicular velocity profiles showing the acceptable models from asymmetric modeling and homogeneous model in the CRF and E-W observed velocities relative to the fault (based on Trinidad and Tobago observed velocities from Table 1).

### 4.1.2. Asymmetric model in the Arima Fault

Similar to the CRF, we propose an asymmetric model with unconstrained parameters: locking depth, far-field velocity and K ratio values. Results show a locking depth of 38.07 with a coefficient rigidity of 0.67 but a little reliable far-field velocity of 38 mm/yr. Therefore, we propose a model considering Tobago sites with a far-field velocity constrained in 20 mm/yr that shows a 14 km locking depth with a K ratio of 0.72 (Figures 6 and 7). For a model excluding CAMB and FTMD sites but similar far-field velocity we obtain 29 km locking depth and K ratio of 1.00.

In the figure 8 we show the fault-perpendicular velocity profile for the 20 mm/yr and 0.72 K model. It show clearly a better adjustment than the simple screw model proposed for this same fault.

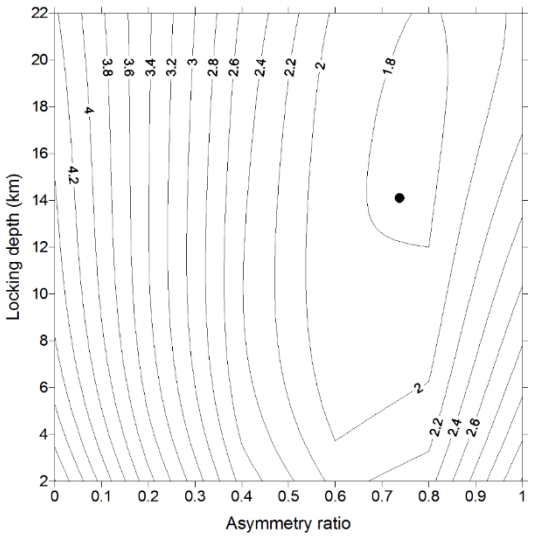


**Figure 6.** Trade-off between the asymmetry ratio (K) and the locking depth on the Arima Fault for the model with far-field velocity fixed at 20 mm/yr. Contoured values are the RMS values and the black dot indicates the best model.

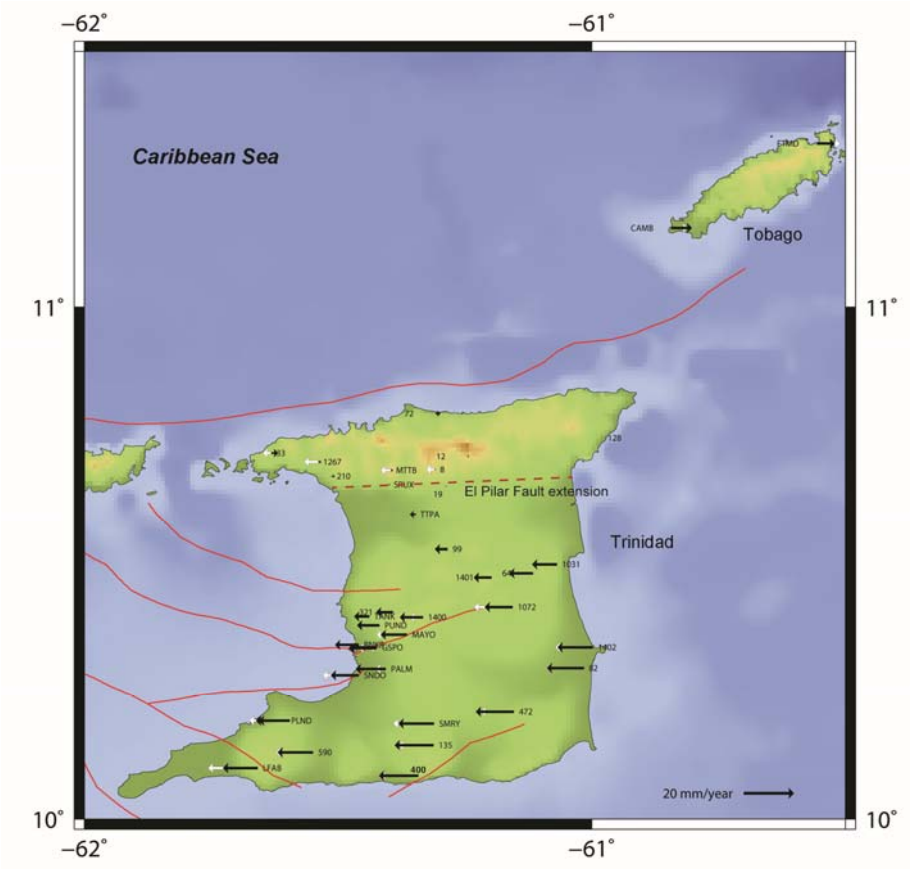


**Figure 7.** E-W observed velocities (white arrows) and simulated velocities (black arrows) from the asymmetric modeling on the Arima fault (The alleged EPF extension) for 20 mm/yr far-field velocity. All displacements are relative to SRUX site close to the Arima fault.

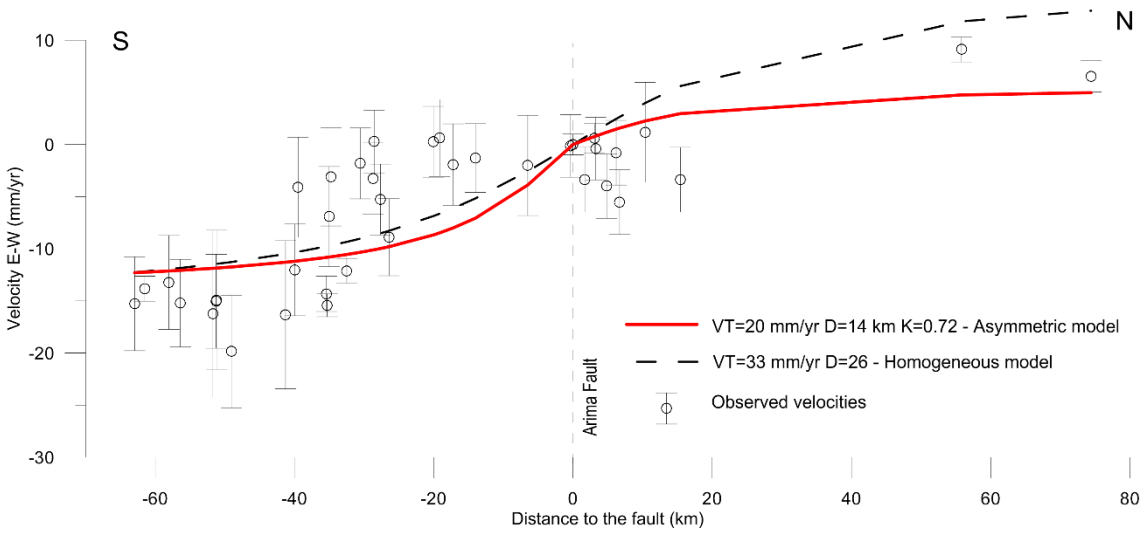


**Figure 8.** Fault-perpendicular velocity profiles showing the acceptable models from the asymmetric model and homogeneous model in the Arima Fault. Also, E-W observed velocities relative to the fault are shown (Values relatives to the EPF are based on Trinidad and Tobago observed velocities from Table 1).

### 4.2. Slip distribution model

Using the slip distribution model, we test if the AF is active or not, if aseismic creep occurs along the CRF and if asperities can be detected along this fault. The fault-slip distribution in multiple finite discrete fault patches from interseismic displacements was applied through the use of a procedure based on the constrained least squares method (*Wang et al.*, 2013). This method of slip inversion is carried out using the SDM2011 software, which has been applied recently in other geodetic studies (*Motagh et al*., 2008, 2010; *Wang et al*., 2009, 2011, *Xu et al*., 2010, *Diao et al*., 2010, 2011). The observed slip data are related to the discrete fault displacement using Green function of the earth model calculated through linear elastic dislocation theory. In order to obtain a slip model with high resolution, the fault plane is presented by a number of small rectangular dislocation patches with uniform slip. The patch size must be reasonably small with the purpose of having a reasonable representation of the true continuous slip distribution, In fact, if the available data does not include enough information for determining the slip distribution with the desired resolution, the inversion system becomes underdetermined. For that reason, an a priori or artificial conditions (fixed fault geometry and restricted variation for the rake angle) and physical constraints (smooth spatial distribution of slip or stress drop) are required to avoid unwieldy large variations in the slip distribution. Based on idea that the areas where large stress drop occurs also have large slip (*Bouchon, 1997*), the slip models are adjusted according to suitable roughness in the stress drop. The objective function is defined as follows:

$$F(\mathrm{b}) = \| \mathrm{Gb-y} \|^2 + \alpha^2 \| \mathrm{H\tau} \|^2 \qquad \text{(eq. 5)}$$

where G is the Green function, b is the slip of sub-faults, y indicates the ground observation, $\tau$ is the shear stress drop related to the slip distribution on the whole fault plane, H represents the

finite difference approximation of the Laplacian operator multiplied by a weighting factor proportional to the slip amplitude, and $\alpha^2$ is the positive smoothing factor.

To invert the velocities field, the observed displacement data related to the discrete fault slips were used considering a homogeneous earth model with a Poisson ratio of 0.25. For the input geometry, a set of important faults across Trinidad was selected: the Central Range Fault, the Arima Fault, the Los Bajos Fault, The South Darien Ridge Fault, and Warm-Springs Fault (Figure 9). The parameters associated to these faults used in the modelling (azimuth, slip, rake; Table 2) are based in previous works (*Audemard et al., 2000; Soto et al., 2007; 2011 Weber, 2007; Prentice et al., 2010; Weber et al., 2011*). The AF (Figure 10) was represented by one segment of ~ 200 km length with an upper and a lower segment split at 12 km depth, according to the depth of dislocation suggested for the Venezuelan portion of EPF. Similarly, Los Bajos Fault was proposed as a large segment of ~170 km length with an upper and other lower dislocation separated at 12 km depth. The CRF is displayed in two segment: the onshore CRF (~50 km length) and the northeast offshore CRF (~50 km length); with a western projection of ~50 km length represented by the WSF. These last three segments show upper and lower parts varying between 10 or 15 km depth. Nevertheless, the best result corresponds to the dislocation at 15 km depth (Figure 11). The (~100 km length) South Darien Ridge Fault was proposed as a segment dipping to northwest.

For onshore portions of CRF and the AF the upper segments are discretized into an array of ~2 km by 2 km patches and the lower parts are discretized in ~20 km by 20 km patches. In order to avoid any artificial boundary effect the limits of segments were considerably extended. The correlation for the model is over 97 per cent using a standard linear least-squares minimization when comparing the interseismic velocities with the simulated velocities. The comparison between observed and simulated velocities is shown in figure 12.

**Table 2.** Summary of geometry fault input parameters to slip distribution model

| | Azimuth | Dip | Rake | Slip (Upper part) | Slip (Lower part) |
|---|---|---|---|---|---|
| CRF (eastward offshore segment) | 68° | 90° | -180 | 12 mm/yr | 20 mm/yr |
| CRF (onshore segment) | 68° | 90° | -180 | 12 mm/yr | 20 mm/yr |
| Arima Fault | 90° | 90°- 60° southward | -180 | Locked | Locked |
| Los Bajos Fault | 296° | 90° | -180 | 7 mm/yr | 20 mm/yr |
| South Darien Ridge Fault | 68° | 70° northward | -135 | 3 mm/yr | |
| Warm Springs Fault | 90° | 90° | -180 | 12 mm/yr | 20 mm/yr |

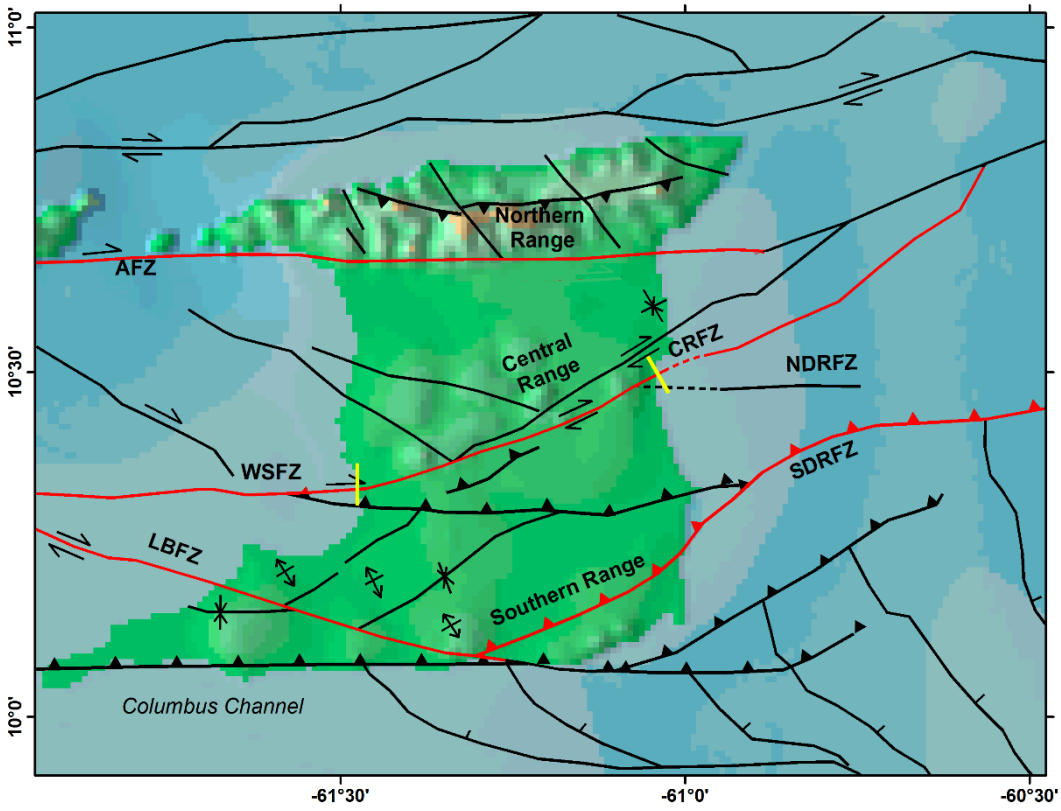


**Figure 9.** Faults included in the geometry input of the slip distributions model (Red lines): the Central Range Fault zone (CRFZ) divided in the onshore and offshore portions, the Arima Fault zone (AFZ), Los Bajos Fault zone (LBFZ), the South Darien Ridge Fault zone (SDRFZ) and Warm Springs Fault zone (WSFZ). The location and characteristics of faults were compiled from *Soto et al*. (2007; 2011).

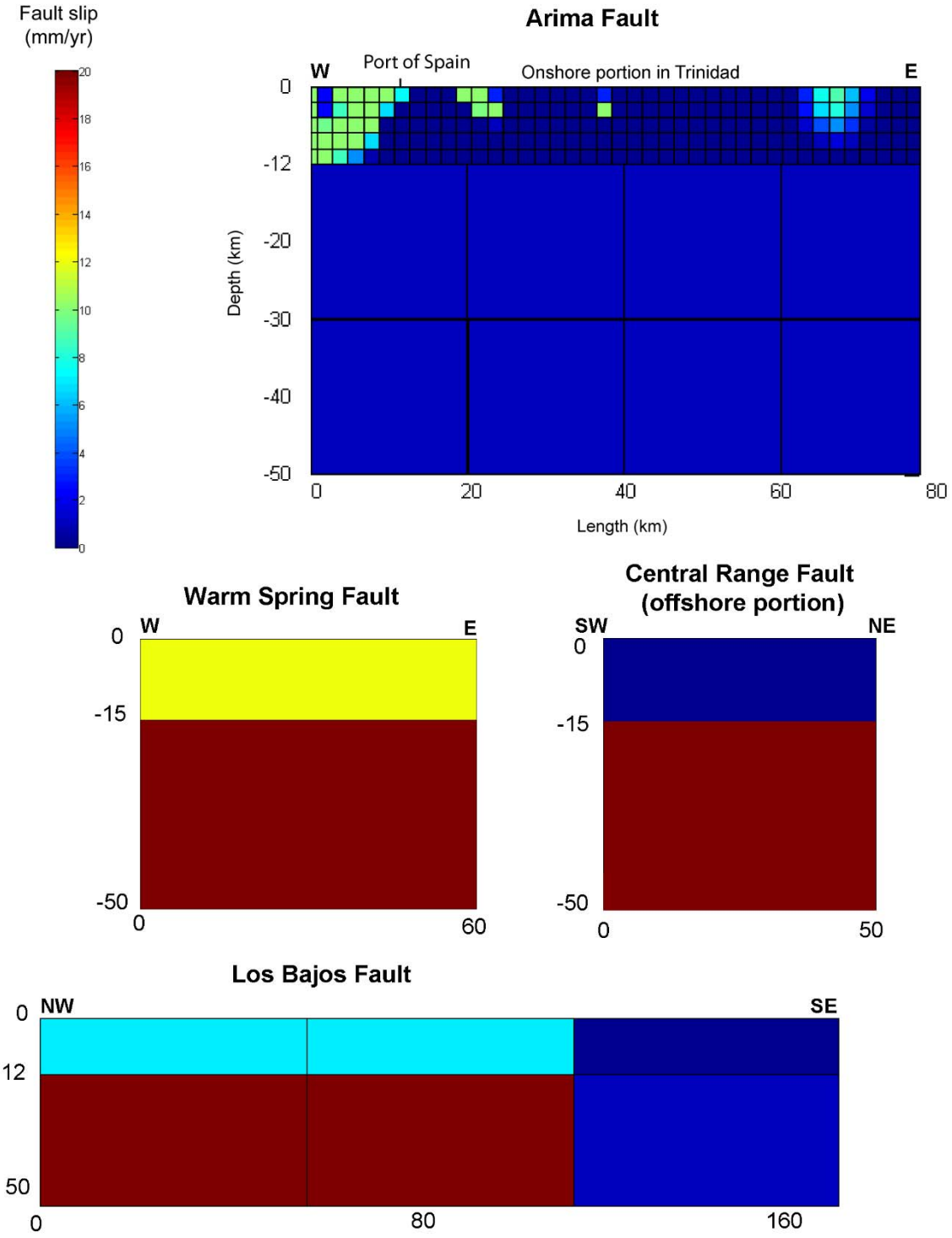


**Figure 10.** Distribution of right-lateral slip (mm/yr) on the Arima Fault, Warm Springs Fault, CRF northeastward offshore portion and Los Bajos fault.

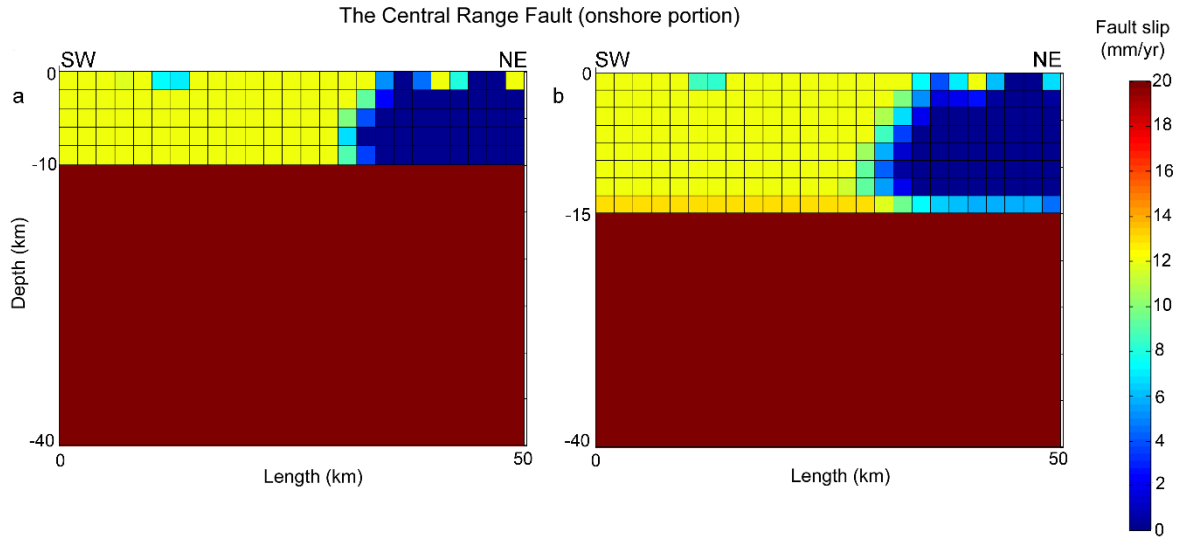


**Figure 11.** Distribution of right-lateral slip (mm/yr) on the CRF from slip distribution modeling considering an upper dislocation part with 10 km (a) and other with 15 km (b). The second example allows observing a more gradually transition between the upper and lower parts.

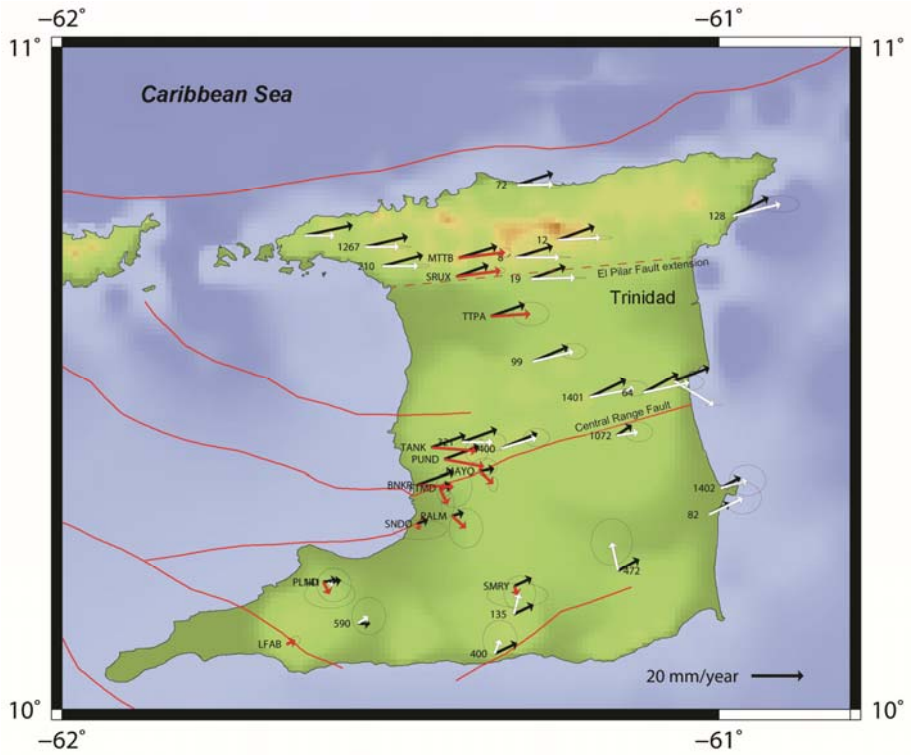


**Figure 12.** Observed velocities from repeat GPS data collected between 1994 and 2005 (red arrows) and 1901–1903 to 1994–1995 triangulation-to-GPS (white arrows) with error ellipses for 66% confidence level. Simulated velocities (black arrows) according to the slip distribution modeling for the main faults in Trinidad and Tobago. All displacements are based in the South America reference frame updated in Webber et al. (2011).

## 5. Discussion and conclusions

### *The Central Range Fault*

The results from the asymmetric model at the CRF point out a rigidity contrast between the north and south sides. The values of 0.21, 0.20 and 0.31 K ratio for several models (Figure 5) show that the northern side has respectively a rigidity 3.8, 3.3 and 2.1 times higher than the sedimentary southern side. Therefore, the idea of geological properties differences on each side of the CRF help to explain the asymmetric velocity field. The 1.5 km locking depth obtained with the 20 mm/yr slip at depth suggests that the CRF is not fully locked between the surface and the locking depth as observed for the EPF in eastern Venezuela. The presence of creep along the onshore CRF is well illustrated by the slip distribution model that determine an important creep along the upper part of the southwestern portion of the CRF whereas its northeastern portion is nearly completely locked. The slip distribution model allows determining a significant creep along the offshore Warm Springs Fault, whereas the northeastern offshore prolongation of CRF presents a completely locked slip along its upper part. Likewise, this model allows concluding that nearly all the relative displacement between the Caribbean and the South America plate is concentrated along the Central Range Fault which implies the existence of a transfer structure between the Central Range Fault and the El Pilar Fault in Venezuela where all the relative displacements between the plates is localized.

The onshore portion of CRF is characterized by a ~20 mm/yr slip at depth (Figure 11) below 10 or 15 km and by a significant creep between the surface and this depth of ~12 mm/yr along its southwestern part, whereas its northeastern portion is clearly locked between the surface and 10 or 15 km depth. This transition suggests the existence of mechanical properties change along the upper part of the CRF.

***The Arima Fault***

From the asymmetric model of the alleged EPF extension, a K ratio of 0.72 shows the southern side with a rigidity 2.5 times higher than the northern side. Nevertheless, in figures 2 and 7 one can observe practically a non-existent displacement gradient close to the fault. This symmetric pattern is observed from 40 km southward to 20 northward with respect to the AF. For this reason, the rigidity coefficient of 0.72 could be more related to the differences among the furthest sites to the fault. The asymmetric and the slip model distribution models both allow concluding that slip along the AF is not needed to simulate observed velocities, the alleged eastern prolongation of the EPF fault can be then considered as inactive as the onshore part of the Los Bajos fault. As mentioned above and reported several authors, The AF in northern Trinidad is clearly inactive. The lack of displacement gradient on both sides of this fault is clearly observed in figure 11.

Finally, as conclusion of this study, if we compare the two hypotheses that depict out the interseismic deformation in Trinidad induced by the AF or by the CRF, our results allow concluding that the CRF is probably the main active fault of Trinidad, as proposed by many authors *(Audemard, 2000; Audemard et al., 2005; Prentice et al., 2010; Weber et al. 2011)*. The slip distribution model has allowed a good representation of the observed velocity field as shown in figure 11 and it has reinforced the observation that the deformation is mainly concentrated along the Los Bajos- Warm Springs- Central Range Fault system fault. This model also allowed identifying a minor contribution of the SDRF and that the AF is inactive.

## REFERENCES:


Audemard, F. A. (2000). Major Active Faults of Venezuela. Proceedings 31st International Geological Congress, Rio de Janeiro, Brasil, 4pp. (extended abstract; in CD-Rom).

Audemard, F. A., G. Romero, H. Rendon, and V. Cano (2005), Quaternary fault kinematics and stress tensors along the southern Caribbean from fault-slip data and focal mechanism solutions, Earth-Science Reviews, 69(3-4), 181-233, doi:10.1016/j.earscirev.2004.08.001.

Audemard, F. A., M. N. Machette, J. W. Cox, R. L. Dart, and K. M. Haller (2000), Map of Quaternary Faults of Venezuela, *USGS Open-File report 00-0018*.

Beltrán, C. (1998), Preliminary observations on Quaternary reverse faulting along the southern foothills of the Northern Range of Trinidad. Proceedings XIV Caribbean Geological Conference, Trinidad, 1995, vol. 1, pp. 233–239.

Boucher, C., Altamimi, Z., Sillard, P., and M. Feissel-Vernier (2004), The ITRF2000. International Earth Rotation and Reference Systems Service (IERS). In: IERS Technical Note 31. Verlag des Bundesamtes für Kartographie und Geodäsie, Frankfurt am Main, Germany. Online version at. http://www.iers.org/iers/publications/tn/tn31/

Bouchon, M. (1997), The state of stress on some faults of the San Andreas System as inferred from near-field strong motion data, Journal of Geophysical Research: Solid Earth, 102(B6), 11731-11744, doi:10.1029/97JB00623.

DeMets, C., P. E. Jansma, G. S. Mattioli, T. H. Dixon, F. Farina, R. Bilham, E. Calais, and P. Mann (2000), GPS geodetic constraints on Caribbean-North America Plate Motion, *Geophys Res Lett*, *27*(3), 437-440, doi:10.1029/1999GL005436.

Diao, F., X. Xiong, and R. Wang (2011), Mechanisms of Transient Postseismic Deformation Following the 2001 Mw 7.8 Kunlun (China) Earthquake, *Pure and Applied Geophysics*, *168*(5), 767-779, doi:10.1007/s00024-010-0154-5.

Diao, F., X. Xiong, R. Wang, Y. Zheng, and H. Hsu (2010), Slip model of the 2008 Mw 7.9 Wenchuan (China) earthquake derived from the coseismic GPS data, *Earth Planets Space* 62, 869–874.

Garciacaro, E., A. Escalona, P. Mann, L. Wood, L. Moscardelli, and S. Sullivan (2011a), Structural controls on Quaternary deepwater sedimentation, mud diapirism, and hydrocarbon distribution within the actively evolving Columbus foreland basin, eastern offshore Trinidad, Marine and Petroleum Geology, 28(1), 149-176, doi:http://dx.doi.org/10.1016/j.marpetgeo.2010.05.007.

Garciacaro, E., P. Mann, and A. Escalona (2011b), Regional structure and tectonic history of the obliquely colliding Columbus foreland basin, offshore Trinidad and Venezuela, Marine and Petroleum Geology, 28(1), 126-148, doi:http://dx.doi.org/10.1016/j.marpetgeo.2009.08.016.

Jolivet, R., R. Bürgmann and N. Houlié (2009), Geodetic exploration of the elastic properties across and within the northern San Andreas Fault zone, *Earth and Planetary Science Letters* 288, 126–131.

Le Pichon, X., C. Kreemer, and N. Chamot-Rooke (2005), Asymmetry in elastic properties and the evolution of large continental strike-slip faults, *J. Geophys. Res.* 110 (B03405).

Lindquist, K., K. Engle, D. Stahlke and E. Price (2004), Global Topography and Bathymetry Grid Improves Research Efforts, *Eos Trans. AGU*, 85(19), 186. Also in: http://www.agu.org/pubs/crossref/2004/2004EO190003.shtml

Motagh, M., B. Schurr, J. Anderssohn, B. Cailleau, T. R. Walter, R. Wang, and J.-P. Villotte (2010), Subduction earthquake deformation associated with 14 November 2007, Mw 7.8 Tocopilla earthquake in Chile: Results from InSAR and aftershocks, *Tectonophysics*, *490*(1–2), 60-68, doi:http://dx.doi.org/10.1016/j.tecto.2010.04.033.

Motagh, M., R. Wang, T. R. Walter, R. Bürgmann, E. Fielding, J. Anderssohn, and J. Zschau (2008), Coseismic slip model of the 2007 August Pisco earthquake (Peru) as constrained by Wide Swath radar observations, *Geophysical Journal International*, *174*(3), 842-848, doi:10.1111/j.1365-246X.2008.03852.x.

Pérez, O. J., R. Bilham, R. Bendick, J. R. Velandía, N. Hernández, C. Moncayo, M. Hoyer, and M. Kozuch (2001b), Velocity Field Across the Southern Caribbean Plate Boundary and Estimates of Caribbean/South-American Plate Motion Using GPS Geodesy 1994-2000, *Geophys Res Lett*, *28*, doi:10.1029/2001gl013183.

Pérez, O. J., R. Bilham, R. Bendick, N. Hernández, M. Hoyer, J. R. Velandia, C. Moncayo and M. Kozuch (2001a), Velocidad relativa entre las placas del Caribe y Sudamérica a partir de observaciones dentro del sistema de posicionamiento global (GPS) en el norte de Venezuela, *Interciencia* 26 (2), 69–74.

Prentice, C. S., J. C. Weber, C. J. Crosby, and D. Ragona (2010), Prehistoric earthquakes on the Caribbean–South American plate boundary, Central Range fault, Trinidad, Geology, 38(8), 675-678, doi:10.1130/g30927.1.

Ritter, J., and J. Weber, J. (2007), Geomorphology and Quaternary geology of the Northern Range, Trinidad and Paria Peninsula, Venezuela: recording quaternary subsidence and uplift associated with a pull-apart basin. In: Proceedings, Geological Society of Trinidad and Tobago, Fourth Geological Conference.

Robson, G.R. (1964), An earthquake catalog for the Caribbean, 1530–1960: Bulletin of the Seismological Society of America, v. 54, p. 785–832.

Rodríguez, A. (2008), Global Positioning System (GPS) Determination of Motions, Neotectonics, and Seismic Hazard in Trinidad and Tobago, McNair Scholars Journal: Vol. 12: Iss. 1, Article 6. Available at: http://scholarworks.gvsu.edu/mcnair/vol12/iss1/6

Saleh, J., K. Edwards, J. Barbaste, S. Balkaransingh, D. Grant, J. Weber, and T. Leong (2004), On some improvements in the geodetic framework of Trinidad and Tobago. Survey Review 37, 604–625.

Savage, J. C., and R. O. Burford (1973), Geodetic determination of relative plate motion in central California, J. Geophys. Res., 78, 832–845, doi:10.1029/JB078i005p00832.

Soto, D. M., P. Mann, A. Escalona, and L. J. Wood (2007), Late Holocene strike-slip offset of a subsurface channel interpreted from three-dimensional seismic data, eastern offshore Trinidad, Geology, 35(9), 859-862, doi:10.1130/g23738a.1.

Soto, D. M., P. Mann, and A. Escalona (2011), Miocene-to-recent structure and basinal architecture along the Central Range strike-slip fault zone, eastern offshore Trinidad, Marine and Petroleum Geology, 28(1), 212-234, doi:10.1016/j.marpetgeo.2010.07.011.

Wang, L., R. Wang, F. Roth, B. Enescu, S. Hainzl, and S. Ergintav (2009), Afterslip and viscoelastic relaxation following the 1999 M 7.4 İzmit earthquake from GPS measurements, *Geophysical Journal International*, *178*(3), 1220-1237, doi:10.1111/j.1365-246X.2009.04228.x.

Wang, R., S. Parolai, M. Ge, M. Jin, T. R. Walter, and J. Zschau (2013), The 2011 Mw 9.0 Tohoku Earthquake: Comparison of GPS and Strong-Motion Data, *Bulletin of the Seismological Society of America*, *103*(2B), 1336-1347, doi:10.1785/0120110264.

Weber, J. C., and J. Ritter (2007), Northern range: structures, metamorphism, and tectonic geomorphology. In: Geological Society of Trinidad and Tobago, Fourth Geological Conference, Guidebook, Field Trip #2, 28 pp.

Weber, J. C., J. Saleh, S. Balkaransingh, T. Dixon, W. Ambeh, T. Leong, A. Rodriguez, and K. Miller (2011), Triangulation-to-GPS and GPS-to-GPS geodesy in Trinidad, West Indies: Neotectonics, seismic risk, and geologic implications, *Marine and Petroleum Geology*, *28*(1), 200-211, doi:http://dx.doi.org/10.1016/j.marpetgeo.2009.07.010.

Weber, J. C., T. H. Dixon, C. DeMets, W. B. Ambeh, P. Jansma, G. Mattioli, J. Saleh, G. Sella, R. Bilham, and O. Pérez (2001), GPS estimate of relative motion between the Caribbean and South American plates, and geologic implications for Trinidad and Venezuela, *Geology*, *29*(1), 75-a-78, doi:10.1130/0091-7613.

Weber, J., 2007. Neotectonics in the Trinidad and Tobago, West Indies segment of the Caribbean-South American Plate boundary. Occasional Papers of the Geological Institute of Hungary, Volume 204.

Xu, C., Y. Liu, Y. Wen, and R. Wang (2010), Coseismic Slip Distribution of the 2008 Mw 7.9 Wenchuan Earthquake from Joint Inversion of GPS and InSAR Data, *Bulletin of the Seismological Society of America*, *100*(5B), 2736-2749, doi:10.1785/0120090253.

# CHAPTER 8:

# GENERAL DISCUSSION, CONCLUSIONS AND PERSPECTIVES

The GNSS methodology applied across this dissertation has allowed having an overview about the geodynamic in western Venezuela, improve the characterization of a main fault in Venezuela as the El Pilar Fault, and likewise, to study the eastward prolongation of El Pilar Fault and principal faults in Trinidad.

## 8.1. Northeast Venezuela

In this study, we test several models to explain the geodetic velocity field recorded in northeastern Venezuela. Compliant zone, non-vertical dislocations, and slip distribution models conclude at the existence of a significant creep along the upper part of the El Pilar Fault along which only 40 to 50% of the slip is locked. This behavior is probably related to either the existence of serpentinite lenses or deep-seated fluid-escaping. The western portion of the western segment of the El Pilar Fault under study corresponds to the portion affected by the 1929 event and the eastern segment has been affected by the 1997 Cariaco Earthquake. Moreover, from discretization of segments in several patches, we conclude that the interseismic slip is not uniform. Nevertheless, creep or partial creep is present in both segments of the El Pilar Fault. The post-seismic afterslip following the 1997 event could help to explain the creep at the eastern segment but for the western segment, the creep might be explained by several reasons; a post-seismic after slip following the 1929 earthquake, after which the creep must continue to decrease with time or by consequence of a post-seismic afterslip following the 1997 earthquake that affected another segment of the El Pilar Fault or by a continuous slip. One can highlight a low slip-rate zone eastward of Cumaná city with roughly 12 km width and 8 km depth and likely related to the rupture zone of the 1929 earthquake that may then correspond to

an asperity along the fault. In a recent study Audemard (2011) revealed at least 13 events around Ms 7.0 (moderate earthquakes) in the last 5.6 ky that represent an average return period of 430 yr which is significantly different from the 195 yr return period estimated in the case of a full locking of the upper 12 km of the El Pilar Fault (Jouanne et al., 2011). This observation supported the hypothesis of significant creep during the interseismic period and not only after major earthquakes. As a consequence, the observed creep cannot be interpreted only as a "classical" after-slip following an important earthquake. The seismicity distribution with depth could suggest the existence of a shallow creep in the upper part with a gradual transition to a partially locked seismogenic zone confined between 3.0 and 12 km, and the existence of a ductile shear below 12 km (Figure 14 – Chapter 6).

**8.2. Trinidad**

The velocity field recorded in Trinidad was explained through several approaches. In this dissertation, we test different models to detect which faults are active in Trinidad. Our approach allows concluding that the The Arima Fault (the alleged westward prolongation of the El Pilar Fault) is inactive, no slip is detected along its upper and lower parts, and that the Central Range Fault concentrates nearly all the relative displacement between the Caribbean and South American plates.

The results from the asymmetric model in the Central Range Fault suggest a rigidity contrast between the north and south sides. The values of 0.21, 0.20 and 0.31 K ratio from different models show that the northern side has respectively rigidity 3.8, 3.3 and 2.1 times higher than the sedimentary southern side. Therefore, the idea of geological property differences on each side of the Central Range Fault helps to explain the asymmetric velocity field. The shallow locking depth obtained from asymmetric models considering a 20 mm/yr far-field velocity suggests a creep along the Central Range Fault. This pattern is also supported by

the slip distribution models where the southwest upper segment of the Central Range Fault shows a slip rate of 12 mm/yr slip whereas its north eastern upper segment is completely locked.

**Perspectives**

A geodetic exploration similar to Northeastern Venezuela and Trinidad must be replicated in Western Venezuela in order to complete the work started in this thesis. At least one or two acquisition campaigns next to the densification of the western network must be carried out in the next years to obtain an accurate velocity field. The seismic profiles crossing the Mérida Andes as part of advances of GIAME project will be considered to model the current deformation. All this work will allows constraining the geometry of the lithospheric structure of the chain and surely of the important faults in western Venezuela. The conception, installation and measuring of a central Venezuela GNSS network is an aspect already considered by FUNVISIS to develop in the next years.

In the future, I will work also to detect potential variation through time and space of the creep recorded along the El Pilar Fault. This will be done, by the installation of one creep-meter along the fault to detect creep pulses or variations through time with a high accuracy, the installation of 2 cGNSS stations, one on each side of the fault, with the collaboration of University of Savoie Mont Blanc (Figure 8.1) and by the realization of interferograms (PhD thesis in progress by Léa Pousse).

In the same context, the NSF-funded COCONET project, running from 2011 through 2015, plans to install 5 cGNSS stations (3 on the Leeward Antilles islands and 2 on mainland at existing seismological BB stations run by FUNVISIS), and help with the installation of a sixth one on Aves Island. In parallel, FUNVISIS has received funding from the LOCTI (Ley Orgánica de Ciencia, Tecnología e Innovación) program in 2012 in order to refresh, enlarge and update the seismological BB station network, as well as to purchase and install 7 cGNSS stations spread over the country. Likewise, the FONACIT-funded 2013000361 (Tsunami)

project is acquiring 11 cGNSS stations and 4 campaign receptors. For the time being, the national seismological network stations are potential sites-under assessment for installing the cGNSS stations guaranteeing the satellite communication and security of equipment (Figure 8.1).

Another important aspect is the creation of a permanent GNSS network linked with the present-day REMOS network (Satellite monitoring network) from IGVSB and neighboring country networks (e.g. GEORED of Colombia, Trinidad & Tobago). In addition, since some time ago we have been promoting the creation of a National GNSS pool for repeated measurement of campaign sites: A set of equipments belonging to public institutions and universities available for campaigns reoccupations and extraordinary events (e.g. large earthquakes, etc).

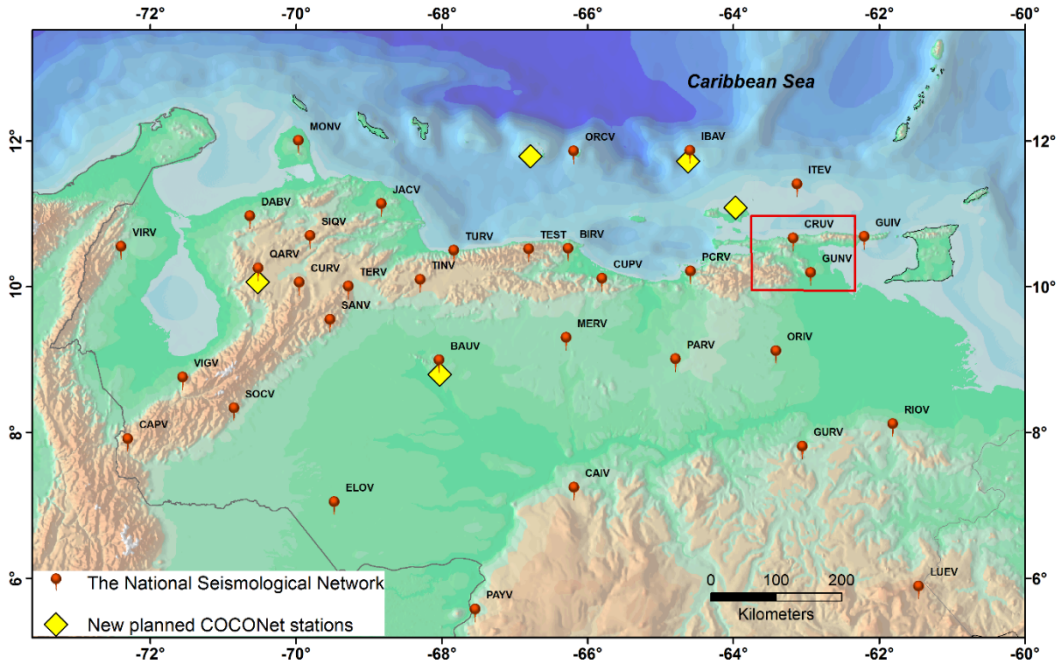


***Figure 8.1.*** *New planned COCONet stations are shown in yellow. The FUNVISIS Seismological network stations (in red) are considered as possible sites for installing the cGNSS receptors (7 LOCTI project and 11 FONACIT 2013000361 project). The red frame points out the zone where it is indented to install the creepmeter and two cGNSS by FUNVISIS-Université de Savoie Mont Blanc collaboration.*

# REFERENCES

# A


Aggarwal, Y. (1983), Neotectonics of the southern Caribbean: Recent data, new ideas, *Acta Cientifica Venezolana*, 34, 1, 17.

Alberding, H., (1957), Application of principles of wrench-fault tectonics of Moddy and Hill to northern South America: Geol. Soc. America Bull., v. 68, p. 785-790.

Altamimi, Z., L. Métivier, and X. Collilieux (2012), ITRF2008 plate motion model, *Journal of Geophysical Research: Solid Earth*, *117*(B7), B07402, doi:10.1029/2011JB008930.

Altamimi, Z., X. Collilieux, J. Legrand, B. Garayt, and C. Boucher (2007), ITRF2005: A new release of the International Terrestrial Reference Frame based on time series of station positions and Earth Orientation Parameters, Journal of Geophysical Research: Solid Earth, 112(B9), B09401, doi:10.1029/2007JB004949.

Ambraseys, N. N. (1970), Some characteristic features of the Anatolian fault zone, *Tectonophysics*, 9(2–3), 143-165, doi:http://dx.doi.org/10.1016/0040-1951(70)90014-4.

Arnaiz-Rodríguez, M. S., and F. Audemard (2014), Variations in elastic thickness and flexure of the Maracaibo block, Journal of South American Earth Sciences, 56(0), 251-264, doi:http://dx.doi.org/10.1016/j.jsames.2014.09.014.

Audemard, F. A. (1993), Néotectonique, sismotectonique et aléa sismique du nord-ouest du Vénézuela (système de failles d'Oca-Ancón), PhD thesis, 369 pp, University of Montpellier II.

Audemard, F. A. (1997), Preliminary Geological Report on the Cariaco Earthquake July 09, 1997, Venezuela, *International Center for Disaster-Mitigation Engineering Newsletter*, 6, 2, 7.

Audemard, F. A. (1998), Evolution géodynamique de la façade nord Sud-américaine: nouveaux apports de l'histoire géologique du Bassin de Falcón, Vénézuéla, paper presented at XIV Caribbean Geological Conference, Trinidad.

Audemard, F. A. (1999a), El sismo de Cariaco del 09 de julio de 1997, edo. Sucre, Venezuela: Nucleación y progresión de la ruptura a partir de observaciones geológicas,

*Proceedings, VI Congreso Venezolano de Sismología e Ingeniería Sísmica, Mérida, Venezuela (CD-ROM).*

Audemard, F. A. (1999b), Nueva percepción de la sismicidad histórica del segmento en tierra de la falla de El Pilar. Venezuela nororiental. A partir de primeros resultados paleosísmicos, *Proceedings VI Congreso Venezolano de Sismología e Ingeniería Sísmica, Mérida*, 10.

Audemard, F. A. (2000), Major Active Faults of Venezuela. Proceedings 31st International Geological Congress, Rio de Janeiro, Brasil, 4pp. (extended abstract; in CD-Rom).

Audemard, F. A. (2001), Quaternary tectonics and present stress tensor of the inverted northern Falcon Basin, northwestern Venezuela, Journal of Structural Geology, 23, 431-453.

Audemard, F. A. (2006), Surface rupture of the Cariaco July 09, 1997 earthquake on the El Pilar fault, northeastern Venezuela, *Tectonophysics*, *424*(1–2), 19-39, doi:http://dx.doi.org/10.1016/j.tecto.2006.04.018.

Audemard, F. A. (2007), Revised seismic history of the El Pilar fault. Northeastern Venezuela. From the Cariaco 1997 earthquake and recent preliminary paleoseismic results. *Journal of Seismology,* 11 (3), 311–326.

Audemard, F. A. (2009), Key issues on the post-Mesozoic southern Caribbean plate boundary, *in* Gloaguen, R., and Ratschbacher, L., eds., Growth and Collapse of the Tibetan Plateau: *Geological Society of London Special Publication*, 328, 569–586, doi:10.1144/SP328.23.

Audemard, F. A. (2011), Multiple-trench investigations across the newly ruptured segment of the El Pilar fault in northeastern Venezuela after the 1997 Cariaco earthquake, *Geological Society of America Special Papers*, *479*, 133-157, doi:10.1130/2011.2479(06).

Audemard, F. A., C. Beck, J. Moernaut, K. De Rycker, M. De Batist, J. Sánchez, M. González, C. Sánchez, W. Versteeg, G. Malavé, M. Schmitz, A. Van Welden, E. Carrillo, and A. Lemus (2007), La depresión submarina de Guaracayal, estado Sucre, Venezuela: Una barrera para la propagación de la ruptura cosísmica a lo largo de la falla de El pilar, *Interciencia, 32*, 735-741.

Audemard, F. A., G. Romero, H. Rendon, and V. Cano (2005), Quaternary fault kinematics and stress tensors along the southern Caribbean from fault-slip data and focal mechanism

solutions, *Earth-Science Reviews*, *69*(3-4), 181-233, doi:10.1016/j.earscirev.2004.08.001.

Audemard, F. A., M. N. Machette, J. W. Cox, R. L. Dart, and K. M. Haller (2000), Map of Quaternary Faults of Venezuela, *USGS Open-File report 00-0018.*

Audemard, F. E., and F. A. Audemard (2002), Structure of the Mérida Andes, Venezuela; relations with the South America-Caribbean geodynamic interaction, Tectonophysics, 345(1-4), 299-327.

# B

Babb, S., and P. Mann (1999), Structural and sedimentary development of a Neogene transpressional plate boundary between the Caribbean and South America plates in Trinidad and the Gulf of Paria, in P. Mann, ed., Caribbean basins: Amsterdam, Elsevier, Sedimentary Basins of the World 4, p. 495–557.

Backé, G., Dhont, D., and Y. Hervouët (2006), Spatial and temporal relationships between compression, strike-slip and extension in the Central Venezuelan Andes: Clues for Plio-Quaternary tectonic escape. Tectonophysics, 425, 25-53.

Barbot, S., Y. Fialko and D. Sandwell (2008), Effect of a compliant fault zone on the inferred earthquake slip distribution, *J. Geophys. Res.*, 113, B06404, doi:10.1029/2007JB005256.

Barbot, S., Y. Fialko and D. Sandwell (2009), Three-dimensional models of elasto-static deformation in heterogeneous media, with applications to the Eastern California Shear Zone, *Geophys. J. Int.*, 179, 500-520.

Baumbach, M., H. Grosser, G. Romero Torres, J. L. Rojas Gonzales, M. Sobiesiak, and W. Welle (2004), Aftershock pattern of the July 9, 1997 Mw=6.9 Cariaco earthquake in Northeastern Venezuela, Tectonophysics, 379(1-4), 1-23.

Baumbach, M., H. Grosser, G. Romero, J. Rojas and M. Sobiesiak (1999), Aftershock studies of the July 9, 1997, Cariaco earthquake: *American Geophysical Union 1999 Spring Meeting*, Boston: Eos (Transactions, American Geophysical Union), 80, 17, supplement S226, abstract S42A-01.

Beck, C. (1986), Géologie de la Chaîne Caraïbe au méridien de Caracas (Vénézuela).Mémoire Soc. Géol. Nord. Lille, 460 pp.

Bellizzia, A., Pimentel, N., and R. Bajo de Osuna (1976), Mapa geológico-estructural de Venezuela. Scale 1: 500.000. Ministerio de Minas e Hidrocarburos. – Ed. Foninves. Caracas.

Beltrán, C. (1994), Trazas activas y síntesis neotectónica de Venezuela a escala 1:2.000.000, *in Proceedings, 7th Congreso Venezolano de Geofísica*: Caracas, p. 541–547.

Beltrán, C. (1998), Preliminary observations on Quaternary reverse faulting along the southern foothills of the Northern Range of Trinidad. Proceedings XIV Caribbean Geological Conference, Trinidad, 1995, vol. 1, pp. 233– 239.

Beltrán, C., A. Singer, and J. A. Rodríguez (1996), The El Pilar fault active trace (northeastern Venezuela): Neotectonic evidences and paleoseismic data, *in Proceedings, 3rd International Symposium on Andean Geodynamics*, Saint-Malo, France, 153–156.

Beltrán, C., and C. Giraldo (1989), Aspectos neotectónicos de la región nororiental de Venezuela, *in VII Congreso Geológico Venezolano*, Caracas, Venezuela, Barquisimeto, 3, 999–1021.

Beltrán, C., compiler (1993), Mapa Neotectónico de Venezuela: Caracas, Venezuela, Fundación Venezolana de Investigaciones Sismológicas, scale 1:2,000,000.

Ben-Zion, Y. and C. G. Sammis (2003), Characterization of fault zones. *Pure Appl. Geophys.*, 160, 677–715, doi:10.1007/PL00012554.

Ben-Zion, Y., Z. Peng, D. Okaya, L. Seeber, J. G. Armbruster, N. Ozer, A. J. Michael, S. Baris, and M. Aktar (2003), A shallow fault-zone structure illuminated by trapped waves in the Karadere–Duzce branch of the North Anatolian Fault, western Turkey, *Geophysical Journal International*, *152*(3), 699-717, doi:10.1046/j.1365-246X.2003.01870.x.

Beutler, G., I. Bauersima, W. Gurtner, M. Rothacher, T. Schildknecht, G. L. Mader, and M. D. Abell (1987), Evaluation of the 1984 Alaska Global Positioning System campaign with the Bernese GPS Software, Journal of Geophysical Research: Solid Earth, 92(B2), 1295-1303, doi:10.1029/JB092iB02p01295.

Beutler, G., M. Rothacher, S. Schaer, T. A. Springer, J. Kouba, and R.E. Neilan (1999), The International GNSS Service (IGS): An interdisciplinary service in support of Earth sciences, *Advances in Space Research*, 23, 631-653.

Bezada, M. J., M. B. Magnani, C. A. Zelt, M. Schmitz, and A. Levander (2010), The Caribbean-South American plate boundary at 65°W: Results from wide-angle seismic data, J. Geophys. Res., 115(B8), B08402, doi:10.1029/2009jb007070.

Bilham, R. (1994), Project CARIVEN: Caribbean /Venezuela relative motion from GPS geodesy. NFS Proposal and Project.

Blewitt, G. (1989), Carrier phase ambiguity resolution for the Global Positioning System applied to geodetic baselines up to 2000 km. J. Geophys. Res. 94 (B8), 10187-10283.

Blewitt, G. (1990), An automatic editing algorithm for GPS data. Geophys. Res. Lett. 17 (3), 199-202.

Blewitt, G., M. B. Heflin, F. H. Webb, U. J. Lindqwister, and R. P. Malla (1992), Global coordinates with centimeter accuracy in the International Terrestrial Reference Frame using GPS, Geophys Res Lett, 19(9), 853-856, doi:10.1029/92GL00775.

Boinet, T. (1985); La Frontière Méridionale de la Plaque Caraïbe aux confins Colombo–Vénézuéliens (Norte de Santander, Colombie): Données Géologiques. PhD thesis, Université Paris VI., 204 pp + appendices.

Boucher, C., Altamimi, Z., and P. Sillard (1999), The 1997 International Terrestrial Reference Frame (ITRF 1997). IERS Technical Note 27, Observatoire de Paris, Paris.

Boucher, C., Altamimi, Z., Sillard, P., and M. Feissel-Vernier (2004), The ITRF2000. International Earth Rotation and Reference Systems Service (IERS). In: IERS Technical Note 31. Verlag des Bundesamtes für Kartographie und Geodäsie, Frankfurt am Main, Germany. Online version at. http://www.iers.org/iers/publications/tn/tn31/.

Bouchon, M. (1997), The state of stress on some faults of the San Andreas System as inferred from near-field strong motion data, Journal of Geophysical Research: Solid Earth, 102(B6), 11731-11744, doi:10.1029/97JB00623.

Bucher, W. H. (1952), Geologic structure and orogenic history of Venezuela. Geol. Soc. Am. Mem. 49, 113 pp.

Bürgmann, R., D. Schmidt, R. M. Nadeau, M. d'Alessio, E. Fielding, D. Manaker, T. V. McEvilly, and M. H. Murray (2000), Earthquake Potential Along the Northern Hayward Fault, California, Science, 289(5482), 1178-1182, doi:10.1126/science.289.5482.1178.

Byerlee, J. (1993), Model for episodic flow of high-pressure water in fault zones before earthquakes, *Geology*, 21, 303–306.

# C

Campos, V. (1981), Une transversale de la Chaîne Caraïbe et de la marge vénézuélienne dans le secteur de Carúpano (Vénézuela oriental): structure géologique et évolution géodynamique. Ph.D. Thesis. Western Bretagne University, Brest, 160 pp.

Chen, Q. and J. T. Freymueller (2002), Geodetic evidence for a near-fault compliant zone along the San Andreas Fault in the San Francisco Bay Area, *Bull. Seismol. Soc. Am.*, 92 (2), 656–671.

Chéry, J. (2008), Geodetic strain across the San Andreas Fault reflects elastic plate thickness variations (rather than fault slip rate). *Earth Planet. Sci. Lett.* 269, 352–365.

Chester, F. M. and J. S. Chester (1998), Ultracataclasite structure and friction processes of the Punchbowl fault, San Andreas system, California, *Tectonophysics*, 295, 199–221, doi:10.1016/S0040-1951(98)00121-8.

Chevalier, Y. (1987), Les zones internes de la Chaînes Sud-Caraïbe sur le transect Ile de Margarita-Péninsule d'Araya. (Vénézuela). Ph.D. Thesis. Western Bretagne University, Brest, 504 pp.

Chinnery, M. A. (1961), The deformation of the ground around surface faults, Bulletin of the Seismological Society of America, 51(3), 355-372.

Christensen, R. M. (1961), Geology of the Paria-Araya Peninsula, northeastern Venezuela: Ph. D. thesis, Dept. Geol., Nebraska Univ., Lincoln, Nebraska.

Christeson, G. L., P. Mann, A. Escalona, and T. J. Aitken (2008), Crustal structure of the Caribbean–northeastern South America arc-continent collision zone, J. Geophys. Res., 113(B8), B08104, doi:10.1029/2007jb005373.

Clark, S. A., C. A. Zelt, M. B. Magnani, and A. Levander (2008), Characterizing the Caribbean-South American plate boundary at 64°W using wide-angle seismic data, J. Geophys. Res., 113(B7), B07401, doi:10.1029/2007jb005329.

Coates, A., L. Collins, M.-P. Aubry, and W. Berggren (2004), The geology of the Darien, Panama, and the late Miocene– Pliocene collision of the Panama arc with

northwestern South America: Geological Society of America Bulletin, v. 116, p. 1327–1344.

Cochran, E., Y.-G. Li, P. Shearer, S. Barbot, Y. Fialko and J. Vidale (2009), Seismic and geodetic evidence for extensive, long-lived fault damage zones, *Geology,* 37(4), 315–318.

Colmenares, L. and M.D. Zoback (2003), Stress field and seismotectonics of northern South America, Geology, 31, 721-724.

# D

Dach, R. and P. Walser (2013), Bernese GPS Software, Version. 5.2, Astronomical Institute, University of Bern.

Dach. R., U. Hugentobler, P. Fridez and M. Meindl (2007), Bernese GPS Software Version. 5.0. Astronomical Institute. University of Bern.

DeMets, C., P. E. Jansma, G. S. Mattioli, T. H. Dixon, F. Farina, R. Bilham, E. Calais, and P. Mann (2000), GPS geodetic constraints on Caribbean-North America Plate Motion, *Geophys Res Lett*, *27*(3), 437-440, doi:10.1029/1999GL005436.

DeMets, C., R. G. Gordon, D. F. Argus, and S. Stein (1990), Current plate motions, Geophysical Journal International, 101(2), 425-478, doi:10.1111/j.1365-246X.1990.tb06579.x.

DeMets, C., R. G. Gordon, D. F. Argus, and S. Stein (1994), Effect of Recent Revisions to the Geomagnetic Reversal Time Scale on Estimates of Current Plate Motions, Geophys Res Lett, 21(20), 2191–2194, doi:10.1029/94gl02118.

Dhont, D., G. Backé, and Y. Hervouët (2005), Plio-Quaternary extension in the Venezuelan Andes: mapping from JERS Radar imagery. Tectonophysics, 399, 293-312.

Diao, F., X. Xiong, and R. Wang (2011), Mechanisms of Transient Postseismic Deformation Following the 2001 Mw 7.8 Kunlun (China) Earthquake, *Pure and Applied Geophysics*, *168*(5), 767-779, doi:10.1007/s00024-010-0154-5.

Diao, F., X. Xiong, R. Wang, Y. Zheng, and H. Hsu (2010), Slip model of the 2008 Mw 7.9 Wenchuan (China) earthquake derived from the coseismic GPS data, *Earth Planets Space* 62, 869–874.

Dixon, T. H., A. Mao, M. Bursik, M. Heflin, J. Langbein, R. Stein, and F. Webb (1997), Continuous monitoring of surface deformation at Long Valley Caldera, California,

with GPS, Journal of Geophysical Research: Solid Earth, 102(B6), 12017-12034, doi:10.1029/96JB03902.

Dixon, T. H., F. Farina, C. DeMets, P. Jansma, P. Mann, and E. Calais (1998), Relative motion between the Caribbean and North American plates and related boundary zone deformation from a decade of GPS observations, Journal of Geophysical Research: Solid Earth, 103(B7), 15157-15182, doi:10.1029/97JB03575.

Dor, O., Y. Ben-Zion, T. Rockwell and J. Brune (2006), Pulverized rocks in the Mojave section of the San Andreas Fault Zone, *Earth Planet. Sci. Lett.*, 245, 642–654.

Dragert, H., K. Wang and T.S. James (2001), A silent event on the deeper Cascadia subduction interface. Science, 292, 1525-1528.

Drewes, H., C. Reigber, K. Stuber, M. Suarez, H. Tremel, H. Henneberg, M. Hoyer, O. Chourio, and S. Rekkedal (1989), The Venezuelan part of the CASA/UNO GPS Project. Manuscripta Geodaetica, 14, 339-344.

Drewes, H., K. Kaniuth, K. Stuber, H. Tremel, H.G. Kahle, C. Straub, N. Hernandez, M. Hoyer, and E. Wildermann (1995), The CASA'93 GPS Campaign for Crustal Deformation Research along the South Caribbean Plate Boundary. J. Geodyn. 20 (2), 129-144.

Drewes, H., W. Torge, R. H. Röder, C. Badell, D. Bravo, and O. Chourio (1991), Absolute and relative gravimetric surveys of national and geodynamic networks in Venezuela, Journal of South American Earth Sciences, 4(4), 273-286.

Duan, B. (2011), Reply to comment by Y. Fialko on "Deformation of compliant fault zones induced by nearby earthquakes: Theorical investigations in two dimensions", *J. geophys. Res.*,116, B12302, doi:10.1029/2011JB008567.

Duque-Caro, H. (1979), Major structural elements and evolution of northwestern Colombia, in J. Watkins, L. Montadert, and P. Dickerson, eds., Geological and geophysical investigations of continental margins: AAPG Memoir 29, p. 329–351.

# E

Egbue, O., and J. Kellogg (2010), Pleistocene to Present North Andean "escape", Tectonophysics, 489(1–4), 248-257, doi:http://dx.doi.org/10.1016/j.tecto.2010.04.021.

Ego, F., M. Sebried, A. Lavenu, H. Yepez and A. Eguez (1993), A new geodynamical model for the northern Ecuador Andes. EUG VII, 4-8 April 1933, Terra abstract 5 (1), 203.

# F

Faulkner, D., A. Lewis and E. Rutter (2003), On the internal structure and mechanics of large strike-slip faults: Field observations from the Carboneras fault, southeastern Spain, *Tectonophysics*, 367, 235–251.

Fialko, Y. (2004), Probing the mechanical properties of seismically active crust with space geodesy: study of the co-seismic deformation due to the 1992 *Mw*7.3 Landers (Southern California) earthquake, *J. geophys. Res.*,109, B03307, doi:10.1029/2003JB002756.

Fialko, Y., D. Sandwell, D. Agnew, M. Simons, P. Shearer, and B. Minster (2002), Deformation on Nearby Faults Induced by the 1999 Hector Mine Earthquake, *Science*, *297*(5588), 1858-1862.

Fulton, P. M., G. Schmalzle, R. N. Harris, and T. Dixon (2010), Reconciling patterns of interseismic strain accumulation with thermal observations across the Carrizo segment of the San Andreas Fault, *Earth and Planetary Science Letters*, *300*(3–4), 402-406, doi:http://dx.doi.org/10.1016/j.epsl.2010.10.024.

Fundación Venezolana de Investigaciones Sismológicas (FUNVISIS) (1994), Estudio Neotectónico y de Geología de Fallas Activas de la Región Nororiental de Venezuela: Proyecto Intevep 92-175: FUNVISIS report for Intevep S.A., 3 volumes.

# G

Garciacaro, E., A. Escalona, P. Mann, L. Wood, L. Moscardelli, and S. Sullivan (2011a), Structural controls on Quaternary deepwater sedimentation, mud diapirism, and hydrocarbon distribution within the actively evolving Columbus foreland basin, eastern offshore Trinidad, Marine and Petroleum Geology, 28(1), 149-176, doi:http://dx.doi.org/10.1016/j.marpetgeo.2010.05.007.

Garciacaro, E., P. Mann, and A. Escalona (2011b), Regional structure and tectonic history of the obliquely colliding Columbus foreland basin, offshore Trinidad and Venezuela, Marine and Petroleum Geology, 28(1), 126-148, doi:http://dx.doi.org/10.1016/j.marpetgeo.2009.08.016.

Garrity, C., D. Hackley, and F. Urbani (2004), Digital shaded – relief map of Venezuela. http://pubs.usgs. gov/of/2004/1322.

Gavotti, P. (2005), Cuantificación del desplazamiento actual de la Falla de Boconó a partir de observaciones GPS. Unpublished Geophysical Engineer disertation, Universidad Simón Bolívar; Caracas, Venezuela, 139 p.

González, J., M. Schmitz, F. A. Audemard, R. Contreras, A. Mocquet, J. Delgado and F. De Santis (2004), Site effects of the 1997 Cariaco, Venezuela earthquake, *Engin. Geol.*, 72, 143-177.

Grosser, H., A. Rietbrock, M. Baumbach, G. Romero Torres, and J. Rojas (2001), Seismic tomography in the aftershock region of the Cariaco earthquake 1997, *Eos Trans. AGU 82* (47) (Fall Meet. Suppl., Abstract S32E-03).

Gutscher, M.-A., W. Spakman, H. Bijwaard, and E. R. Engdahl (2000), Geodynamics of flat subduction: Seismicity and tomographic constraints from the Andean margin, Tectonics, 19(5), 814-833, doi:10.1029/1999TC001152.

# H

Hamiel, Y., and Y. Fialko (2007), Structure and mechanical properties of faults in the North Anatolian Fault system from InSAR observations of coseismic deformation due to the 1999 Izmit (Turkey) earthquake, *J. geophys. Res.*, 112, B07412, doi:10.1029/2006JB004777.

Hatanaka, Y. (2008), A Compression Format and Tools for GNSS Observation Data. Bulletin of the Geospatioal Information Authority of Japan. 55. 21-30

Henneberg, H. G. (1983), Geodetic control of neotectonics in Venezuela. Tectonophysics, 97 (1-4), 1-15.

Henneberg, H. G. and C. Schubert (1986), Geodetic networks along the Caribbean-South-American plate boundary. Tectonophysics, 130 (1-4), 77-94.

Houlié, N., and B. Romanowicz (2011), Asymmetric deformation across the San Francisco Bay Area faults from GPS observations in northern California, *Phys. Earth Planet. Inter.*, 184, 143-153.

Hugentobler, U., R. Dach, and P. Fridez (2005), Bernese GPS Software. Version 5.0. Astronomical Institute. University of Bern, Switzerland, 388 pp.

Hugentobler, U., S. Schaer, P. Fridez, G. Beutler, H. Bock, E. Brockmann, R. Dach, W. Gurtner, D. Ineichen, J. Johnson, M. Meindl, L. Mervart, M. Rothacher, T. Springer and R. Weber (2001), Bernese GPS Software, Version 4.2, University of Bern.

# J

Jacome, M. I., N. Kusznir and S. Flint (1999), Structural and isostatic modelling of Serranía del Interior thrust belt and Monagas foreland basin: Eastern Venezuela. *Fourth International Symposium on Andean Geodynamics Göttingen (Germany)*, Oct. 4 –6, pp. 367–371. Extended abstract.

Jolivet, R., R. Bürgmann and N. Houlié (2009), Geodetic exploration of the elastic properties across and within the northern San Andreas Fault zone, *Earth and Planetary Science Letters* 288, 126–131.

Jolivet, R., R. Cattin, N. Chamot-Rooke, C. Lasserre and G. Peltzer (2008), Thin-plate modelling of interseismic deformation and asymmetry across the Altyn Tagh fault zone, *Geophys. Res. Lett.*, 35 (L02309).

Jouanne, F., F. A. Audemard, C. Beck, A. Van Welden, R. Ollarves, and C. Reinoza (2011), Present-day deformation along the El Pilar Fault in eastern Venezuela: Evidence of creep along a major transform boundary, *Journal of Geodynamics, 51*(5), 398-410, doi:http://dx.doi.org/10.1016/j.jog.2010.11.003.

# K

Kachanov, L. (1986), Introduction to Continuum Damage Mechanics, *Martinus Nijhoff Publishers*, Dordrecht.

Kearey, P; K. A. Klepleis, and F. Vine (2009), Global Tectonis, 3rd edn, 496 pp. Wiley-Blackwell.

Kellogg, J. N. (1984), Cenozoic tectonic history of the Sierra de Perijá, Venezuela–Colombia, and adjacent basins, in W. Bonini, R. Hargraves, and R. Shagam, eds.,TheCaribbean–SouthAmerican plate boundary and regional tectonics: Geological Society of America Memoir 162, p. 239–261.

Kellogg, J. N., and T.H. Dixon (1990), Central and South America GPS geodesy - CASA Uno. Geophys. Res. Lett. 17(3), 195–198, doi:10.1029/GL017i003 p00195.

Kellogg, J. N., and W. E. Bonini (1982), Subduction of the Caribbean plate and basement uplifts in the overriding South American plate, Tectonics, 1(3), 251-276.

King G., and C. Nostro (1999), Almond Lite v. 2.02: A program to calculate Coulomb stresses around rectangular faults or dykes, Manual d'Utilisation, Institute de Phisique du Globe, Paris.

# L

Ladd, J., M. Truchan, M. Talwani, P. Stoffa, P. Buhl, R. Houtz, A. Mauffret, and G. Westbrook (1984), Seismic reflection profile across the southern margin of the Caribbean, in W. Bonini, R. Hargraves, and R. Shagam, eds., The Caribbean–South American plate boundary and regional tectonics: Geological Society of America Memoir 162, p. 153–159.

Lasserre, C., G. Peltzer, F. Crampé, Y. Klinger, J. Van der Woerd, and P. Tapponnier (2005), Coseismic deformation of the 2001 Mw = 7.8 Kokoxili earthquake in Tibet, measured by synthetic aperture radar interferometry, Journal of Geophysical Research: Solid Earth, 110(B12), B12408, doi:10.1029/2004JB003500.

Le Pichon, X., C. Kreemer, and N. Chamot-Rooke (2005), Asymmetry in elastic properties and the evolution of large continental strike-slip faults, *J. Geophys. Res.* 110 (B03405).

Lees, J. M., and P. E. Malin (1990), Tomographic images of P-wave velocity variation, California, *J. Geophys. Res.*, 95, 21,793–21,804.

Li, Y., J. Vidale, K. Aki, C. Marone and W. Lee (1994), Fine-structure of the Landers fault zone—segmentation and the rupture process, *Science,* 265, 367–370.

Lichten, S. M., and J.S. Border (1987), Strategies for High-Precision Global Positioning System Orbit Determination. J. Geophys. Res. 92(B12), 12,751–12,762, doi:10.1029/JB092iB12p12751.

Liddle, R. A. (1946), The geology of Venezuela and Trinidad, 2d ed.: Ithaca, New York, Paleon, Research Inst., p. 1-890.

Lindquist, K., K. Engle, D. Stahlke and E. Price (2004), Global Topography and Bathymetry Grid Improves Research Efforts, *Eos Trans. AGU,* 85(19), 186. Also in: http://www.agu.org/pubs/crossref/2004/2004EO190003.shtml

Lindsey, E. O., and Y. Fialko (2013), Geodetic slip rates in the southern San Andreas Fault system: Effects of elastic heterogeneity and fault geometry, Journal of Geophysical Research: Solid Earth, 118(2), 689-697, doi:10.1029/2012JB009358.

Lisowski, M., J. C. Savage, and W. H. Prescott (1991), The velocity field along the San Andreas Fault in central and southern California, Journal of Geophysical Research: Solid Earth, 96(B5), 8369-8389, doi:10.1029/91JB00199.

Liuzzi, D., M. Schmitz, M. Jácome and J. Sánchez (2006), Adelgazamiento de sedimentos Cretácicos-Oligocenos bajo la Serranía del Interior, Noreste de Venezuela: Evidencia a partir de observaciones de sísmica profunda, *IX Simposio Bolivariano de Exploración Petrolera en las Cuencas Subandinas, Cartagena, Colombia.* CD. 1-8.

Lyakhovsky, V., Y. Ben-Zion, and A. Agnon (2001), Earthquake cycle, fault zones, and seismicity patterns in a rheologically layered lithosphere, *J. Geophys. Res.*, 106, 4103–4120.

Lyons, S. N., Y. Bock, and D. T. Sandwell (2002), Creep along the Imperial Fault, southern California, from GPS measurements, Journal of Geophysical Research: Solid Earth, 107(B10), 2249, doi:10.1029/2001JB000763.

# M

Malavé, G., and G. Suárez (1995), Intermediate-depth seismicity in northern Colombia and western Venezuela and its relationship to Caribbean plate subduction, Tectonics, 14, 617-628, doi:10.1029/95tc00334.

Malservisi, R., K. P. Furlong, and T. H. Dixon (2001), Influence of the earthquake cycle and lithospheric rheology on the dynamics of the Eastern California shear zone, *Geophys. Res. Lett.*, *28*(14), 2731-2734.

Mann, P., and K. Burke (1984), Neotectonics of the Caribbean: Reviews of Geophysics and Space Physics, v. 22, p. 309–362.

Mann, P., C. Schubert, and K. Burke (1990), Review of Caribbean neotectonics. in The Caribbean Region, pp. 307-338, ed. G.Dengo, J. E. C. The Geological Society of America, Boulder, CO.

Maxwell, J. C. and G. Dengo (1951), The Carupano area and its relation to the tectonics of northeastern Venezuela. Transactions, American Geophysical Union, volume 32, issue 2. P. 259-267.

McGeary, S., A. Nur, and Z. Ben-Avraham (1985), Spatial gaps in arc volcanism: The effect of collision or subduction of oceanic plateaus, Tectonophysics, 119(1–4), 195-221, doi:http://dx.doi.org/10.1016/0040-1951(85)90039-3.

McHugh, S., and M. Johnston (1997), Surface shear stress, strain, and shear displacement for screw dislocations in a vertical slap with shear modulus contrast. Geophys. J. R. Astr. Soc. 49, 715-722.

Melbourne, W. G. (1985), The Case in GPS-Based Geodetic Systems, in Goad C.C. (ed), Proc. of First Int. sym. on Precise Position with GPS Rockville, Maryland, 373-386.

Mendoza, C. (2000), Rupture history of the 1997 Cariaco, Venezuela, earthquake from teleseismic P waves, *Geophys. Res. Lett.*, 27 (10) 1555-1158.

Metz, H. (1965), Geology of the El Pilar Fault Zone. State of Sucre, Venezuela, *IV Caribbean Geological Conference*, Trinidad, 293–298.

Minster, J., and T. Jordan (1978), Present-day plate motions, *J. Geophys. Res*, 83, 5, 331–335, 354.

Mocquet, A., C. Beltrán, M. Lugo, J. A. Rodriguez and A. Singer (1996), Seismological interpretation of the historical data related to the 1929 Cumaná earthquake, Venezuela, *Third International Symposium on Andean Geodynamics*, Saint-Malo (France), Sept. 17–19, 203– 206. Extended abstract.

Molina, L. (2006), Campo de velocidades de la Falla de Boconó a partir de observaciones GPS. Unpublished Geophysical Engineer disertation, Universidad Simón Bolívar; Caracas, Venezuela, 84 p.

Molnar, P., and L. Sykes (1969), Tectonics of the Caribbean and Middle America regions from focal mechanisms and seismicity, *Geological Society of America Bulletin*, 80, 1639–1684, doi:10.1130/0016-7606 (1969)80[1639:TOTCAM]2.0.CO;2.

Moore, D., D. A. Lockner, M. Shengli, R. Summers and J. Byerlee (1997), Strengths of serpentinite gouges at elevated temperatures, *J. geophys. Res.*,102, 14787–14801.

Motagh, M., B. Schurr, J. Anderssohn, B. Cailleau, T. R. Walter, R. Wang, and J.-P. Villotte (2010), Subduction earthquake deformation associated with 14 November 2007, Mw 7.8 Tocopilla earthquake in Chile: Results from InSAR and aftershocks, *Tectonophysics*, *490*(1–2), 60-68, doi:http://dx.doi.org/10.1016/j.tecto.2010.04.033.

Motagh, M., R. Wang, T. R. Walter, R. Bürgmann, E. Fielding, J. Anderssohn, and J. Zschau (2008), Coseismic slip model of the 2007 August Pisco earthquake (Peru) as constrained by Wide Swath radar observations, *Geophysical Journal International*, *174*(3), 842-848, doi:10.1111/j.1365-246X.2008.03852.x.

Müller, D., J. Royer, S. C. Cande, W. R. Roest, and S. Maschenkov (1999), New constraints on the Late Cretaceous/Tertiary plate tectonic evolution of the Caribbean, in P. Mann, ed., Caribbean basins: Amsterdam, Elsevier, Sedimentary Basins of the World 4, p. 33– 59.

# O

Okada, Y. (1985), Surface deformation due to shear and tensile faults in a half-space. *Bull. seism. Soc. Am.* **75** (4), 1135–1154.

Oskin, M. and A. Iriondo (2004), Large-magnitude transient strain accumulation on the Blackwater fault, Eastern California shear zone, *Geology*, 32, 313–316.

Ostini, L., R. Dach, M. Meindl, S. Schaer, and U. Hugentobler (2008), *FODITS:* A new tool of the Bernese GPS software, in *Proceedings of EUREF 2008 Symposium*, edited by Torres, J. A., and H. Hornik, Brussels, Belgium.

# P

Paige, S. (1930), The earthquake at Cumaná, Venezuela, January 17, 1929, *Bulletin of the Seismological Society of America*, 20**,** 1-10.

Palma, M., F. Audemard and G. Romero, 2010, New focal mechanism solutions for Venezuela and neighbouring areas 2005–2008: importance of the National Seismological Network's density and distribution. Rev. Téc. Ing. Univ. Zulia 33, 1–14.

Parker, S. P. (Editor) (2003), McGraw-Hill Dictionary of Earth Science. Second Edition. McGraw-Hill, New York.

Peng, Z., and Y. Ben-Zion (2006), Temporal changes of shallow seismic velocity around the Karadere-Duzce branch of the north Anatolian fault and strong ground motion, *Pure Appl. Geophys.* 163, 567–600.

Pennington, W. D. (1981), Subduction of the Eastern Panama Basin and Seismotectonics of Northwestern South America, J Geophys Res, 86, doi:10.1029/JB086iB11p10753.

Pérez, O. J. (1998), Seismological report on the Mw = 6.8 strong shock of 9 July 1997 in Cariaco, northeastern Venezuela, *Bulletin of the Seismological Society of America, Short Notes*, 23, 2, 101–106.

Pérez, O. J., and Y. P. Aggarwal (1981), Present-day tectonics of the southeastern Caribbean and northeastern Venezuela, *J Geophys Res, 86*(B11), 10791-10804, doi:10.1029/JB086iB11p10791.

Perez, O. J., M. Jaimes, E. Garciacaro (1997), Microseismicity evidence for subduction of the Caribbean plate beneath the South-American plate in northwestern Venezuela. J. Geophys. Res. 102, 17875-17881.

Pérez, O. J., R. Bilham, M. Sequera, L. Molina, P. Gavotti, H. Codallo, C. Moncayo, C., Rodríguez, R. Velandia, M. Guzmán, and P. Molnar (2011), Campo de Velocidades GPS en el Occidente de Venezuela: Componente Lateral Derecha asociada a la Falla de Boconó y Componente Convergente perpendicular a Los Andes. Interciencia, Vol. 36, No. 1, 39-44.

Pérez, O. J., R. Bilham, R. Bendick, J. R. Velandía, N. Hernández, C. Moncayo, M. Hoyer, and M. Kozuch (2001b), Velocity Field Across the Southern Caribbean Plate Boundary and Estimates of Caribbean/South-American Plate Motion Using GPS Geodesy 1994-2000, *Geophys Res Lett, 28*, doi:10.1029/2001gl013183.

Pérez, O. J., R. Bilham, R. Bendick, N. Hernández, M. Hoyer, J. R. Velandia, C. Moncayo and M. Kozuch (2001a), Velocidad relativa entre las placas del Caribe y Sudamérica a partir de observaciones dentro del sistema de posicionamiento global (GPS) en el norte de Venezuela, *Interciencia* 26 (2), 69–74.

Pindell, J. L., and J. F. Dewey (1982), Permo-Triassic reconstruction of western Pangea and the evolution of the Gulf of Mexico/Caribbeanregion, Tectonics, 1.

Pindell, J. L., and L. Kennan (2007), Cenozoic kinematics and dynamics of oblique collision between two convergent plate margins: The Caribbean– South America collision in

eastern Venezuela, Trinidad and Barbados, *in* Kennan, L., Pindell, J., and Rosen, N., eds., The Paleogene of the Gulf of Mexico and Caribbean Basins; Processes, Events, and Petroleum Systems: Proceedings, 27th Bob F. Perkins Research Conference, Gulf Coast Section of the Society of Economic Paleontologists and Mineralogists: Houston, Texas, Society of Economic Paleontologists and Mineralogists, 458–553.

Pindell, J. L., and S. Barrett (1990), Geologic evolution of the Caribbean: A plate-tectonic perspective. in The Geology of North America. Vol, The Caribbean Region, pp. 405-432, eds. Dengo, G. & Case, J. E. Geological Society of America.

Prentice, C. S., J. C. Weber, C. J. Crosby, and D. Ragona (2010), Prehistoric earthquakes on the Caribbean–South American plate boundary, Central Range fault, Trinidad, Geology, 38(8), 675-678, doi:10.1130/g30927.1.

# R

Ritter, J., and J. Weber, J. (2007), Geomorphology and Quaternary geology of the Northern Range, Trinidad and Paria Peninsula, Venezuela: recording quaternary subsidence and uplift associated with a pull-apart basin. In: Proceedings, Geological Society of Trinidad and Tobago, Fourth Geological Conference.

Robson, G.R. (1964), An earthquake catalog for the Caribbean, 1530–1960: Bulletin of the Seismological Society of America, v. 54, p. 785–832.

Rod, E. (1956), Strike-slip faults of northern Venezuela: Am. Assoc. Petroleum Geologist Bull., v. 40, p.457-476.

Rodríguez, A. (2008), Global Positioning System (GPS) Determination of Motions, Neotectonics, and Seismic Hazard in Trinidad and Tobago, McNair Scholars Journal: Vol. 12: Iss. 1, Article 6. Available at: http://scholarworks.gvsu.edu/mcnair/vol12/iss1/6

Rodríguez, J. A., and C. A. Chacín (1996), Contribución al estudio del sismo de Cumaná año 1929, Compilación y notas. *Bol. Hist. Geocienc. Venez.* 2, 1 –77.

Romero, G., F. A. Audemard, H. Rendón, and N. Orihuela (2002), Mapa de Soluciones Focales de Sismos Sentidos en Venezuela y Regiones Vecinas entre 1957 y 2002, *Edición Conmemorativa XXX Aniversario de FUNVISIS*, Caracas, FUNVISIS, scale ~1:2,450,000.

Rossi, T., J. F. Stéphan, R. Blanchet, and G. Hernandez, 1987. Etude géologique de la Serrania del Interior oriental sur le transect Cariaco-Maturin: Revue de l'Institut Français du Pétrole. 42(1), 3-30.

Rothacher, M., G. Beutler, W. Gurtner, E. Brockmann, and L. Mervart (1993), Bernese GPS Software version 4.0 Documentation, Astronomical Institute, University of Berne.

Rybicki, K., and K. Kasahara (1977), A strike-slip fault in a laterally inhomogeneous medium, Tectonophysics, 42(2–4), 127-138, doi:http://dx.doi.org/10.1016/0040-1951(77)90164-0.

# S

Saleh, J., K. Edwards, J. Barbaste, S. Balkaransingh, D. Grant, J. Weber, and T. Leong (2004), On some improvements in the geodetic framework of Trinidad and Tobago. Survey Review 37, 604–625.

Sánchez-Rojas, J., and M. Palma (2014), Crustal density structure in northwestern South America derived from analysis and 3-D modeling of gravity and seismicity data, Tectonophysics(0), doi:http://dx.doi.org/10.1016/j.tecto.2014.07.026

Savage, J. C. (1987), Effect of crustal layering upon dislocation modeling, Journal of Geophysical Research: Solid Earth, 92(B10), 10595-10600, doi:10.1029/JB092iB10p10595.

Savage, J. C., and R. O. Burford (1973), Geodetic determination of relative plate motion in central California, J. Geophys. Res., 78, 832–845, doi:10.1029/JB078i005p00832.

Schmalzle, G., T. Dixon, R. Malservisi, and R. Govers (2006), Strain accumulation across the Carrizo segment of the San Andreas Fault, California: Impact of laterally varying crustal properties, *Journal of Geophysical Research: Solid Earth*, *111*(B5), B05403, doi:10.1029/2005JB003843.

Schmitz, M., E. Gil, F. Mazuera, J. Avila, L. Yegres, N. Orihuela, S. Klarica, F. A. Audemard, J. Sánchez, and GIAME working group, (2014), The GIAME integrated geoscientific project in Mérida Andes, Venezuela: Objectives and first images of deep seismic profiles. 16th SEISMIX International Symposium, Barcelona, Spain.

Scholz, C. H. (1988), The brittle-plastic transition and the depth of seismic faulting. *Geol. Runds.* **77,** 319–328.

Schubert, C. (1984), Basin formation along the Bocono-Moron-El Pilar Fault System, Venezuela, *J. Geophys. Res.*, *89*(B7), 5711-5718, doi:10.1029/JB089iB07p05711.

Silver, E., J. Case, and H. Macgillavry (1975), Geophysical study of the Venezuelan borderland: Geological Society of America Bulletin, v. 86, p. 213– 226.

Singer, A., and F. A. Audemard (1997), Aportes de Funvisis al desarrollo de la geología de fallas activas y de la paleosismología para los estudios de amenaza y riesgo sísmico, *in* Grases, J., ed., *Diseño Sismorresistente: Especificaciones y Criterios Empleados en Venezuela*, Academia de las Ciencias Naturales, Matemáticas y Físicas Publicación Especial 33, 25–38.

Smith-Konter, B., D. Sandwell and P. Shearer (2011), Locking depths estimated from geodesy and seismology along the San Andreas Fault System: Implications for seismic moment release, *J. Geophys. Res.*, 116, B06401.

Soto, D. M., (2007), Structural and basinal architecture and active strike-slip faulting of the eastern offshore area of Trinidad, unpubl. MS thesis, Univ. of Texas at Austin, p. 96.

Soto, D. M., P. Mann, A. Escalona, and L. J. Wood (2007), Late Holocene strike-slip offset of a subsurface channel interpreted from three-dimensional seismic data, eastern offshore Trinidad, Geology, 35(9), 859-862, doi:10.1130/g23738a.1.

Soto, D. M., P. Mann, and A. Escalona (2011), Miocene-to-recent structure and basinal architecture along the Central Range strike-slip fault zone, eastern offshore Trinidad, Marine and Petroleum Geology, 28(1), 212-234, doi:10.1016/j.marpetgeo.2010.07.011.

Soulas, J.-P. (1986), Neotectónica y tectónica activa en Venezuela y regiones vecinas, *Proceedings of 6th Congreso Geológico Venezolano* (1985): Caracas, Venezuela, 10, 6639–6656.

Speed, R., R. Russo, J. Weber and K. C. Rowley (1991), Evolution of Southern Caribbean plate boundary, vicinity of Trinidad and Tobago, *The American Association of Petroleum Geologists Bulletin*, 75, 11, 1789–1794.

Stéphan, J.-F. (1982), Evolution Géodinamique du Domaine Caraïbe, Andes et Chaîne Caraïbe sur la Transversale de Barquisimeto (Vénézuéla) [Ph.D. thesis]: Brest, France, Université de Bretagne Occidentale, 512 pp.

Stéphan, J.-F. (1985), Andes et Chaıîne Caraîbe sur la Transversale de Barquisimeto (Vénézuéla), Evolution géodynamique: Géodynamique des Caraïbes, Symposium: Paris, Editions Technip p. 505– 529.

Stéphan, J.-F., B. Mercier de Lépinay, E. Calais, M. Tardy, C. Beck, J.-C. Carfantan, J.-L., Olivet, J.-M. Vila, P. Bouysse, A. Mauffret, J. Bourgois, J.-M. Théry, J. Tournon, R. Blanchet, and J. Dercourt (1990), Paleogeodynamic maps of the Caribean: 14 steps from Lias to Present. Bulletin of the French Geological Society, (8), t. VI, 6:915-919, 14 maps.

Stéphan, J.-F., C. Beck, A. Bellizzia, R. Blanchet (1980), La Chaîne Caraïbe du Pacifique à l'Atlantique. XXVIth International Geological Congress, Paris, c-5, pp. 38–59.

# T

Taboada, A., L. A. Rivera, A. S. Fuenzalida, A. Cisternas, H. Philip, H. Bijwaard, J. Olaya, and C. Rivera (2000), Geodynamics of the northern Andes: Subductions and intracontinental deformation (Colombia), Tectonics, 19, 787-813, doi:10.1029/2000tc900004.

Thurber, C., S. Roecker, K. Roberts, M. Gold, L. Powell, and K. Rittger (2003), Earthquake locations and three-dimensional fault zone structure along the creeping section of the San Andreas fault near Parkfield, CA: Preparing for SAFOD, *Geophys Res Lett*, *30*(3), 1112, doi:10.1029/2002GL016004.

Trenkamp, R., J. N. Kellogg, H. Mora, J. Freymueller, T. Dixon, and L. Leffer (1995), Active Panama arc, northern Andes collision, GPS displacement vectors 1988–1994 (abs.): Transactions, American Geophysical Union, 1995 Fall Meeting, San Francisco, California, p. 613.

Trenkamp, R., J. N. Kellogg, J. T. Freymueller, and H. P. Mora (2002), Wide plate margin deformation, southern Central America and northwestern South America, CASA GPS observations, Journal of South American Earth Sciences, 15(2), 157-171.

Turcotte, D., W. Newman and R. Shcherbakov (2003), Micro and macroscopic models of rock fracture, *Geophys. J. Int.*, 152, 718–728.

# U

Unsworth, M. J., P. E. Malin, G. D. Egbert and J. R. Booker (1997), Internal structure of the San Andreas fault at Parkfield, California, *Geology* 25, 359–362.

# V

Van Daele, M., A. Van Welden, J. Moernaut, C. Beck, F. A. Audemard, J. Sánchez, F. Jouanne, E. Carrillo, G. Malavé, A. Lemus, A., and M. De Batist (2011), Reconstruction of Late-Quaternary sea- and lake-level changes in a tectonically active marginal basin using seismic stratigraphy: The Gulf of Cariaco, NE Venezuela, Marine Geology, 279, 37-51.

Van der Hilst, R., and P. Mann (1994), Tectonic implications of tomographic images of subducted lithosphere beneath northwestern South America, Geology, 22(5), 451-454.

Van Welden, A. (1997), Enregistrements sédimentaires imbriqués d'une activité sismique et de changements paléoenvironnementaux. Etude de différents sites : Golfe de Corinthe (Grèce), Lac de Shkodra (Albanie/Monténégro) et Golfe de Cariaco (Vénézuela). PhD. Thesis, Université de Savoie, France, 287 pp.

Vierbuchen, R.C. (1984), The geology of the El Pilar fault zone and adjacent areas in northeastern Venezuela. In: Bonini, W.E., Hargraves, R.B., Shagam, R. (Eds.), The Caribbean –South America boundary and regional tectonics. *Geol. Soc. Am.*, Memoir 162. Boulder, CO, 189– 212.

# W

Wang, L., R. Wang, F. Roth, B. Enescu, S. Hainzl, and S. Ergintav (2009), Afterslip and viscoelastic relaxation following the 1999 M 7.4 İzmit earthquake from GPS measurements, *Geophysical Journal International*, *178*(3), 1220-1237, doi:10.1111/j.1365-246X.2009.04228.x.

Wang, R., B. Schurr, C. Milkereit, Z. Shao, and M. Jin (2011), An Improved Automatic Scheme for Empirical Baseline Correction of Digital Strong-Motion Records, *Bulletin of the Seismological Society of America*, *101*(5), 2029-2044, doi:10.1785/0120110039.

Wang, R., S. Parolai, M. Ge, M. Jin, T. R. Walter, and J. Zschau (2013), The 2011 Mw 9.0 Tohoku Earthquake: Comparison of GPS and Strong-Motion Data, *Bulletin of the Seismological Society of America*, *103*(2B), 1336-1347, doi:10.1785/0120110264.

Wdowinski, S. (2009), Deep creep as a cause for the excess seismicity along the San Jacinto fault, *Nature Geoscience*, 2, 882 – 885.

Weber, J. C. (2007), Neotectonics in the Trinidad and Tobago, West Indies segment of the Caribbean-South American Plate boundary. Occasional Papers of the Geological Institute of Hungary, Volume 204.

Weber, J. C., and J. Ritter (2007), Northern range: structures, metamorphism, and tectonic geomorphology. In: Geological Society of Trinidad and Tobago, Fourth Geological Conference, Guidebook, Field Trip #2, 28 pp.

Weber, J. C., J. Saleh, S. Balkaransingh, T. Dixon, W. Ambeh, T. Leong, A. Rodriguez, and K. Miller (2011), Triangulation-to-GPS and GPS-to-GPS geodesy in Trinidad, West Indies: Neotectonics, seismic risk, and geologic implications, *Marine and Petroleum Geology*, *28*(1), 200-211, doi:http://dx.doi.org/10.1016/j.marpetgeo.2009.07.010.

Weber, J. C., T. H. Dixon, C. DeMets, W. B. Ambeh, P. Jansma, G. Mattioli, J. Saleh, G. Sella, R. Bilham, and O. Pérez (2001), GPS estimate of relative motion between the Caribbean and South American plates, and geologic implications for Trinidad and Venezuela, *Geology*, *29*(1), 75-a-78, doi:10.1130/0091-7613.

Weertman, J. and J. Wertman (1964), Elementary Dislocation Theory, The Macmillan Company, New York. 213 pp.

Wilson, B., T. Dewers, Z. Reches, and J. Brune (2005), Particle size and energetics of gouge from earthquake rupture zones, *Nature*, *434*(7034), 749-752.

Wübbena, G. (1985), Software Development for Geodetic Positioning with GPS Using TI 4100 Code and Carrier Measurements, in Goad C.C. (ed), Proc. of First Int. sym. on Precise Position with GPS Rockville, Maryland, pp.403-412.

# X

Xu, C., Y. Liu, Y. Wen, and R. Wang (2010), Coseismic Slip Distribution of the 2008 Mw 7.9 Wenchuan Earthquake from Joint Inversion of GPS and InSAR Data, *Bulletin of the Seismological Society of America*, *100*(5B), 2736-2749, doi:10.1785/0120090253.

# Y

Yegres, L., M. Schmitz, E. Gil, F. Mazuera, J. Avila, and J. Alcalá (2014), First insights into the crustal structure of the Mérida Andes, Venezuela, from Deep seismic of GIAME Project, Central Profile, Preliminary Results. 16th SEISMIX International Symposium, Barcelona, Spain.

# Z

Zumberge, J. F., M. B. Heflin, D. C. Jefferson, M. M. Watkins, F. H. Webb (1997), Precise point positioning for the efficient and robust analysis of GPS data from large networks. J. Geophys. Res. 102(B3), 5005–5017, doi:10.1029/96JB03860.

## List of figures

## List of tables

## Appendix A

# TIME SERIES

## A.1. cGNSS stations

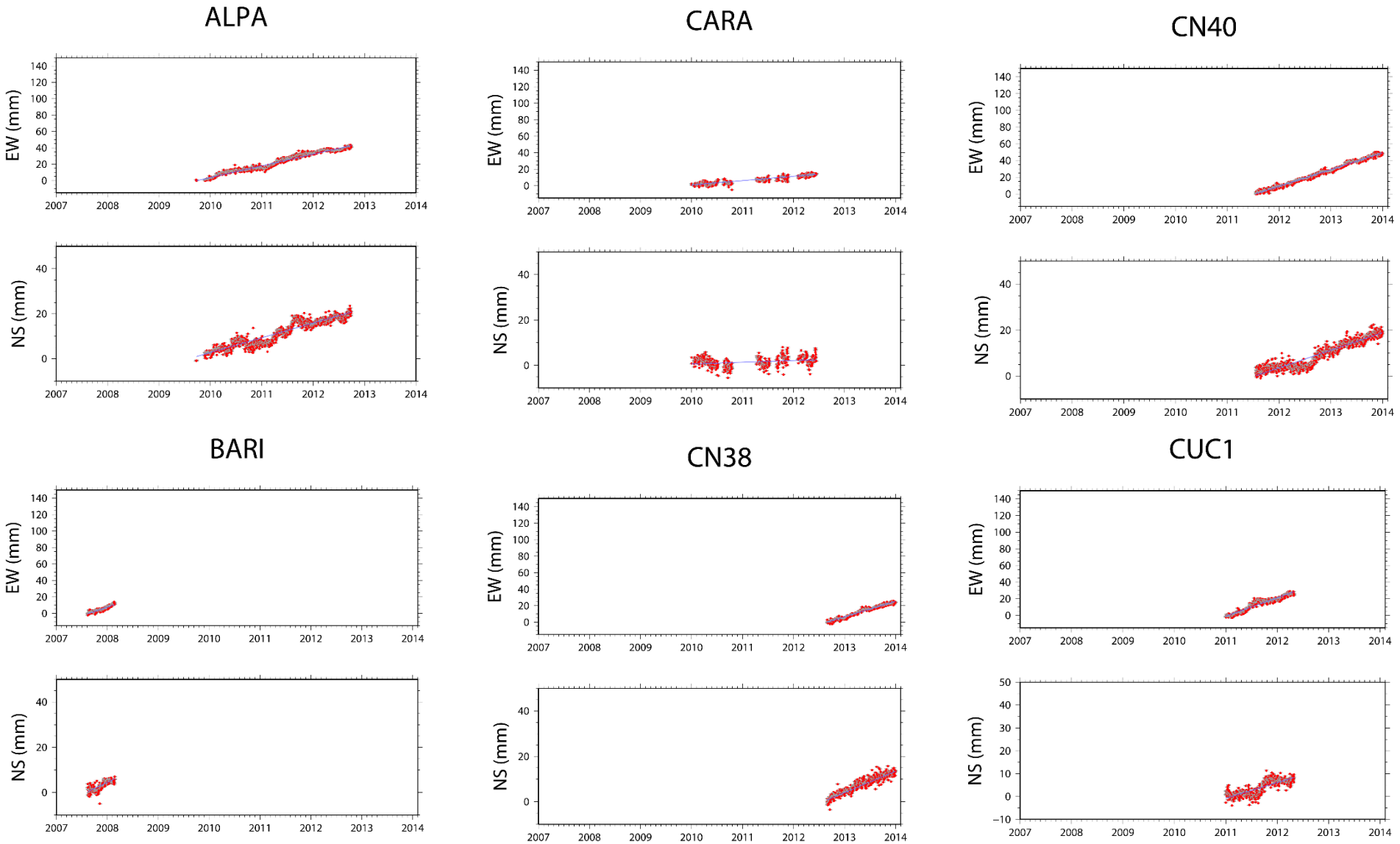

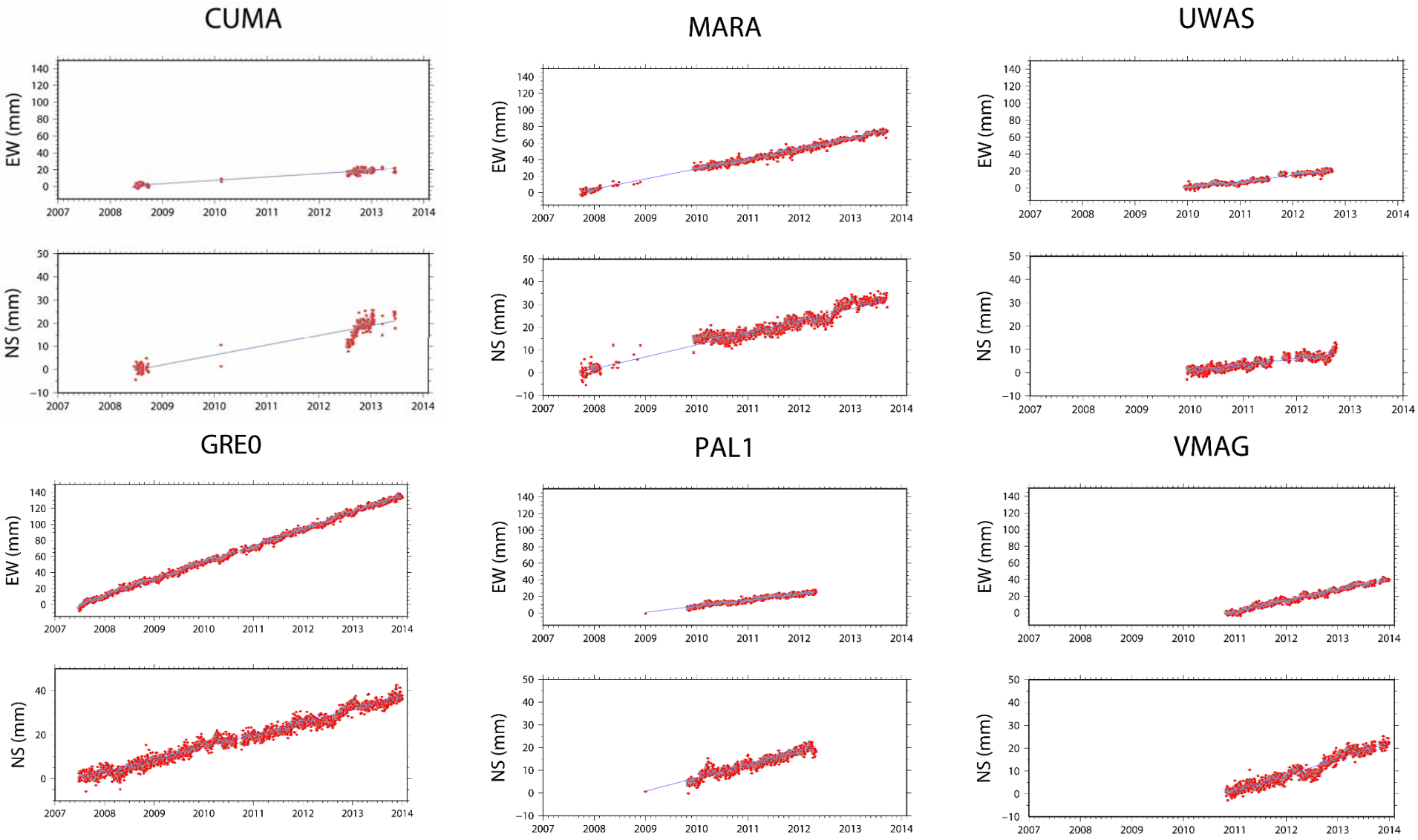
CUMA
MARA
UWAS
GRE0
PAL1
VMAG
EW (mm)
NS (mm)
2007
2008
2009
2010
2011
2012
2013
2014

## A.2. Campaign stations

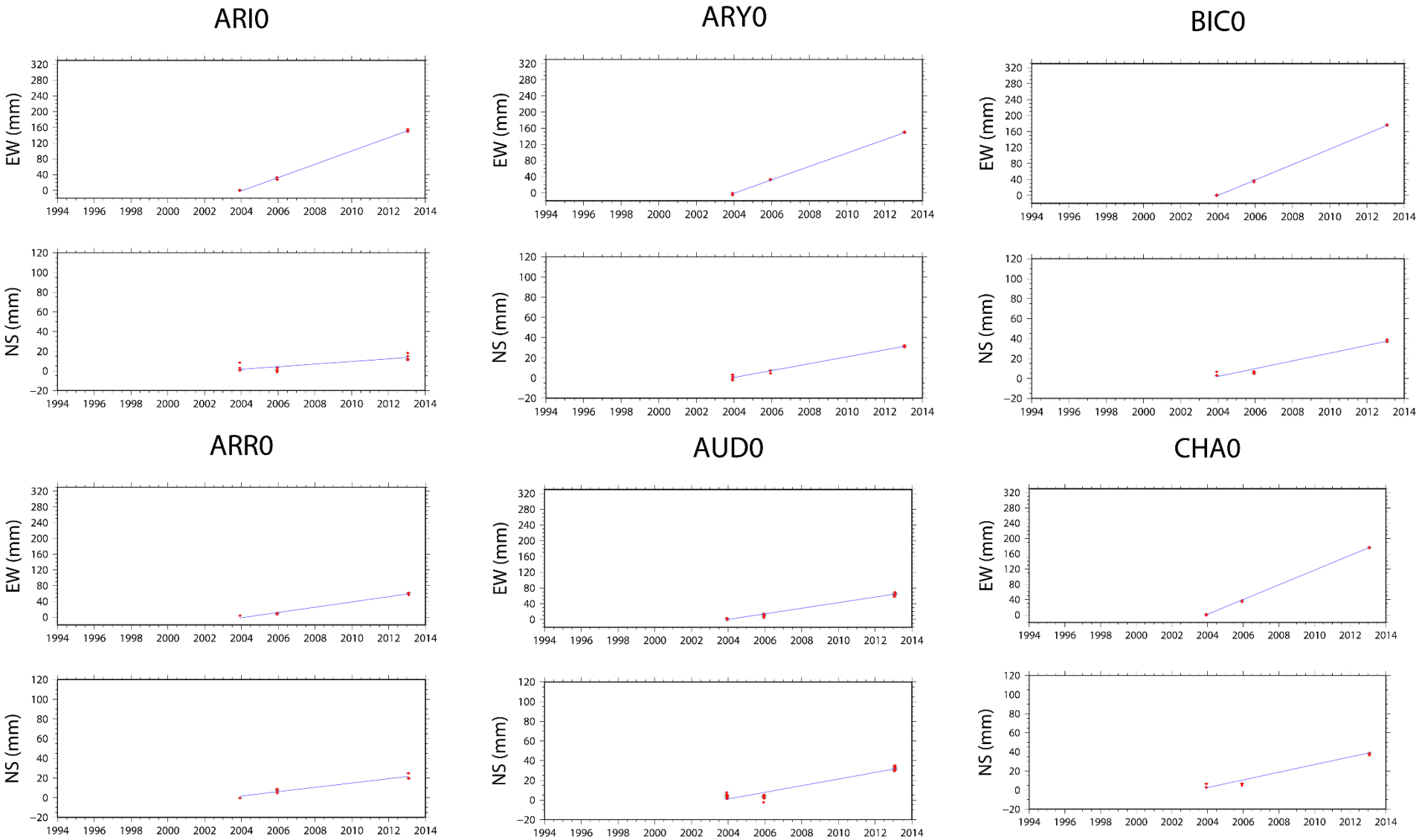

COI0

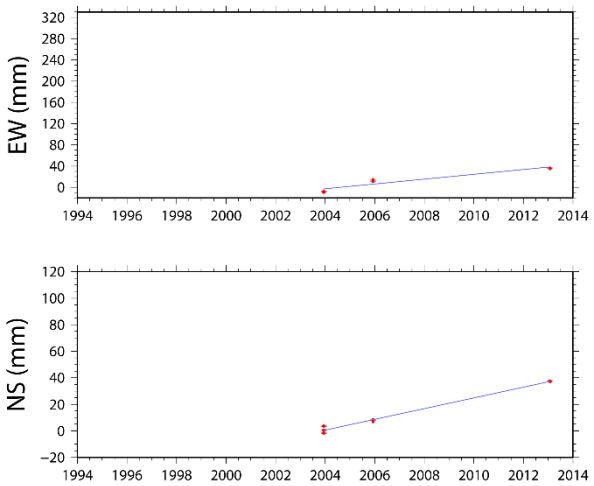


GAL0

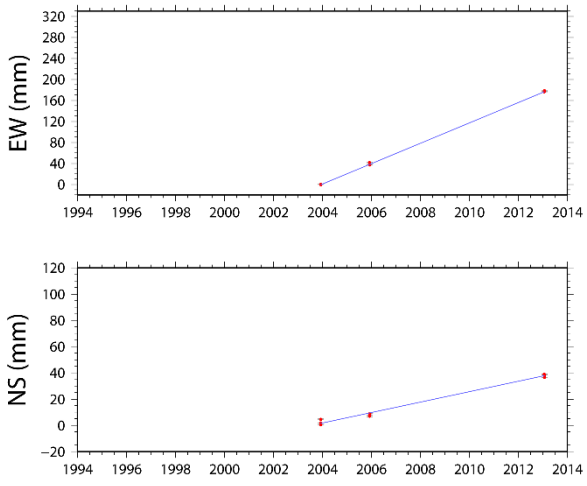


ISL0

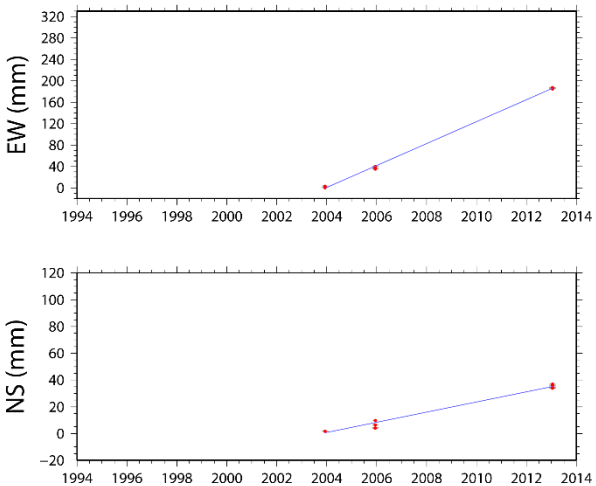


COV0

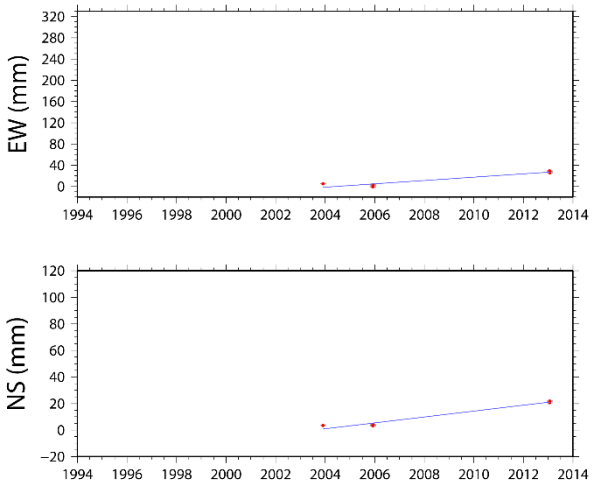


HOR0

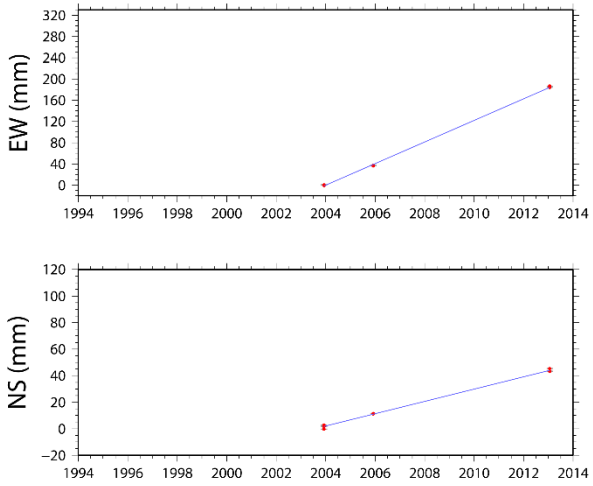


MARG

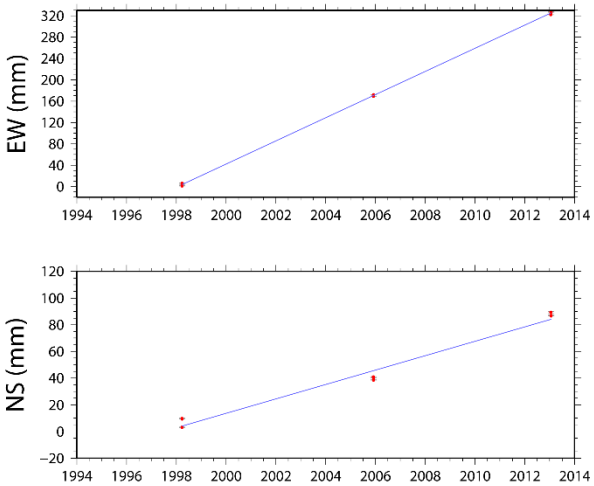

MCH0

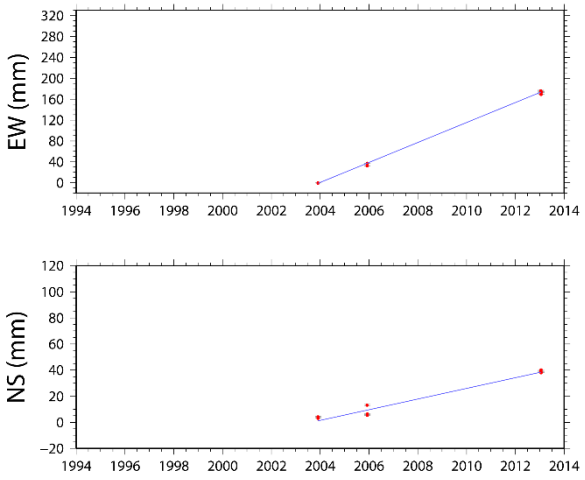


PAR0

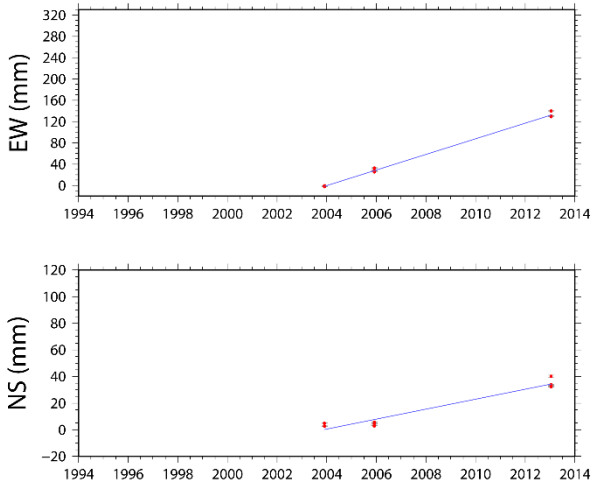


PER0

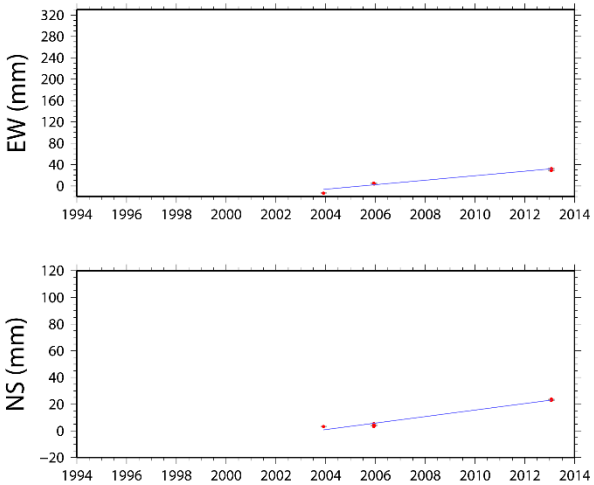


MOC0

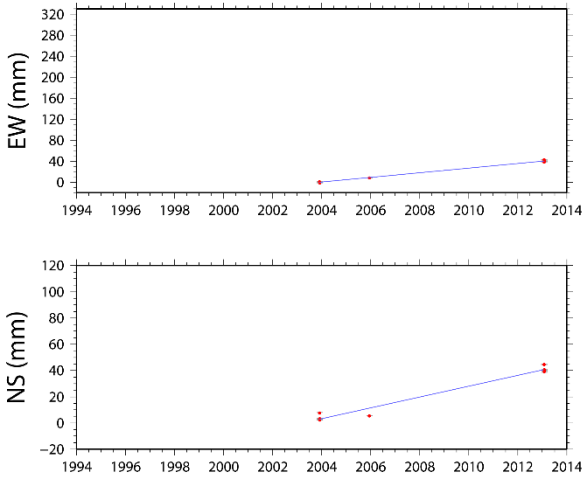


PCN0

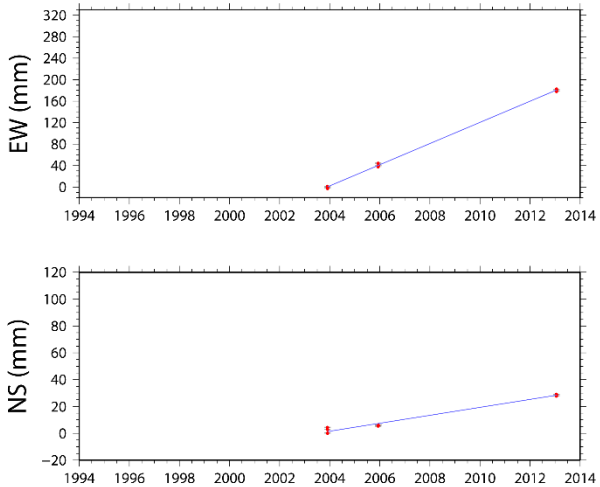


QUI0

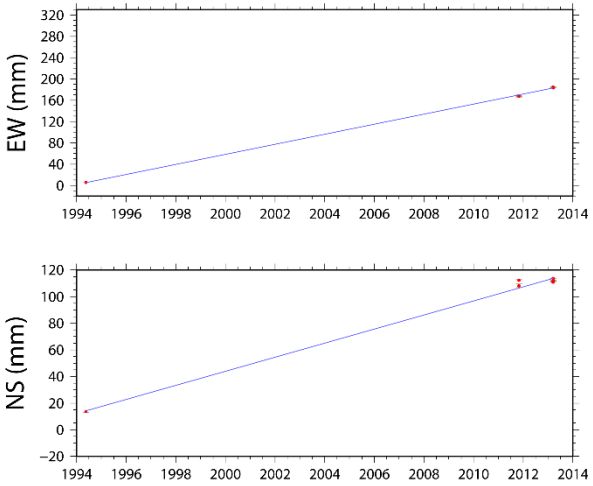

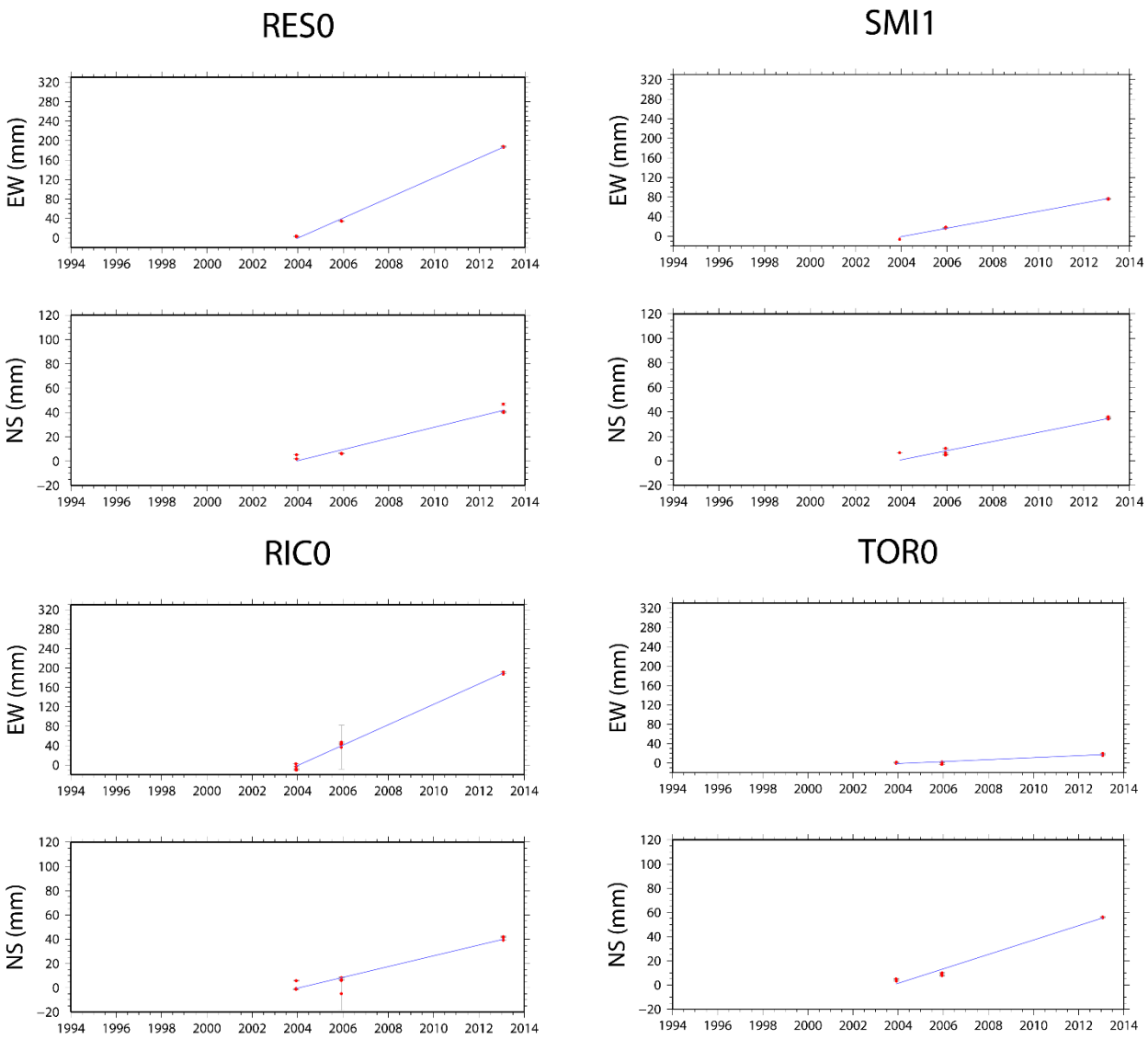
RES0
SMI1
RIC0
TOR0
EW (mm)
NS (mm)
1994 1996 1998 2000 2002 2004 2006 2008 2010 2012 2014

## Appendix B

# OBSERVED VELOCITIES

***Table B.1.*** *Velocities expressed in the IGb08 reference frame*

| Station | Long (deg) | Lat (deg) | Ve (mm/yr) | Vn (mm/yr) | σVe (mm/yr) | σVn (mm/yr) |
|---|---|---|---|---|---|---|
| **Eastern and Western Venezuela Campaigns** | | | | | | |
| AMU0 | -70.188 | 11.753 | 10.02 | 18.41 | 1.6 | 1.6 |
| ARAY | -63.711 | 10.655 | 18.71 | 18.31 | 0.4 | 0.4 |
| ARI0 | -63.749 | 10.511 | 11.07 | 12.32 | 0.2 | 0.2 |
| ARR0 | -64.291 | 10.370 | 0.80 | 13.18 | 0.3 | 0.2 |
| ARY0 | -64.236 | 10.571 | 10.75 | 14.28 | 0.2 | 0.2 |
| AUD0 | -64.081 | 10.447 | 1.32 | 14.29 | 0.1 | 0.1 |
| BAU0 | -68.158 | 9.118 | -1.65 | 9.06 | 2.1 | 1.7 |
| BIC0 | -63.965 | 10.770 | 13.52 | 14.95 | 0.2 | 0.2 |
| BOZ0 | -70.746 | 10.819 | 12.17 | 18.39 | 2.9 | 2.2 |
| BTA0 | -70.367 | 8.726 | -1.02 | 14.02 | 1.4 | 1.1 |
| CAC0 | -63.837 | 10.553 | 11.63 | 12.80 | 0.3 | 0.3 |
| CHA0 | -64.156 | 10.841 | 13.69 | 15.08 | 0.3 | 0.2 |
| COI0 | -63.116 | 10.415 | -1.59 | 14.99 | 0.4 | 0.4 |
| COP0 | -69.454 | 10.442 | 9.70 | 19.87 | 1.9 | 1.6 |
| COR0 | -64.184 | 10.831 | 13.88 | 15.10 | 0.3 | 0.2 |
| COV0 | -63.603 | 10.136 | -2.74 | 13.16 | 0.2 | 0.2 |
| DAL0 | -72.314 | 8.267 | -0.56 | 8.79 | 1.8 | 1.6 |
| GAL0 | -64.188 | 10.802 | 13.69 | 14.90 | 0.2 | 0.2 |
| HOR0 | -64.291 | 10.965 | 14.61 | 15.62 | 0.2 | 0.2 |
| HSR0 | -68.538 | 9.661 | -3.29 | 16.89 | 1.6 | 1.4 |
| IPU0 | -63.751 | 10.122 | -2.91 | 12.00 | 1.0 | 0.9 |
| ISL0 | -63.896 | 10.884 | 14.66 | 14.72 | 0.2 | 0.2 |
| KYP0 | -69.999 | 8.524 | -7.57 | 20.21 | 1.8 | 1.6 |
| MAC0 | -70.204 | 12.089 | 14.64 | 16.87 | 1.6 | 1.3 |
| MAN0 | -63.895 | 11.156 | 14.99 | 14.61 | 1.0 | 0.9 |

| | | | | | | |
|---|---|---|---|---|---|---|
| MARG | -64.360 | 11.042 | 16.65 | 16.48 | 0.2 | 0.2 |
| MCH0 | -63.811 | 10.707 | 13.24 | 14.95 | 0.2 | 0.2 |
| MNG0 | -63.875 | 10.314 | 4.15 | 10.66 | 1.0 | 0.9 |
| MOC0 | -64.344 | 10.346 | -1.27 | 15.26 | 0.2 | 0.2 |
| NIR0 | -68.536 | 10.152 | -6.00 | 15.23 | 1.5 | 1.3 |
| PAR0 | -64.231 | 10.508 | 8.67 | 14.36 | 0.2 | 0.2 |
| PAV0 | -71.120 | 10.189 | 10.32 | 7.77 | 1.9 | 1.5 |
| PCN0 | -63.637 | 10.636 | 14.03 | 13.94 | 0.2 | 0.2 |
| PED0 | -71.566 | 7.540 | -8.58 | 12.22 | 1.7 | 1.4 |
| PER0 | -63.767 | 10.446 | -2.42 | 13.30 | 0.4 | 0.3 |
| PIA0 | -63.337 | 7.358 | 0.74 | 11.92 | 1.0 | 0.9 |
| PIG0 | -64.083 | 10.637 | 11.86 | 13.81 | 0.3 | 0.2 |
| POR0 | -69.917 | 11.789 | 13.22 | 22.29 | 3.2 | 2.8 |
| PPI0 | -62.404 | 10.547 | 12.67 | 14.02 | 1.0 | 0.9 |
| PRE0 | -71.775 | 8.029 | 3.47 | 10.40 | 1.5 | 1.2 |
| QUI0 | -69.646 | 9.871 | 3.94 | 16.12 | 0.3 | 0.4 |
| RAG0 | -62.974 | 10.582 | 15.00 | 15.10 | 0.4 | 0.4 |
| RES0 | -64.209 | 11.053 | 14.73 | 15.17 | 0.2 | 0.2 |
| RIC0 | -63.120 | 10.701 | 15.01 | 15.33 | 0.2 | 0.2 |
| RSA0 | -62.205 | 10.636 | -0.22 | 3.77 | 3.9 | 4.4 |
| SAL0 | -62.274 | 10.604 | 12.60 | 17.78 | 1.5 | 1.3 |
| SAR0 | -70.001 | 12.180 | 16.73 | 15.71 | 3.1 | 2.9 |
| SMI1 | -63.519 | 10.492 | 2.78 | 14.54 | 0.2 | 0.2 |
| SUL0 | -63.910 | 10.757 | 14.13 | 14.65 | 0.3 | 0.2 |
| TAC0 | -63.977 | 9.954 | -3.75 | 16.30 | 0.3 | 0.3 |
| TAL0 | -71.681 | 7.801 | 6.94 | 3.35 | 2.1 | 1.8 |
| TET0 | -64.127 | 10.963 | 14.94 | 15.66 | 0.3 | 0.3 |
| TOR0 | -63.569 | 10.352 | -3.82 | 16.88 | 0.2 | 0.2 |

| | | | | | | |
|---|---|---|---|---|---|---|
| UMU0 | -72.050 | 8.235 | 3.14 | 16.78 | 1.4 | 1.2 |
| URI0 | -71.743 | 7.913 | -3.28 | 19.12 | 1.7 | 1.4 |
| VAN0 | -71.882 | 8.092 | 3.72 | 9.07 | 1.6 | 1.3 |
| VIC0 | -71.327 | 10.379 | 7.62 | 24.05 | 2.7 | 2.1 |
| YAG0 | -70.530 | 10.062 | 10.64 | 9.59 | 2.4 | 1.9 |
| **Complementary stations** | | | | | | |
| 0115* | -61.658 | 10.098 | 3.06 | 13.70 | 0.6 | 0.7 |
| ABMF | -61.528 | 16.262 | 11.88 | 16.71 | 0.2 | 0.2 |
| ABRE* | -73.226 | 8.087 | 1.71 | 22.72 | 5.4 | 5.7 |
| ACHI* | -73.577 | 8.246 | -12.55 | 5.80 | 3.0 | 2.4 |
| ALBN | -61.515 | 10.663 | 12.68 | 15.09 | 1.5 | 1.2 |
| ALPA | -72.918 | 11.528 | 8.56 | 17.00 | 0.2 | 0.2 |
| AVES* | -63.618 | 15.667 | 17.31 | 15.81 | 0.4 | 0.3 |
| BARI | -70.239 | 8.613 | -8.84 | 14.10 | 1.1 | 0.8 |
| BDOS | -59.609 | 13.088 | 13.00 | 15.94 | 0.1 | 0.1 |
| BOGT[1] | -74.081 | 4.640 | -0.69 | 16.84 | 0.1 | 0.1 |
| BRAZ[1] | -47.878 | -15.947 | -1.14 | 10.79 | 0.1 | 0.1 |
| BRFT[1] | -38.426 | -3.877 | 0.72 | 11.23 | 0.1 | 0.1 |
| BRMU[1] | -64.696 | 32.370 | -11.14 | 13.91 | 0.1 | 0.1 |
| BYSP | -66.161 | 18.408 | 9.64 | 17.31 | 0.2 | 0.2 |
| CARA | -66.914 | 10.503 | -0.45 | 11.88 | 0.1 | 0.1 |
| CART | -75.534 | 10.391 | 15.41 | 9.65 | 0.9 | 0.7 |
| CHPI | -44.985 | -22.687 | -0.55 | 7.32 | 0.1 | 0.1 |
| CIC1[1] | -116.666 | 31.871 | -45.25 | 23.30 | 0.1 | 0.1 |
| CLDR | -60.731 | 11.196 | 14.09 | 20.90 | 1.3 | 1.1 |
| CN10 | -75.971 | 17.415 | 8.39 | 13.43 | 0.2 | 0.2 |
| CN36 | -75.821 | 8.820 | 7.76 | 16.63 | 0.5 | 0.4 |
| CN37 | -75.263 | 10.793 | 10.90 | 20.80 | 0.2 | 0.2 |

| | | | | | | |
|---|---|---|---|---|---|---|
| CN38 | -71.988 | 12.222 | 12.98 | 20.00 | 0.2 | 0.2 |
| CN40 | -68.958 | 12.180 | 13.81 | 17.71 | 0.1 | 0.1 |
| CORD | -64.470 | -31.528 | -2.42 | 6.09 | 0.2 | 0.2 |
| CORO | -75.288 | 9.328 | 11.16 | 16.78 | 0.2 | 0.2 |
| COYU | -100.081 | 17.008 | -2.32 | 13.23 | 0.1 | 0.1 |
| CRO1[1] | -64.584 | 17.757 | 11.42 | 16.44 | 0.1 | 0.1 |
| CUC1 | -72.513 | 7.932 | 15.61 | 16.33 | 0.3 | 0.2 |
| CUMA | -64.195 | 10.429 | 1.17 | 15.03 | 0.1 | 0.1 |
| DOAR | -99.651 | 17.021 | -1.73 | 16.48 | 0.1 | 0.1 |
| FORT[1] | -38.426 | -3.877 | 0.98 | 13.98 | 0.1 | 0.1 |
| FRTN | -61.683 | 10.171 | -0.21 | 19.72 | 1.5 | 1.2 |
| FTMD* | -60.843 | 11.154 | 31.01 | 41.63 | 0.7 | 0.7 |
| GLPS[1] | -90.304 | -0.743 | 46.86 | 9.02 | 0.1 | 0.1 |
| GLTA | -60.995 | 10.147 | 0.24 | 8.83 | 1.3 | 1.1 |
| GMAS[1] | -15.634 | 27.765 | 23.68 | 18.97 | 0.3 | 0.3 |
| GRE0 | -61.640 | 12.222 | 14.94 | 17.83 | 0.2 | 0.2 |
| GRND | -61.128 | 10.586 | 11.64 | 15.92 | 1.4 | 1.2 |
| GUAT[1] | -90.520 | 14.590 | 1.76 | 5.41 | 0.1 | 0.1 |
| JAMA | -76.781 | 17.939 | -10.79 | 0.43 | 1.5 | 1.3 |
| JUAN* | -63.369 | 10.357 | -11.03 | 18.29 | 1.6 | 1.7 |
| KOU1 | -52.806 | 5.252 | -2.50 | 13.05 | 0.1 | 0.1 |
| KOUR | -52.806 | 5.252 | -2.12 | 13.81 | 0.1 | 0.1 |
| KYW1 | -81.653 | 24.582 | -9.16 | 5.94 | 0.4 | 0.4 |
| LMMF | -60.996 | 14.595 | 12.50 | 17.44 | 0.2 | 0.1 |
| LMNL | -85.053 | 10.268 | 10.35 | 21.60 | 0.2 | 0.2 |
| MANA[1] | -86.249 | 12.149 | 3.48 | 8.69 | 0.1 | 0.1 |
| MARA | -71.624 | 10.674 | 6.48 | 15.57 | 0.2 | 0.2 |
| MAS1[1] | -15.633 | 27.764 | 24.20 | 20.81 | 0.4 | 0.3 |

| | | | | | | |
|---|---|---|---|---|---|---|
| MDO1[1] | -104.015 | 30.681 | -18.19 | -1.59 | 0.2 | 0.2 |
| P780 | -66.579 | 18.075 | 9.47 | 16.55 | 0.2 | 0.2 |
| PAL1 | -73.189 | 7.136 | 2.33 | 16.21 | 0.1 | 0.1 |
| PUR3 | -67.067 | 18.463 | 8.56 | 15.81 | 0.1 | 0.1 |
| QSEC | -85.357 | 9.840 | 11.46 | 26.07 | 0.2 | 0.2 |
| QUI2[1] | -78.494 | -0.215 | 7.32 | 10.92 | 0.1 | 0.1 |
| RIOP | -78.651 | -1.651 | -0.16 | 8.06 | 0.2 | 0.2 |
| SA27 | -110.961 | 29.082 | -15.86 | -2.68 | 0.2 | 0.2 |
| SAN0 | -81.716 | 12.580 | 9.22 | 8.95 | 0.2 | 0.2 |
| SANT[1] | -70.669 | -33.150 | 8.31 | 2.76 | 0.1 | 0.1 |
| SCUB[1] | -75.762 | 20.012 | -6.43 | 8.81 | 0.1 | 0.1 |
| SG21 | -99.189 | 19.741 | -12.61 | 2.51 | 0.4 | 0.3 |
| SSIA[1] | -89.117 | 13.697 | 3.77 | 7.85 | 0.1 | 0.1 |
| UWAS | -72.391 | 6.451 | 2.18 | 13.57 | 0.2 | 0.2 |
| VMAG | -74.847 | 9.287 | 7.36 | 17.05 | 0.2 | 0.2 |

(*) Stations measured in field acquisition campaigns.

(1) Stations defined in the IGb08 reference frame for BERNESE GNSS Software 5.2

***Table B.2.*** *Eastern and Western Venezuela Velocities expressed in the stable South America reference frame proposed by Altamimi et al. (2012).*

| Station | Long (deg) | Lat (deg) | Ve (mm/yr) | Vn (mm/yr) | σVe (mm/yr) | σVn (mm/yr) |
|---|---|---|---|---|---|---|
| AMU0 | -70.188 | 11.753 | 16.00 | 8.08 | 1.6 | 1.6 |
| ARAY | -63.711 | 10.655 | 24.36 | 7.32 | 0.4 | 0.4 |
| ARI0 | -63.749 | 10.511 | 16.71 | 1.33 | 0.2 | 0.2 |
| ARR0 | -64.291 | 10.370 | 6.45 | 2.24 | 0.3 | 0.2 |
| ARY0 | -64.236 | 10.571 | 16.41 | 3.33 | 0.2 | 0.2 |
| AUD0 | -64.081 | 10.447 | 6.97 | 3.33 | 0.1 | 0.1 |
| BAU0 | -68.158 | 9.118 | 4.02 | -1.49 | 2.1 | 1.7 |
| BIC0 | -63.965 | 10.770 | 19.19 | 3.98 | 0.2 | 0.2 |
| BOZ0 | -70.746 | 10.819 | 18.08 | 8.13 | 2.9 | 2.2 |
| BTA0 | -70.367 | 8.726 | 4.67 | 3.71 | 1.4 | 1.1 |
| CAC0 | -63.837 | 10.553 | 17.28 | 1.82 | 0.3 | 0.3 |
| CHA0 | -64.156 | 10.841 | 19.37 | 4.13 | 0.3 | 0.2 |
| COI0 | -63.116 | 10.415 | 4.02 | 3.94 | 0.4 | 0.4 |
| COP0 | -69.454 | 10.442 | 15.53 | 9.46 | 1.9 | 1.6 |
| COR0 | -64.184 | 10.831 | 19.56 | 4.15 | 0.3 | 0.2 |
| COV0 | -63.603 | 10.136 | 2.87 | 2.15 | 0.2 | 0.2 |
| DAL0 | -72.314 | 8.267 | 5.14 | -1.29 | 1.8 | 1.6 |
| GAL0 | -64.188 | 10.802 | 19.37 | 3.95 | 0.2 | 0.2 |
| HOR0 | -64.291 | 10.965 | 20.31 | 4.68 | 0.2 | 0.2 |
| HSR0 | -68.538 | 9.661 | 2.44 | 6.38 | 1.6 | 1.4 |
| IPU0 | -63.751 | 10.122 | 2.70 | 1.01 | 1.0 | 0.9 |
| ISL0 | -63.896 | 10.884 | 20.34 | 3.74 | 0.2 | 0.2 |
| KYP0 | -69.999 | 8.524 | -1.91 | 9.86 | 1.8 | 1.6 |
| MAC0 | -70.204 | 12.089 | 20.65 | 6.54 | 1.6 | 1.3 |
| MAN0 | -63.895 | 11.156 | 20.69 | 3.63 | 1.0 | 0.9 |

| | | | | | | |
|---|---|---|---|---|---|---|
| MARG | -64.360 | 11.042 | 20.46 | 5.32 | 0.2 | 0.2 |
| MCH0 | -63.811 | 10.707 | 18.90 | 3.96 | 0.2 | 0.2 |
| MNG0 | -63.875 | 10.314 | 9.78 | -0.32 | 1.0 | 0.9 |
| MOC0 | -64.344 | 10.346 | 4.38 | 4.32 | 0.2 | 0.2 |
| NIR0 | -68.536 | 10.152 | -0.23 | 4.72 | 1.5 | 1.3 |
| PAR0 | -64.231 | 10.508 | 14.33 | 3.41 | 0.2 | 0.2 |
| PAV0 | -71.120 | 10.189 | 16.18 | -2.45 | 1.9 | 1.5 |
| PCN0 | -63.637 | 10.636 | 19.68 | 2.94 | 0.2 | 0.2 |
| PED0 | -71.566 | 7.540 | -2.98 | 2.05 | 1.7 | 1.4 |
| PER0 | -63.767 | 10.446 | 3.22 | 2.31 | 0.4 | 0.3 |
| PIA0 | -63.337 | 7.358 | 6.13 | 0.89 | 1.0 | 0.9 |
| PIG0 | -64.083 | 10.637 | 17.52 | 2.85 | 0.3 | 0.2 |
| POR0 | -69.917 | 11.789 | 19.19 | 11.93 | 3.2 | 2.8 |
| PPI0 | -62.404 | 10.547 | 18.27 | 2.91 | 1.0 | 0.9 |
| PRE0 | -71.775 | 8.029 | 9.13 | 0.25 | 1.5 | 1.2 |
| QUI0 | -69.646 | 9.871 | 9.72 | 5.73 | 0.3 | 0.4 |
| RAG0 | -62.974 | 10.582 | 20.62 | 4.04 | 0.4 | 0.4 |
| RES0 | -64.209 | 11.053 | 20.43 | 4.22 | 0.2 | 0.2 |
| RIC0 | -63.120 | 10.701 | 20.65 | 4.28 | 0.2 | 0.2 |
| RSA0 | -62.205 | 10.636 | 5.38 | -7.36 | 3.9 | 4.4 |
| SAL0 | -62.274 | 10.604 | 18.20 | 6.66 | 1.5 | 1.3 |
| SAR0 | -70.001 | 12.180 | 22.74 | 5.36 | 3.1 | 2.9 |
| SMI1 | -63.519 | 10.492 | 8.41 | 3.53 | 0.2 | 0.2 |
| SUL0 | -63.910 | 10.757 | 19.80 | 3.67 | 0.3 | 0.2 |
| TAC0 | -63.977 | 9.954 | 1.86 | 5.33 | 0.3 | 0.3 |
| TAL0 | -71.681 | 7.801 | 12.57 | -6.81 | 2.1 | 1.8 |
| TET0 | -64.127 | 10.963 | 20.63 | 4.70 | 0.3 | 0.3 |
| TOR0 | -63.569 | 10.352 | 1.81 | 5.87 | 0.2 | 0.2 |

| | | | | | | |
|---|---|---|---|---|---|---|
| UMU0 | -72.050 | 8.235 | 8.83 | 6.67 | 1.4 | 1.2 |
| URI0 | -71.743 | 7.913 | 2.37 | 8.97 | 1.7 | 1.4 |
| VAN0 | -71.882 | 8.092 | 9.39 | -1.07 | 1.6 | 1.3 |
| VIC0 | -71.327 | 10.379 | 13.50 | 13.85 | 2.7 | 2.1 |
| YAG0 | -70.530 | 10.062 | 16.47 | -0.70 | 2.4 | 1.9 |
| BARI* | -70.239 | 8.613 | -3.16 | 3.78 | 1.1 | 0.8 |
| CARA* | -66.914 | 10.503 | 5.30 | 1.20 | 0.1 | 0.1 |
| CUMA* | -64.195 | 10.429 | 6.82 | 4.08 | 0.1 | 0.1 |
| MARA* | -71.624 | 10.674 | 12.40 | 5.41 | 0.2 | 0.2 |

(*) cGNSS stations.